## INFORMATION TO USERS

The most advanced technology has been used to photograph and reproduce this manuscript from the microfilm master. UMI films the text directly from the original or copy submitted. Thus, some thesis and dissertation copies are in typewriter face, while others may be from any type of computer printer.

The quality of this reproduction is dependent upon the quality of the copy submitted. Broken or indistinct print, colored or poor quality illustrations and photographs, print bleedthrough, substandard margins, and improper alignment can adversely affect reproduction.

In the unlikely event that the author did not send UMI a complete manuscript and there are missing pages, these will be noted. Also, if unauthorized copyright material had to be removed, a note will indicate the deletion.

Oversize materials (e.g., maps, drawings, charts) are reproduced by sectioning the original, beginning at the upper left-hand corner and continuing from left to right in equal sections with small overlaps. Each original is also photographed in one exposure and is included in reduced form at the back of the book. These are also available as one exposure on a standard 35mm slide or as a 17" x 23" black and white photographic print for an additional charge.

Photographs included in the original manuscript have been reproduced xerographically in this copy. Higher quality 6" x 9" black and white photographic prints are available for any photographs or illustrations appearing in this copy for an additional charge. Contact UMI directly to order.

UMI

University Microfilms International
A Bell & Howell Information Company
300 North Zeeb Road, Ann Arbor, MI 48106-1346 USA
313/761-4700 800/521-0600

Order Number 8911648

# Equatorial wave-mean flow interaction: The long Rossby waves

Proehl, Jeffrey Alan, Ph.D.

University of Washington, 1988

U·M·I

300 N. Zeeb Rd.
Ann Arbor, MI 48106

Equatorial Wave-Mean Flow Interaction: The Long Rossby Waves

by

Jeffrey A. Proehl

A dissertation submitted in partial fulfillment
of the requirements for the degree of

Doctor of Philosophy

University of Washington

1988

Approved by Michael J. McPhaden
(Chairperson of Supervisory Committee)

Program Authorized
to Offer Degree School of Oceanography

Date 22 NOVEMBER 1988

In presenting this dissertation in partial fulfillment of the requirements for the Doctoral degree at the University of Washington, I agree that the Library shall make its copies freely available for inspection. I further agree that extensive copying of this dissertation is allowable only for scholarly purposes, consistent with "fair use" as prescribed in the U.S. Copyright Law. Requests for copying or reproduction of this dissertation may be referred to University Microfilms, 300 North Zeeb Road, Ann Arbor, Michigan, 48106, to whom the author has granted "the right to reproduce and sell (a) copies of the manuscript in microform and/or (b) printed copies of the manuscript made from microform."

Signature 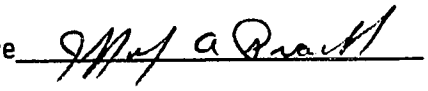

Date 22 NOVEMBER 1988

University of Washington

Abstract

Equatorial Wave-Mean Flow Interaction: The Long Rossby Waves

by Jeffrey A. Proehl

Chairperson of the Supervisory Committee: Professor Michael J. McPhaden
School of Oceanography

The interaction of long equatorial Rossby waves with mean zonal currents in the ocean is investigated in a continuously stratified finite difference numerical model. The model allows for realistic specification of the mean state including both vertical and meridional shear of the mean flow.

In addition to stretching of wave scales expected from slowly varying wave theory, one effect of strongly sheared mean flows is to cause meridional scattering of wave energy. This scattering, which cannot be treated by slowly varying theory, causes wave energy input at the surface in an equatorially confined structure to be sent poleward. This scattering of wave activity, depicted by reflection of the Eliassen-Palm flux off the mean shear, causes structural changes to the no-flow wave solutions. As a result, for realistic mean flows, wave energy appears at higher latitudes and a shadow zone occurs below the Equatorial Undercurrent in the near equatorial zone. The lateral shear of the Undercurrent also causes equatorward focusing of wave energy input at higher latitudes.

The case of westward flow shows that the changes in resonant phase speeds and wave structures can be very large. Due to the scattering nature of rapidly varying flow, the presence of an equatorially confined critical layer does not preclude the radiation of wave activity into the deep ocean as it does for the Kelvin waves (McPhaden *et al.*, 1986). However, wave activity which reaches the deep ocean does so at higher latitudes.

The wave induced mean accelerations for both the resting ocean and for an eastward Undercurrent in this model are dominated by frictional dissipation of wave energy and, therefore, are relatively weak. The induced accelerations for westward flows, where $(c-U)\rightarrow 0$, show behavior similar to Kelvin waves in eastward flow in that large divergences of the EP flux exist leading to large momentum transfers from wave to mean states. The primary difference from the Kelvin waves is that the wave-induced residual circulation is important locally and leads to significant accelerations. These accelerations are primarily due to Coriolis torque with a lesser contribution from the residual advection of mean momentum.

TABLE OF CONTENTS

LIST OF FIGURES

# LIST OF TABLES

Number Page

## ACKNOWLEDGEMENTS

I wish to express extreme gratitude to my 'co-advisors' in this work ... Mike McPhaden and Lew Rothstein. Without their interest and enthusiasm this work would have clearly been impossible. In addition, I am deeply indebted to my earlier advisors, Björn Kjerfve, who sparked my interest in physical oceanography, and Donald Winter and Maurice Rattray, Jr., who gave me the solid foundation on which to set forth.

A large debt of gratitude, however, goes to my fellow students who helped pass the time with many fascinating discussions tempered with just enough idle banter and never enough espresso. In particular, my office mates and pseudo-office mates, Bruce Long, Mary Landsteiner, Susan Lozier, David Pierce, Francisco Werner, Eric Lindstrom and David Battisti were crucial to maintaining what little sanity I possess. I will never forget!

But mostly I am grateful for the love and support of my wife, Jean without whom I might have long ago given up and my son, Christopher, who taught me that, while they are not equal, there are indeed two 5 o'clock's in every day.

"... He who crosses this bridge must answer me these questions three ..." —— The Bridge Tender, *Monty Python and the Holy Grail.*

# Chapter 1: Background

Past equatorial modelling efforts have been concerned with either the pure linear wave theory in the absence of flow or the steady state dynamics. The details of many of these models, including reduced gravity and continuously stratified models, have been recently reviewed by McCreary (1985). One aspect of equatorial dynamics which has yet to be fully clarified is the effect of the narrow, intense equatorial current system on Rossby wave propagation in this region.

The interaction of equatorial waves with mean flows has received relatively little attention in the oceanographic literature. From a theoretical standpoint, the main focus of the few studies that have occurred is the interaction of the Kelvin waves with flow with much less work done on Rossby waves. Complementary studies by McPhaden and Knox (1979) and Philander (1979) investigated the effects of latitudinally sheared jets on zonal wave propagation in a two-layered context using a perturbation approach. The two-layered approach necessarily prohibits the inclusion of realistic vertical shears in the mean flows. The study of McPhaden and Knox (1979), which was limited to the Kelvin and inertia-gravity wave range of dispersion space, avoided the possibility of critical layers and instability by restricting attention to eastward phase speeds everywhere greater than the mean flow. They reported significant Doppler shifting of both wave types. The case of the Kelvin wave showed only slight distortion of the latitudinal structure. While the pressure field for the inertia-gravity wave also was only slightly affected, this wave showed substantial distortion of

the zonal velocity structure due to flow. Philander (1979) suggested that the Rossby waves, which were included in his study, might scatter to higher latitudes in the presence of the Equatorial Undercurrent. He found that for eastward background flows which lacked meridional shear, short Rossby waves, which normally propagate phase westward, could be swept downstream through the action of Doppler shifting resulting in eastward phase propagation. For flows possessing meridional shear this eastward propagation was eliminated although significant Doppler shifting was still apparent. Ripa and Marinone (1983) investigated a one-layer reduced gravity equatorial ocean using a perturbation expansion similar to McPhaden and Knox (1979). In addition to investigating changes to wave dispersion, they derived numerical solutions for both stable and unstable wave modes. In all of these studies, the layered formulation still led to a sufficiently complicated ordinary differential equation such that numerical treatment was necessary.

More recently, McPhaden *et al.* (1986) investigated the interaction of long equatorial Kelvin waves with background flow in a continuously stratified ocean. The formulation used in that study is identical to that which is employed here. In particular, the inclusion of continuous stratification, which for that study was limited to a constant $N^2$ resting state, allows for a more realistic treatment of vertical structure of the mean flow. Principal results of that work were that baroclinic mean flows cause significant modifications of the structure of the wave fields, critical layers present a strong, if not impenetrable, barrier to vertical wave radiation and that significant energy transfer occurs between the waves and the mean state. In a companion

study, McPhaden *et al.* (1987) considered the case of variable $N^2$ and concentrated on the structural variations of low baroclinic modes induced by the flow. Results showed that the inclusion of realistic mean flows in the upper ocean could shift the location of the first zero crossing of the lowest modes up to 100m in the vertical and introduce small scale vertical/meridional features where $u \neq 0$.

Recently, Chang and Philander (1988) revisited the ray tracing work of Schopf, *et al.* (1981) by including zonal mean flows trapped to the equator. Their reduced gravity model necessarily assumed the flows to be slowly varying latitudinally and neglected the effect of vertical shear. Nevertheless, their results showed that the meridional propagation of Rossby wave rays can be strongly affected by the presence of mean flows. The tendency found was for eastward flows to enhance the meridional propagation and westward flows to inhibit it.

Analogous numerical problems were first investigated in the atmosphere nearly two decades ago (Holton, 1970; Lindzen, 1970). The study of Lindzen (1970) included continuous stratification but only vertical shear was considered. Holton (1970), however, included both meridional and vertical shears in his geostrophically balanced zonal wind field. In his study of the Kelvin waves only, an analytic form was chosen for the wind profile and damping was included in the form of Rayleigh friction and Newtonian cooling. The primary results were: 1) waves approaching a critical surface undergo a contraction of vertical and meridional scales; 2) Kelvin wave energy is absorbed at the height of the critical layer on the equator even though the height of the critical surface may vary with latitude and; 3) momentum exchange

between the waves and the mean state is due to distortion of the wave field by the mean shear. Subsequent to these numerical studies, it was realized that the zonal wind was sufficiently "slowly varying" to allow treatment of the equations through the WKBJ approximation (Lindzen, 1971; 1972). Comparison with the WKBJ solutions validated the results obtained numerically and therefore demonstrated that for this problem the effects of critical layers can be parameterized in this way. In recent years, advances have been made which depend upon the background fields possessing sufficiently slowly varying vertical structure alone (Boyd, 1978) as occurs in the atmosphere. In this case, flow fields possessing arbitrary meridional structure can be treated using analytical procedures, ordinary perturbation methods or Hermite spectral methods depending upon the specific type of meridional structure present.

Beginning in the early sixties, Eliassen and Palm (1961) and Charney and Drazin (1961) began investigating the effects that the waves have upon the zonal mean flow. Out of this emerged a formalism for treating these problems. In particular, it was realized early on that under certain conditions the waves in fact can propagate through a zonal mean flow and leave it unaffected. These are the so called conditions for 'non-acceleration' or 'non-interaction' and occur whenever the waves are conservative and non-transient and the flow lacks critical surfaces with respect to the wave field. The early work has been refined and extended by various workers [for a review see Hoskins, 1983; McIntyre and Shepard, 1987]. The treatment revolves around reducing the equations for the acceleration of the mean state by

cancelling out that portion of the wave fluxes of heat and momentum which drive a mean meridional circulation cell but do not act to accelerate the zonal flow. In doing so, one defines a new vector quantity, termed the Eliassen-Palm (or EP) flux which represents the flux of wave activity and whose divergence is the sole wave driving of the acceleration of the mean state. The results of this formalism will be used to address the wave induced changes to the mean state.

From an observational standpoint the effect of the mean currents on the free wave structure and/or dispersion characteristics is of interest. The first sign of the presence of Rossby wave energy in the equatorial ocean appeared in the work of Meyers (1979). Meyers found westward phase propagation at the annual cycle in the 14° isotherm in the Pacific Ocean from the historical data. Shortly thereafter more evidence surfaced in the results of the Hawaii-Tahiti Shuttle experiment. Lukas and Firing (1985) reported the presence of a first meridional mode Rossby wave in the XBT data from that study. They were able to isolate the particular meridional mode using three different techniques to estimate the equivalent depth, h, all of which gave essentially the same result. The three estimates of the equivalent depth came from: 1) the dominant wavenumber component in the wind stress, 2) the meridional decay scale, $\alpha$, through use of the Rossby dispersion relation and 3) the vertical wavelength estimated from the vertical structure. Subsequent to this, Johnson (1987), using acoustic Doppler log data, reexamined the work of Lukas and Firing (1985) and attempted to improve the results by considering the effects of the mean flow. His approach was to perform a least squares fit to the annual

cycle and thereby map the vertical and meridional structures present. He found that the structure was indeed very much like the m=1 wave with significant change in the meridional structure occurring with depth consistent with the effects of flow predicted with the present model.

The broad goal of the present study is to address the effects that the strongly sheared equatorial flows have upon the equatorially trapped Rossby wave modes and vice-versa. In particular, the primary motivation is to find the resonant normal mode solutions for a specified mean flow. The type of forcing used, which is an imposed vertical velocity field, is designed to obtain these solutions in the most straightforward manner. As a result the forcing is not easily comparable to a more realistic wind stress forcing. However, many of the results from this study will shed light upon the results of wind forcing in the presence of mean flows in the equatorial ocean.

## Chapter 2: Equatorial Wave Theory with Background Flow:

### 2.1 Background State

The most pervasive characteristic of the equatorial zone in the ocean is the presence of strong zonal mean flows. These flows reside in the upper few hundred meters and have associated with them large vertical and meridional shears. A representative vertical-meridional section of the flow and density structure of this system from the Hawaii-Tahiti Shuttle experiment is presented in Fig. 2.1. Principle flows to note are the eastward flowing Equatorial Undercurrent (EUC) on the equator which is centered at 150 meters depth, the westward South Equatorial Current (SEC) on the equator at the surface south of 4.5°N and the eastward North Equatorial CounterCurrent (NECC) just visible near the surface at 5°N. Clearly the intricate structure of these currents is impossible to achieve using a two-layer formulation.

Therefore, we formulate the present model in a continuously stratified ocean. The ocean is assumed infinite zonally to avoid the effects of boundaries and to allow for a spectral treatment zonally. This assumption is important because it allows for a consistent treatment of the mean state. Therefore, while zonal boundary effects are certainly important for the adjustment of the ocean to changing wind forcing, they are beyond the scope of this study.

We begin by performing a Reynolds decomposition (*i.e.* $u=U+u'$, $v=v'$, ...) based upon the assumption of a time scale separation between wave and mean. For linearity we require the perturbations $(u',v',...)$ to be small, $O(\epsilon)$, compared to the mean. The lowest order zonally and temporally invariant mean state is assumed to be in thermal wind

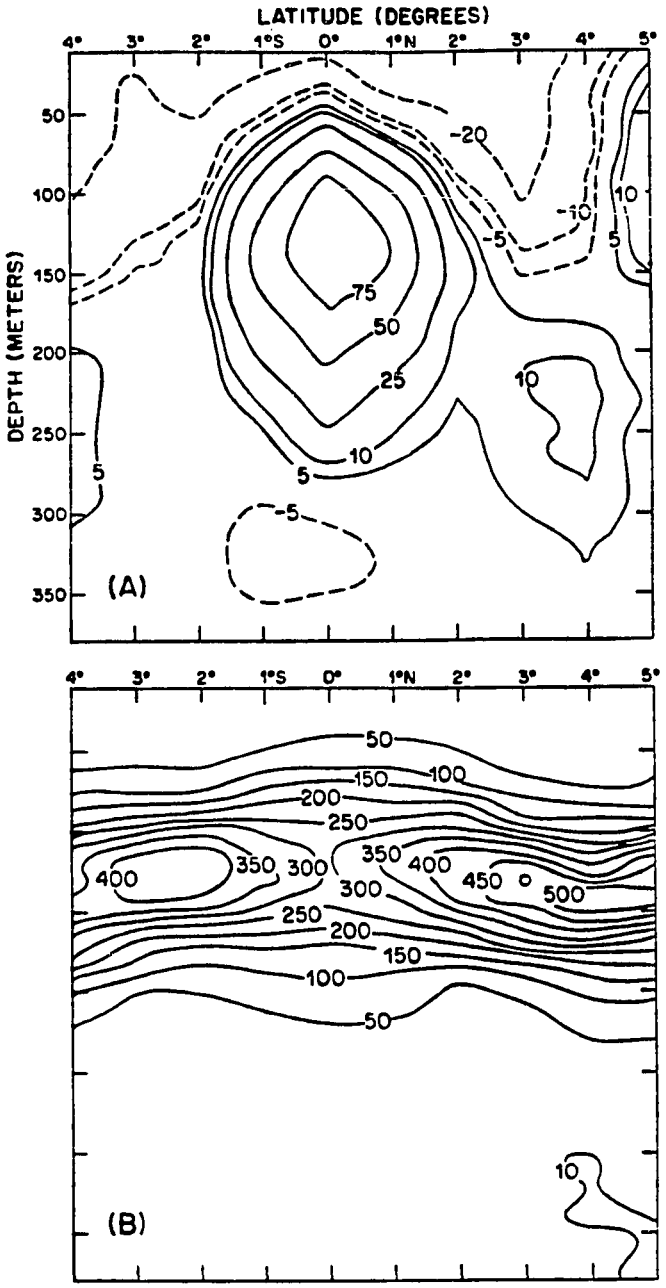


Figure 2.1: Observed mean state from Hawaii-Tahiti Shuttle experiment. (A) Zonal velocity (cm/s), (B) Squared Buoyancy Frequency ($x10^{-6}$ $s^{-2}$).

balance, inviscid and Boussinesq. Therefore, the governing equations are:

$$-\beta y U_{0zz} = N^2{}_y \tag{2.1}$$

$$V_0 = W_0 = 0 \tag{2.2}$$

Where $N^2 = \frac{-g}{\rho_*}\rho_{0z}$ and letter subscripts denote differentiation. In this construct, the background flow in the interior, U(y,z), and the background stratification, $N^2(y,z)$, are related by a constant in y and a function of z which are free to be specified. The only constraint imposed here is that the resulting stratification in the interior remain stable (*i.e.* $N^2>0$ for all y and z). For realistic simulations a further constraint will arise later which is tied to the idea of stability of the mean flow. From integrating the thermal wind balance, 2.1, meridionally the background stratification in the interior is given by

$$N^2(y,z) = N^2(\infty,z) + \int_y^\infty [\beta y U_{0zz}]dy \tag{2.3}.$$

So from this we see that stable stratification depends both upon the resting state density field, $N^2(\infty,z)$, and upon the integral of the vertical curvature of the background zonal flow field. It is noteworthy that in the absence of zonal boundaries or other x dependence, a zonally and temporally independent zonal background flow of this type satisfies the inviscid fully nonlinear Navier-Stokes equations exactly.

## 2.2 Wave dynamics

The dynamics of the perturbations, $O(\epsilon)$, is assumed to be linear, hydrostatic and Boussinesq. We introduce damping into the system through Rayleigh friction and Newtonian cooling with the same coefficient, $\kappa$. This is identical to the treatment of Holton (1970) and McPhaden *et al.* (1986) and is done to allow for investigation of the critical layer, where the differential equations would be singular. This form of friction, by parameterizing the critical layer as a highly dissipative layer, acts to remove the mathematical singularity which would otherwise be present. Assuming zonally propagating wave solutions, $e^{\iota(kx-\sigma t)}$ the governing equations, linearized about the background state $U_0$ and $\rho_0$, at this order become

$$-\iota(\sigma-kU_0)u + vU_{0y} + wU_{0z} - \beta yv = -\iota kp - \kappa u \qquad (2.4),$$

$$-\iota(\sigma-kU_0)v + \beta yu = -p_y - \kappa v \qquad (2.5),$$

$$\rho_* p_z = -g\rho \qquad (2.6),$$

$$\iota ku + v_y + w_z = 0 \qquad (2.7),$$

$$-\iota\sigma\rho + \iota kU_0\rho + v\rho_{0y} + w\rho_{0z} = -\kappa\rho \qquad (2.8).$$

The total density is given by $\rho^t(x,y,z,t) = \rho_* + \rho_0(y,z) + \rho(x,y,z,t)$, with $1/\rho_*$ having been absorbed into the definition of pressure. In the present study, we make the longwave approximation which reduces (2.5) to geostrophic balance (*ie.* neglect acceleration and damping terms in 2.5). For the special case $U_0$=constant, the governing equations (2.4)-(2.8) are separable in y and z and their equatorially trapped solutions in the inviscid limit are the well-known free equatorial waves (Moore and Philander, 1977; McCreary, 1981; also see Chapter 3).

In an ocean unbounded in latitude, these waves form a doubly countable infinite set which possess Hermite function dependence in latitude and vertical normal mode dependence with depth. They also have the property that they form complete orthogonal sets in both y and z, respectively.

The properties of the Hermite functions (aka parabolic cylinder functions), which are a weighted product of a Gaussian, ($e^{-\frac{1}{2}y^2}$), and the Hermite polynomials, $H_m(y)$, are well known as the solutions for a quantum oscillator (Arfken, 1970). For our purposes, we note that the solutions are equatorially confined due to the Gaussian dependence, the meridional velocity of the $m^{th}$ meridional mode possesses m zero crossings in latitude, the meridional modes can be defined to be orthonormal and that odd (even) numbered meridional modes possess odd (even) symmetry for v and even (odd) symmetry for all other variables.

However, in the presence of a zonal background flow of arbitrary y,z structure, the resulting set of equations is not separable and the above properties do not necessarily hold. The approach employed in this case involves deriving from the governing equations an equation for the perturbation pressure alone. Pressure was chosen over meridional velocity because it includes the Kelvin wave as a non-trivial solution. After manipulation, the resulting differential equation, dropping the subscript on $U_0$, is

$$p_{yy} + Ap_{yz} + Bp_{zz} + Cp_y + Dp_z + Ep = 0 \qquad (2.9)$$

where

$$A = \frac{2\beta y}{N^2}U_z$$

$$B = \frac{\beta y}{N^2}(\beta y - U_y)$$

$$C = \frac{-2}{y} - \frac{S_y}{S} + \beta y S\left[\frac{U_z}{N^2 S}\right]_z$$

$$D = \frac{\beta^2 y^2 S}{N^4}\left[\frac{U_z^2}{S}\right]_z + \beta y\left[\frac{U_z}{N^2}\right]_y - \frac{\beta^2 y^2 N^2}{N^4}\left[S + \frac{2U_z^2}{N^2}\right] - \frac{\beta U_z}{N^2 S}[yS]_y$$

$$E = \frac{1}{c^*}\left(\beta^2 y^2\left[\frac{U_z}{N^2 S}\right]_z - \frac{\beta}{S}(yS)_y\right)$$

where the intrinsic phase speed, $c^*$, is given by $c^* = c - U + \iota\kappa/k$, subscripts denote differentiation and S is defined by

$$S = 1 - \frac{U_z^2}{N^2} - \frac{U_y}{\beta y}.$$

This equation is equivalent to that derived by Holton (1970) except that we have retained terms involving the spatial derivatives of the background buoyancy field ($N^2$) which can be important for strongly sheared equatorial flows.

The solution procedure of (2.9) depends strongly upon the sign of the discriminant $\Gamma = A^2 - 4B = -4\beta^2 y^2 S/N^2$. An evaluation of $\Gamma$ from the Hawaii-Tahiti Shuttle experiment (Fig. 2.2) shows that $\Gamma$ is negative everywhere except at the equator (where $\Gamma=0$) and within a narrow region at the surface in the vicinity of both the North and South Equatorial Countercurrents. Consequently, (2.9) is elliptic for the currents used herein (EUC and SEC). Therefore, in solving (2.9) we must specify p, a non-tangential derivative of p or a linear combination of both on the bounding contour.

The problem is initially posed on an infinite strip in y bounded below by the ocean bottom, assumed flat, and above by the upper surface. In practice, the strip is truncated at latitudes sufficiently removed from the equator that all equatorial solutions have decayed to

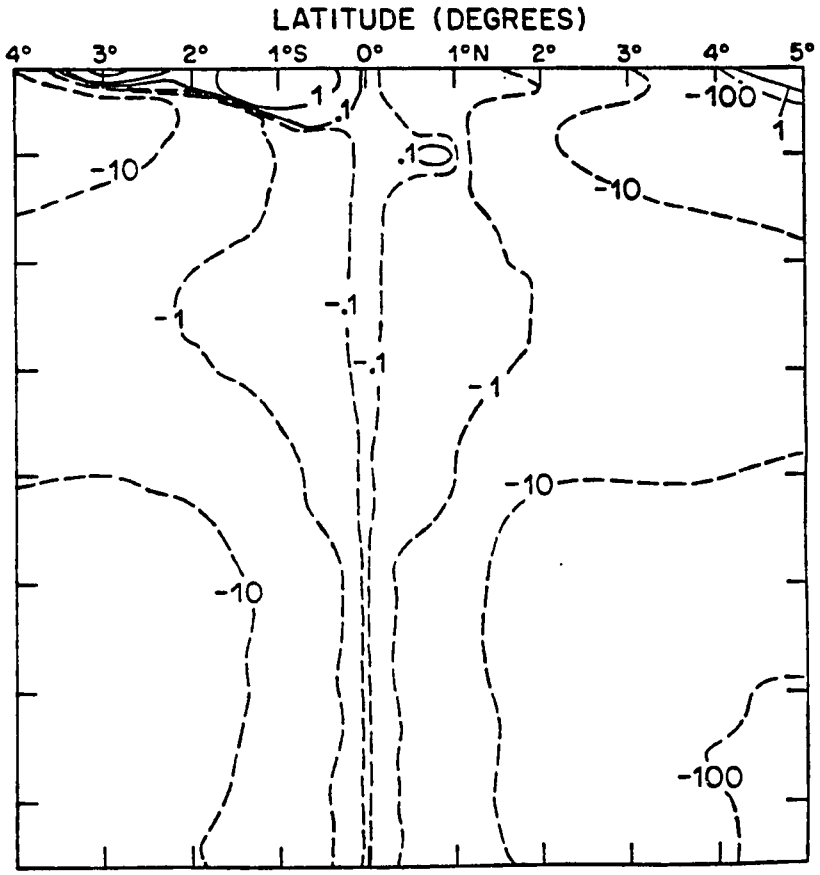


Figure 2.2: Discriminant of Eq. 2.9 for the Hawaii-Tahiti Shuttle Experiment profiles presented in Fig. 2.1.

zero. This truncation can be successfully done for all but the barotropic Rossby wave which possesses an infinite equatorial trapping scale. As a result, the boundary condition at this boundary must be specified as a radiation condition to allow for outward propagation of any barotropic Rossby wave energy. Otherwise, any small numerical error or wave scattering could lead to a resonance due to a meridionally standing barotropic wave.

The structure of the observed background flows and the properties of the equatorial waves allow for a considerable simplification. The fact that the Equatorial Undercurrent / South Equatorial Current system (Fig. 2.1) is very nearly symmetric about the equator, allows us to define the background flow, $U_0$, to be identically symmetric without significant loss of applicability. Therefore, the governing equation (2.9) is also symmetric. Combined with the symmetry properties of the equatorial wave modes, this allows us to redefine the domain as a semi-infinite strip bounded at the equator and subject to symmetry conditions there. We then specify a symmetric condition for odd m Rossby modes or anti-symmetric condition for even m. At the bottom we specify no normal flow, which is written in terms of a linear combination of p, $p_y$ and $p_z$. At the surface we force the solution with a specified w distribution, which is expressed in terms of p and and its vertical and meridional greadients. This assures that we do not obtain the trivial solution, p=0, everywhere. These conditions then are:

$$\left.\begin{array}{lll} p_y = 0 & \text{symmetry} & \\ \text{or} & & \text{at } y=0, \\ p = 0 & \text{antisymmetry} & \end{array}\right\}$$

$$p_y = \iota \ell p \qquad \text{barotropic radiation} \qquad \text{at } y=y_{max}.$$

| | | |
|---|---|---|
| $w = 0$ | rigid bottom | at z=-H, |
| $w = \Xi_m(y)$ | Surface pumping | at z=0, |

where $\ell$ is the meridional wavenumber of the poleward group velocity barotropic Rossby wave at the chosen $\sigma$ and k and $\Xi_m(y)$ is the meridional structure function for the vertical velocity of the $m^{th}$ meridional mode Rossby wave.

Our interest is in how the normal modes in the absence of flow are modified by the presence of mean shear. Due to the rigid bottom, we expect that analogues for vertical modes exist. Therefore, we specify the vertical velocity at the surface with the structure of the particular zero mean flow meridional mode of interest. A spectral sweep is performed by adjusting the zonal wavenumber at a fixed $\sigma$ until a resonant solution, as identified by an increase in the variance of the pressure solution, is attained. In the presence of a sheared background flow, however, the problem is no longer separable and the exact resonant structure functions are unknown. To illustrate this, consider the case of vertical wave propagation in an n-layer ocean. We assume, $U_0$ and $N^2$ are constant in each layer, so the problem becomes a meridional one with a constant Doppler shift in each layer. The meridional structure functions are the no-flow modes with $\omega=\sigma-kU_0$ in each layer. Associated with the change in the Doppler shift are changes in the vertical and meridional scales. Problems arise due to rapid variations in $U_0$, which introduce physically unrealistic jumps in the Doppler shift (and therefore the meridional scale) across the interfaces. These jumps lead to a mismatch in the meridional scale of the wave structures at the interface between any two layers. This mismatch

leads to scattering into other wave modes in order to satisfy the matching condition at the interface. This is the layered model's analogue of the physical process which occurs in the continuously stratified case. Therefore, it is reasonable to investigate the effect of a particular background flow upon a particular meridional mode by specifying w(y) at the surface as w(y) for a no-flow mode using $\omega=\sigma-kU_0$. In principle, what we desire is that some energy be input into the system to excite a particular resonant response. The structures discussed above are those that are likely to most efficiently excite the desired response. In practice, as long as the solution in the interior is resonant or because of the frictional damping, nearly resonant, its amplitude greatly exceeds that of the upper boundary condition. Therefore, for all practical purposes the solution satisfies w=0 at z=0 and is consequently a resonant mode of the new system. Therefore we are interested in comparing the resonant solutions to (2.9) obtained with this forcing to the modes in the resting ocean.

## 2.3 Wave Energetics

An important aspect of the interaction problem is the exchange of energy between wave and mean fields. The consideration of these exchanges yields information about the mechanisms involved in the radiation, scattering and/or absorption of wind forced equatorial wave energy. Consequently, here we derive the equation governing this flow of energy near the equator in the presence of strongly sheared flows.

Begin by forming the dot product of the velocity with the momentum equations to obtain:

$$\tfrac{1}{2}D(u^2+v^2) - wb = -uvU_y - uwU_z - \iota ku p - vp_y - wp_z \qquad (2.10)$$

where $D()=\partial_t() + \iota kU_0() + 2\kappa$ and $b=-g\rho/\rho_*$. Now from the heat equation, 2.8, we have

$$w = [-D\rho - v\rho_{0_y}]/\rho_{0_z} = [-Db + \beta y U_{0_z} v]/N^2 \qquad (2.11).$$

Therefore, we can write wb as

$$wb = -[\tfrac{1}{2}Db^2 - \beta y U_{0_z} vb]/N^2 \qquad (2.12).$$

Combining 2.7, 2.10 and 2.12 gives

$$\tfrac{1}{2}D[u^2+v^2+b^2/N^2] = -uvU_{0_y} - (uw - \beta yvb/N^2)U_{0_z} - \nabla\cdot(\vec{u}p) \qquad (2.13).$$

Now integrate over one wavelength in x, the depth and meridional width of the domain, denote $\int(\ )dx = \bar{(\ )}$ and define the wave energy, $\bar{E}$, as

$$\bar{E} = \tfrac{1}{2}\int_{-H}^{0}\int_{0}^{L} [\overline{u^2} + \overline{v^2} + \overline{b^2}/N^2]dydz \qquad (2.14).$$

Then the equation for the temporal change in the wave energy is

$$\bar{E}_t = -\int_{-H}^{0}\int_{0}^{L} [\overline{uv}U_{0_y} + \overline{uw}U_{0_z} - \beta y\overline{vb}U_{0_z}/N^2]dydz$$
$$- \int_{-H}^{0} \overline{vp}\Big|_0^L dz - \int_0^L \overline{wp}\Big|_{-H}^{0} dy - 2\kappa\bar{E} \qquad (2.15).$$

Since the wave field is not transient, by virtue of the harmonic x-t dependence, then $\bar{E}_t = 0$. The terms in the double integral represent work against horizontal shear, vertical shear and the background density field, respectively. The single integral terms represent pressure work on the waves at the boundaries (external forcing and

radiation) and the last term being energy loss due to frictional damping. Monitoring these fields helps to identify the sources and sinks of wave energy.

## 2.4 Wave Effects on the Mean Flow

To close the study of the interaction of waves and mean flows we study the dynamics for the wave induced changes to the mean state. This problem has been studied extensively in the atmospheric literature by Eliassen and Palm (1961), Charney and Drazin (1961), Lindzen and Holton (1968), Lindzen (1971, 1972), Holton and Lindzen (1972), Boyd (1976), Andrews and McIntyre (1976, 1978), Holton (1979) and others. For a review of the atmospheric literature on this topic see Hoskins (1983). Herein we follow the derivation of Boyd (1976) applied to the oceanic regime.

Carrying the perturbation expansion to $O(\epsilon^2)$, we find the dynamics for the wave induced acceleration of the mean zonal velocity field and associated adjustment of the mean baroclinic pressure field. The dynamics at this order reveal how the momentum exchanges between wave and mean are manifested in terms of mean field accelerations. These accelerations of the mean state arise from wave driving due to divergence of both the Reynolds stresses and heat fluxes in the meridional-vertical plane. The governing equations are:

$$U_t + (U_{0y} - \beta y)V + WU_{0z} = -(\overline{uv})_y - (\overline{uw})_z \tag{2.16}$$

$$V_y + W_z = 0 \tag{2.17}$$

$$\beta yU + P_y = 0 \tag{2.18}$$

$$P_t - \beta y V U_{0_z} + WN^2 = -(\overline{vp_z})_y - (\overline{wp_z})_z \qquad (2.19).$$

Here we distinguish between the zeroth order mean state, $U_0$, with a subscript and the $O(\epsilon^2)$ corrections, U, V, W and P without and we do not burden the background buoyancy field, $N^2$, with a 0 subscript. Following the work of Boyd (1976), the eddy flux terms are eliminated from (2.16) in favor of the heat flux terms by employing the governing equations for the perturbations. Begin by eliminating w between (2.4) and (2.8) to get

$$[-\iota k(c-U_0)+\kappa][u - U_{0_z}p_z/N^2] + v[U_{0_y} + \beta y U_{0_z}{}^2/N^2 - \beta y] = -\iota k p \qquad (2.20).$$

Now let $\hat{\kappa}=\kappa/\iota k$ and rewrite (2.20) as

$$\iota k[(c-U_0-\hat{\kappa})(u - U_{0_z}p_z/N^2) - p] = \{U_{0_y} - \beta y + \beta y U_{0_z}{}^2/N^2\}v \qquad (2.21).$$

Note that $\iota k() \equiv ()_x$, so that multiplying both sides by the [ ] term on the left and averaging over one wavelength in x eliminates the left hand side. Dividing the result by the zonally independent term on the right hand side of 2.21 (term in {}, which is the background potential vorticity) provided it does not vanish, we obtain

$$\overline{vp} = (c-U_0-\hat{\kappa})[\overline{uv} - U_{0_z}\overline{vp_z}/N^2] \qquad (2.22).$$

Now following analogous steps to eliminate v between (2.5) and (2.8) leads to

$$\overline{wp} = (c-U_0-\hat{\kappa})[\overline{uw} + (U_{0_y} - \beta y)\overline{vp_z}/N^2] \qquad (2.23).$$

In obtaining (2.23) we have expressed the vertical heat flux, $\overline{wp_z}$, in terms of the meridional heat flux, $\overline{vp_z}$. This is done by multiplying (2.8) by $(c-U_0-\hat{\kappa})p_z$ and averaging zonally to get

$$N^2(c-U_0-\hat{\kappa})\overline{wp_z} = \beta y U_{0z}(c-U_0-\hat{\kappa})\overline{vp_z} \qquad (2.24).$$

For later convenience, define

$$\overline{wp}^* = (c-U_0)[\overline{uw} + (U_{0y} - \beta y)\overline{vp_z}/N^2] \qquad (2.25)$$

$$\overline{vp}^* = (c-U_0)[\overline{uv} - U_{0z}\overline{vp_z}/N^2] \qquad (2.26).$$

Boyd (1976) has shown that the physical implication of the heat flux terms above is to cause additional wave momentum fluxes due to horizontal (in 2.25) and vertical (in 2.26) wave induced particle displacments of the mean field. The zonally averaged energy equation then is

$$(\overline{vp})_y + (\overline{wp})_z + U_{0y}\overline{uv} + U_{0z}\overline{uw} - \beta y U_{0z}\overline{vp_z} = 0 \qquad (2.27).$$

Substitution of (2.22) and (2.23), performing cancellations and then using (2.25) and (2.26) gives

$$\nabla\cdot\overrightarrow{EP} \equiv \left[\frac{-\overline{vp}^*}{c-U_0}\right]_y + \left[\frac{-\overline{wp}^*}{c-U_0}\right]_z = \frac{-\hat{\kappa}}{(c-U_0)}\left\{\left[\overline{uv} - U_{0z}\overline{vp_z}/N^2\right]_y + \left[\overline{uw} + (U_{0y} - \beta y)\overline{vp_z}/N^2\right]_z\right\} \qquad (2.28).$$

This is the equation governing the wave action flux which is not conserved here due to the presence of linear damping. From this we can reformulate the $O(\epsilon^2)$ momentum and thermodynamic balances eliminating eddy momentum fluxes in favor of eddy heat fluxes. Substitution from (2.25), (2.26) and (2.28) into (2.16) and (2.19) gives

$$U_t + (U_{0y} - \beta y)V + WU_{0z} = -[U_{0z}\overline{vp_z}/N^2]_y + [(U_{0y} - \beta y)\overline{vp_z}/N^2]_z + \nabla\cdot\overrightarrow{EP} \qquad (2.29)$$

and

$$P_{zt} - \beta y U_{0z}V + N^2W = -[\overline{vp_z}]_y - [\overline{wp_z}]_z \qquad (2.30).$$

Note that after eliminating $\rho$ in favor of p from 2.8, multiplying by $p_z$ and zonally averaging we obtain

$$-\beta y U_{0z}\overline{vp_z} + N^2\overline{wp_z} = -\kappa\overline{p_z^2} \qquad (2.31).$$

From (2.17) we can define a streamfunction in the vertical-meridional plane by $\Psi_z = V$ and $\Psi_y = -W$. Now if we assume, motivated by the form of (2.29), that $\Psi = \overline{vp_z}/N^2 + \chi$, then using (2.31) we get

$$U_t + (U_{0y} - \beta y)\chi_z - U_{0z}\chi_y = \nabla\cdot\vec{EP} \qquad (2.32)$$

and

$$P_{zt} - \beta y U_{0z}\chi_z - N^2\chi_y = \kappa[\overline{p_z^2}]_z \qquad (2.33).$$

We can see that the wave acceleration of the mean flow arises through the divergence of the Eliassen-Palm flux ($\nabla\cdot\vec{EP}$) as well as the advection of mean momentum through the circulation of the residual ($O(\epsilon^2)$) streamfunction $\chi$. Due to the coupling of U and P imposed by thermal wind, the wave forcing, $\nabla\cdot\vec{EP}$, cannot independently accelerate the mean field but must also drive the meridional circulation. It is the primary role of the residual circulation to redistribute the mean density field so as to maintain the thermal wind balance.

Since the form of the expression for the mean flow acceleration has not changed significantly, it is not immediately clear what progress has been made. The obvious net result of the above manipulation is that we have removed the meridional heat flux in (2.33) due to the waves. This is done by cancelling that portion of the wave induced mean field circulation in the meridional plane, (V,W), which balances the heat flux and hence does not act to accelerate the mean flow. This avoids the problem of taking differences of large quantities which are

in near balance to obtain a small but dynamically important term. In fact, Charney and Drazin (1961) and Eliassen and Palm (1961) established that under certain conditions these two fields are in exact balance. Under these circumstances $\nabla\cdot\overrightarrow{EP}$ and $\chi$ are both exactly zero and the mean fields, U and P, are completely unaffected by the waves. This is the so called 'non-acceleration' or 'non-interaction' theorem. The conditions for this are that the wave field be statistically steady, conservative and that critical surfaces not exist in the flow.

In cases where the conditions for non-acceleration are not met, as here, there still exists a portion of the wave transport which induces a compensating mean meridional circulation. In the absence of this circulation, the wave fluxes of momentum and heat would tend separately to alter the zonal mean flow and pressure distribution, tending to force the mean state away from thermal wind balance (Holton, 1983). Therefore, it is the primary role of the induced mean circulation to negate this tendency of the wave forcing and maintain the thermal wind balance. Consequently, it is desirable to take account of this near cancellation by studying the above "transformed Eulerian mean" (TEM) equations (Andrews and McIntyre, 1976), 2.32 and 2.33.

However, the real strengths of the EP flux construct are made clear by considering the physical implications. From above, we can see that the EP flux divergence represents an important contribution of the wave field in forcing the mean field. In addition, in can be shown (Edmon *et al.*, 1980; Andrews, 1983) that if the dynamics for the perturbations are wave-like, as here, then the EP flux enters in as the flux in a conservation law for the wave action of the form,

$$\partial A/\partial t + \nabla\cdot\overrightarrow{EP} = D + O(a^3) \qquad (2.34),$$

where $A$ is the density of wave activity, D represents any nonconservative forces and $a$ is a measure of the wave amplitude. Here $A$, $\overrightarrow{EP}$ and D are zonal mean $O(a^2)$ wave properties. This conservation law demonstrates that the EP flux is a direct measure of the net rate of transfer of wave activity in the medium. Therefore it is a useful indicator of the direction of wave propagation and as such is more useful than consideration of the energy flux. For purely harmonic waves, the transient term in (2.34), $\partial A/\partial t$, vanishes and the conservation relation reduces to (2.28). Another advantage of the above formulation is that, because of the above arguments, $\nabla\cdot\overrightarrow{EP}$ is a more direct measure of the wave-mean interaction than are the individual Reynolds' stress and heat flux terms of 2.16 and 2.19.

In mid-latitude quasigeostrophic theory, the divergence of the EP flux can be shown to be equivalent to the meridional flux of mean potential vorticity. An analogous result holds near the equator, if the equations are reformulated in isopycnal coordinates and the flux is considered along isopycnal surfaces (Rothstein, *pers. comm.*). This modification is due to the ageostrophic equatorial flows which lead to relatively large isopycnal slopes. Under quasigeostrophic scaling, the potential vorticity flux is also along isopycnal surfaces, which are flat to lowest order. This result shows the close link between the mean field acceleration and the vorticity dynamics. In this case, we clearly see that it is the wave induced flux of mean potential vorticity which results in mean field accelerations.

To examine the acceleration of the mean flow we clearly must solve for the residual streamfunction, $\chi$. So, combining 2.18, 2.17 and 2.33 into a single equation for $\chi$ gives

$$\chi_{yy} + A\chi_{yz} + B\chi_{zz} + C\chi_z = D \qquad (2.35).$$

where

$$A = \frac{2\beta y}{N^2}U_z$$

$$B = \frac{\beta y}{N^2}(\beta y - U_y)$$

$$C = \frac{\beta}{N^2}U_z$$

$$D = \frac{1}{N^2}\left\{-\beta y(\nabla\cdot\overrightarrow{EP})_z + \left[\kappa\left[\frac{\overline{p_z^2}}{N^2}\right]_z\right]_y\right\} .$$

Since A and B are identical to those in 2.9, the discriminant for 2.35 is identical to that of 2.9. So 2.35 is also elliptic and as before, we must specify $\chi$, its normal derivative or a linear combination on the bounding contour. To isolate wave-driven mean tendencies, we choose to specify $\chi$=0 on the boundaries. This is equivalent to assuming that the total streamfunction is just the meridional heat flux of the wave field on the boundary, which from the conditions on p is just due to the wave forcing at the surface boundary. For discussion of the possible boundary conditions on $\chi$ see Andrews *et al.* (1987).

Due to the similarity of 2.9 and 2.35, the same solution procedure is used here and we see that the numerical solution for $\chi$ is as difficult as that for the perturbation pressure. However, the considerations in Chapter 4 and the results in Appendix A with respect to accuracy and methodology apply. Therefore the grid spacing and other numerical considerations remain unchanged for the solution of $\chi$.

# Chapter 3: Approximate Analytic Solutions

## 3.1 The Slowly Varying Limit

For oceanic background flows with shear there is little analytic methodology available to us except in the cases of slowly varying or small amplitude flow. The latter case was treated by McPhaden and Knox (1979) and Ripa and Marinone (1983) but is included here for completeness. For the former case, the governing equations for the perturbations take the particularly simple form:

$$\iota(\sigma - kU_0)u - \beta yv = -\iota kp \qquad (3.1),$$

$$\iota(\sigma - kU_0)v + \beta yu = -p_y \qquad (3.2),$$

$$-\rho g = \rho p_z \qquad (3.3),$$

$$\iota ku + v_y + w_z = 0 \qquad (3.4),$$

$$-\iota(\sigma - kU_0)\rho + w\rho_{0z} = 0 \qquad (3.5),$$

where the only effect of the background flow is to introduce a Doppler shifting of the frequency, $\omega = \sigma - kU_0$. Combining (3.3) and (3.5) and solving for w gives

$$w = \iota\omega p_z/N^2 \qquad (3.6),$$

which combined with (3.4) gives

$$\iota ku + v_y + \iota\omega\{p_z/N^2\}_z = 0 \qquad (3.7).$$

Now separating variables by letting $u,v,p(y,z) = u^h, v^h, p^h(y)\Phi(z)$ leads to

$$\frac{d}{dz}\left[\frac{1}{N^2}\frac{d\Phi}{dz}\right] + \lambda^2\Phi = 0 \qquad (3.8),$$

for the vertical problem and the horizontal part of Eqs. (3.1) and (3.2) (ie. $u,v,p \rightarrow u^h, v^h, p^h$) and

$$\iota k u^h + v^h{}_y - \iota\omega\lambda^2 p^h = 0 \qquad (3.9),$$

for the horizontal problem. The solution to the vertical problem depends upon the stratification, $N^2$ with $\lambda$ (with dimensions of inverse velocity) playing the role of eigenvalue. While (3.8) can be solved numerically for any $N^2$ distribution (assuming it varies slowly enough for the concept of vertical wavenumber to apply), for constant N used here, the solutions are trigonometric with wavenumber $\gamma=\lambda N$. The solution to the meridional problem is most simply found by deriving an equation for the meridional velocity, v. Combining (3.1), (3.2) and (3.9), dropping the h superscript denoting the horizontal structures, making the longwave approximation and eliminating in favor of v leads to

$$\frac{d^2v}{dy^2} + [\frac{-k\beta}{\omega} - \lambda^2\beta^2y^2]v = 0 \qquad (3.10).$$

Now rescale the meridional variable as $\xi = \sqrt{\lambda\beta}y$ to obtain

$$\frac{d^2v}{d\xi^2} + [\frac{-k}{\omega\lambda} - \xi^2]v = 0 \qquad (3.11).$$

This equation is a form of Hermite's equation for which bounded solutions ($v\to 0$ as $y\to\pm\infty$) exist when

$$\frac{-k}{\omega\lambda} = 2m + 1 \qquad (3.12).$$

The solutions are given by

$$v = V_m e^{-\frac{1}{2}\xi^2} H_m(\xi)\Phi(z) \qquad (3.13),$$

where $H_m(\xi)$ is the Hermite polynomial of order m. The Hermite polynomials satisfy the recursion relations (Gradshteyn and Ryzhik, 1980)

$$\frac{d}{d\xi}[H_m(\xi)] = 2mH_{m-1}(\xi) \qquad (3.14),$$

$$\xi H_m(\xi) = \tfrac{1}{2}H_{m+1}(\xi) + mH_{m-1}(\xi) \qquad (3.15).$$

From these, Eq. (3.12) and the solution v, we derive the expressions for u, w and p

$$u = \frac{-\iota}{2}\left[\frac{(2m+1)\beta}{-\omega k}\right]^{\frac{1}{2}}\left[H_{m-1}(\xi) - \frac{H_{m+1}(\xi)}{2(m+1)}\right]V_m e^{-\frac{1}{2}\xi^2}\Phi_n(z) \qquad (3.16),$$

$$w = \frac{-1}{2N^2}\left[\frac{(2m+1)^3\beta\omega^3}{(-k)^3}\right]^{\frac{1}{2}}\left[H_{m-1}(\xi) + \frac{H_{m+1}(\xi)}{2(m+1)}\right]V_m e^{-\frac{1}{2}\xi^2}\frac{d\Phi_n}{dz} \qquad (3.17),$$

$$p = \frac{\iota}{2}\left[\frac{(2m+1)^3\beta\omega}{(-k)^3}\right]^{\frac{1}{2}}\left[H_{m-1}(\xi) + \frac{H_{m+1}(\xi)}{2(m+1)}\right]V_m e^{-\frac{1}{2}\xi^2}\Phi_n(z) \qquad (3.18).$$

In the presence of variation in the background field, the fundamental conserved quantity is no longer the energy of the waves but rather the wave action (Andrews and McIntyre, 1978; Bretherton and Garrett, 1969; LeBlond and Mysak, 1978). Integrating the conservation equation for the wave action flux (Eq. 2.28 with $\kappa$=0 and $U_{0y}$ in Eq. 2.25 ignored for slow variations in the flow considered here) vertically and meridionally, one derives the requirement that the generalized integrated momentum flux, M, must be independent of depth (Holton, 1975). That is

$$M = \int_{-\infty}^{\infty}\left[\overline{uw} - \frac{\beta y}{N^2}\overline{vp_z}\right]dy = \text{constant} \qquad (3.19).$$

Performing the integration using (3.13), (3.16)-(3.18) leads to

$$M = \left[\frac{\sqrt{\pi}(2m+1)^7(m-1)!2^{m-1}}{4(m+1)N}\right]\omega^{\frac{1}{2}}\beta^{\frac{1}{2}}(-k)^{-3/2}V_m^2 \qquad (3.20).$$

Therefore the expression for the amplitude coefficient, $V_m$, is

$$V_m = \left[\frac{4(m+1)M}{\sqrt{\beta\pi}(2m+1)^7(m-1)!2^{m-1}}\right]^{\frac{1}{2}}(-k)^{-3/2}N^{\frac{1}{2}}\omega^{-\frac{1}{4}} \qquad (3.21).$$

The important physical statement is that $V_m \approx \omega^{-\frac{1}{4}}$ all else being constant for a particular mode (except perhaps N, which is fixed for

this discussion). Defining the square bracketed term of (3.21) as $\mu$, we rewrite the expressions for the other dynamic variables, u, w, p, as

$$u = -\tfrac{1}{2}\iota k^{-2}[(2m+1)N\beta\mu]^{\frac{1}{2}}\omega^{-3/4}\left[H_{m-1}(\xi) - \frac{H_{m+1}(\xi)}{2(m+1)}\right]e^{-\frac{1}{2}\xi^2}\Phi_n(z) \quad (3.22),$$

$$w = \tfrac{1}{2}k^{-3}[(2m+1)^3N^{-3}\beta\mu]^{\frac{1}{2}}\omega^{5/4}\left[H_{m-1}(\xi) + \frac{H_{m+1}(\xi)}{2(m+1)}\right]e^{-\frac{1}{2}\xi^2}\frac{d\Phi_n}{dz} \quad (3.23),$$

$$p = \tfrac{1}{2}\iota k^{-3}[(2m+1)^3N^{-3}\beta\mu]^{\frac{1}{2}}\omega^{\frac{1}{4}}\left[H_{m-1}(\xi) + \frac{H_{m+1}(\xi)}{2(m+1)}\right]e^{-\frac{1}{2}\xi^2}\Phi_n(z) \quad (3.24).$$

Now collecting with these results those from (3.12), (3.21) and the scaling of (3.11) we conclude that as a wave propagates vertically into a slowly varying mean flow, due to the change in the Doppler shifted frequency, $\omega$, there will be changes in:

1) the meridional wave scale in proportion to $\omega^{\frac{1}{2}}$.

2) the vertical wave scale in proportion to $\omega$.

3) the amplitude of the pressure and vertical velocity in proportion to $\omega^{\frac{1}{4}}$ and $\omega^{5/4}$, respectively.

4) the amplitude of the horizontal components of velocity in proportion to $\omega^{-3/4}$ for u and $\omega^{-\frac{1}{4}}$ for v.

These results are demonstrated by Figs. 3.1 and 3.2. Figure 3.1 shows a meridional-vertical section of an eastward flow and $N^2$ field which is slowly varying in both y and z. The amplitude and phase of the analytic pressure solution for this flow are shown in Fig. 3.2a and 3.2b, respectively. In this case the solution is forced at the surface with an Ekman pumping velocity which has the meridional structure of the first meridional mode and, for simplicity, is allowed to radiate freely out the bottom of the domain. Therefore, at the bottom we specify that

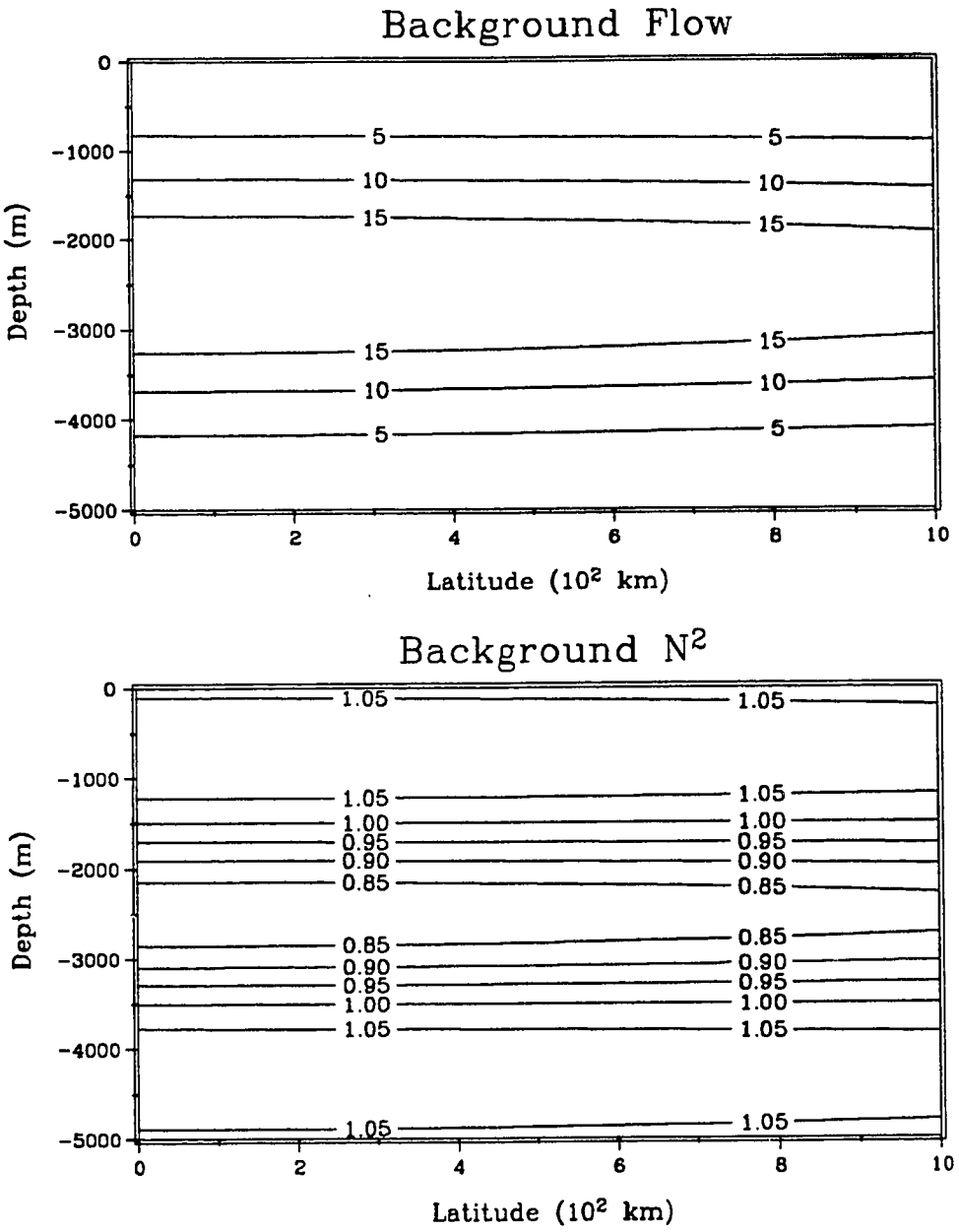


Figure 3.1: Slowly varying mean state used in ray computations. (Top) Zonal flow (cm/s) (Bottom) $N^2$ field ($x10^{-4}s^{-2}$).

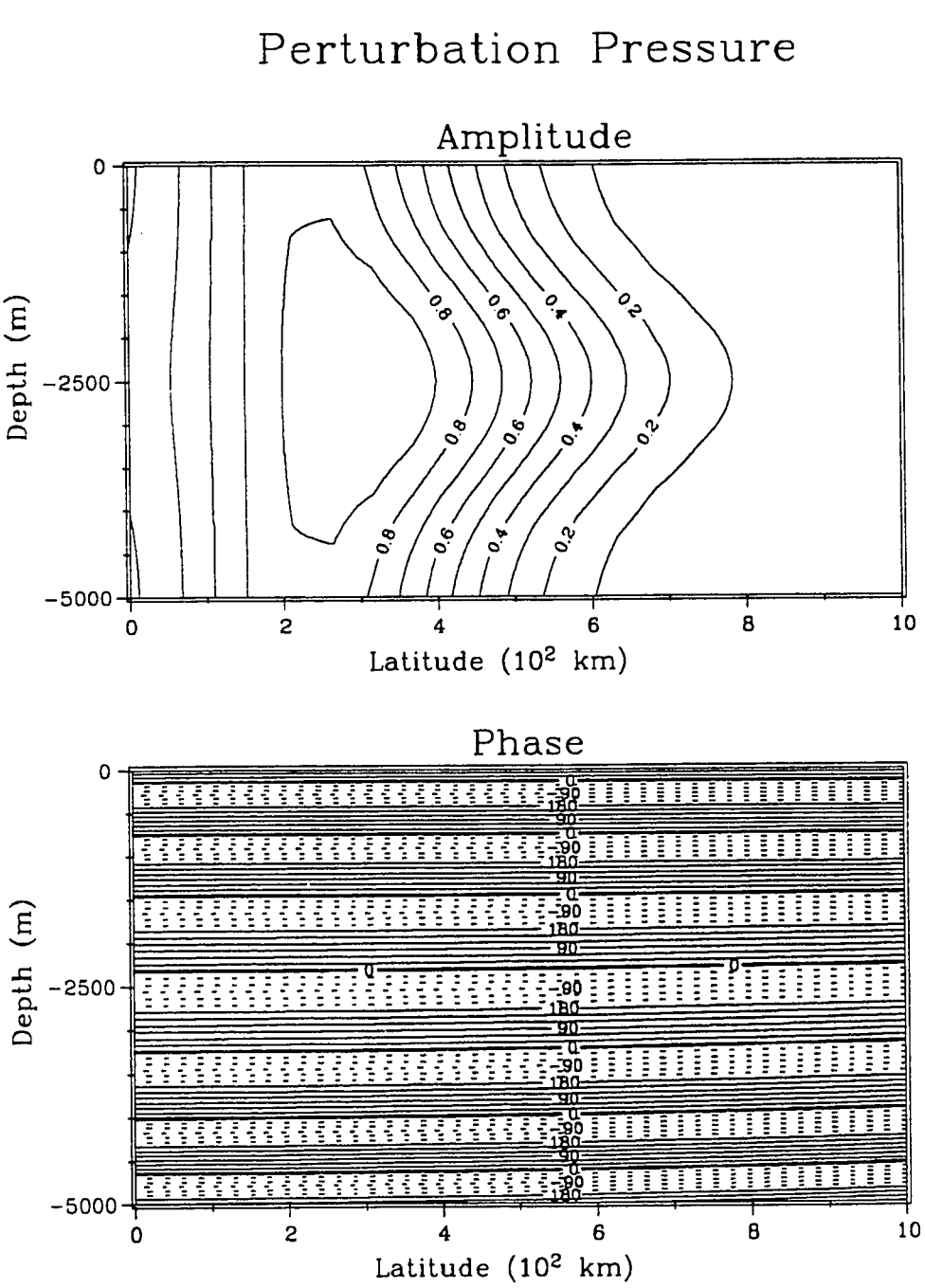


Figure 3.2: Slowly varying pressure solution, (a) Amplitude (normalized to maximum value of 1.0), (b) Phase (°).

$p_z=-\iota\gamma p$ (where $\gamma$ is the vertical wavenumber) and not a w=0 condition. From Fig. 3.2a, the stretching of the meridional wave scales and amplification of the pressure field is easily seen. The phase plot, Fig. 3.2b, shows the stretching of the vertical scales expected. Analogous plots for u, v and w are not presented.

A complementary way to understand the effects of a slowly varying flow is to consider the ray paths. The required assumptions are identical to those above with the equation for the conservation of crests (LeBlond and Mysak, 1978) leading to the equations for the ray paths:

$$\frac{dy}{dt} = c_g^{(y)} \quad \text{and} \quad \frac{dz}{dt} = c_g^{(z)} \tag{3.25},$$

and for the change in wavenumbers along the ray paths moving at the group velocity:

$$\frac{d\ell}{dt} = -\frac{\partial\omega}{\partial y} = -k\frac{\partial U_0}{\partial y} - \frac{\partial\omega}{\partial f}\frac{\partial f}{\partial y} - \frac{\partial\omega}{\partial N^2}\frac{\partial N^2}{\partial y} \tag{3.26},$$

$$\frac{d\gamma}{dt} = -\frac{\partial\omega}{\partial z} = -k\frac{\partial U_0}{\partial\varphi} - \frac{\partial\omega}{\partial N^2}\frac{\partial N^2}{\partial z} \tag{3.27}.$$

In general there may be terms in (3.27) due to vertical variations in vertical gradient of $N^2$, however for a resting state constant N (used here) and slowly varying mean flow these are assumed small. Manipulation of the longwave equations (3.1-3.5) for plane wave solutions of the form $e^{-\iota(kx+\ell y+\gamma z-\sigma t)}$ leads, in the low frequency limit, to the Rossby dispersion relation:

$$\sigma = kU_0 - \frac{k\beta}{\ell^2 + \beta^2 y^2\gamma^2/N^2} \tag{3.28}.$$

By definition

$$c_g^{(y)} = \frac{\partial \sigma}{\partial \ell} = \frac{-2\omega\ell}{\ell^2 + \beta^2 y^2 \gamma^2 / N^2} = 2\omega^2 \ell / k\beta \qquad (3.29),$$

and

$$c_g^{(z)} = \frac{\partial \sigma}{\partial \gamma} = \frac{-2\gamma\omega\beta^2 y^2 / N^2}{\ell^2 + \beta^2 y^2 \gamma^2} = \frac{2\gamma\beta\omega^2 y^2}{kN^2} \qquad (3.30),$$

where the definition of Doppler shifted frequency, $\omega$, has been used. The final forms for the group velocities are used to clearly show the dependence of the group velocities on $\ell$ and $\gamma$. In making the last substitution we have used the fact that for a temporally and zonally invariant medium the frequency, $\sigma$, and zonal wavenumber, k, remain constant. Therefore, the dependence on $y^2$, $\gamma^2$ and $\ell^2$ in the denominator of the first expression does not directly lead to a change in $\vec{c}_g$. Now the equations for the variation of the meridional and vertical wavenumbers along a ray become

$$\frac{d\ell}{dt} = -kU_{0_y} - \frac{2\omega^2\beta y\gamma^2}{kN^2} - \frac{\omega^2\beta y^2\gamma^2}{kN^4} N^2{}_y \qquad (3.31),$$

$$\frac{d\gamma}{dt} = -kU_{0_z} - \frac{\omega^2\beta y^2\gamma^2}{kN^4} N^2{}_z \qquad (3.32).$$

The ray equations [3.25, 3.31-3.32] can be integrated sequentially through time to predict the wavenumbers and the positions of the ray as a function of time. This was done for the flow field in Fig. 3.1 and two trajectories and depth history of the two wavenumbers, $\gamma$ and $\ell$, are presented in Fig. 3.3. For later applicability, we choose the annual frequency, the first meridional mode (m=1) and the eigenvalue, $\lambda$, of a third vertical mode in the no-flow rigid bottom ocean. The eigenvalue then determines the zonal wavenumber through Eq. 3.12 and in concert with the stratification the initial vertical wavenumber, $\gamma$. The meridional wavenumber, $\ell$, then remains to be determined from the two roots of the dispersion relation, (3.28). The two rays for $\pm\ell$ are

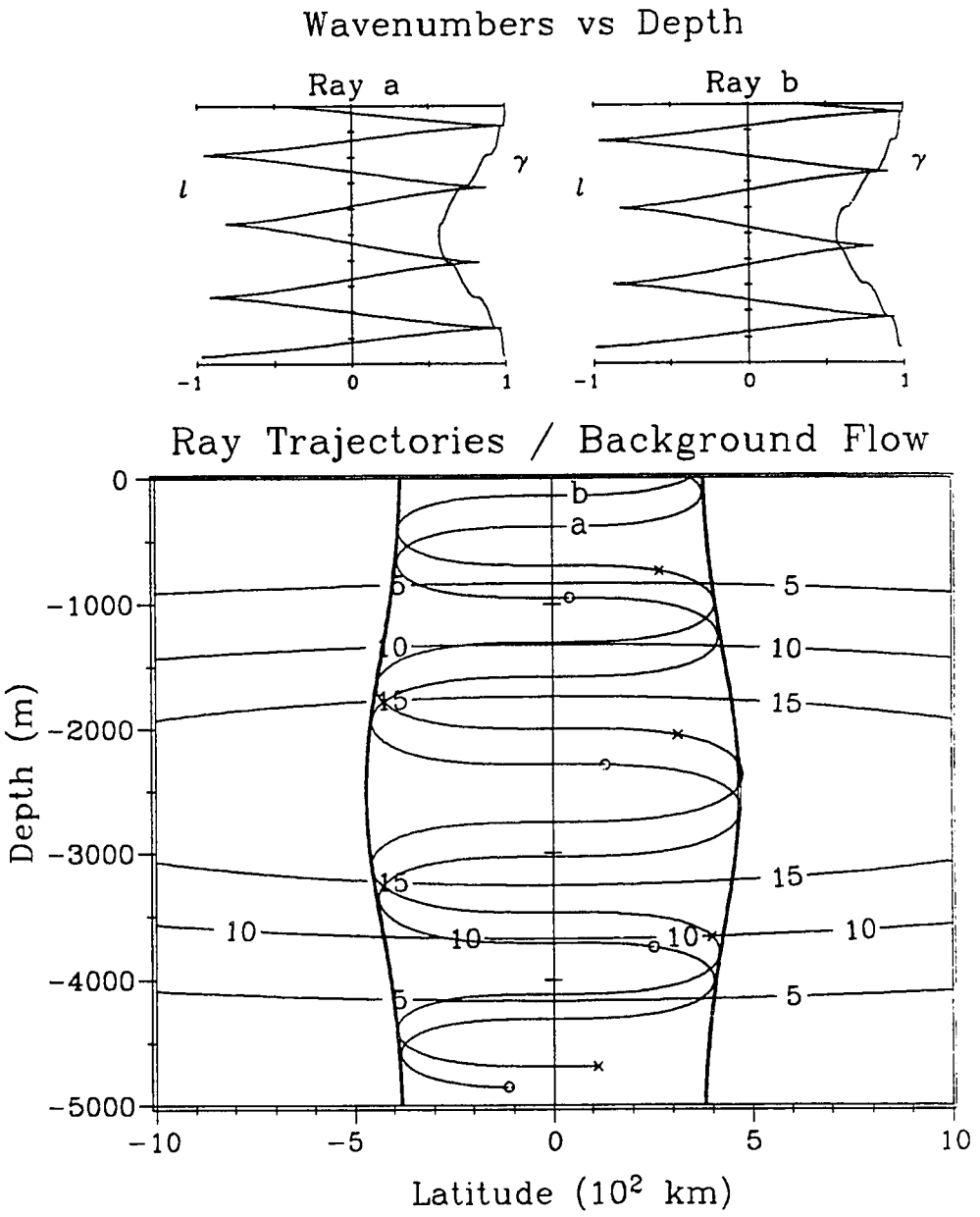


Figure 3.3: Ray theory results in slowly varying flow, (Top) normalized vertical ($\gamma$) and meridional ($\ell$) wavenumbers as a function of depth, (Bottom) Ray trajectories for both $\ell$ roots of dispersion relation launched from the surface at 3.5°N.

launched from 3.5°N, traced for a total of 4 years and marked annually. We see from Fig. 3.3, that near the depth of the core the ray paths extend further poleward and have a longer vertical distance between successive equatorial crossings. One effect of this is to expand the turning latitudes or caustic surfaces, (drawn in Fig. 3.3 using the Doppler shifted phase speed at the equator), poleward at the depth of the core consistent with the meridional stretching of the previous analysis. While the increase in the vertical and meridional scale of the rays implies a possible decrease in the wave amplitude due to the decrease in ray spatial density, this is not the case. To find the amplitude from this analysis we must integrate along the rays down from the surface employing the conservation of wave action. This necessarily would include the complicated treatment of the caustic surface and involve multiple ray crossings. However, the conservation of wave action suggests that upon entering the eastward flow the increase in the intrinsic frequency must lead to an increase in the average energy density, <E>, and hence amplification of the wave field. Rather than expend a large amount of effort to show this from ray tracing, we accept this result with the supporting evidence from the previous analysis which predicts the wave amplification near the core.

The effect of this current on the wavenumber vector is to rotate it towards the horizontal. This is due to the region of negative vertical shear above the core which decreases the vertical wavenumber. The vertical shear is strong enough to decrease the vertical wavenumber at the core to about 52% of its surface value (Fig. 3.3, top). The primary effect of this flow upon the meridional wavenumber arises

through the Doppler shifted frequency both directly and indirectly. For this flow, the meridional shear was extremely weak and consequently has a negligible effect on $\ell$. The direct effect of the Doppler shift is clear from the $\omega^2$ dependence in 3.31, however the poleward spreading of the rays introduces an indirect change in $\ell$ through the dependence on y in 3.31.

A consequence of both the direct and indirect Doppler effect is to increase the rate of energy transfer vertically and meridionally. As with the wavenumbers, the group velocities depend both on $\omega$ directly through $\omega^2$ and indirectly through $\gamma$, $\ell$ and y. In Fig. 3.4, we present the ray paths in an ocean at rest. As in Fig. 3.3, the ray paths are marked annually and traced for 4 years. Comparison shows that the rays in the presence of the slowly varying flow have penetrated to a greater depth than for the resting ocean. This suggests that one important effect of a slowly varying Undercurrent may be to increase the rate of vertical energy transfer of wind forced wave energy input near the equator. This is consistent with the scale dependence from the earlier treatment which shows that the vertical energy flux, $\overline{wp}$, scales as $\omega^{3/2}$.

In summary, the slowly varying theory tells us to expect that the action of an eastward Undercurrent on long Rossby waves will:

1) Stretch the wave field both meridionally and vertically,

2) Amplify the pressure field,

3) Doppler shift resonances toward slower westward phase speed,

4) Increase the turning latitude,

5) Increase the energy transfer rate in the vertical direction.

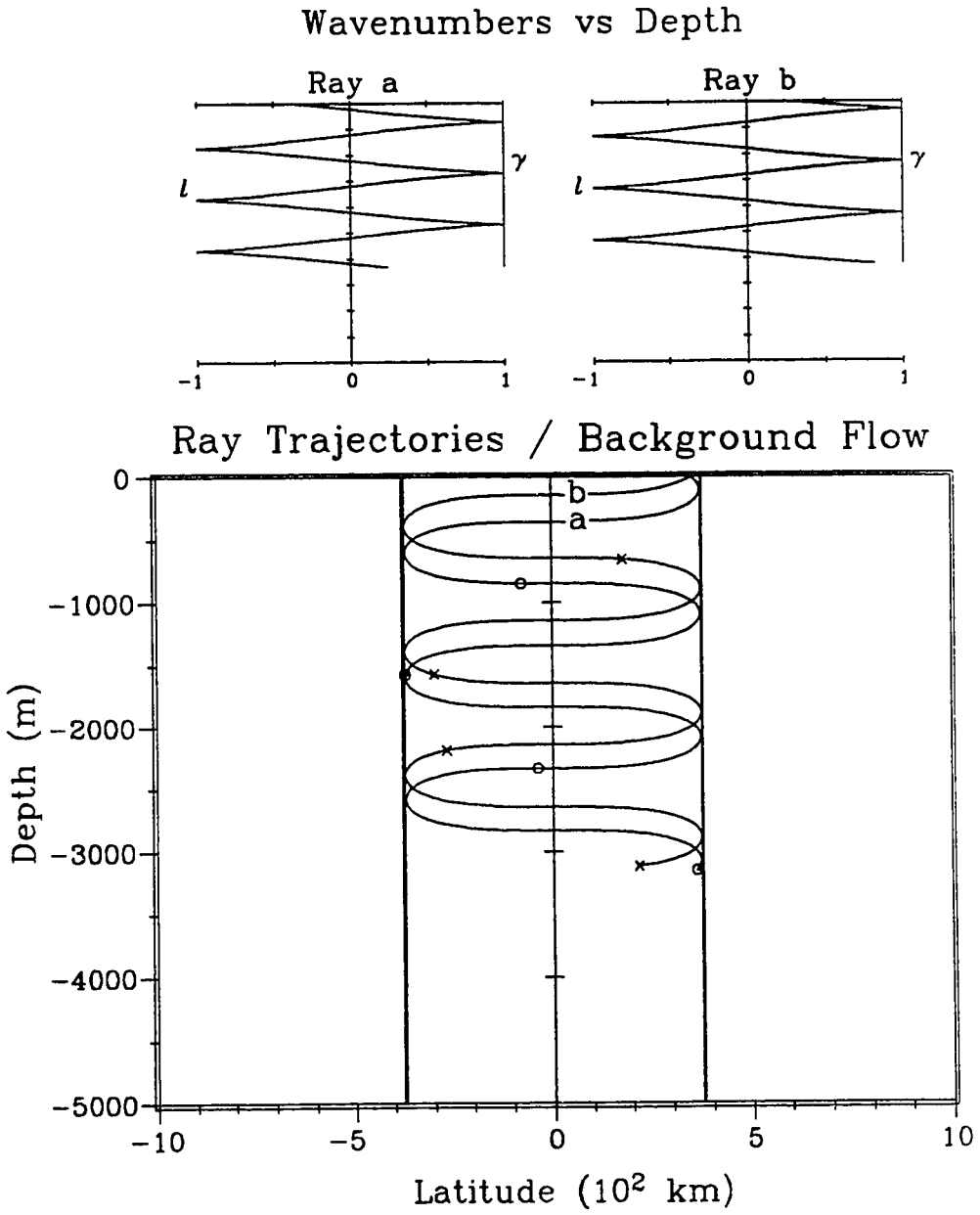


**Figure 3.4:** As with Fig. 3.3 except for resting state ocean

For rapidly varying flows, none of the above necessarily will occur. However, departures from the above will be more easily understood since they can be attributed to the rapid variations in the medium.

## 3.2 Perturbation Expansion Approach

Another way to analytically investigate the propagation of waves in shear which avoids the slowly varying assumption is to perform a perturbation expansion. While the usefulness of this for the equatorial ocean is limited, one can calculate tendencies for both Doppler shifting and wave scattering for a particular background configuration. In this way, the terms responsible for certain aspects of the interaction problem can be identified and better understood.

Assuming that the corrections to the wave structure are small amplitude and denoting all background variables with a * subscript and wave variables without we write

$$
\begin{aligned}
u &= R_0 U_* + \epsilon u_0 + \epsilon R_0 u_1 + \epsilon R_0^2 u_2 + \ldots \\
w &= \epsilon w_0 + \epsilon R_0 w_1 + \epsilon R_0^2 w_2 + \ldots \\
v &= \epsilon v_0 + \epsilon R_0 v_1 + \epsilon R_0^2 v_2 + \ldots \\
\rho &= \rho + \rho_*(z) + R_0 \rho_{*1} + \epsilon \rho_0 + \epsilon R_0 \rho_1 + \epsilon R_0^2 \rho_2 + \ldots \\
\sigma &= \sigma_0 + R_0 \sigma_1 + \epsilon \sigma_2 + \ldots
\end{aligned}
\qquad (3.33),
$$

Where we assume the Rossby number, $R_0$, and $\epsilon$ satisfy $\epsilon \ll R_0 \ll 1$. With these definitions the governing equations for the $O(\epsilon)$ wave fields yield the Hermite equation for the meridional velocity of the $n^{th}$ vertical mode (with separation constant $\lambda_n$)

$$v_{0yy} - [\lambda_n^2\beta^2y^2 + \frac{k\beta}{\sigma_0}]v_0 = 0 \qquad (3.34).$$

The solutions to (3.34) are the countably infinite set of long nondispersive equatorial Rossby waves discussed by Moore and Philander (1977) and McCreary (1981). The equations at order $\epsilon R_0$ are:

$$-\imath\sigma_0 u_1 - \beta y v_1 + \imath k p_1 = -\imath k U_* u_0 - v_0 U_{*y} - w_0 U_{*z} + \imath\sigma_1 u_0 \qquad (3.35)$$

$$\beta y u_1 + p_{1y} = 0 \qquad (3.36)$$

$$\imath k u_1 + v_{1y} + w_{1z} = 0 \qquad (3.37)$$

$$\rho_1 g + \rho_* p_{1z} = 0 \qquad (3.38)$$

$$-\imath\sigma_0\rho_1 + w_1\rho_{*1y} = -\imath k U_*\rho_0 - v_0\rho_{*1y} - w_0\rho_{*1z} + \imath\sigma_1\rho_0 \qquad (3.39).$$

Now the left hand sides of the set 3.35-3.39 are identical in form to the $O(\epsilon)$ set. Therefore, after separating variables in y and z, the equation for the meridional velocity at $O(\epsilon R_0)$, $v_{1_n}$, is an inhomogeneous Hermite equation forced by correlations of the $O(\epsilon)$ solutions with background state. From this equation we can calculate the $O(R_0)$ frequency shift and corrections to the wave structures. The form of the equation is

$$v_{1_n yy} - [\lambda_n^2\beta^2y^2 + \frac{k\beta}{\sigma_0}]v_{1_n} = \mathfrak{C}_{n_y} + [\beta y + \frac{\sigma_0}{k}\frac{\partial}{\partial y}][\mathfrak{I}_n - \frac{k}{\sigma_0}\mathfrak{R}_n] \equiv \Lambda_n \qquad (3.40)$$

where

$$\mathfrak{C}_n = \int_{-H}^{0} [\frac{\sigma_0\lambda^2{}_n}{k} - \frac{k}{\sigma_0}][\imath k U_* u_0 + v_0 U_{*y} + w_0 U_{*z} - \imath\sigma_1 u_0]\Phi_n dz \qquad (3.41),$$

$$\mathfrak{I}_n = \int_{-H}^{0} \{[\imath k U_* u_0 + v_0 U_{*y} + w_0 U_{*z} - \imath\sigma_1 u_0]_z/N^2\}_z\Phi_n dz \qquad (3.42),$$

$$\mathfrak{R}_n = \int_{-H}^{0} \frac{g}{\rho_*}\{[\imath k U_*\rho_0 + v_0\rho_{*1y} + w_0\rho_{*1z} - \imath\sigma_1\rho_0]/N^2\}_z\Phi_n dz \qquad (3.43),$$

and $\lambda_n$, k and $\sigma_0$ are fixed by the $O(\epsilon)$ solution. Now take the $O(\epsilon)$ solution as an $i^{th}$ meridional and $j^{th}$ vertical mode. Then the zonal wavenumber, k, is given by

$$k = -\sigma_0\lambda_j(2i+1) \tag{3.44}$$

To proceed with solution, expand $v_{1_n}$ and $\Lambda_n$ into sums over the meridional basis function set, so that $v_{1_n}=\sum v_{1_{mn}}\Psi_m$ and $\Lambda_n=\sum\Lambda_{mn}\Psi_m$. Now operating on (3.40) with

$$\mathcal{L}[\ ] \equiv \int_{-\infty}^{\infty} \{\Psi_m(y)[\ \ ]\}dy \equiv [\ ]_m \tag{3.45}$$

(where $\Psi_m$ are the Hermite functions) and employing the recursion relations for the Hermite functions gives the amplitudes of the velocity components arising from the $O(\epsilon)$ wave forcing as

$$V_{mn} = \{(2i+1)\beta\lambda_j-(2m+1)\beta\lambda_n\}^{-1}\Lambda_{mn} \tag{3.46}.$$

Then to assure that there is no self-resonance of the $O(\epsilon)$ solution, $\sigma_1$ is set such that $\Lambda_{ij}=0$. Now for any background flow, U*, and modal solution [i,j mode] we have the $O(R_0)$ portion of the frequency shift, $\sigma_1$, and the coefficients of a modal expansion, $V_{mn}$, of the $O(\epsilon R_0)$ changes to the wave structure.

From the expressions 3.41-3.43, one can see that part of the $O(R_0)$ shift in the frequency occurs due to the traditional Doppler shift, $\iota kU_0$, which is weighted by the structure of the $O(R_0)$ zonal velocity or density field and projected onto the meridional velocity structure function, $\Psi_m$. However, additional frequency shifts can occur through the projection of the advection of background momentum and density fields by the meridional circulation of the $O(\epsilon)$ wave field, $(v_0,w_0)$, upon the wave structures.

Due to the complexity of expressions 3.41-3.43 the results for modal scattering are less apparent. However, from equation 3.46, we see that, assuming the forcing projections are non-zero, the wave forcing of a particular $O(\epsilon R_0)$ wave should tend to increase as the difference in the phase speed with the $O(\epsilon)$ wave decreases. This makes sense, as wave modes moving at similar speeds should be the most strongly forced. Numerical results of this coupling are presented in chapter 4 and therefore we defer most of the discussion of the implications of 3.38-3.40 until then.

In summary, the perturbation theory provides a tool for the dissection of the modification to the waves structure and dispersion characteristics for rapidly varying mean flows. However, the application is limited to weak interactions where $\epsilon$ and $R_0$ are small. Results presented later show that the most significant portion of the frequency shift and modification to the wave structures occurs due to the action of Doppler shifting.

## Chapter 4: Numerical Method

Now that we have a simple understanding of some of the effects idealized zonal mean currents can have upon long Rossby wave propagation near the equator, we move on to study the problem at hand. This involves the numerical solution of the governing partial differential equation, (2.9). Before we present the numerical solutions, however, we give an overview of the solution procedure. For a more detailed discussion of these considerations see Appendix A.

The choice for boundary conditions is dictated both by the elliptic nature of the differential equation and the goals of the study. In short, we wish to study modifications to the free equatorial wave modes induced by the zonal mean flow and the resulting wave induced changes to the mean state. As a result, we should employ conditions consistent with these modal solutions. Consequently, the ocean bottom is assumed flat and rigid (w=0). In addition, we choose the domain to extend further poleward than any equatorially trapped internal wave mode and allow the barotropic solution to freely radiate. Use of the symmetry condition at the equator cuts the number of necessary grid points in half for symmetric background flows with no loss of generality. At the surface boundary, however, we specify a non-zero w distribution which is clearly not consistent with free wave solutions. This is necessary since specifying the free wave condition, w=0 at z=0, gives homogeneous boundary conditions at all boundaries which leads to the trivial solution, p=0. The particular meridional distribution chosen for w, however, does match the meridional structure of the desired free wave

mode. For the first meridional mode Rossby wave with an eigenspeed of $\lambda^{-1}$=106 cm/s this distribution is shown in Fig. 4.1. The distribution is identical for all eigenspeeds, c, except the meridional scale adjusts with $\sqrt{c}$ so that slower (faster) eigenspeeds are narrower (broader) meridionally. Because of the contradiction in w boundary condition at the top, we must add frictional damping to avoid a perfect resonance which would lead to an infinite amplitude pressure solution.

To obtain numerical solutions we first approximate the continuous partial differential equation with a finite difference equation. We begin by discretizing the domain in y and z such that

$$y_i = (i-\tfrac{1}{2})\delta y \qquad \text{for } i = 1,2,3,\ldots,NY$$

$$z_j = j\delta z \qquad \text{for } j = 1,2,3,\ldots,NZ$$

The finite difference equation is obtained from the partial differential equation by substitution of the Taylor's series expansions for $p_{yy}$, $p_{yz}$, $p_{zz}$, $p_y$ and $p_z$ accurate to $O(\delta y^2,\delta z^2)$. Then at each grid point, $(y_i,z_j)$, we have an equation which depends upon the values for $p_{k,l}$ where k ranges from i-1 to i+1 and l from j-1 to j+1. The boundary values required for this equation act to close the problem. For example, at i=1, which due to the shift of $\frac{1}{2}\delta y$ in the grid occurs at $y=\frac{1}{2}\delta y$, the symmetry condition specifies that the value of $p_{-1}$ is equal to $p_1$ so that no values for p from outside the domain are needed.

Since the solution at a particular grid point depends upon unknown values for p at the surrounding points, we obtain a matrix equation, $\tilde{\tilde{A}}\vec{X}=\vec{B}$, which must be solved simultaneously. Due to the form of the finite difference equation, the coefficient matrix, $\tilde{\tilde{A}}$, is banded tridiagonal. While this particular type of matrix form has certain

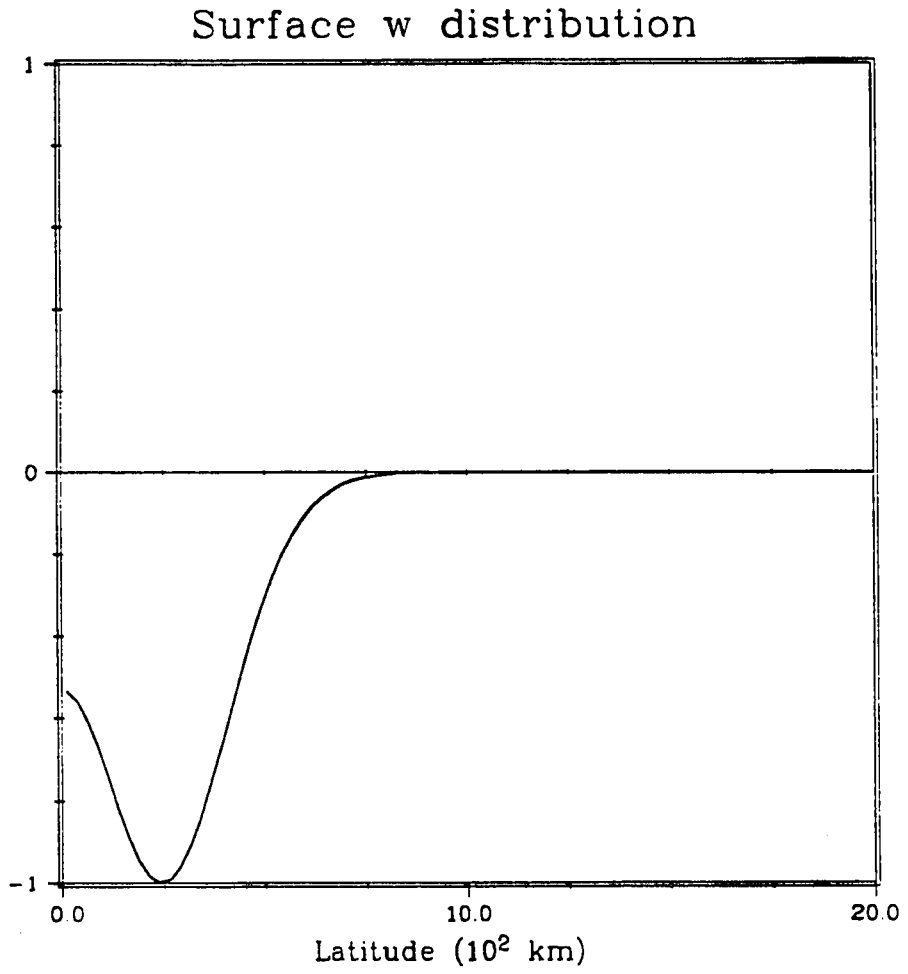


Figure 4.1: Vertical velocity distribution. Wave forcing at the surface employed for a 1st meridional, 3rd vertical mode annual Rossby wave as a function of latitude.

characteristics, for the purposes here we note only that this implies that the matrix is sparse with elements placed symmetrically about the main diagonal. In fact, of the NYxNZ elements (O(5,000-10,000)) on a particular row of the coefficient matrix, there are at most 9 non-zero elements. In addition, these non-zero elements lie within a band of width equal to the smaller of 2NY and 2NZ about the main diagonal. The usefulness of this is that performing a Gaussian elimination algorithm can generate non-zero elements only within this band. The approach used here employs a modified Gaussian elimination algorithm which takes advantage of this fact to store the minimum necessary number of elements of $\tilde{\tilde{A}}$ and to perform a minimum number of computations.

For computational accuracy we found that for constant $N^2$ cases a grid of size (NY,NZ)=(80,131) was necessary (see Appendix A). Whereas for variable $N^2$ cases the vertical resolution needed to be increased to 201 points. These resolutions were sufficient to accurately obtain the pressure field as well as to approximate the momentum exchanges between wave and mean state. This result is based upon direct accuracy comparison for the no mean flow case and upon acceptably small (O(5%)) imbalances in the mass and energy budgets for cases with flow.

For presentational purposes, the numerical pressure fields, which are complex, are separated into amplitude (which is normalized to one) and phase and contoured. In all other contour plots, the amplitude is normalized to one and the magnitudes are reported on the right hand margin. Vector plots are annotated with a vector scale at lower right.

# Chapter 5: Numerical Solutions

## 5.1 Methodology

In this chapter we present the numerical results for the Rossby wave interaction with more realistic flow configurations. The two flow configurations chosen are the Equatorial Undercurrent alone and the combination of the EUC and the South Equatorial Current. Emphasis here will be placed on the study of the Undercurrent. The EUC alone is first investigated in an attempt to isolate the effect of a somewhat simple background flow on the wave fields.

Considering the structure of the mean flow field shown in Fig. 2.1, to a sufficient degree of realism the equatorial currents (EUC and SEC) can be approximated by Gaussian distributions vertically and meridionally. Therefore, for each background flow field centered on the equator we assume

$$U(y,z) = U_0 e^{-\frac{1}{2}[\{(z-z_c)/\delta z\}^2+\{y/\delta y\}^2]} \qquad (5.1),$$

where $U_0$, $z_c$, $\delta z$ and $\delta y$ are adjustable parameters describing the mean state. For this configuration, parameter variations are carried out to aid understanding of the roles of Doppler shifting, mean shear, spatial extent of the current, location of the current core and friction. Except for one variable $N^2$ case in the parameter study, all are posed in the presence of the same resting state constant N profile. This linear resting state density field represents the simplest means to introduce stratification in that the vertical basis set consists of trigonometric functions. The case of variable N employs an EUC field and N profile approximating that measured in the NORPAX Hawaii-Tahiti

Shuttle experiment. Upon this $N^2$ field we also present the results for a realistic simulation of the EUC/SEC current system. This case illustrates that the processes present in the parameter study are also apparent in a mean state more closely resembling realistic oceanic conditions.

Throughout the investigation we restrict attention to the first meridional mode Rossby wave. This choice is motivated both by practicality, there being a countably infinite number of meridional modes, and the results of observational studies, (Lukas and Firing, 1985; Johnson, 1987), which point to the existence of the first mode in the tropical Pacific Ocean. Additionally, we limit attention to low vertical modes (1, 2 and 3). As mentioned, in the presence of a mean flow varying in y and z the concept of mathematically separable modes is not applicable. However, for weak or slowly varying flow they are clearly a useful description. For strongly sheared flows the presence of a rigid bottom assures that, if wave energy can traverse the flow, vertically resonant solutions analogous to the vertical-meridional $U_0=0$ modes exist. The questions of interest become where in dispersion space do these resonant solutions exist and what structure, both meridionally and vertically, do they have in the presence of these strongly varying flow fields. Consequently, we make comparisons of the wave structures in the presence of mean flow with the no-flow, slowly varying and small flow amplitude cases to aid understanding.

As a result, the numerical solutions derived are analyzed by performing a modal decomposition in both y and z using the no flow modal solutions as the basis set. The simple justification for this is

the mathematical one, in that these modes form a complete orthonormal basis set. In addition, the perturbation expansion approach shows that for small amplitude flow the structure of the resulting wave field can be described by a mix of no-flow wave modes. Since the coupling is weighted by the inverse of the difference in phase speeds, this mix should be dominated by wave modes nearby in dispersion space to the imposed frequency and zonal wavenumber. It seems reasonable to expect that given the relatively small area covered by the flow, if an expansion is to be performed the most compact one, and therefore most efficient, is that using the no flow basis set.

There is also reason to believe that an expansion of the above type will yield physically relevant results. As justification, consider the case where the background flow is strongly confined and rapidly varying. In this case the domain can be broken up into near and far field regions. Away from the flow, in the far field, the freely propagating solutions are the linear no-flow waves. The solutions in the near field, however, will be strongly affected by the rapid variations in the medium, are likely complicated and not physically represented by simple linear wave modes. However, the small extent of the flow means that the resulting modal decomposition, which is an integral over the entire domain, is likely to be dominated by the linear wave solutions in the far field. In other words, this decomposition will identify coherent wave structures which exist outside the flow. But this in itself is a very useful result. Since only one wave type was forced in the far field, any other types must arise through processes due to the mean flow such as scattering or reflection. If

the decomposition is a very compact one (*i.e.* only a few modes), then it identifies the particular wave types into which the background flow is preferentially scattering wave energy.

The resulting solutions are also analyzed from an energetics standpoint. This is done by consideration of both the sources and sinks of wave energy and the propagation of wave activity (in the form of EP fluxes). In the first case, both the spatially integrated exchange of energy between wave and mean as expressed by equation 2.15 and the pointwise energy fields are analyzed. In the latter case, the net EP fluxes of the wave field are presented and discussed. The net EP flux in the presence of mean flow is a very useful indicator of the scattering of equatorial wave activity. From it we can better understand the modifications to the structures of the resonant pressure fields. The divergence of the EP flux is also presented and discussed due to its importance as a measure of the wave driving of the background state. From consideration of these diagnostics we gain an understanding of the momentum exchanges involved in the wave mean flow interaction and gain valuable insight into the wave forcing of the mean state. As a companion to these, the direct calculation and discussion of the $O(\epsilon^2)$ accelerations is also considered. While we present the results of the calculation for the $\chi$ field for only a few cases, we note here that, unlike the case for the Kelvin waves (McPhaden *et al.*, 1986), the induced mean accelerations due to the residual circulations ($\chi$) are not negligible.

The final analysis tool we employ is the perturbation analysis outlined in chapter 3. This is used to estimate the relative contribu-

tions of the various interaction terms in the modification of both wave structure and dispersion. The results of this theory are compared with the numerical solutions and agreements and disagreements are discussed. The strength of this tool is that it is an analytic tool which identifies the particular terms responsible for a certain aspect of the interaction. The weakness of this tool arises from its limitation to weak interactions with flows possessing small Rossby number and large Richardson number.

## 5.2 The Equatorial Undercurrent

The standard background configuration (U and adjusted $N^2$) chosen for the investigation of the EUC in a resting state constant $N^2$ ocean are shown in Fig. 5.1. The EUC is assumed to be centered on the equator at 400m depth with an amplitude of 50cm/s and decay scales of 1.5° in y and 100m in the vertical. The current is placed deeper than observed to allow for visualization of variations in the shear zone above the core. The ocean is assumed to be only 1000m deep with a resting state $N^2$ of $10^{-4}s^{-2}$. These values were chosen to yield a reasonable eigenspeeds with a first vertical mode speed of 318 cm/s. This configuration is identical to that used in McPhaden *et al.* (1986) in the study of Kelvin waves in intensely sheared flows. It is used here to enable simple comparison with that study. Differences between the Kelvin wave results and those for the Rossby waves will be noted and discussed where appropriate.

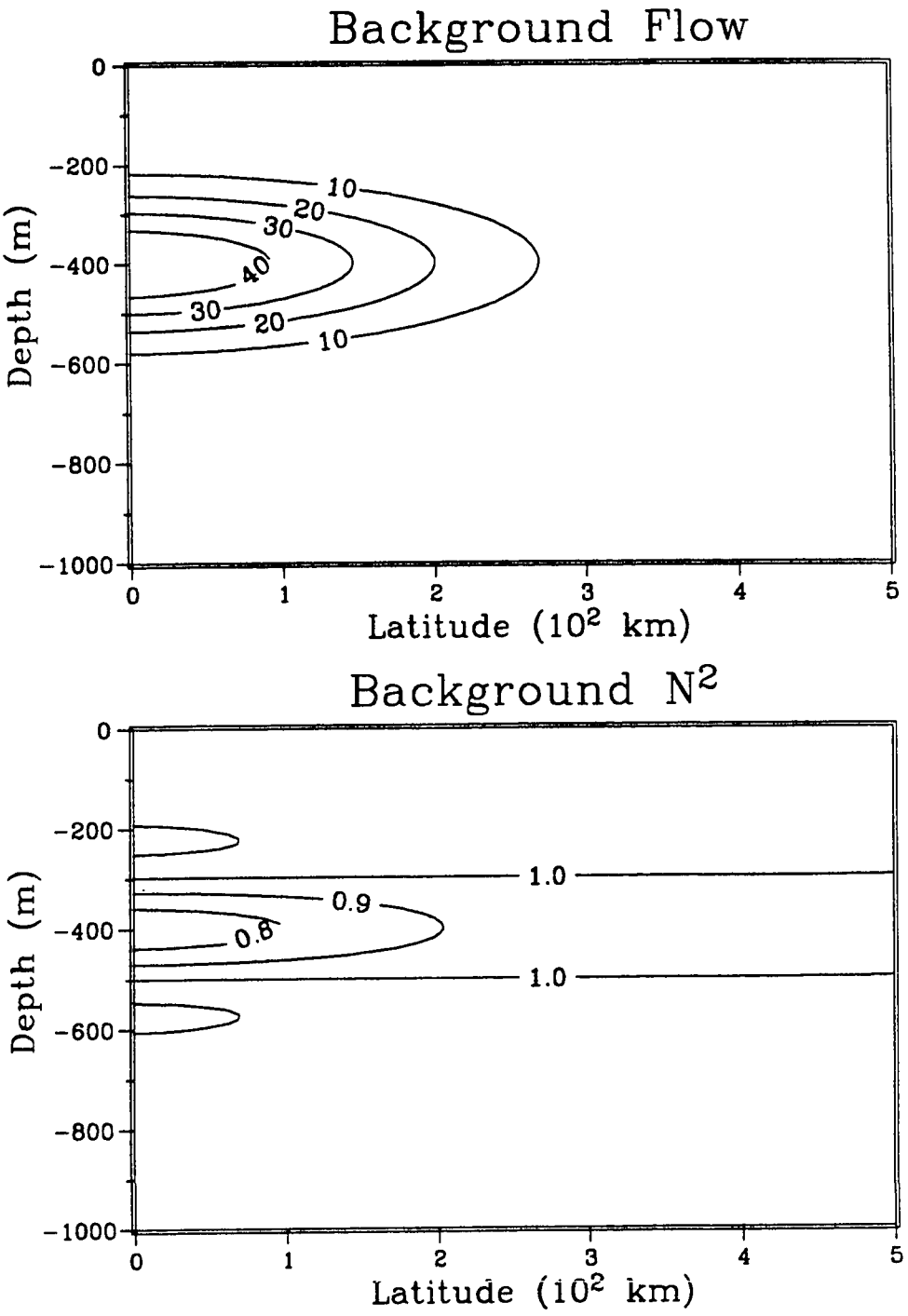


Figure 5.1: Background state for standard Undercurrent, (Top) Zonal velocity (cm/s), (Bottom) Mean $N^2$ distribution ($x10^{-4}$ $s^{-2}$).

The result of the spectral sweep in the absence of a mean flow is presented in Fig. 5.2. This spectra demonstrates the ability of the model to identify resonant solutions for a case in which the resonant wavenumbers are known. The spectral results, which show resonant solutions at c=-106.1, -53.1 and -35.4 cm/s, are in agreement with the theoretical eigenspeeds to within the resolution of the spectra which is ±0.1 cm/s. The resulting numerical perturbation pressure solutions for the first 3 of these resonances are presented, Fig. 5.3, here for later comparison with mean flow cases. These fields differ from the simple normal mode solutions discussed in Chapter 3 primarily due to the Rayleigh friction which smooths the phase contours and spreads the 180° phase transitions slightly. Although weak and not apparent in the amplitude plot, we also see a barotropic signal in the phase poleward of roughly 15° likely due to weak frictional coupling of wave modes. The barotropic signal is first seen here due to the decay of all other equatorial wave modes. In mean flow cases, we expect that the mean flows themselves may also lead to scattering into barotropic waves which due to their meridional propagation must be allowed to exit the domain. An important point to note is that the smooth meridional variation in the barotropic phase lines (for y>15°N), attests to the freely radiative nature of the northern boundary to barotropic energy. The fact that barotropic Rossby wave energy can freely escape the domain is apparent because we do not set up large barotropic amplitude or phase jumps indicative of meridional standing waves.

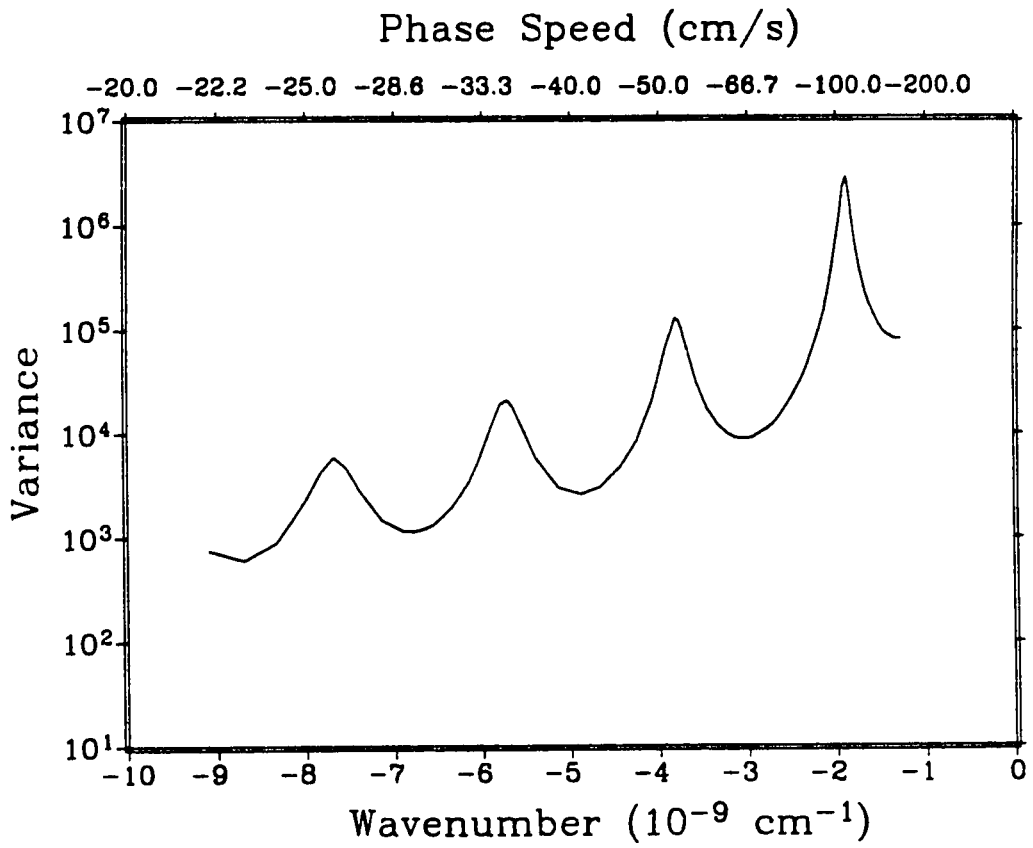


Figure 5.2: Model response spectra for resting ocean (U=0).

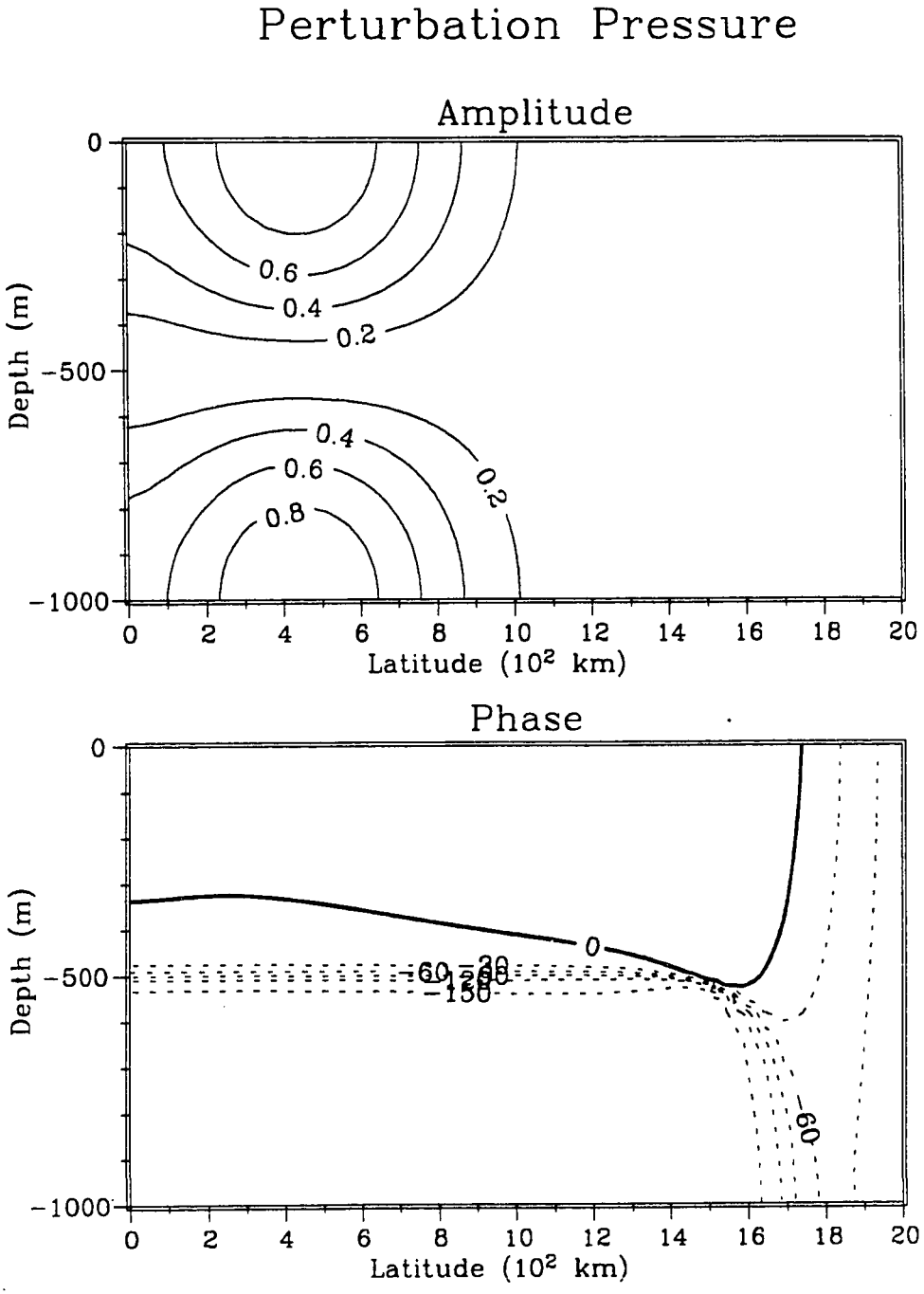


Figure 5.3a Pressure structure function for U=0 for the 1st vertical, 1st meridional mode Rossby wave.

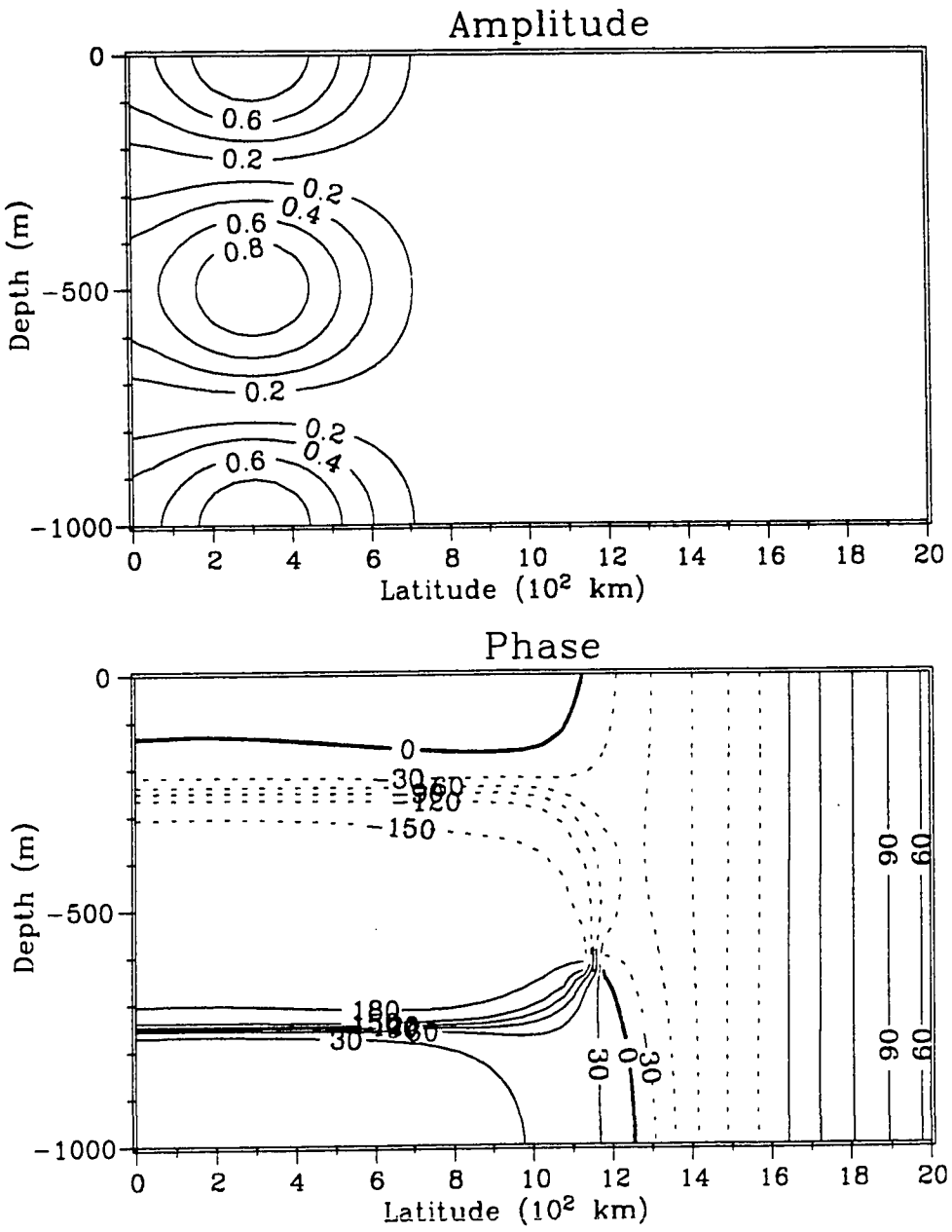


**Figure 5.3b: as in 5.3a except for the 2nd vertical mode.**

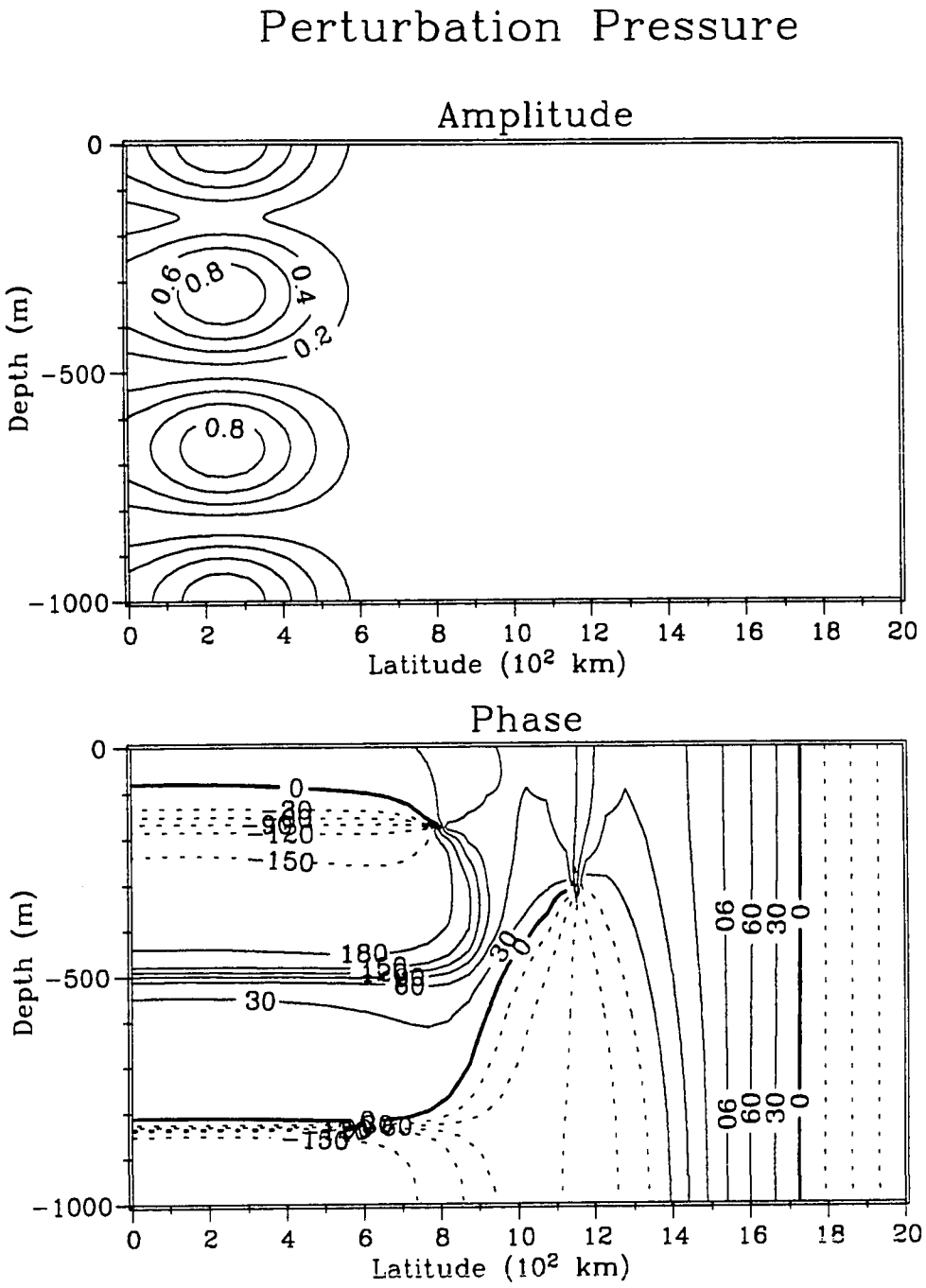


**Figure 5.3c: as in 5.3a except for the 3rd vertical mode.**

The results of the computation of the wave EP flux and its divergence in the vertical-meridional plane is presented in Fig. 5.4 for the third vertical mode. Only one mode is shown because the generalization to other vertical modes is straightforward. Due to the stronger interaction with eastward mean flows caused by smaller intrinsic phase speed, $c-U_0$, and shorter wave scales the third mode is chosen here and in the parameter study presented shortly. In the absence of friction, the net EP flux of the wave field is identically zero due to the exact balance of upward-downward and north-south wave propagation. However, the Rayleigh friction used here introduces a slight asymmetry in the amplitudes of the upward and downward components which leads to a net downward vertical EP flux. For the no flow case, this is manifested as the weak, $O(10^{-2}\ cm^2/s^2)$, linearly decreasing downward EP flux seen in Fig 5.4. The presence of this asymmetry, introduced by the friction, is useful in the study of the structural modification because it helps to reveal the underlying wave propagation away from the source region (*i.e.* the surface). As a result, we see the modified pathways of wave propagation in the presence of mean flow which help to illuminate the scattering and reflective nature of the flow.

In addition to the importance of the EP flux for diagnosing wave propagation, we see from Fig. 5.4 that associated with the frictional damping is an EP flux divergence field. This divergence field is wavelike in structure and according to the theory, by itself, induces a westward acceleration of the mean state at $O(\epsilon^2)$. This can be seen by rewriting equation (17) in McPhaden *et al.* (1986), using the present definition for the EP flux (differs in sign), in the form

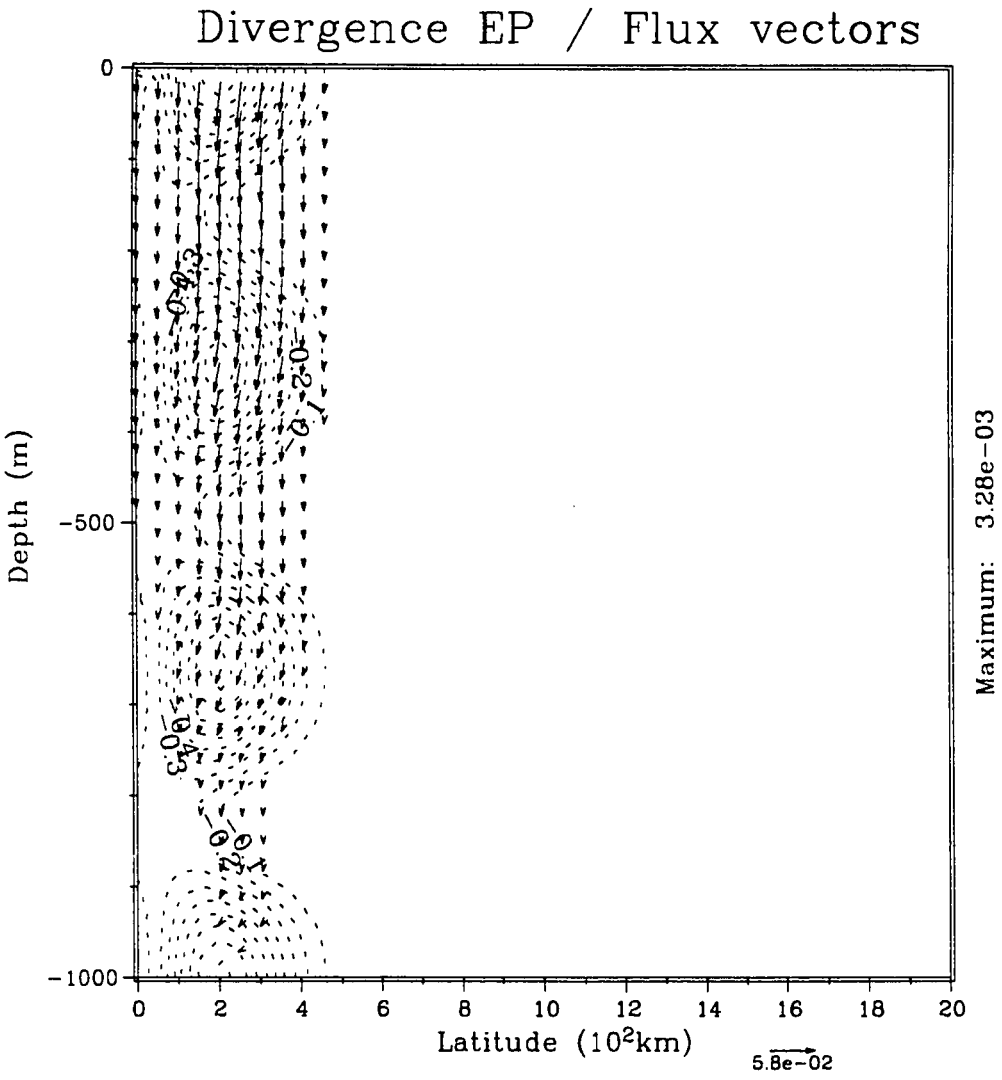


Figure 5.4: Eliassen-Palm flux vectors and divergence for the 3rd vertical, 1st meridional mode Rossby wave for U=0. Maximum absolute value of divergence (cm/s²) is noted at right, maximum flux magnitude (cm²/s²) is noted at bottom right.

$$\nabla\cdot\overrightarrow{EP} = 2\kappa(c-U_0+\imath\kappa/k)^{-1}\bar{E} \qquad (5.2),$$

where $\bar{E}$ is the non-spatially (in y and z) integrated form of Eq. 2.14. Therefore, far from critical surfaces where $|c-U_0| >> |\kappa/k|$, the EP flux divergence is proportional to the energy density of the wave field and alone leads to mean field accelerations everywhere in the direction of the intrinsic phase speed, $c-U_0$, which here is westward for $U_0>c$. Due to the importance of the $\chi$ field, at any particular position in the interior the accelerations can be either sign. However, in an integrated sense the acceleration is always in the direction of the intrinsic phase speed, as expected. This can be shown by integrating Eq. 2.32 over the domain and employing $\chi=0$ on the boundaries. Doing so gives

$$\iint U_t\,dydz = \iint\nabla\cdot\overrightarrow{EP}dydz \approx 2\kappa\iint(c-U_0)^{-1}\bar{E}dydz \qquad (5.3).$$

Therefore, in this case, the structure in the divergence field and mean flow acceleration clearly arises from the frictional dissipation of the wave energy. The structure is important to remember because, in the flow cases, the effects of the interaction with the current will be superimposed upon a basic structure similar to this.

The accelerations computed for this case are presented in Fig. 5.5. From this we see alternating regions of eastward and westward acceleration with the westward zones being stronger than the eastward ones. The meridional structure of the acceleration is essentially the same as the pressure field structure. While the vertical structure of this acceleration is such that regions of westward acceleration occur around the antinodes in the pressure field and regions of eastward acceleration occur around the nodes. The net result will be that the

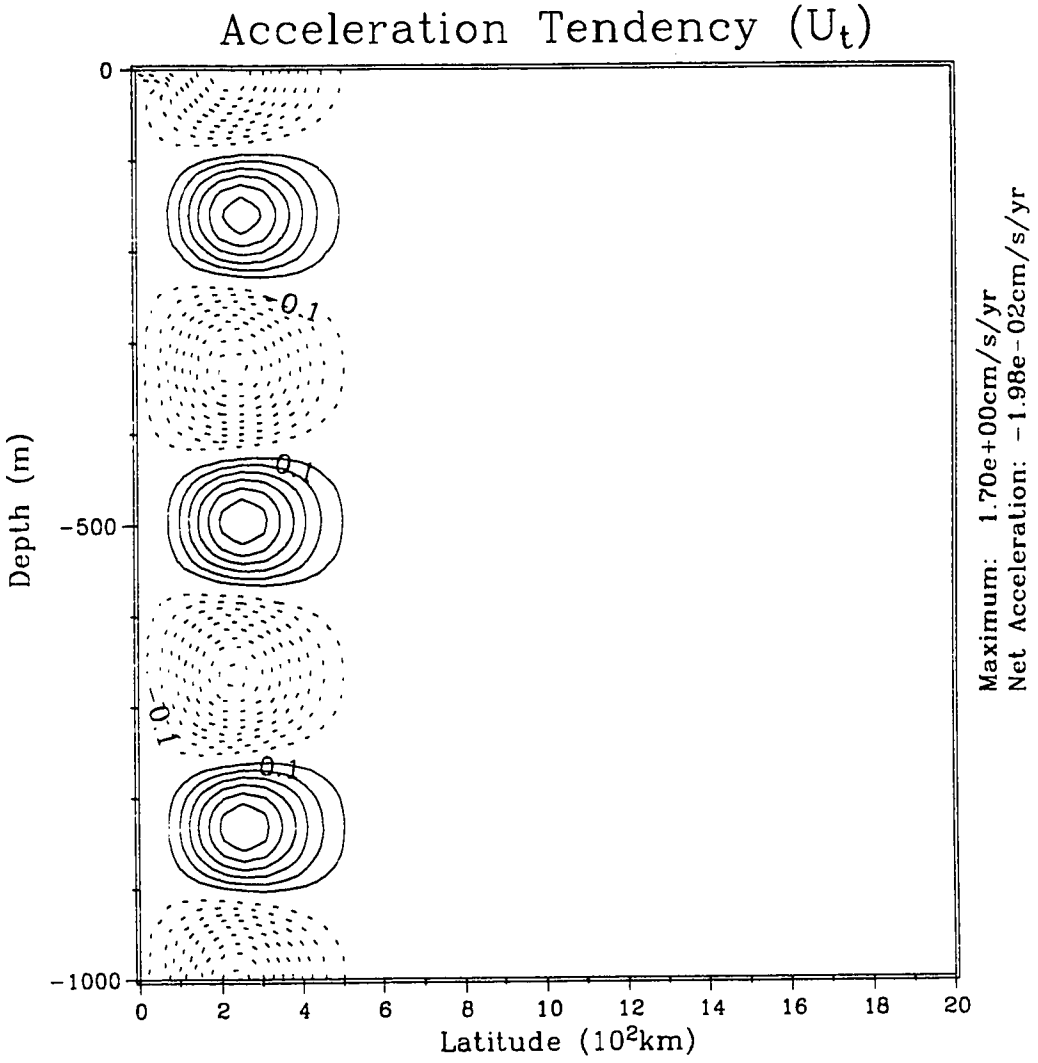


Figure 5.5: $O(\epsilon^2)$ wave induced mean acceleration for the 1st meridional, 3rd vertical mode Rossby wave in the absence of mean flow.

acceleration field will have twice the number of zero crossings in the vertical than the associated pressure field. This basic structure is mainly due to the contributions from the $\chi$ field. The action of the EP flux divergence is to cause the westward accelerating zones to be stronger than the eastward ones. Recall that the net acceleration induced by the $\chi$ field is zero. Assuming that the perturbation zonal velocity has an amplitude of 10cm/s leads to a very weak net westward acceleration of the mean state of 0.020 cm/s/yr with peak westward accelerations of 1.70 cm/s/yr. To be consistent throughout, for all accelerations presented here we assume an amplitude for the perturbation zonal velocity of 10cm/s and an $\epsilon$ value of 0.1. Since the acceleration is an $O(\epsilon^2)$ field, increasing the amplitude of the perturbation zonal velocity by a factor of 2 increases the induced acceleration by a factor of 4.

### 5.2.1 Standard Undercurrent

The results of the spectral sweep (not shown) for the standard flow field, Fig. 5.1, yields resonant peaks at c=-103.0, -46.6 and -29.8 cm/s. Therefore, one effect of the eastward flow is to weakly Doppler shift the resonances to slower westward phase speed. This shifting from the no-flow phase speeds is more pronounced for the second (6.5 cm/s $\approx$ 12% of no flow speed) and third (5.5 cm/s $\approx$ 16%) resonances as compared to the first (3.1 cm/s $\approx$ 3%). The perturbation theory, applied to a 50 cm/s amplitude flow with the above structure, Table 5.1, predicts the strongest shift in phase speed for the second

Table 5.1: Predicted shifts in phase speed (cm/s) for the first meridional mode structure for the first 3 vertical modes.

| Mode # | Components | | | | | Total shift |
|---|---|---|---|---|---|---|
| | $\iota kU_0$ | $v_0U_y$ | $w_0U_z$ | $v_0\rho_y$ | $w_0\rho_z$ | |
| 1 | 2.75 | 0.80 | -0.75 | -0.40 | -0.10 | 2 30 |
| 2 | 6.55 | 2.20 | 0.20 | 0.20 | 0.10 | 9.25 |
| 3 | 7.10 | 1.60 | 0.10 | 0.10 | 0.05 | 8.95 |

(9.25 cm/s), nearly as strong for the third (8.95 cm/s) and weaker for the first (2.30 cm/s) resonance. The results of this theory, while not in exact quantitatively agreement, nonetheless are qualitatively correct. The quantitative discrepancies are likely due to the fact the flow considered is not a small Rossby number flow ($R_0 \approx 2$) and friction is ignored in the theory. The stronger shifts for the latter resonances, according to the theory, arise from the more efficient projection of the flow structure upon the zero order waves structures. In general, the shift in phase speed predicted by this theory is dominated by the Doppler effect, Table 5.1, which goes as $\iint(U\Phi_n^2\Psi_m^2)dzdy$. Therefore, the stronger projection of the latter two modes occurs due to the shorter vertical and meridional scales for these waves in concert with the limited size of the EUC structure. The meridional shear tends to act together with the Doppler effect to increase the shift for this flow configuration due to correlation of wave v field with the mean meridional shear $U_y$. This portion of the shift was on the order of 20-30% of the Doppler term. Except for the first vertical mode, the remaining terms cause small frequency shifts, an order of magnitude smaller than the meridional shear term. In the first vertical mode case, the interaction is weaker and the vertical shear term is comparable but opposite in sign to the meridional shear term.

The resulting pressure fields for the first three resonances in this flow are presented in Fig. 5.6 to compare with the no-flow solutions of Fig. 5.3. As with the frequency shift results, the first vertical resonance (Fig. 5.6a) is affected little. A modal decomposition shows that 99.5% of the variance in the meridional velocity field

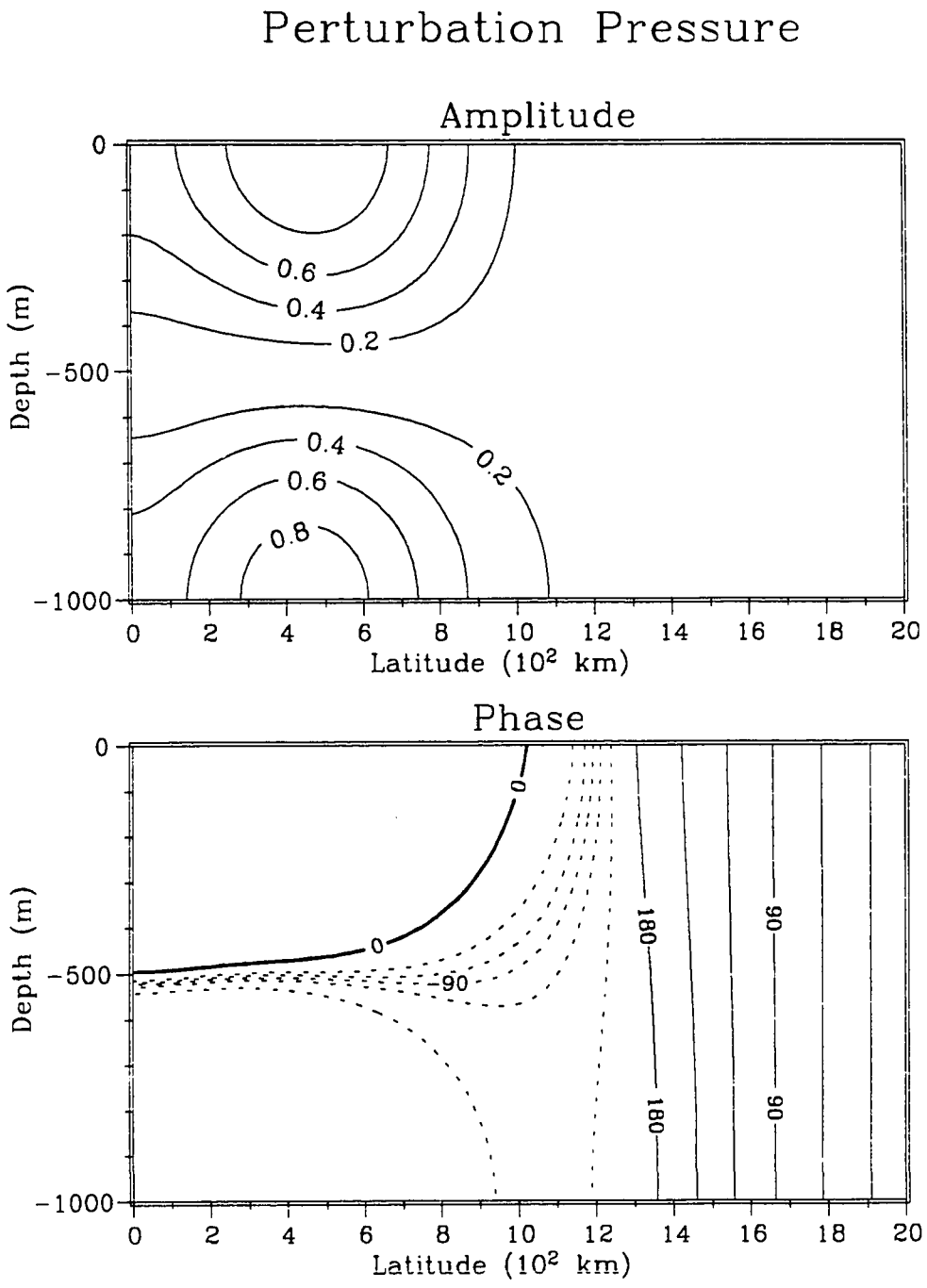


**Figure 5.6a Pressure structure function for the standard Undercurrent case, Case A, for the 1st resonance.**

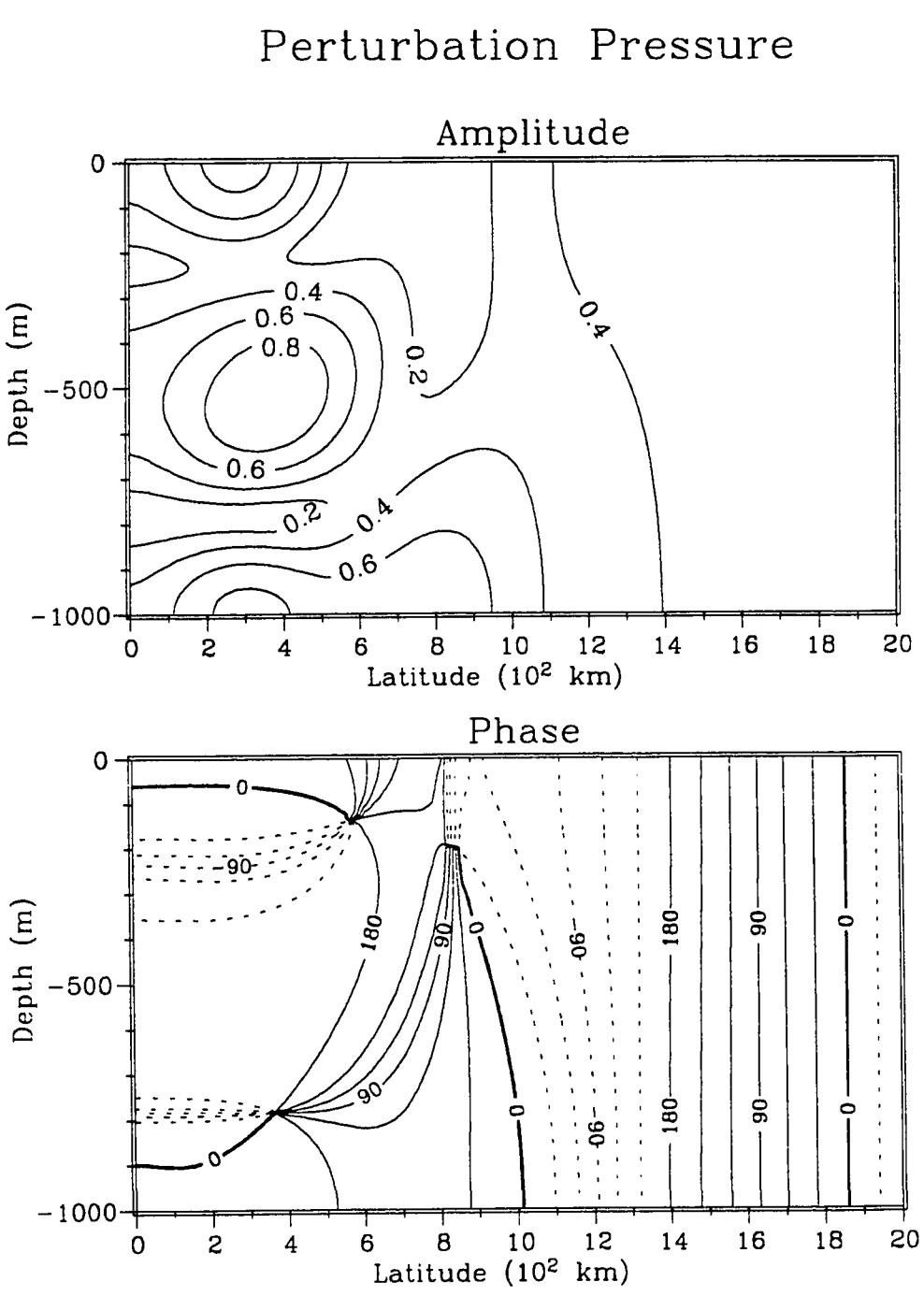


**Figure 5.6b: as in 5.6a except for the 2nd resonance.**

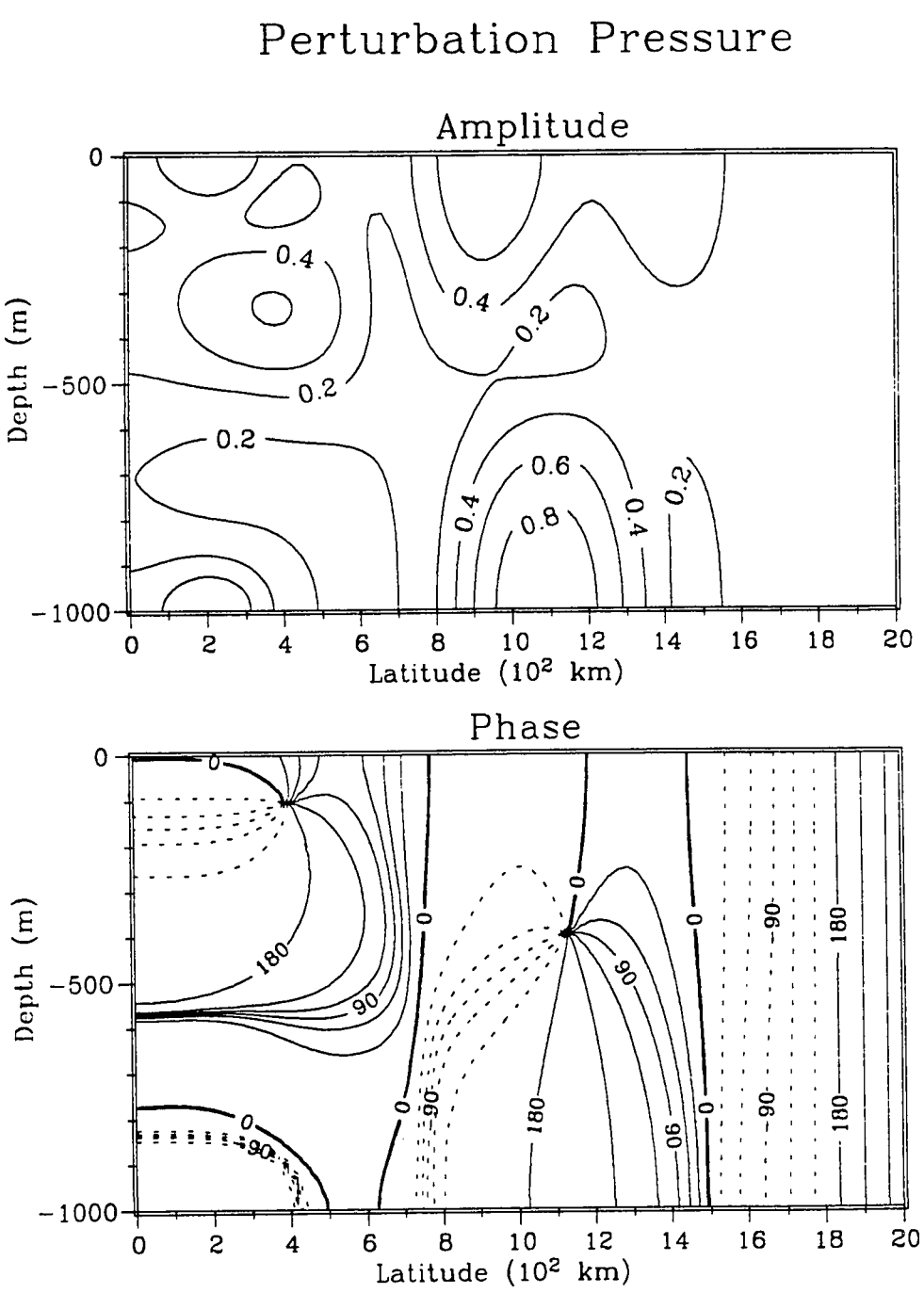


**Figure 5.6c: as in 5.6a except for the 3rd resonance.**

projects onto the first meridional (m=1), first vertical mode (n=1) structure. The weakness of the interaction agrees with that found in McPhaden *et al.* (1986) for the first vertical mode Kelvin wave. Clearly, the first mode is too fast and has too broad a scale in the vertical to be strongly affected by this flow field.

However, this is not true for the other 2 resonances. In the case of the second resonance, Fig. 5.6b, the modal decomposition shows that 90.7% of the variance projects onto the (m,n)=(1,2) wave mode with 4.2% on the (3,1) mode, 1.8% on the (1,4) mode and 1.4% on the (1,1) mode. While the majority of the variance remains in the (1,2) mode and the pressure field has much of the character of this mode, the presence of the higher meridional mode, (3,1), can be seen near the bottom in the vicinity of 8°N. Additionally, one can see evidence of meridional and vertical stretching and amplification of the pressure field in the vicinity of the flow, as seen in the slowly varying theory.

The results for the third resonance, Fig. 5.6c, show an even stronger interaction. Only 57.8% of the variance projects onto the (1,3) mode, 29.5% onto the (5,1) mode, 3.8% onto the (1,5) and 3.6% onto the (1,2) mode. Here we see that the resulting pressure field is considerably different than the (1,3) mode alone. Although reminiscent of the (1,3) mode near the equator, in that it appears to have 3 zero crossings in the vertical and a meridional maximum near 2-3°N, the pattern is very complicated. We see the maximum perturbation pressure in the vicinity of 11°N near the bottom. There is also a somewhat smaller maxima at the surface which is displaced equatorward from the deep maxima by roughly 2°. These maxima are the primary manifestation

of the (5,1) mode signal which appears in the modal decomposition.

The energy balances for these three resonant solutions, Fig 5.7, are consistent with the above results. In all three cases, wave energy is gained by direct pressure work at the surface and by extraction through the vertical shear work and work on the meridional density gradients. Conversely, in all cases, energy is lost from the perturbations through dissipation, meridional radiation through the northern boundary and by work against the horizontal shear. We also see, consistent with weak net westward acceleration, that all resonances extract a small quantity of energy from (*i.e.* decelerate) the eastward flowing mean state.

For the first resonance approximately 100% of the energy input is dissipated by friction. The energy exchanges with the flow and loss due to meridional radiation, which in this case are O(1-2%) of the forcing amplitude, are nearly self-cancelling. The smallness of the individual exchanges further supports the contention that the first resonance is only weakly affected by this flow field. The balances for the other two resonances, again, point to the stronger interaction. Comparison of these balances shows that while both resonances extract a small quantity of net energy from the mean, the individual exchanges with the mean state for the third resonance are roughly twice that of the second. For the second resonance we see stronger meridional radiation at the northern boundary which is nearly compensated for in the budget by weaker dissipation.

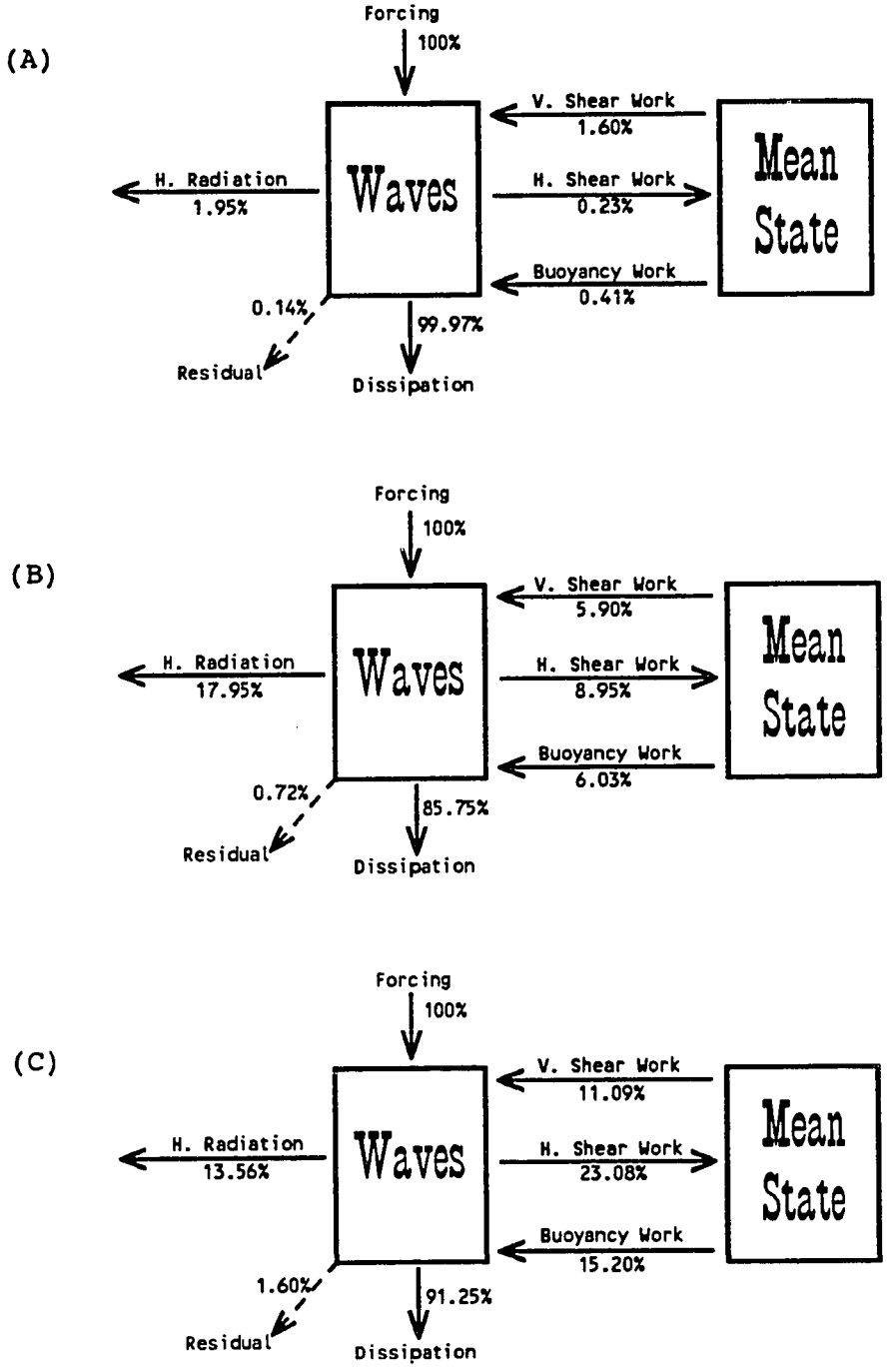


Figure 5.7: Energy budgets for the first 3 resonances in the standard mean flow case. (a) 1st resonance, (b) 2nd resonance, (c) 3rd resonance.

The results of the integrated energy budget suggest that, in all cases, the net effect of the waves on this flow will tend to weaken the vertical shear and strengthen the meridional shear. Consideration of the spatial dependence of the energy exchange shows that this is likely the case, Fig. 5.8. The spatial dependence of these results is insensitive to the particular resonance considered, so we present only the results for the third resonance. This particular resonance was chosen because, in general, the effects are the strongest of the three. We see from the meridional buoyancy work, $\overline{v\rho}yU_z/N^2$, and work against vertical shear, $\overline{uw}U_z$, that the waves gain energy from the shear zone above the core and lose it below. Due to the unequal areas/amplitudes these exchanges clearly result in the net gain of energy by the wave field. The waves tend to lose energy to the flow towards the poleward flanks by working against the meridional shear, $\overline{uv}U_y$. These results also suggest that the waves will tend to weaken the shear above the core and strengthen it below and to the sides. The direct calculation of the induced acceleration confirming this is presented below.

The EP flux results for these three resonances are presented in Fig. 5.9. For the first mode, Fig. 5.9a, there is only a small deviation from the analogous results for a resting ocean solution (not shown since it can easily be inferred from the third vertical mode case). The principle effect is a poleward bending of the EP flux vectors around the mean flow. This effect is relatively small but consistent with the meridional stretching seen in the slowly varying pressure field. For the second resonance, Fig. 5.9b, the EP flux results show that the flow induces a similar bending of the flux vectors. However,

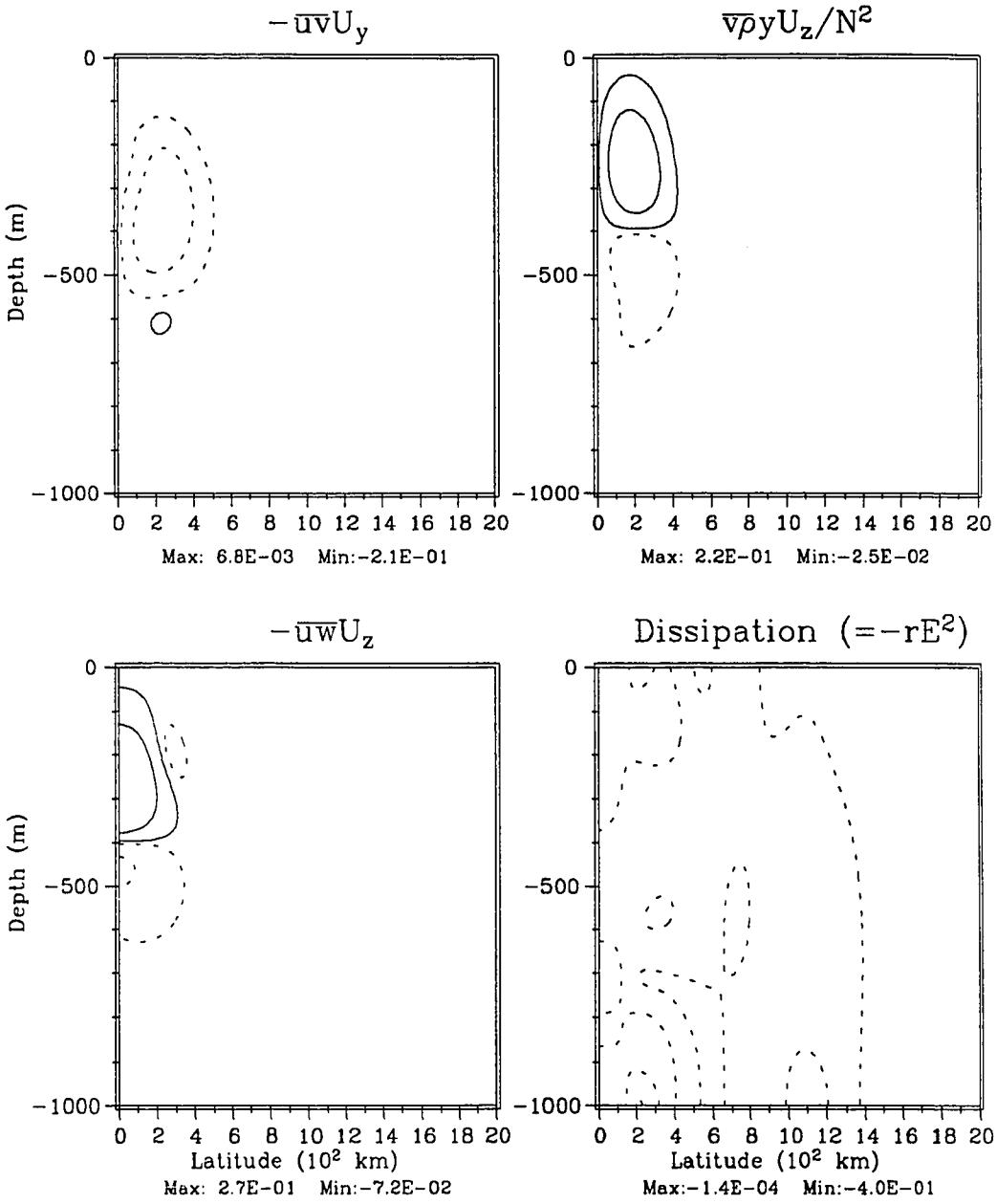


**Figure 5.8: Energy exchange terms between wave and mean for the third resonance. (Top left) horizontal shear work, (top right) buoyancy work, (bottom left) vertical shear work, (bottom right) dissipation.**

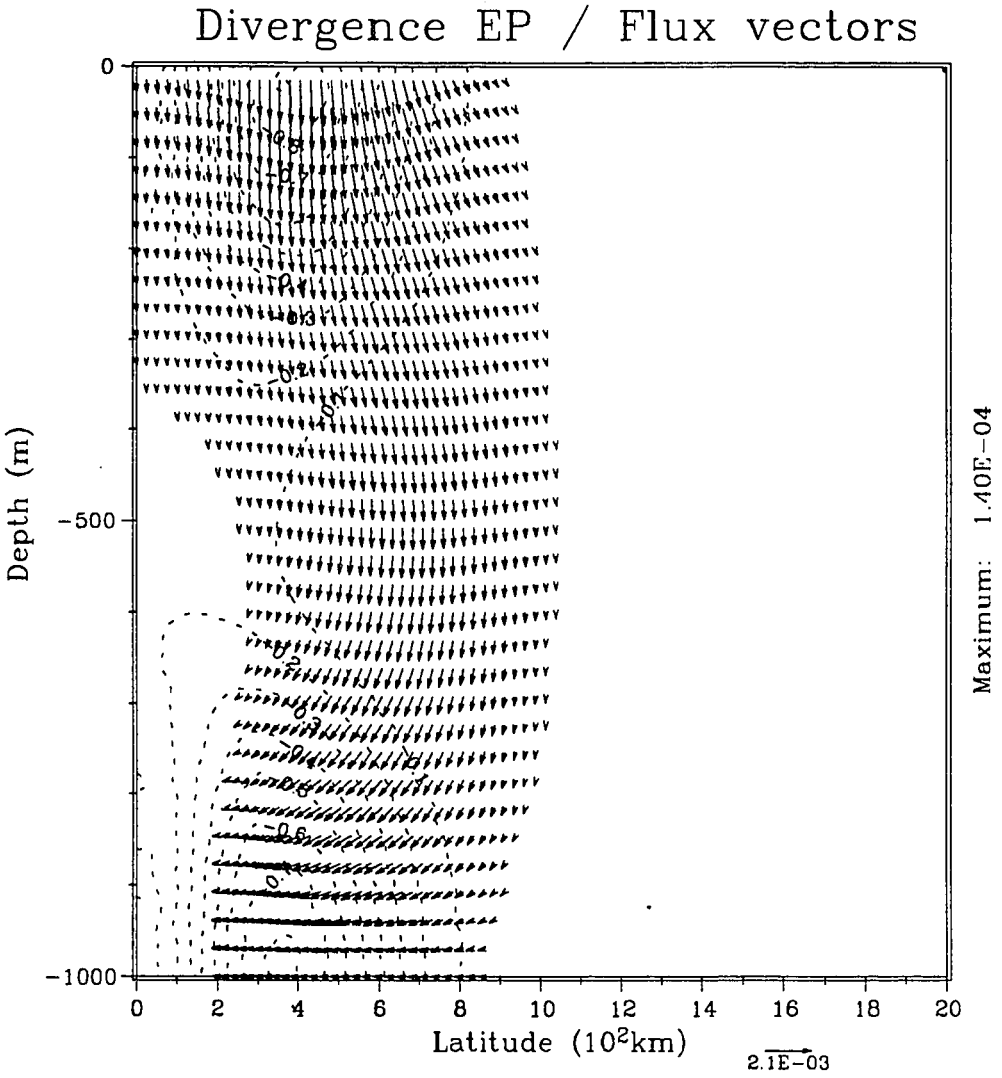


Figure 5.9a: E-P flux vectors ($cm^2/s^2$) and divergence ($cm/s^2$) for the 1st resonance for the standard Undercurrent.

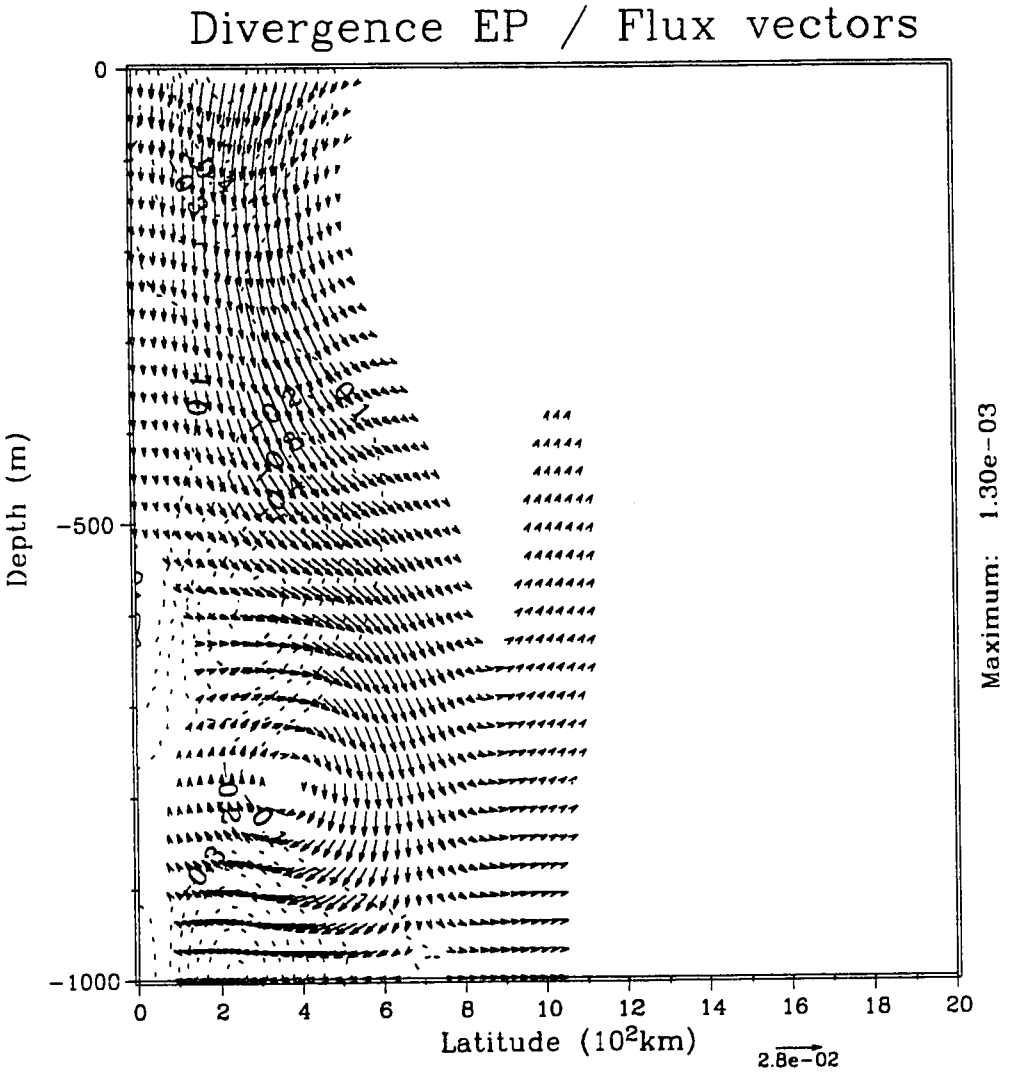


Figure 5.9b: Same as 5.9a except for the 2nd resonance.

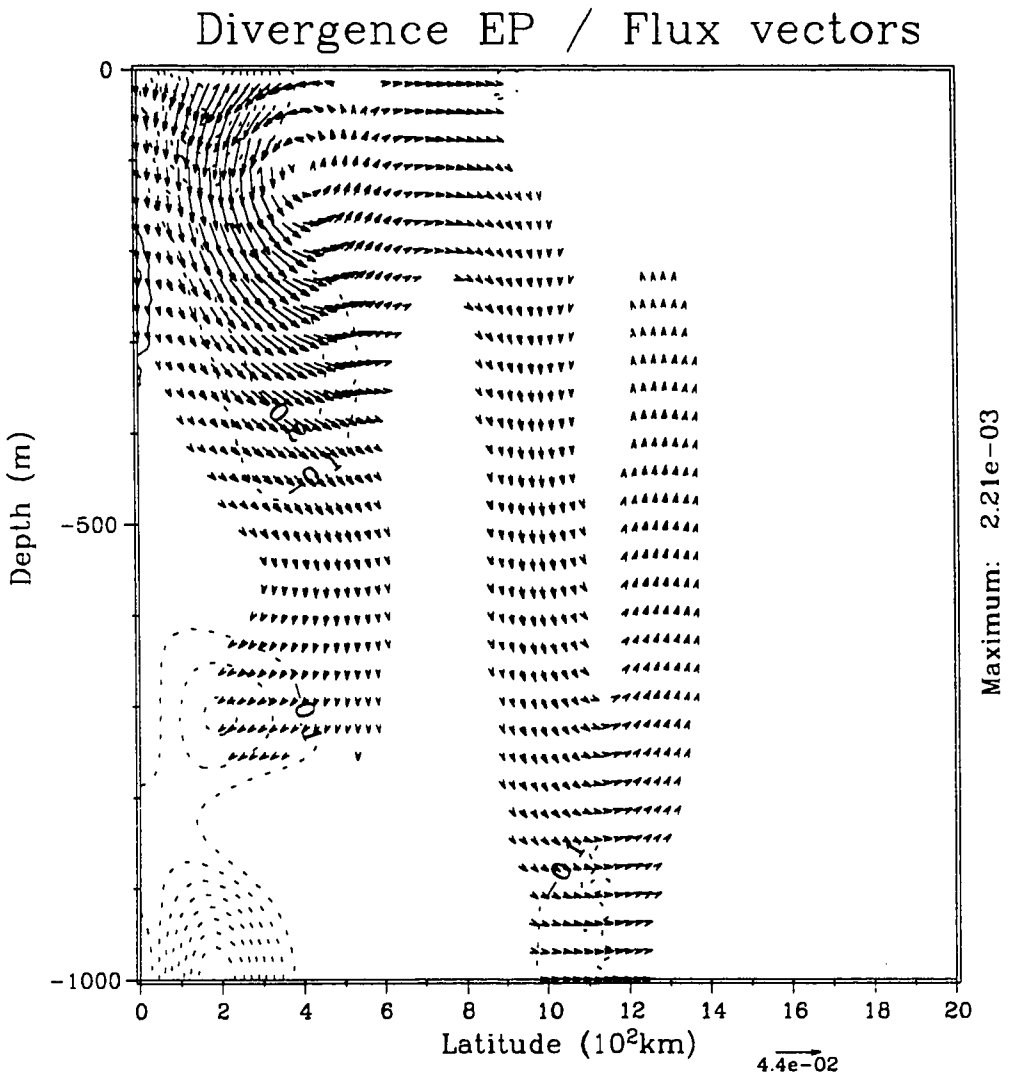


Figure 5.9c: Same as 5.9a except for the 3rd resonance.

in this case the bending is stronger and leads to a deflection of a portion of the wave activity off the equator. This scattering results in the reflection of the wave activity off the bottom near 9°N with subsequent radiation upwards and polewards. It is this scattering which is responsible for the leakage of wave activity into other wave modes, manifested here as the pressure variance signal appearing in the (3,1) wave mode. The case of the third resonance, Fig. 5.9c, shows that the further decrease in the vertical wave scale and intrinsic phase speed leads to significant reflection of wave activity directly off the flow near the core. Here, the scattered wave strikes the surface near 8°N and reflects downward encountering the bottom near 11°N. These various reflection points off the surface and bottom for the latter two resonances coincide exactly with the off equatorial maxima seen in the pressure fields for these two resonances. In both cases, the flow has scattered wave activity poleward leading to a relative shadow zone below the current in the vicinity of the equator. So, consistent with the modal decompositions, we see the modifications to the wave modes in the resting ocean increasing with decreasing intrinsic phase speed. In addition, we see clearly that the EP flux vectors provide a simple way to understand the effect of the mean flow upon the equatorial wave modes.

We present the $O(\epsilon^2)$ wave-induced mean field accelerations for the three resonances in Fig. 5.10. Due to the weak changes in the EP flux divergence, the induced accelerations for these resonances is nearly what would be expected from viscous damping of the wave field. These results appear contradictory to the accelerations hypothesized from the

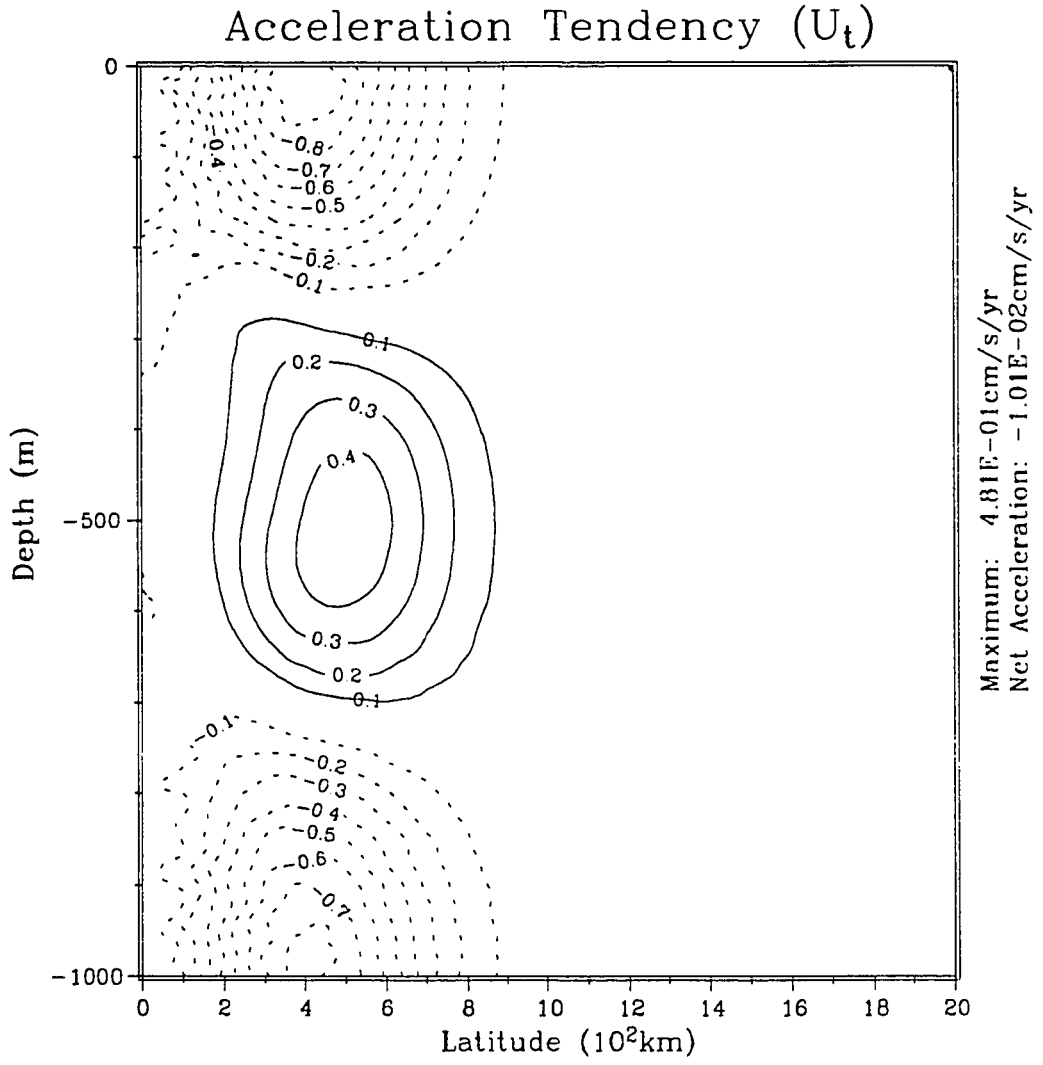


Figure 5.10a: $O(\epsilon^2)$ mean accelerations for the 1st resonance in the standard flow case. Peak magnitude of acceleration (max) and y-z spatially averaged (net) values are given at right for perturbation u field amplitude of 10cm/s.

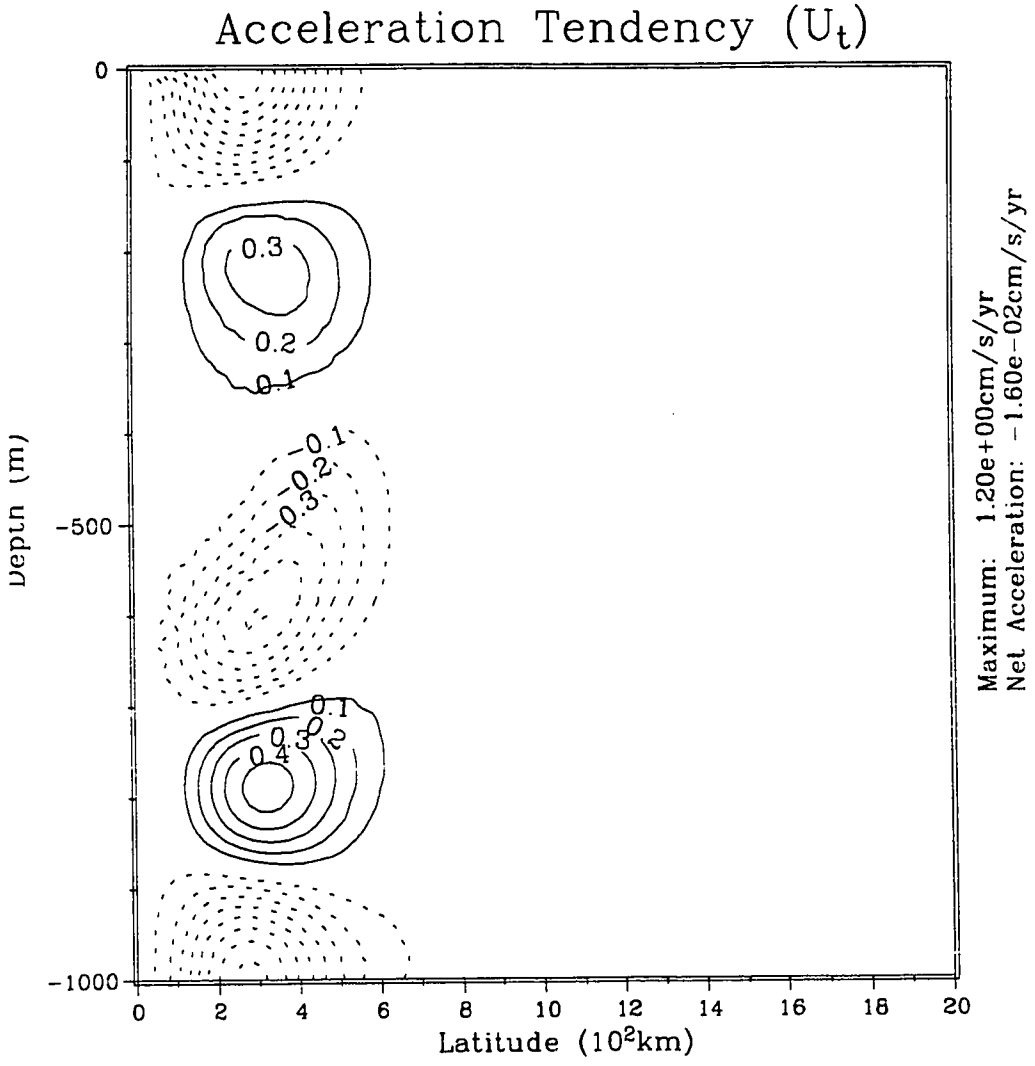


Figure 5.10b: Same as 5.10a except for the 2nd resonance.

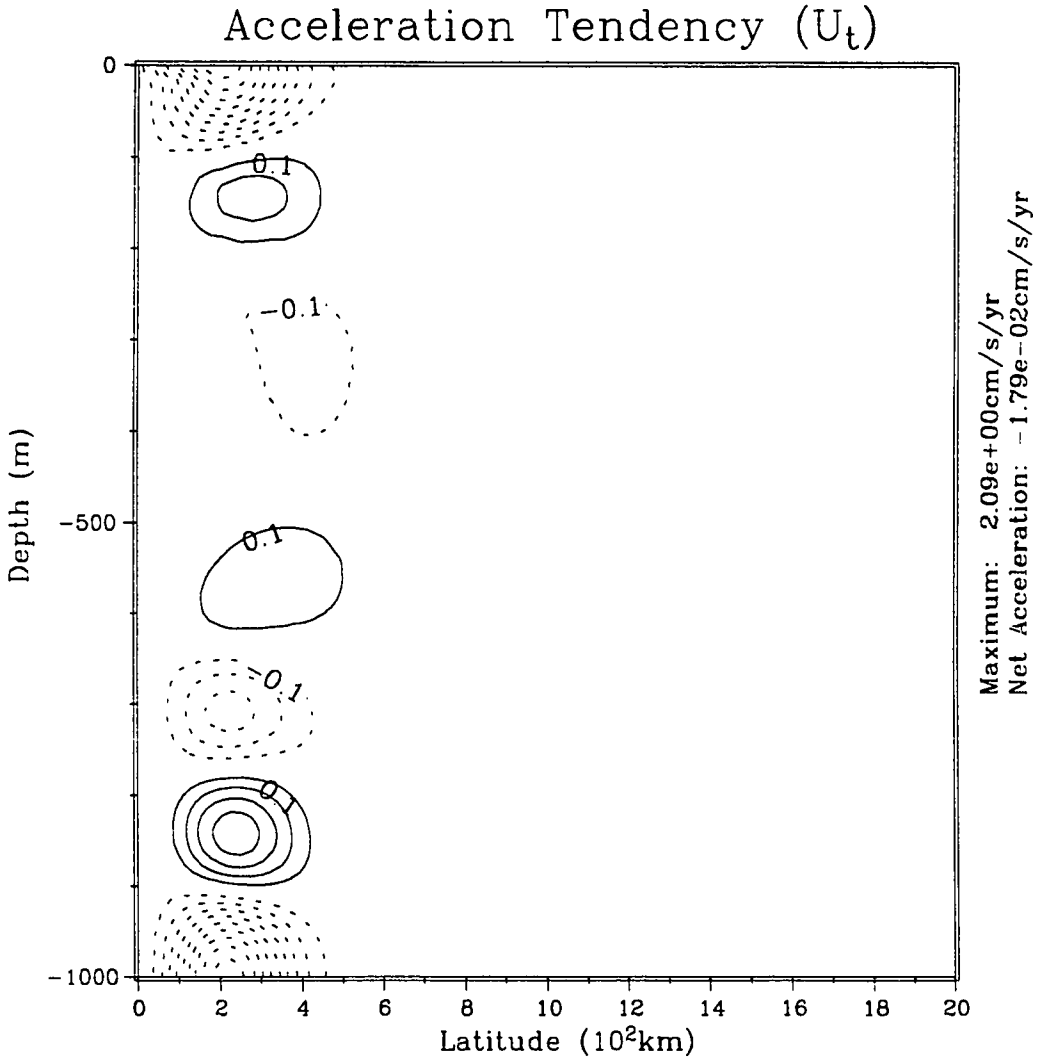


Figure 5.10c: Same as 5.10a except for the 3rd resonance.

energy considerations alone. What we have is the viscously damped portion of the acceleration masking the accelerations due to momentum exchanges with the mean shears. Remember that the energy budget for these waves showed that the dissipation was from 4 to 60 times greater than the momentum exchanges with the flow. The y-z structure of the acceleration in these cases is consistent with that for viscous damping observed in the absence of flow.

For the first resonance, Fig. 5.10a, where the momentum exchanges are weak, O(1/60) of the dissipation, there is very little modification to the no-flow acceleration pattern. The second resonance, Fig. 5.10b, shows that the effect of the flow has been to decrease the amplitude of the acceleration and move the locations of the peak accelerations away from the core. The induced accelerations for the third resonance, Fig. 5.10c, show results similar to the second resonance but the weakening of the accelerations near the core is greater. These changes in $U_t$ near the flow are likely due to the decreasing of the $(U-c)^{-1}$ factor on the right hand side of Eq. 2.28. This effect causes a decrease in the effective damping which weakens the EP flux divergence, Fig. 5.7b, in that region. In addition, we expect the meridional scattering of wave activity to further reduce the near-equatorial component of the mean accelerations for both resonances. The deflection of a portion of the wave activity poleward, by scattering, reduces the amount of the wave activity dissipated near the equator. Ignoring the frictionally damped portion of the acceleration (*i.e.* noting the changes from Fig. 5.5 to 5.10c), we see that the changes to the acceleration patterns due to interaction with the mean flow are a region of relatively strong east-

ward acceleration above the core near the equator and somewhat weaker westward acceleration below and to the flanks of the Undercurrent. The changes to the acceleration pattern, therefore, are consistent with the pattern of energy exchange seen in Fig. 5.8. However, we note here that the induced accelerations in this and other eastward mean flow cases are very weak (net westward accelerations are O(0.01 cm/s/yr) with peak values of 1-2 cm/s/yr) owing to relatively weak dissipation. (Recall that for the purposes of mean flow acceleration we fix the amplitude of the perturbation zonal velocity. Therefore, in this case, dissipation, with a decay time of 5 yrs, is relatively small.)

Consideration of the modification to the wave structures using the perturbation theory yields unsatisfactory results. The $O(\epsilon)$ structural coupling coefficients for these 3 vertical modes are presented in Table 5.2. These results indicate that this meridional wave mode should couple strongest to the same meridional structure but differing vertical structures in disagreement with the numerical solution. This is probably due to the failure of the small amplitude assumption. This aside, the perturbation theory does point to stronger coupling as the intrinsic frequency decreases. In general, the largest contributors to a particular coupling coefficient are the Doppler terms, $\iota kU_0$, in 3.38-3.39. For the 1st vertical mode, the next largest contribution is the vertical advection of momentum. Whereas for the 2nd and 3rd modes it is the meridional advection of momentum, $v_0 U_y$, and density, $v_0 \rho_y$, which tend to be the next in importance.

Table 5.2: Coupling coefficients ($\times 10^4$) of the largest 4 $O(\epsilon)$ modes for the first 3 vertical modes and first meridional O(1) mode in a constant N ocean for the standard flow field (see text). Modes are denoted as (m,n).

| O(1) Mode # | $O(\epsilon)$ Mode # | Component Terms | | | | | Total |
|---|---|---|---|---|---|---|---|
| | | $v_0 U_y$ | $w_0 U_z$ | $v_0 \rho_y$ | $w_0 \rho_z$ | $\imath k U_*$ | |
| (1,1) | (1,2) | 0.26 | 0.62 | 0.24 | 0.18 | 0.00 | 1.30 |
| | (1,3) | 0.40 | -0.49 | 0.08 | -0.13 | 1.44 | 1.30 |
| | (1,5) | -0.08 | 0.06 | -0.04 | 0.01 | -0.44 | -0.48 |
| | (3,1) | 0.04 | 0.16 | -0.05 | -0.03 | 0.65 | 0.46 |
| (1,2) | (1,3) | -1.23 | -0.53 | -0.86 | -0.41 | -3.59 | -6.62 |
| | (1,4) | 0.70 | -0.46 | 0.28 | -0.17 | 3.41 | 3.76 |
| | (1,5) | 0.49 | -0.24 | 0.39 | -0.03 | 2.46 | 3.06 |
| | (3,1) | -0.35 | -0.82 | -0.66 | -0.22 | -0.96 | -3.01 |
| (1,3) | (1,5) | 1.02 | -0.34 | 0.74 | -0.02 | 6.26 | 7.66 |
| | (1,2) | 1.64 | 0.74 | 0.60 | 0.30 | 4.29 | 7.57 |
| | (3,1) | 0.85 | 0.31 | -0.51 | -0.12 | 5.63 | 6.17 |
| | (5,1) | -0.38 | 0.21 | -0.30 | -0.09 | 5.33 | 4.77 |

All of these results show that, with the exception of the shifts in phase speed, the effects of the flow tends to increase with vertical mode number due to smaller wave scales and smaller intrinsic phase speed. For this reason, for the remainder of this discussion of the Undercurrent only results for the third resonance will be presented. As shall be seen, the most prevalent effect of the type of flow field used here is to cause the meridional scattering of the wave activity input near the equator. This effect occurs for all of the cases to be presented. The results also suggest that the scattering, for this meridional mode, tends to generate lower mode vertical structure, i.e. barotropic and first baroclinic. The signature of the first baroclinic mode in the pressure fields can be easily seen in both amplitude and phase near 10°N while the barotropic energy is apparent primarily in phase. This preference for low modes is consistent with an idea presented by Killworth (1979) for an idealized current. He showed that a background flow possessing the vertical structure of a free normal mode permits meridional propagation for only vertical modes of lower vertical order and decay for those of higher vertical order. However, a more likely explanation is that the energy being scattered to higher latitude appears in the low vertical modes because, of the modes which possess variance at those latitudes, they are the nearest ones in dispersion space. The equatorial trapping scale increases (decreases) with increasing horizontal (vertical) mode number. This is illustrated by the longwave dispersion diagram presented in Fig. 5.11. From this we see that the two modes nearest to the (1,3) in dispersion space are the faster (3,1) and the slower (5,1). Since both of these modes can

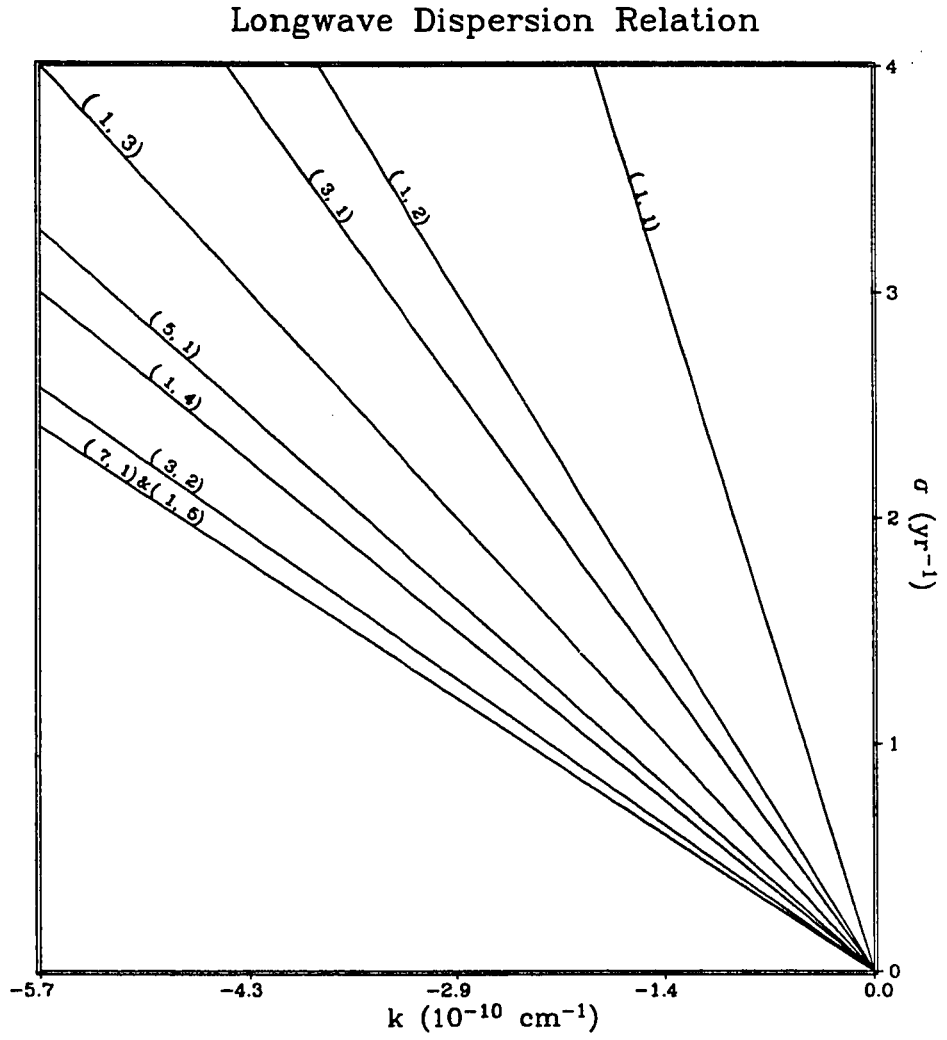


Figure 5.11: Long Rossby wave dispersion relation. The (1,3) mode is presented along with the 3 faster (longer at fixed $\sigma$) and nearest 5 slower (shorter) modes.

explain variance at higher latitudes, poleward scattering could easily excite them. The geometry of the particular flow field is likely very important in determining where the wave activity will be scattered and is probably responsible for the stronger (5,1) content as opposed to (3,1) in this case.

### 5.2.2 Parameter Variations

To attempt to understand the roles of the various scales of the background state in the response of the wave modes, a series of parameter variations is performed. These variations include scale changes as well as flow amplitude, location, $N^2$ changes and frictional magnitude and are summarized in Table 5.3. In all cases, the spectral sweep from high eigenspeed (small wavenumbers) toward lower (larger wavenumbers) is performed and the 3$^{rd}$ fastest resonance is found and examined. In all cases, except for the westward flow (which will be discussed later), the resonant eigenspeed is not drastically different from the no flow speed. Therefore, we expect that the pressure fields obtained for these parameter variations do represent the modified pressure field of the desired resonance. Consequently, we choose to maintain the convention of using the third resonance as the analogue for studying the modifications to the third vertical mode. Due to the weakness of the resulting accelerations in the presence of eastward flows, we do not present the acceleration fields for the eastward mean flow cases. Discussion of the $O(\epsilon^2)$ wave induced mean accelerations is restricted to westward flow cases where they are strong enough to be significant.

Table 5.3: Parameter variations for Equatorial Undercurrent

| Case # | Amplitude | $\delta_y$ | $\delta_z$ | $z_0$ | $\kappa$ |
|---|---|---|---|---|---|
| A | 50cm/s | 150km | 100m | 400m | 0.2 |
| B | 100cm/s | 150km | 100m | 400m | 0.2 |
| C | 50cm/s | 250km | 100m | 400m | 0.2 |
| D | 50cm/s | 150km | 200m | 400m | 0.2 |
| E | 50cm/s | 150km | 100m | 300m | 0.2 |
| F | 50cm/s | 150km | 100m | 400m | 0.1 |
| G* | 70cm/s | 150km | 75m | 150m | 0.2 |
| H | -40cm/s | 150km | 100m | 400m | 0.2 |

* Variable $N^2$ possessing thermocline (see Eq 5.4 - p 106).

The resulting pressure field for the standard flow field, Case A, is presented in Fig. 5.6c and is identical to the case of the third resonance discussed above. For the purposes of this discussion, recall that the pressure field is complicated in the near equatorial zone. This field also possesses a strong first vertical mode-like structure whose maximum expression is centered at 11°N at the bottom. In addition, the 1$^{st}$ vertical mode structure is skewed such that its surface expression occurs at about 9°N. Other characteristics of this field will be recalled for comparison in the ensuing discussion as needed. For reference, the three largest components of the modal decompositions for the various cases of the parameter study, are summarized in Table 5.4 and will be discussed as needed.

Before we consider variations in the structure of the Undercurrent, we wish to investigate a higher meridional mode in the standard Undercurrent. For this we specify a vertical velocity distribution similar to the 3$^{rd}$ meridional mode and again find the 3$^{rd}$ resonant phase speed. For this case the phase speed is -14.75 cm/s and has been shifted from a resting ocean phase speed of -15.16 cm/s. In Fig. 5.12a we present the resulting pressure field. For comparison the no-flow solution is presented in Fig. 5.12b. The principal effects of the flow are meridional stretching of the near-surface pressure field, equatorward bending below the core and scattering of a portion of the solution to high latitudes. The solution in the near equatorial zone (within 2°) below the core seems to be of smaller scale both vertically and meridionally and that at high latitudes appears to possess larger vertical scales.

Table 5.4: Modal decompositions for the parameter study of the Equatorial Undercurrent. Largest 3 contributors are listed in the form: Wave mode (m,n) / % of variance of projection.

| Case | Principle Modes | | |
|---|---|---|---|
| | 1st | 2nd | 3rd |
| $A_1$ | (1,3) / 57.8% | (5,1) / 29.5% | (1,5) / 3.8% |
| $A_3$ | (3,3) / 51.6% | (1,6) / 17.8% | (1,8) / 7.8% |
| B | (5,1) / 67.4% | (1,3) / 15.0% | (3,1) / 3.7% |
| C | (1,3) / 64.7% | (5,1) / 19.2% | (1,2) / 5.2% |
| D | (1,3) / 46.2% | (5,1) / 21.7% | (3,1) / 6.0% |
| E | (1,3) / 64.3% | (5,1) / 16.9% | (1,4) / 6.3% |
| F | (1,3) / 58.8% | (5,1) / 30.5% | (1,5) / 4.0% |
| G | (5,1) / 67.4% | (1,3) / 8.1% | (1,2) / 6.7% |
| H | (1,3) / 31.7% | (3,1) / 28.2% | (1,2) / 15.7% |

Note: Case $A_1$ is the standard Undercurrent case for the 1st meridional mode and Case $A_3$ is for the 3rd mode.

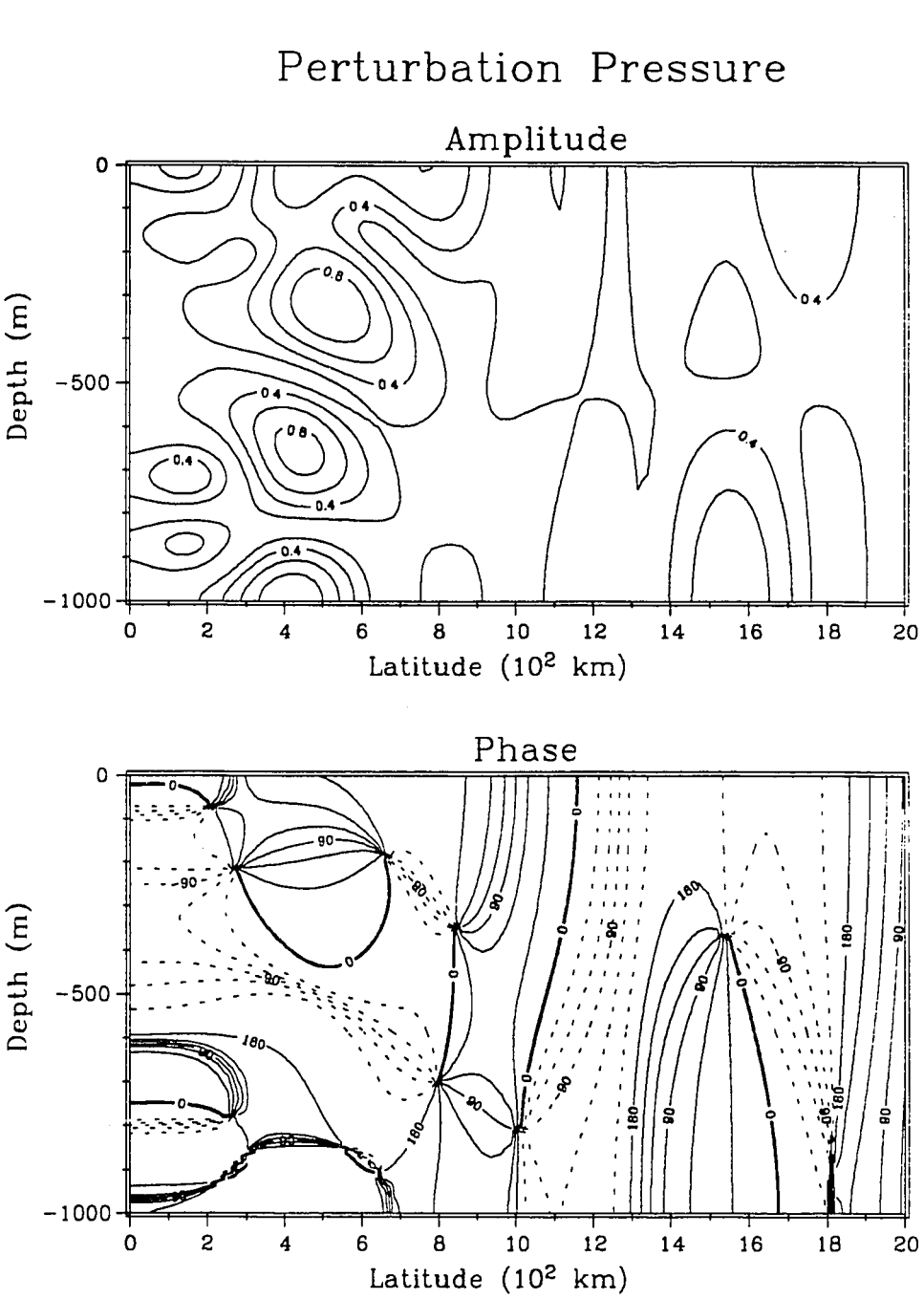


**Figure 5.12a: Pressure solution for the 3rd resonance for the 3rd meridional mode in the standard Undercurrent**

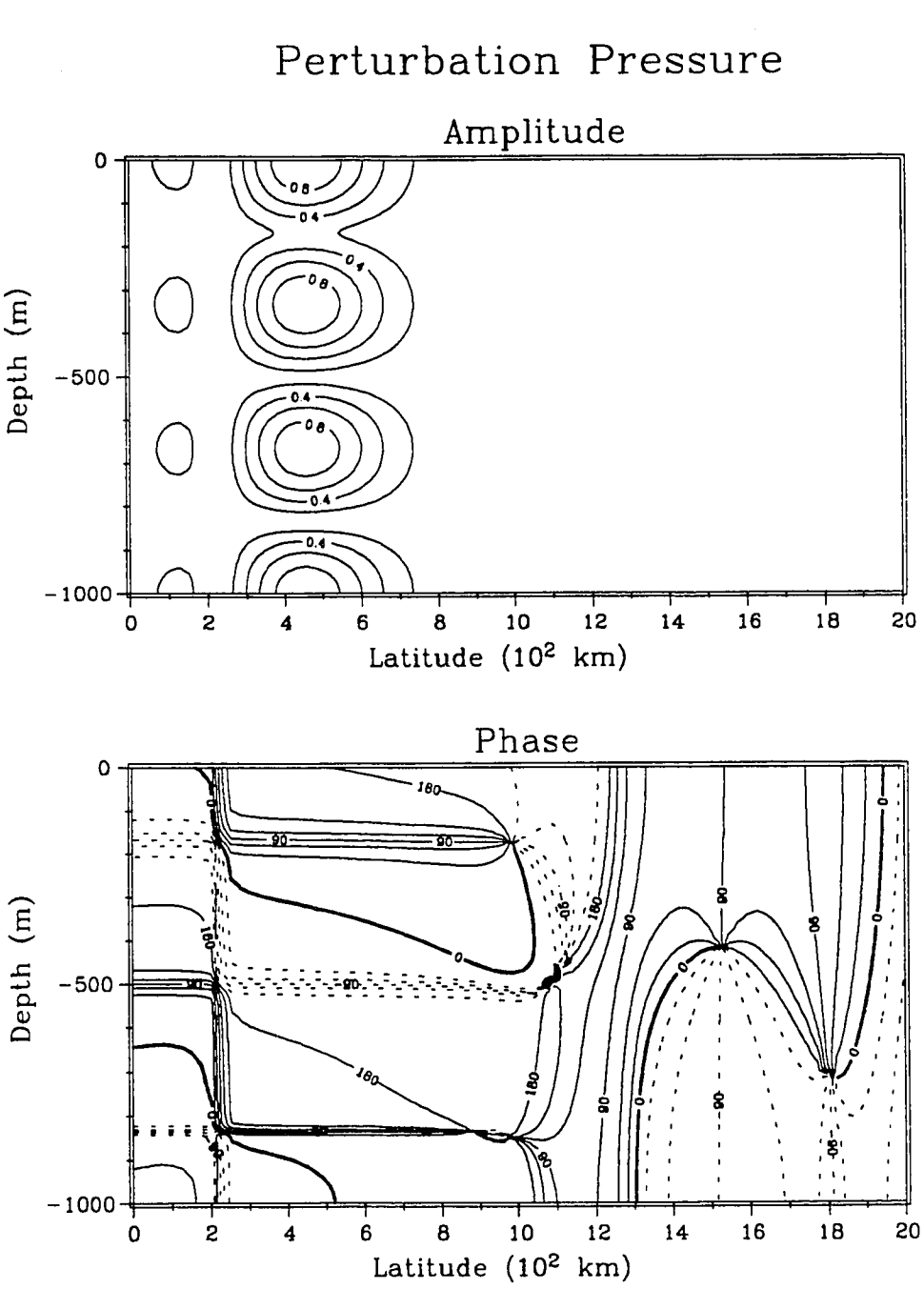


**Figure 5.12b: Pressure solution for the 3rd resonance for the 3rd meridional mode in a resting ocean.**

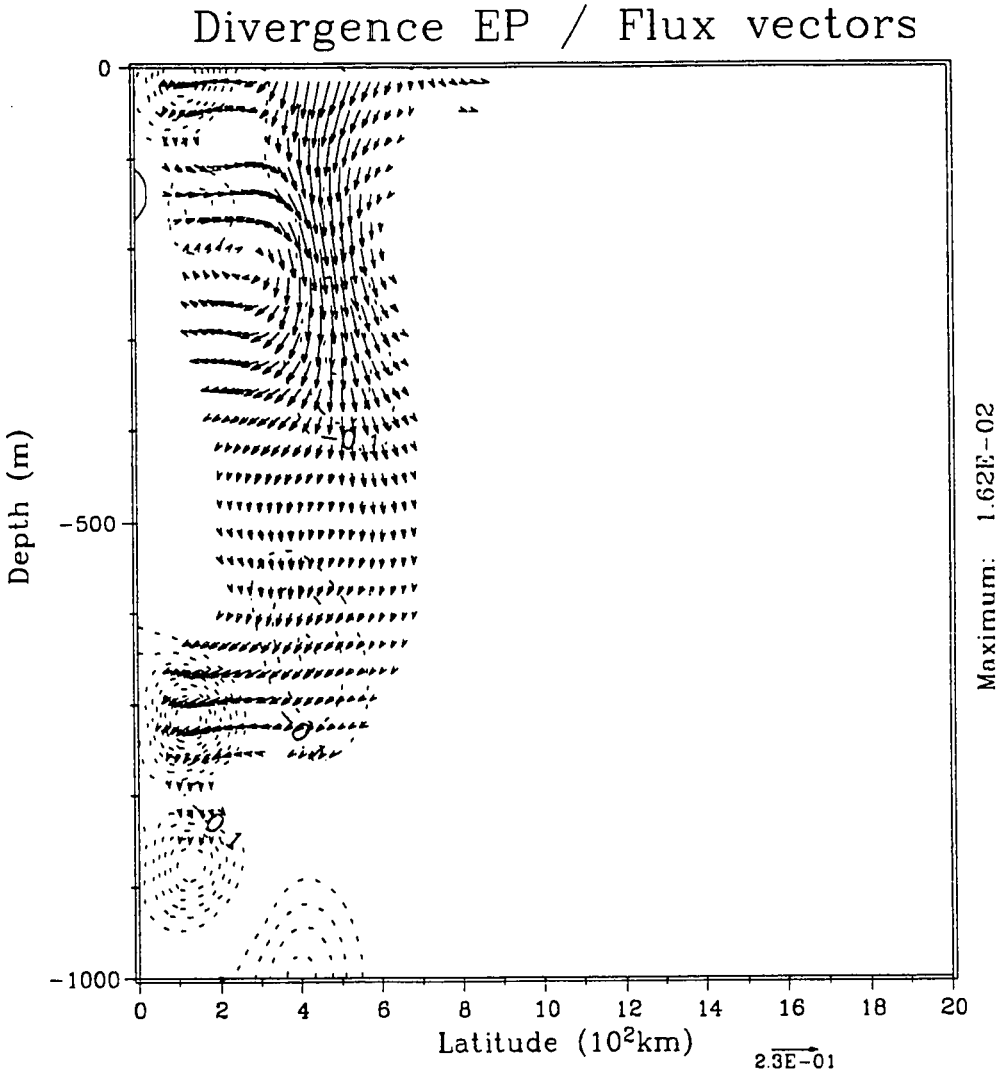


Figure 5.12c: E-P Flux results for the 3rd resonance for the 3rd meridional mode in the standard Undercurrent.

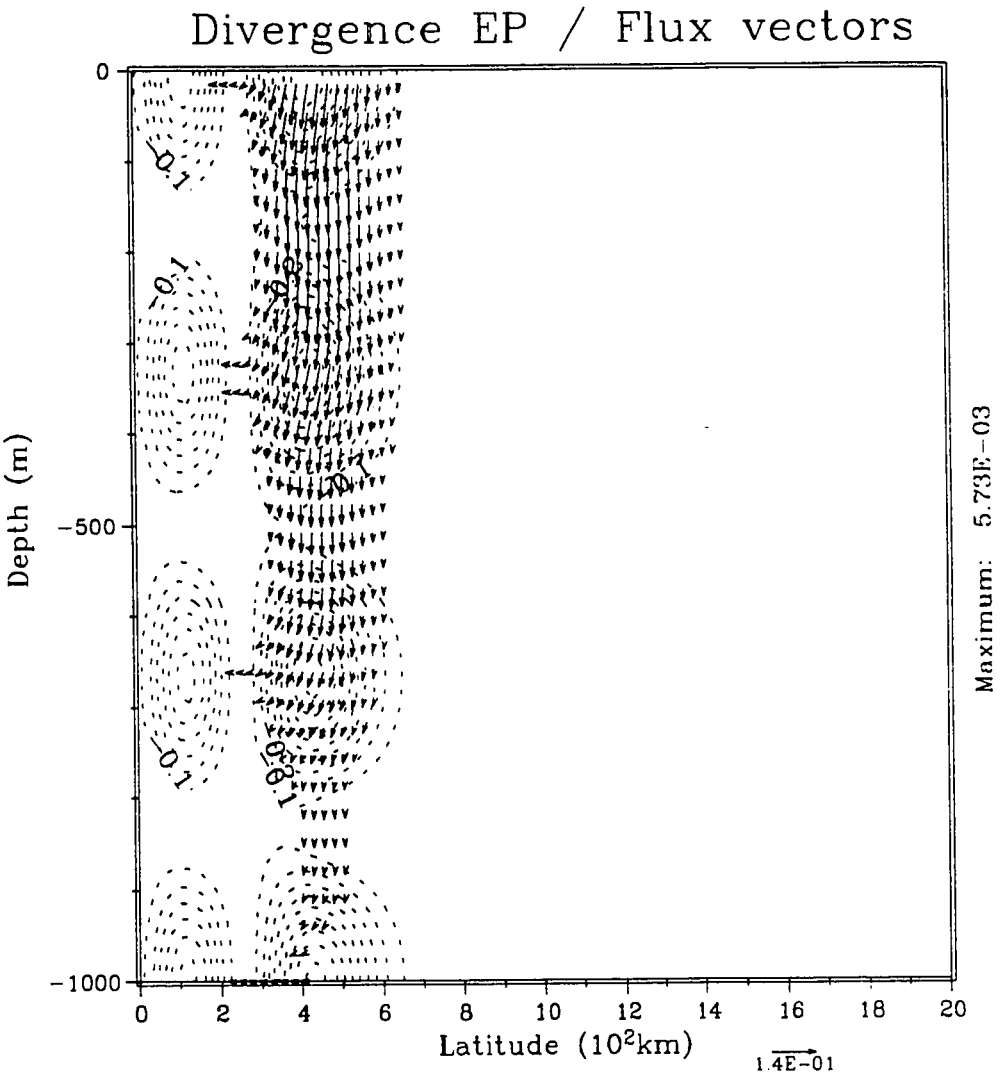


Figure 5.12d: E-P Flux results for the 3rd resonance for the 3rd meridional mode in a resting ocean.

The modal decomposition for the 3rd meridional mode case shows that 51.6% of the energy can be accounted for by the (3,3) modal structure, 17.8% projects upon the (1,6) mode and 7.8% upon the (1,8) structure. So we see that the small vertical and meridional scales observed in the pressure field near the equator are associated with the 1st meridional mode and vertical modes 6 and 8. The EP flux field gives insight into the reasons for this. In contrast to the resting ocean, Fig. 5.12d, the flux vectors here, Fig. 5.12c, are bent equatorward below the core. This is likely due to the interaction with the meridional shear at the flanks of the current and leads to a concentration of wave activity below the core. As a result, the modal decomposition possesses significant 1st meridional mode content.

Since the theoretical phase speed for the (1,7) mode (15.14 cm/s) is identical to that of the (3,3), one might expect from Eq. 3.46 a strong coupling to this mode. Therefore, the relative absence of the 7th vertical mode (~2.7%) is surprising. It is likely that the geometry of this flow field vis-à-vis the wave field is responsible. The equatorward deflection of the EP flux field around the flow leads to a strong convergence near the equator below the core. The structure of the EP flux convergence resembles that of the pressure field equatorward of 2° which closely matches the vertical scale of the 6th vertical mode which explains its presence in the decomposition.

The first variation we consider is the effect of doubling the flow amplitude to 100 cm/s. For this case the phase speed has only been shifted to -28.0 cm/s as compared to -29.8 cm/s for the standard case. In Fig. 5.13a we present the resulting pressure field. The obvious

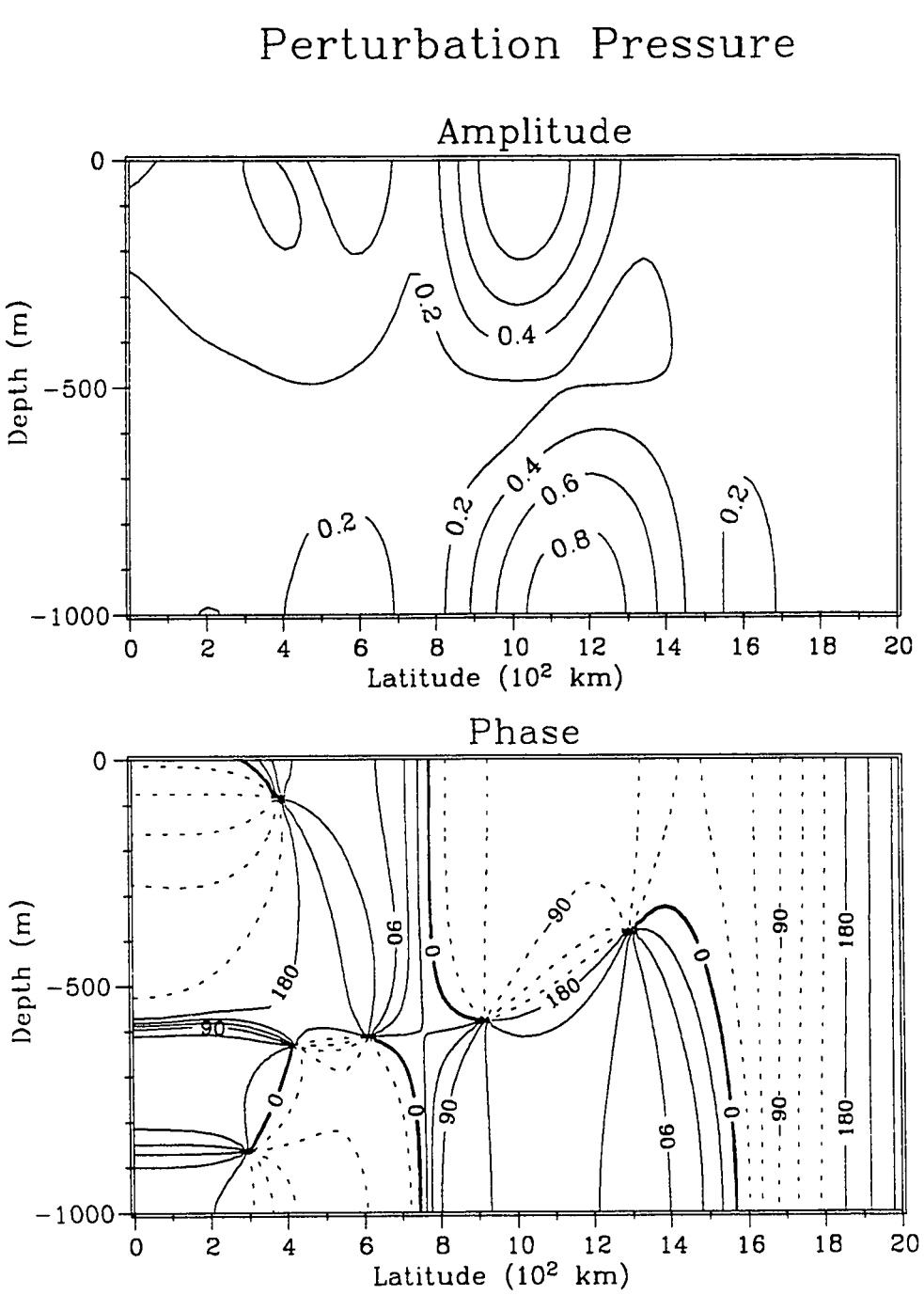


**Figure 5.13a: Pressure solution for the 3rd resonance for the fast Undercurrent case, Case B.**

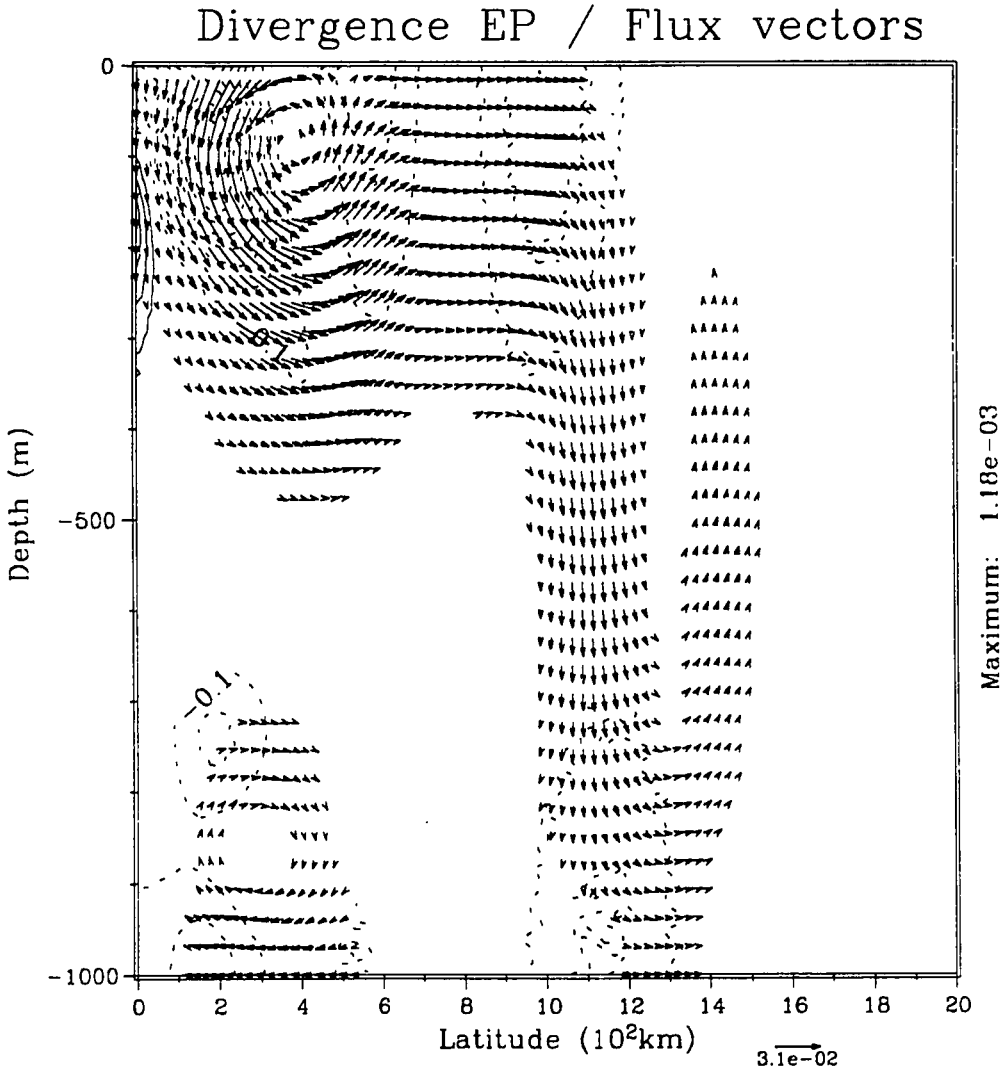


Figure 5.13b: E-P Flux results for the 3rd resonance for the fast Undercurrent case.

effect of the increased flow is to leave a nearly complete shadow zone below the core near the equator. In fact, the entire solution in the near equatorial zone seems to be of smaller amplitude. Recalling that the directly forced region is essentially confined to less than 6-7°, we see clearly this flow is more efficient at sending wave energy to higher latitudes. While this scattering is present in all of the eastward flow cases, it shows up the cleanest here due to the lack of other structures. We also see that the off-equatorial maxima has moved poleward from its location in the standard case by about 1°.

The modal decomposition for Case B shows that 67.4% of the energy can be accounted for by the (5,1) modal structure, 15.0% projects upon the (1,3) mode (which is presumably directly forced) and 3.7% upon the (3,1) structure. The fact that the (5,1) mode is now dominant is consistent with the observation that the pressure field near the equator is much weaker than in the standard case. Consideration of the EP flux field gives insight into the reasons for this difference. In contrast to the standard case (Case A), Fig. 5.9c, the flux vectors here, Fig. 5.13b, do not significantly penetrate the current and are nearly totally reflected upward and poleward. Since the flux is reflected upward initially instead of deflected downward, the latitude at which they strike the bottom and set up vertical modes is further poleward. As a result, the pressure field possesses strong (5,1) modal content instead of (3,1).

Next we consider the role of the meridional decay scale, Case C. For this we increase the meridional decay scale to 250km, weakening the meridional shear and increasing the area of the flow in the meridional

direction. The resulting pressure field for the 3rd resonance is presented in Fig. 5.14a. Weakening of the meridional shear has caused the pressure solution near the equator to be stronger, relative to the off-equatorial portion, than in the standard case. Also, with respect to the off-equatorial maxima, the relative difference in the amplitudes between top and bottom is smaller.

The modal decomposition gives 64.7% of the variance in the (1,3) mode, 19.2% in the (5,1) mode and 5.2% in the (1,2). In contrast to the strong flow case, this is consistent with the enhanced equatorial pressure field. The flux vectors, Fig. 5.14b, show that slightly more of the wave activity appears to get directly through than in the standard case. This explains why this pressure field has a bit more of its variance in the (1,3) mode (64.7%) than the standard (57.8%). As with the faster flow, some wave activity is reflected upward leading preferentially to (5,1) modal content at higher latitudes.

Next we consider the role of the vertical decay scale. For this we double the vertical decay scale to 200m, weakening the vertical shear but increasing the area of the flow in the vertical direction. The resulting pressure field for the third resonance is presented in Fig. 5.15a. Visually, the weakening of the vertical shear has not led to drastic changes in the pressure field. There is some redistribution of the amplitude, for example the surface maxima near 10°N has increased and moved slightly poleward and the near-surface region near the equator is weaker, but little else is apparent.

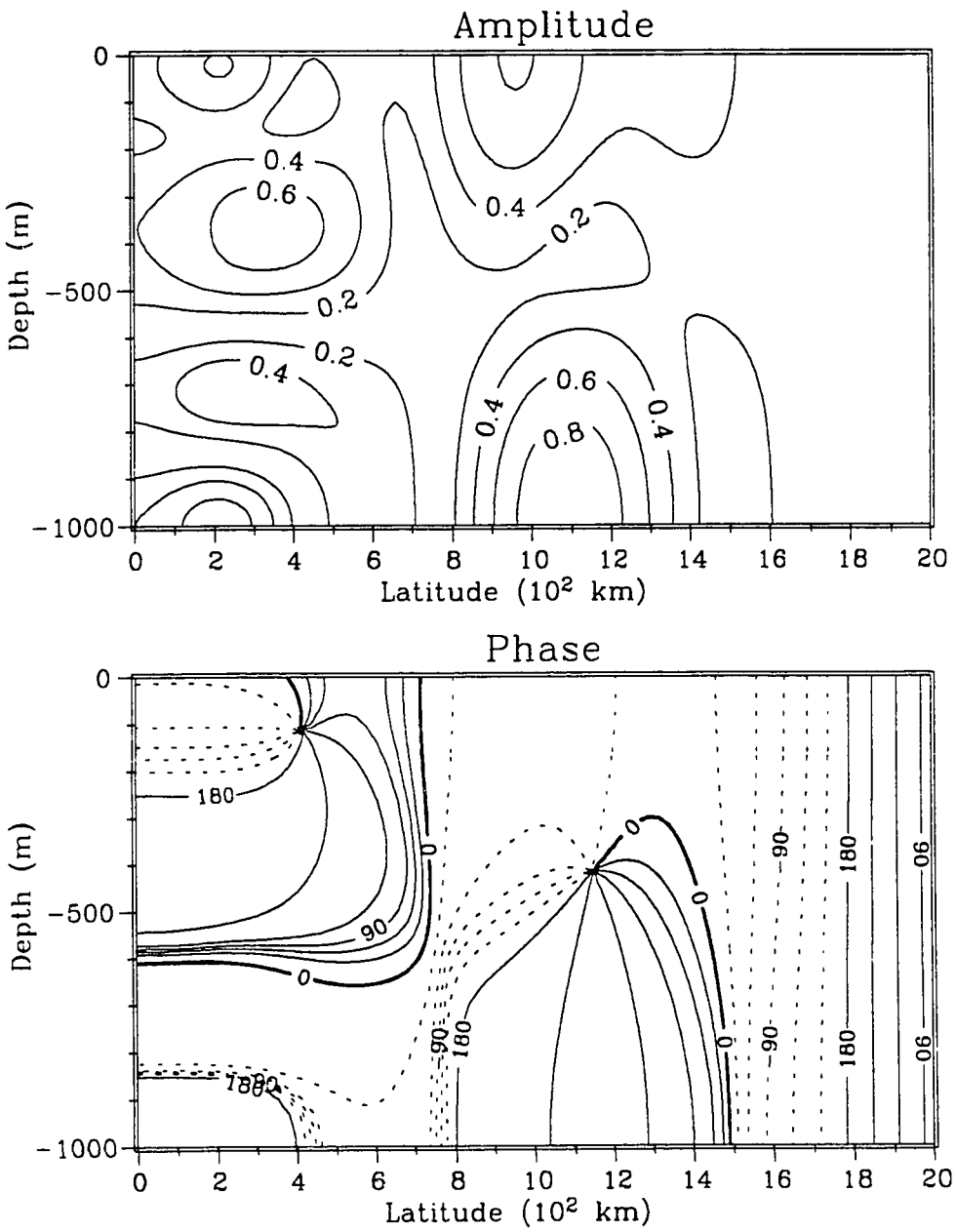


**Figure 5.14a: Pressure solution for the 3rd resonance for the broad Undercurrent case, Case C.**

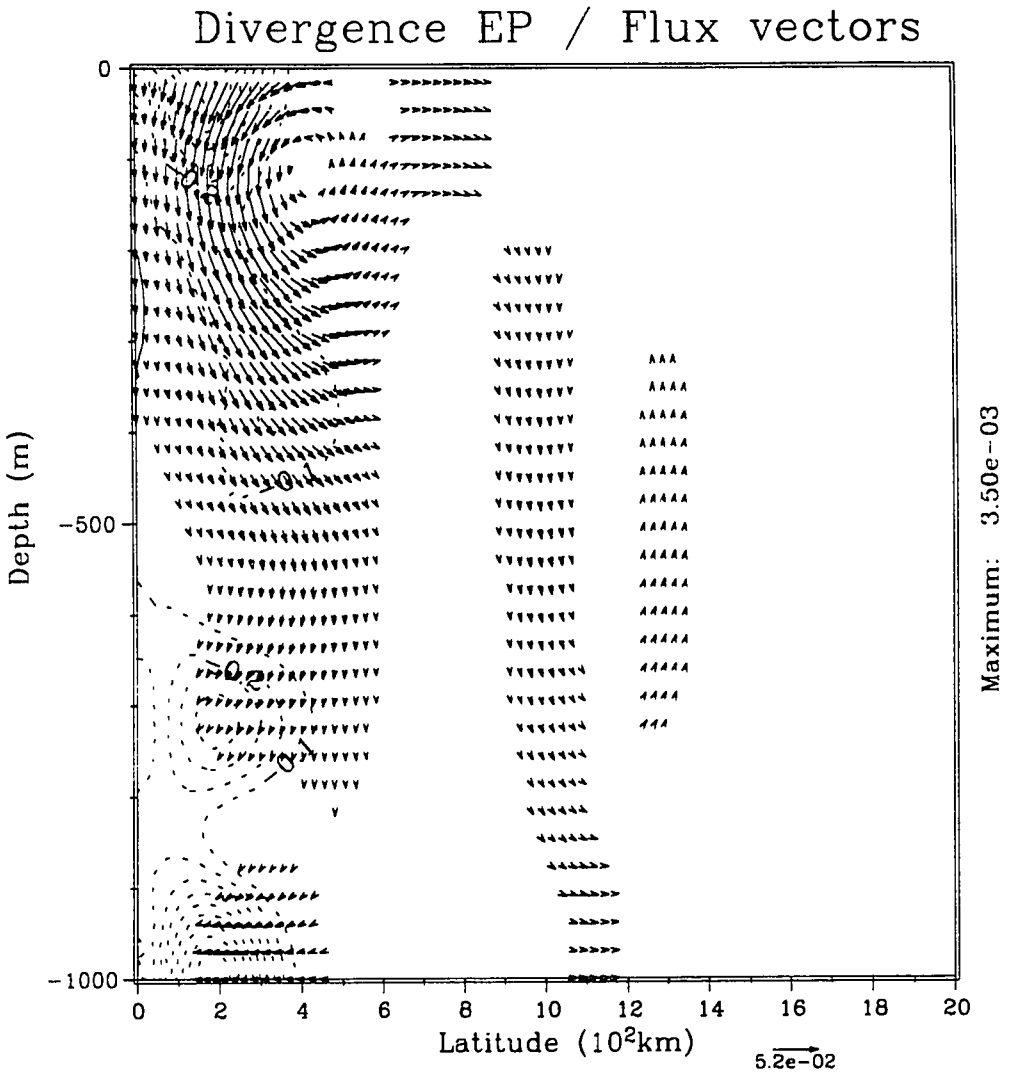


Figure 5.14b: E-P Flux results for the 3rd resonance for the broad Undercurrent case.

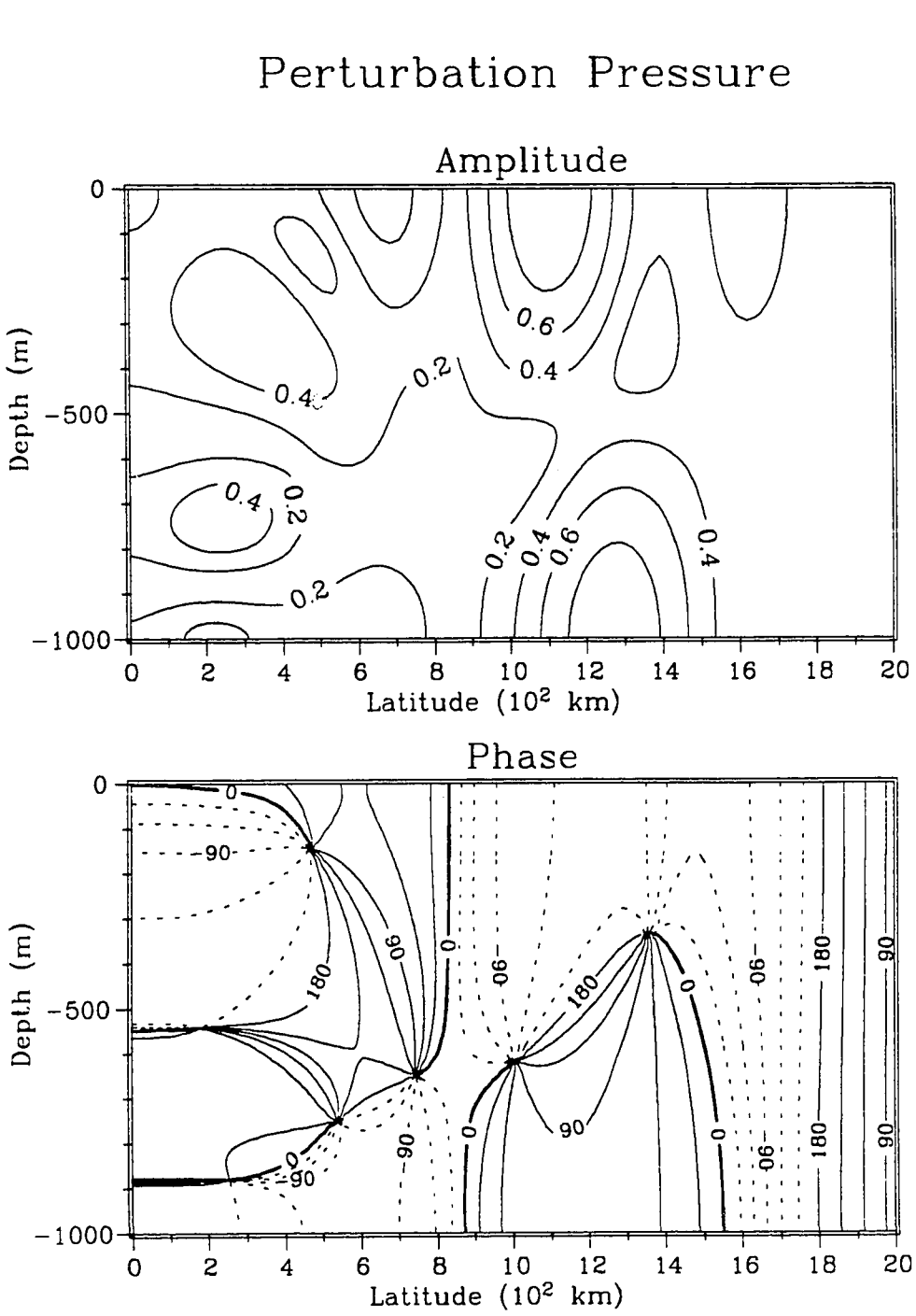


**Figure 5.15a: Pressure solution for the 3rd resonance for the thick Undercurrent case, Case D.**

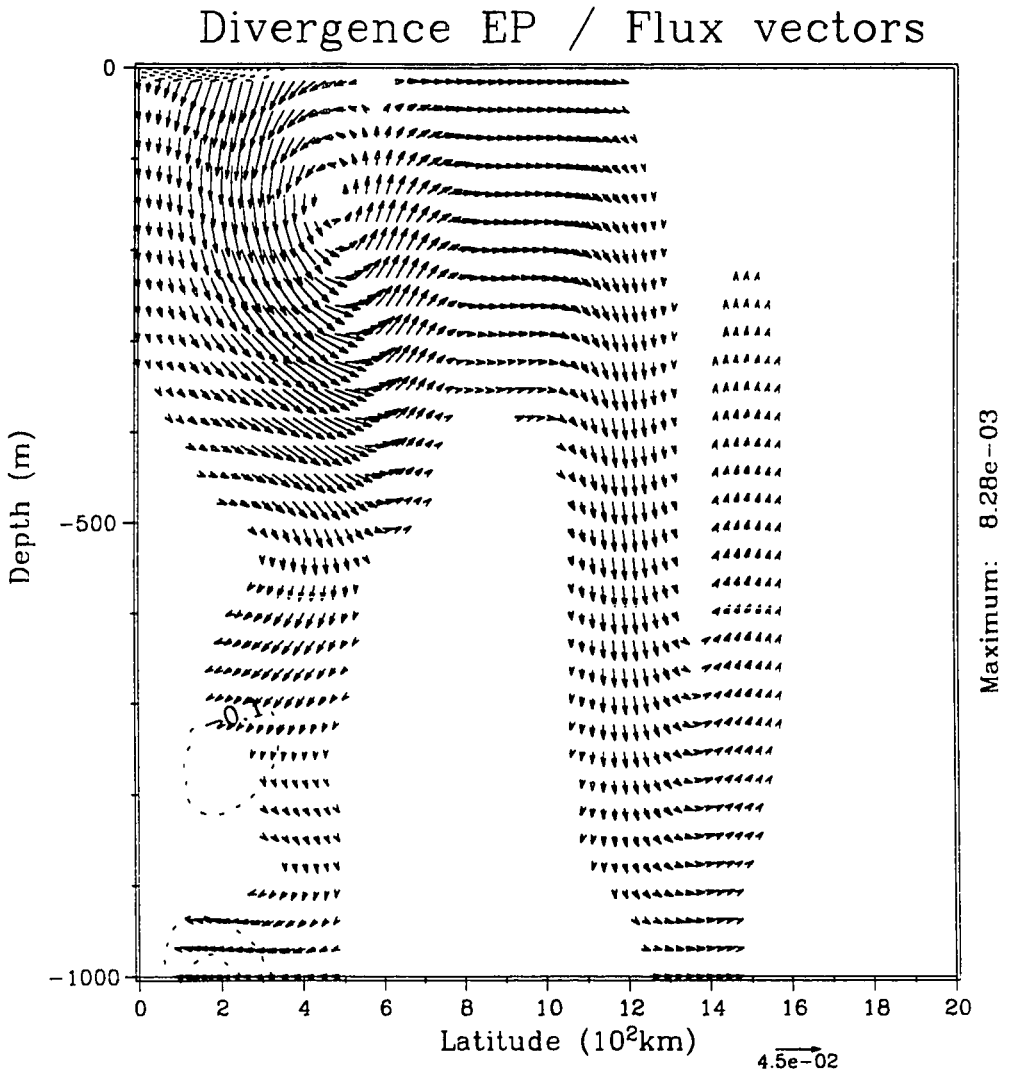


Figure 5.15b: E-P Flux results for the 3rd resonance for the thick Undercurrent case.

The modal decomposition shows that 46.2% of the variance projects onto the (1,3) mode, 21.7% onto the (5,1) and 6.0% onto the (3,1). While the amplitude of the pressure field in the near-equatorial zone is strong in the bottom 500m, near the surface it is weakened relative to the standard flow. This in concert with the stronger, cleaner first vertical mode signal near 12°N results in less of the variance in the (1,3) modal structure and more in the (5,1). The EP flux vectors, Fig. 5.15b, show that while more wave activity appears to traverse the flow vertically, the reflection is strong and sends wave activity to higher latitudes than does the standard flow. The former effect is responsible for the stronger pressure field in the bottom zone near the equator. While the latter effect is responsible for the strength of the (5,1) modal signal.

The pressure field for the case of a shallower undercurrent, Case E, is shown in Fig. 5.16a. For this case, the Undercurrent is moved up 100m in the water column. The upward movement of the core brings the shear zone nearer to the surface. The pressure field in this case is very similar to the standard case with the main difference being that the field is slightly stronger near the equator.

The enhanced pressure field near the equator is manifested in the decomposition where 64.3% of the variance is explained by the (1,3) mode, 16.9% by the (5,1) mode and 6.3% by the (1,4) mode. These numbers are not drastically different than the standard case. The only change is that a different vertical mode enters in as the third highest percent of variance ($4^{th}$ vs $5^{th}$). The EP flux results, Fig. 5.16b, show that, in comparison to the standard case, more wave activity

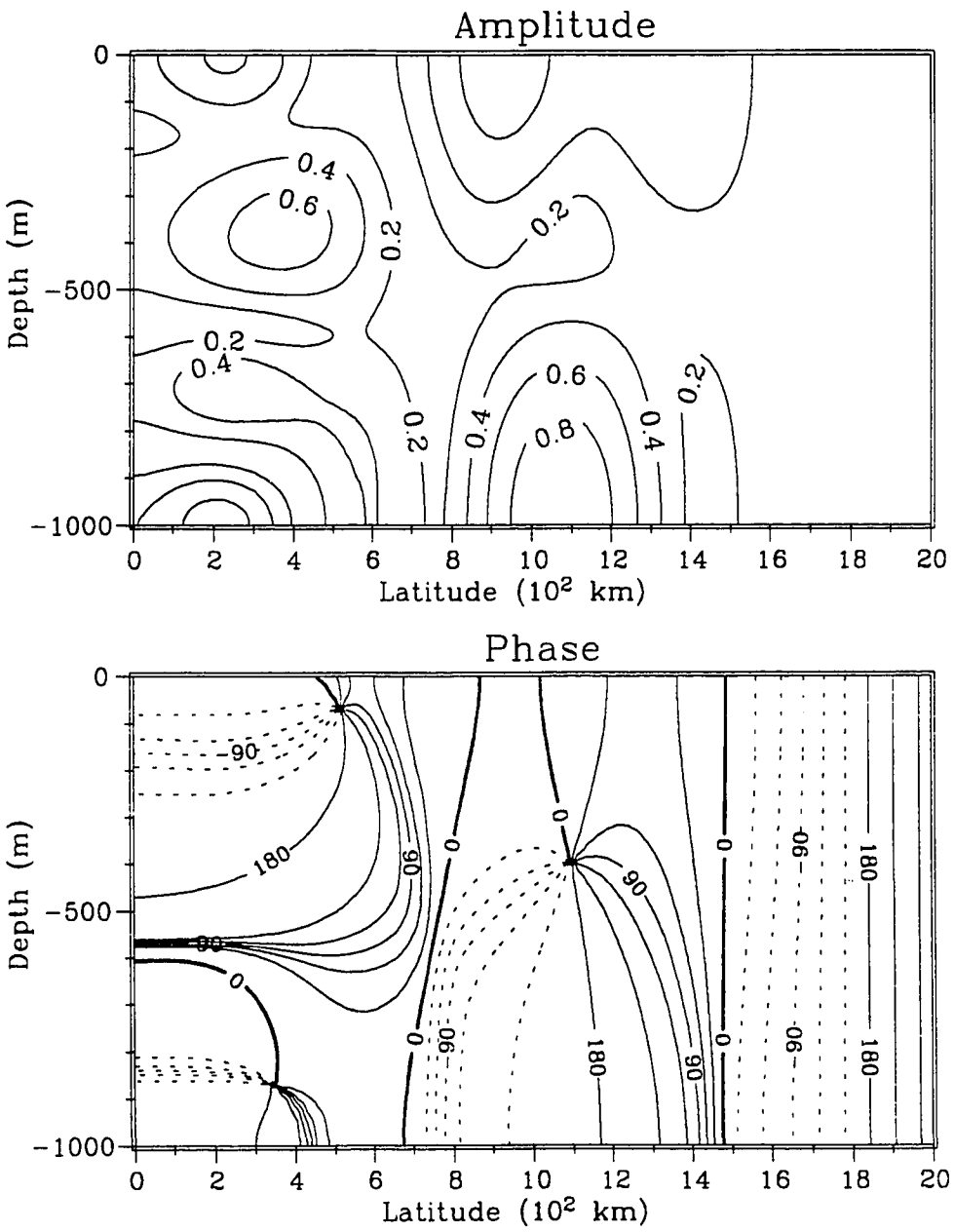


**Figure 5.16a: Pressure solution for the 3rd resonance for the shallow Undercurrent case, Case E.**

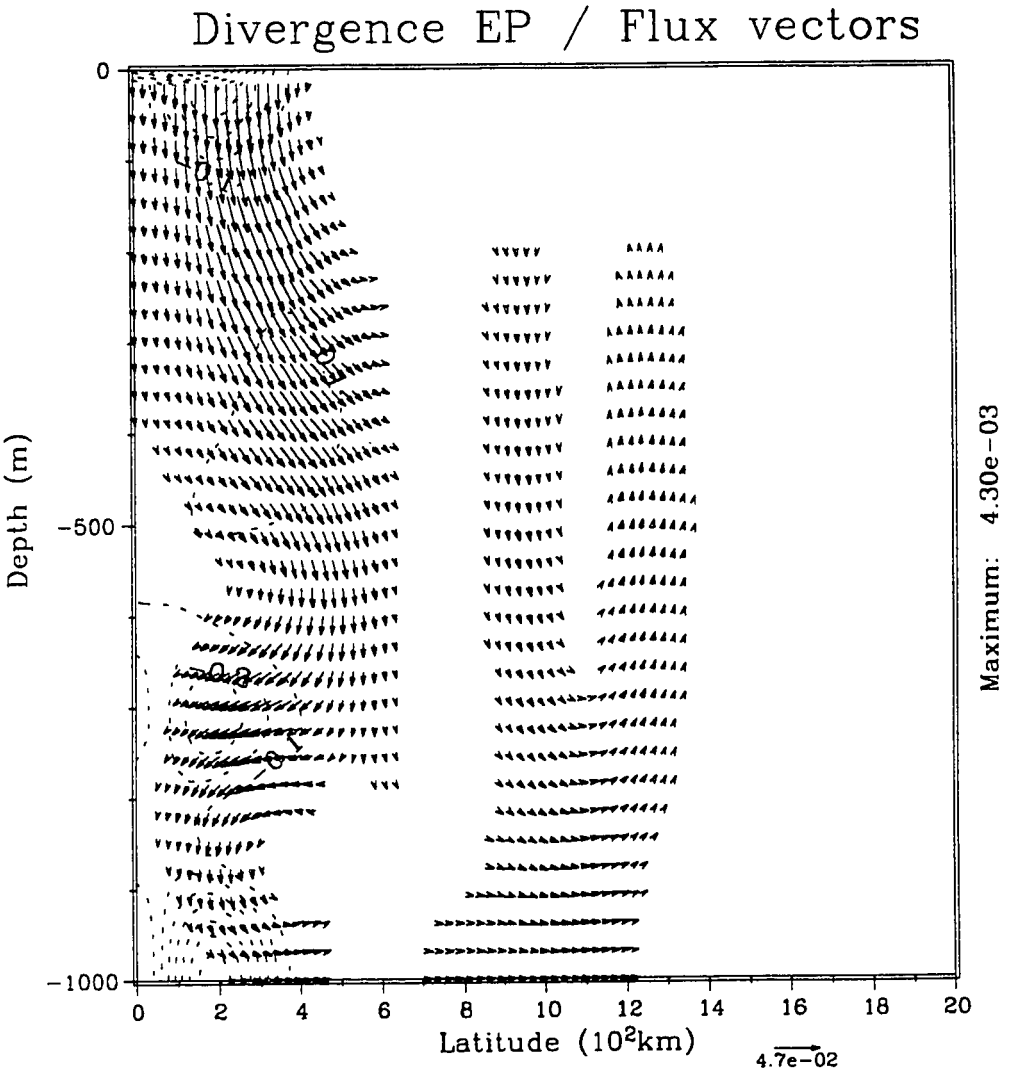


Figure 5.16b: E-P Flux results for the 3rd resonance for the shallow Undercurrent case.

appears to get directly through the flow than is reflected. This explains the slightly stronger (1,3) modal content. While the EP flux vectors are deflected poleward as in the other cases, because the resulting mean current covers less area (an exponential tail extends out of the domain) the resulting vectors exit the flow before they are strongly reflected. Therefore, more of the net wave activity is directly transmitted through the current.

The pressure field for the case of lower friction, Case F, is presented in Fig. 5.17a. For this case, the frictional decay time has been doubled to 10 years. Comparison to the standard case, Fig. 5.6c, shows very little structural difference. The only apparent change is that the pressure field for this case is a bit weaker in the near-surface equatorial zone. The maximum pressure perturbation in this case, however, is roughly twice as strong as in the standard flow case ($p_{max}$=1x10$^7$cm$^2$/s$^2$ *vs.* $p_{max}$=5.6x10$^6$cm$^2$/s$^2$) as might be expected.

The modal decompositions for the low friction case yield results which are very similar to the standard case. In these we see that 58.8% of the variance is explained by the (1,3) mode, 30.5% by the (5,1) mode and 4.0% by the (1,5) mode. This translates into a slight decrease, about 2%, in the (1,3) and a small increase, about 5%, in the (5,1) mode. This is most simply explained by consideration of the EP flux results, Fig. 5.17b. The principle effect is that the EP flux vectors extend considerably further along their apparent energy ray path than in case A, Fig. 5.9c. We see that the energy path near the equator reaches the bottom. The higher latitude path which reflects off the bottom near 12°N again reaches the surface. Here it bends back

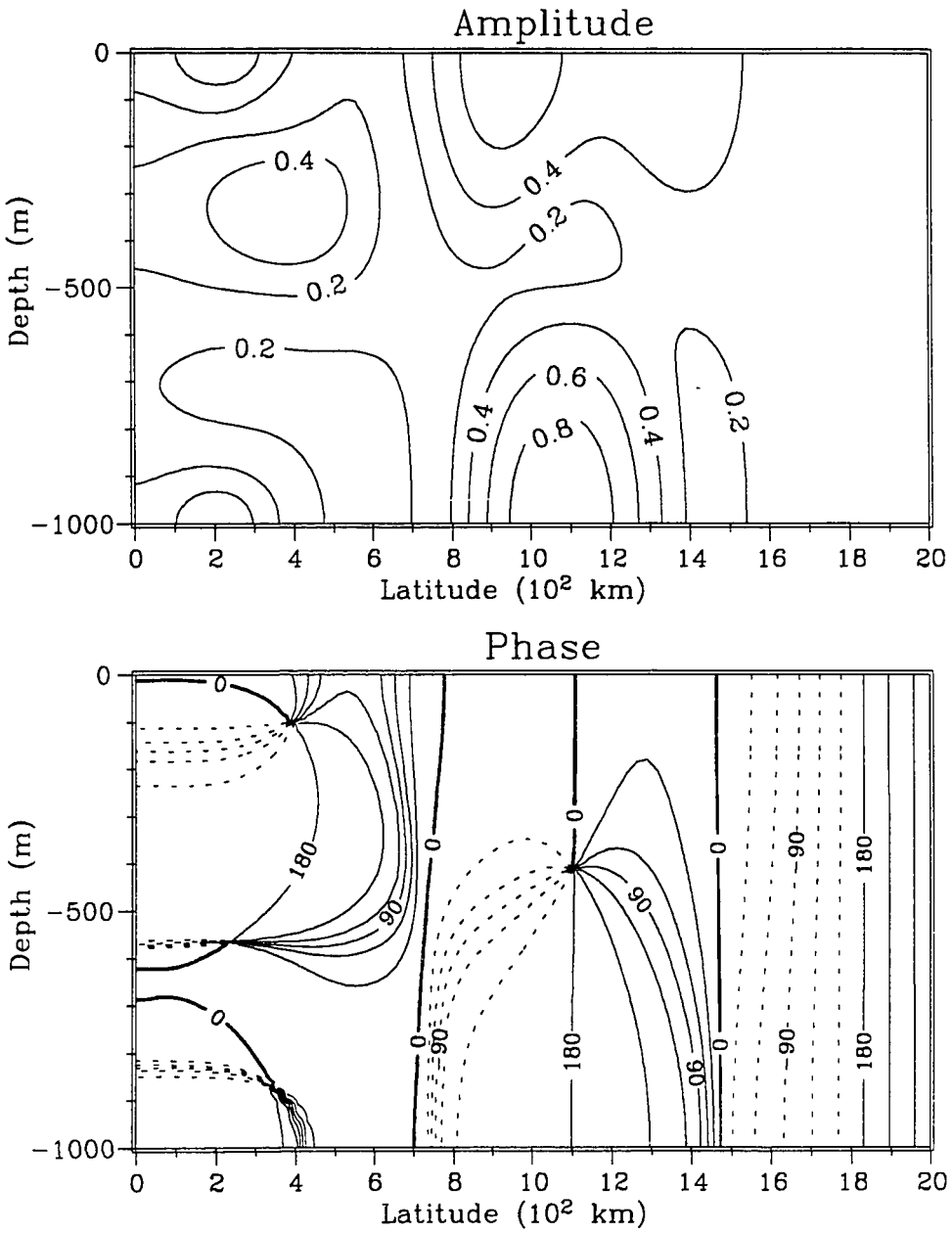


**Figure 5.17a: Pressure solution for the 3rd resonance for the low friction case, Case F.**

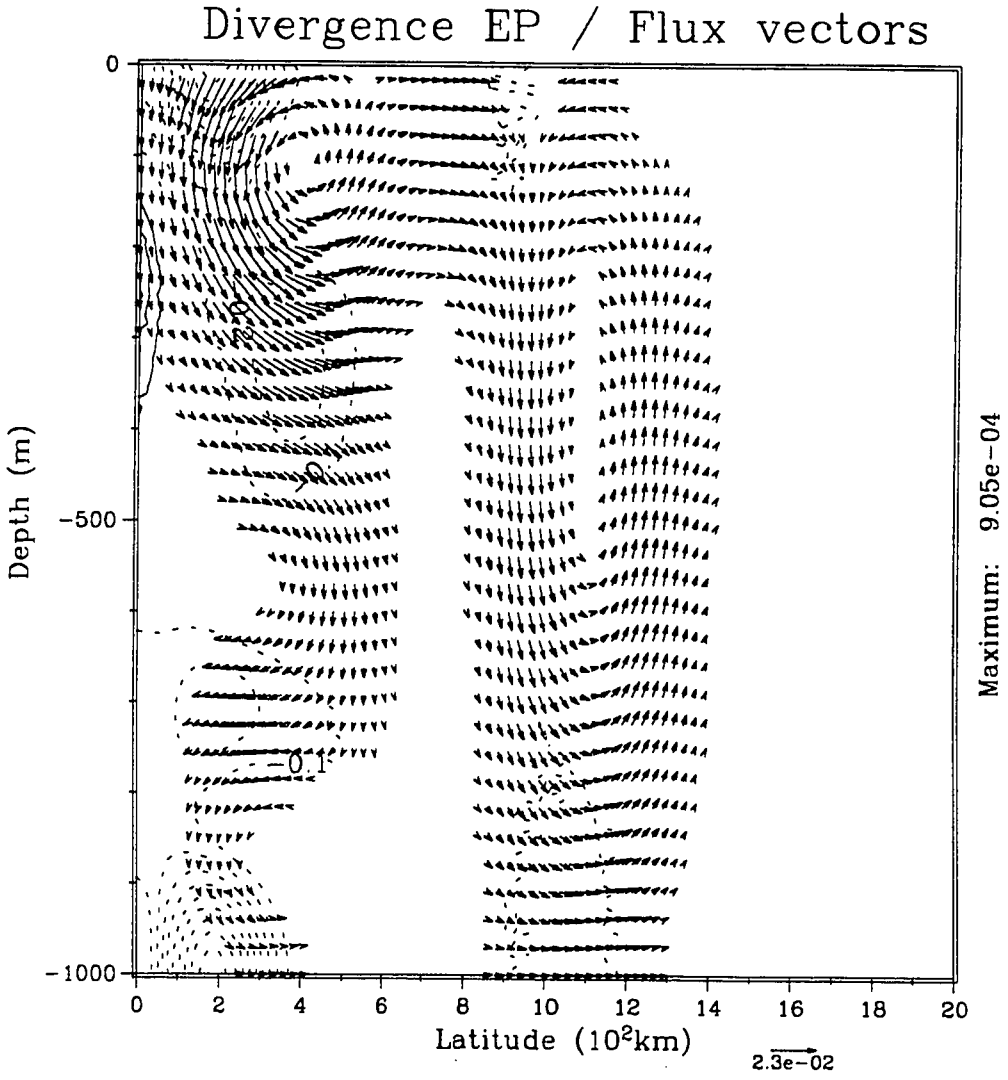


Figure 5.17b: E-P Flux results for the 3rd resonance for the low friction case.

equatorward. Therefore the reflected wave energy which is more slowly damped leads to a relative increase in (5,1) modal content in the solution. In fact, the net result of this is to set up a closed cell centered at 11°N spanning the entire depth over 4° latitudinally. This closed cell is a remnant of the spin-up of the higher meridional mode via wave radiation (*i.e.* scattering) from lower latitudes. The EP pathways tell us that the wave energy propagates downward and poleward between 8 and 11°N. However, in propagating upward from the bottom the energy which has characteristics of the (5,1) mode reaches the turning latitude for that mode near 12.4° and is turned equatorward. Again, this propagation signal is revealed only due to the frictional decay of wave energy.

The case of variable N ocean, Case G, adds more realism to the present modelling study. As we have seen from the other cases in this parameter study, the vertical structure of the wave modes as compared to the background state may be important in determining the character of the wave mean flow interaction. Therefore we include in this study a more realistic background configuration based upon a reasonable background stratification. To achieve this we employ a resting state $N^2$ profile similar to that found in the Hawaii-Tahiti Shuttle experiment, Fig. 2.1. The resting state vertical $N^2$ distribution chosen to model this field is given by

$$N^2(z) = N_0[1 + N_1 e^{-\frac{1}{2}\{(z-z_N)/\delta z_N\}^2}] \qquad (5.4)$$

where $N_0=1.125\times10^{-5}s^{-2}$, $N_1=39.0$, $z_N=150m$ and $\delta z_N=75m$ and is shown in Fig. 5.18 along with the first 3 eigenfunctions and their associated eigenspeeds. The location, $z_N$, and scale, $\delta z_N$, which are assumed to be

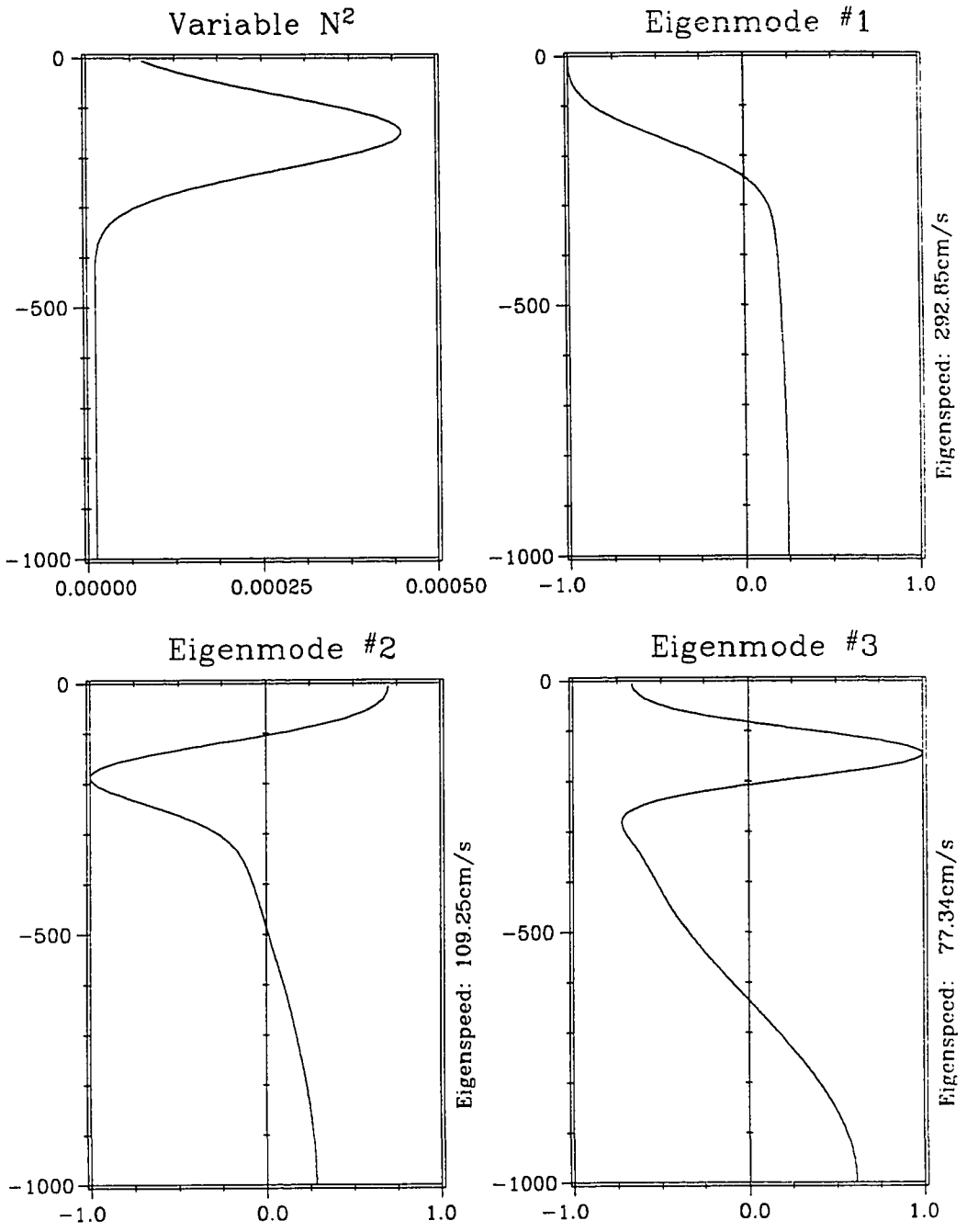


**Figure 5.18:** Resting $N^2$ profile for the variable N ocean case, Case G, and the first 3 vertical eigenfunctions along with their associated eigenspeeds.

identical to those of the Undercurrent structure (see Table 5.3), are chosen to approximate that of the Hawaii-Tahiti Shuttle data. The amplitude parameters, $N_0$ and $N_1$, are then chosen to yield reasonable values for the separation constants, $\lambda_i$, and hence the eigenspeeds. Due to the weaker amplitude (70 cm/s) but shorter vertical scale (75m), this flow possesses shears similar to the fast undercurrent case (Case B) to which the results here compare favorably. The ocean depth (1000m) is still unrealistically small. However, adjusting this to a more realistic value involves adjusting the $N^2$ profile to get reasonable eigenspeeds. The net effect of these would counteract. Here we desire only a significant region below the core for which the flow is negligible to model the deep ocean. For this purpose a depth of 1000m is adequate. In addition, by choosing to shrink the size of the deep ocean, we are effectively increasing the grid resolution (which is uniform in z) in the upper ocean where the interaction is taking place.

For comparison, the pressure fields for the third vertical mode in the absence of mean flow is presented in Fig. 5.19a. In addition, the associated net EP flux vectors are shown in Fig. 5.19b. Here we see a difference from the constant N case in that the decay of the EP flux with depth is more rapid in the near surface region. This is due to the vertical structure of the modal solutions and not unexpected.

The results for the first three resonances in the variable N ocean are analogous to those in constant N. The $1^{st}$ vertical mode shows very little change, the $2^{nd}$ is affected more and the $3^{rd}$ is affected most. The pressure field for the third resonance in the presence of this flow is shown in Fig. 5.20a. When compared to the no-flow solution, we see

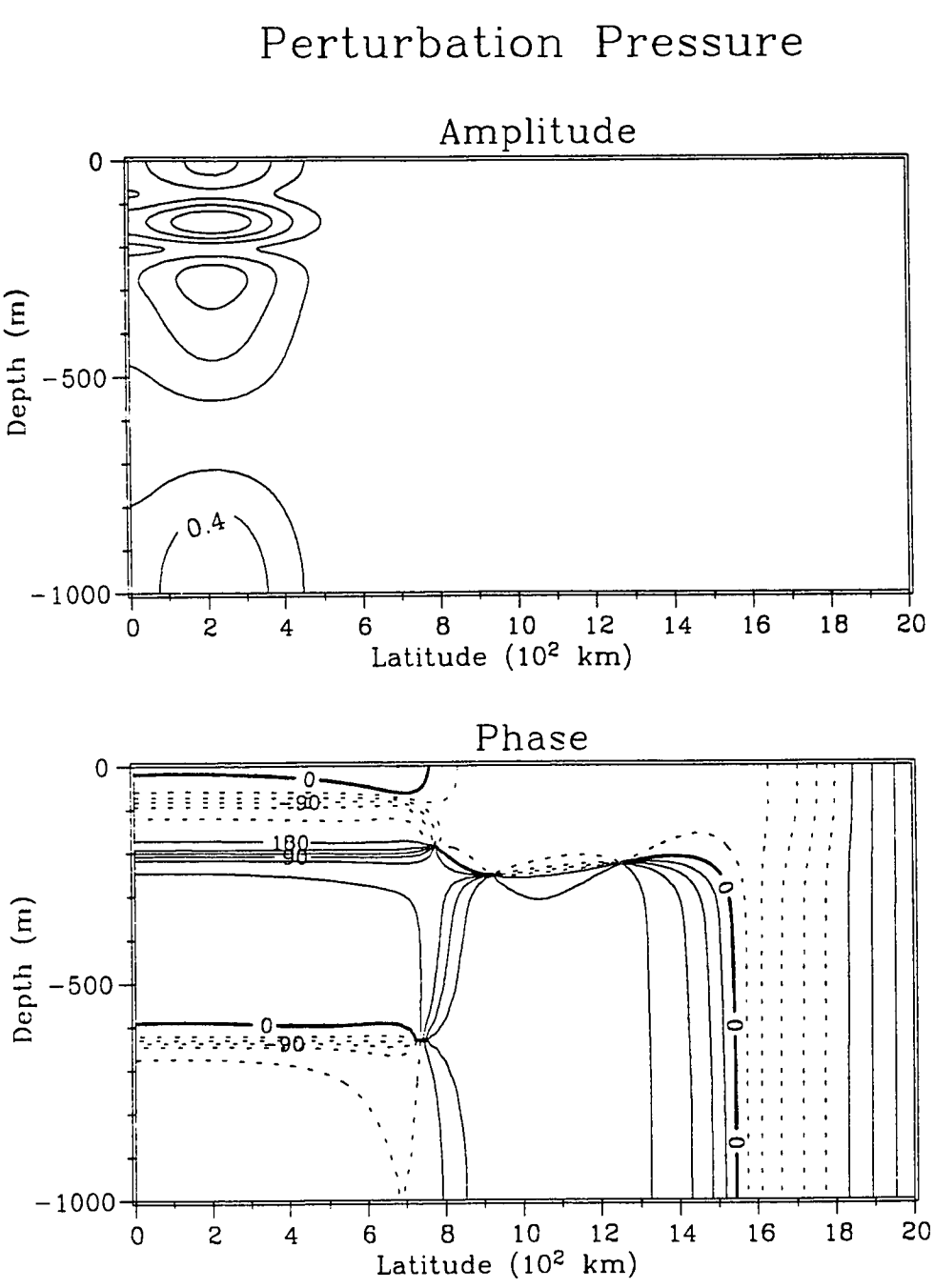


**Figure 5.19a: Pressure solution for the 3rd vertical mode in a variable N resting ocean.**

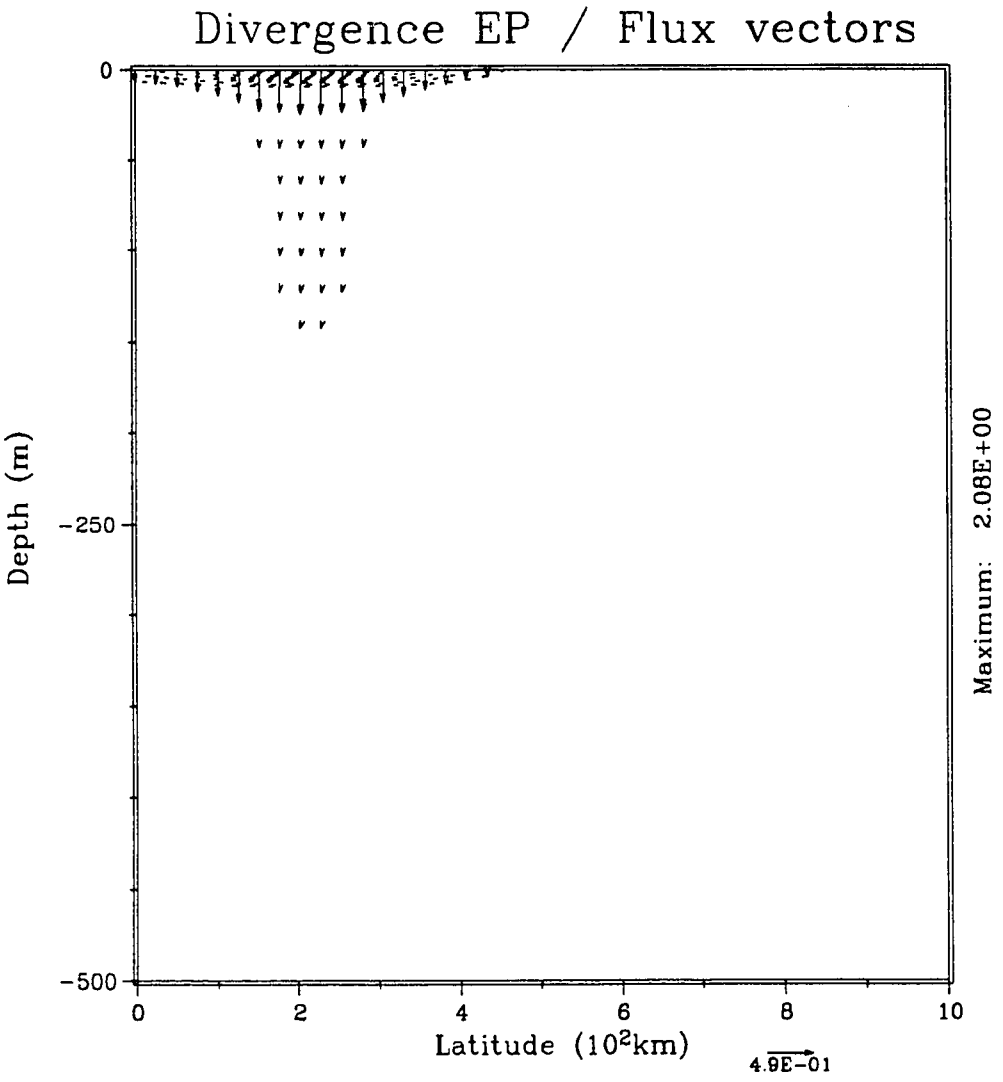


Figure 5.19b: E-P Flux results for the 3rd vertical mode in a variable N resting ocean.

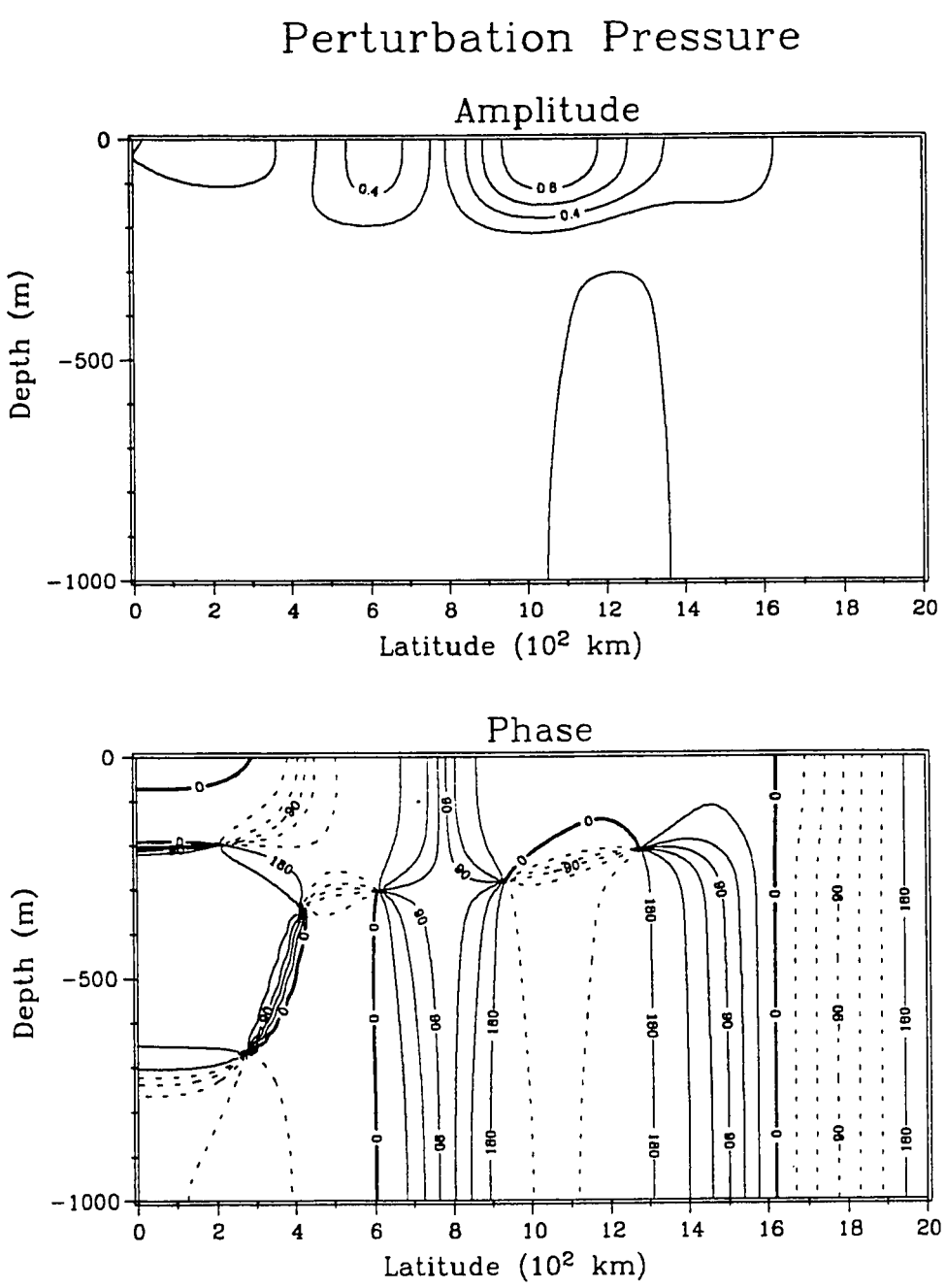


Figure 5.20a: Pressure solution for the 3rd resonance for the Undercurrent in a variable N ocean, Case G.

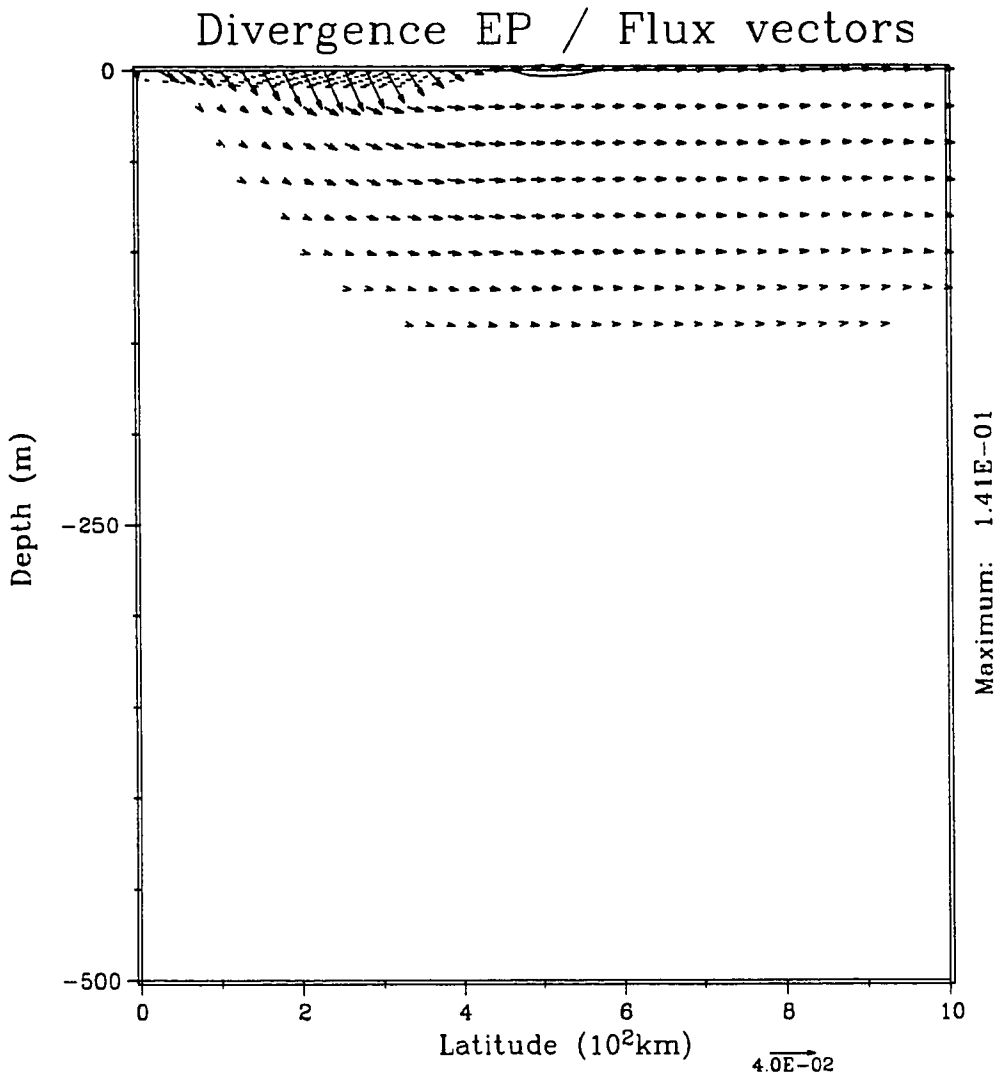


Figure 5.20b: E-P Flux results for the 3rd resonance for the Undercurrent in a variable N ocean.

that this flow causes strong surface trapping and meridional spreading of the pressure perturbation near the equator. As a result, a shadow zone, which extends out to roughly 8°, appears below the core. The meridional dependence shows modulations indicative of a higher meridional mode structure. The solution also possesses apparent first vertical mode structure at higher latitudes (centered at 10°N).

The modal decomposition, using the variable N vertical structures, shows that 67.4% of the pressure variance projects upon the (5,1) mode, with 8.1% on the (3,1), 6.7% on the (1,2), 6.6% on the (7,1) and only 4.5% projects onto the (1,3) mode which was directly forced. Here we see that roughly 83% of the variance appears in modes other than the directly forced mode. Due to the strong shear, this flow is strongly reflective to the vertical propagation of these waves. Here, the reflection acts to scatter wave energy into a structure which projects strongly onto the fifth meridional, first vertical mode.

The EP fluxes for this resonance, Fig 5.20b, show this effect clearly. The meridional scattering of wave activity above the core generates the broad meridional structure with a maxima near 9-10°N. As with the constant N cases, the energy budgets for the waves show that the waves tend to extract energy from the vertical shear and the density field and lose energy working against the meridional shear. In this case the integrated energy exchange with the flow (a loss of 13.2% of surface forcing) and the meridional loss through barotropic radiation (11.5%) are both significant. The exchanges with the flow are strong, with roughly half (47.2%) of the energy input at the surface going into work against meridional shear, 18% being extracted from

vertical shear work and 16.1% extracted from density work.

The results of the parameter study for the eastward flows lead to some interesting conclusions. First, for wave energy input near the equator, the reflective and/or scattering nature of the eastward Undercurrent is a robust feature. For wave energy input at higher latitudes, the Undercurrent can also bend significant portions of the wave activity equatorward. Which of these occurs is determined by the scales of the wave verses those of the mean state. Therefore, the scales of the background are important in determining exactly how the wave energy will be affected. As expected, weakening either the vertical or meridional current shear increases the direct transmission of the imposed wave component. Conversely, strengthening the shear in either direction leads to enhanced reflection and/or scattering into other wave components. Moving the mean flow up in the water column has little effect upon the interaction with the flow except that scattered energy appears in different wave modes. The effect of variation in the frictional parameter has little or no effect on the structure of the solution. Friction of this type acts only to control the resonant amplitudes. Results for scale dependent friction may be different, however, for realistic parameter values the presented modal structures should not be drastically altered. Inclusion of variable N, while altering the details, does not change the fundamental results found in the constant N ocean. In fact, the results for the variable N case are remarkably similar to the fast Undercurrent case whose shears are comparable. The strong reflection into higher meridional mode structures, the equatorial shadow zone at depth, the dominance of a wave

mode other than that directly forced and the fraction of momentum exchanged with the mean state are all very similar between the two cases.

### 5.2.3 Westward flow in a Constant N Ocean.

We wish to study the effect westward flow has upon the structure and dispersion characteristics of equatorial Rossby waves. From the results for Kelvin waves in the presence of eastward flows, we expect the interaction to intensify as the intrinsic phase speed, Re(c-U), decreases. However, for the Rossby waves there exists the likelihood of a more complicated interaction. The eastward flow parameter study showed conclusively that rapid variations in the medium lead to wave scattering and/or reflection in the case of the Rossby waves. None of this was seen in our study of the Kelvin waves. The difference arises from the spectral richness of the westward propagating waves as opposed to the eastward ones. In the case of the Kelvin waves, no other eastward propagating meridional structure was present in the longwave limit to scatter wave energy into.

For the case of westward flow, Case H, the flow has been reversed and weakened to 40cm/s from the standard eastward flow case. For the scales used, this weakening is required by static stability constraints. To allow for comparison with the results for the eastward flows, we again find the third resonant solution. However, the Doppler shifting, which is strongly enhanced as Re(c-U)$\rightarrow$0, leads to a relatively large shift in phase speed from the third resonance in the absence

of flow. Consequently, we note that there is difficulty involved in identification of this particular resonance for the westward flow cases with a particular no flow mode. The presence of critical surfaces complicates this problem further still. For this flow field we present the results for two cases. The first is that for a Rossby wave which sees no critical surface in this flow field, *i.e.* $U_0/c<1$ everywhere and the second is for a wave which does, *i.e.* $U_0/c>1$ somewhere in the domain. The results obtained will be compared with both the no-flow solutions and with the solution for the standard eastward flow case.

The pressure field in the non-critical flow case is presented in Fig. 5.21a. The phase speed for this solution is -51 cm/s. In this case the resulting pressure field is considerably different than the resting state solution and the standard eastward flow case. The most prevalent feature being the bimodal distribution of amplitude centered at the core of the flow at roughly 2°N. In addition to this, we see the off-equatorial maximum is shifted equatorward by about 3°.

The modal decomposition shows that 31.7% of the variance is projected upon the (1,3) mode, 28.2% on the (3,1), 15.7% on the (1,2) and 13.0% on the (1,4). We note that the resonant phase speed for this case (-51.0cm/s) showed a strong displacement from the speed in the absence of flow (-35.3cm/s). The fact that the decomposition yields the (1,3) mode as the largest component, albeit barely, is significant since this was the mode that was directly forced. The strong coupling into the same meridional but other vertical no-flow modes points to vertical scale changes caused by the flow. Recall that the results of the slowly varying theory imply that westward flow will tend

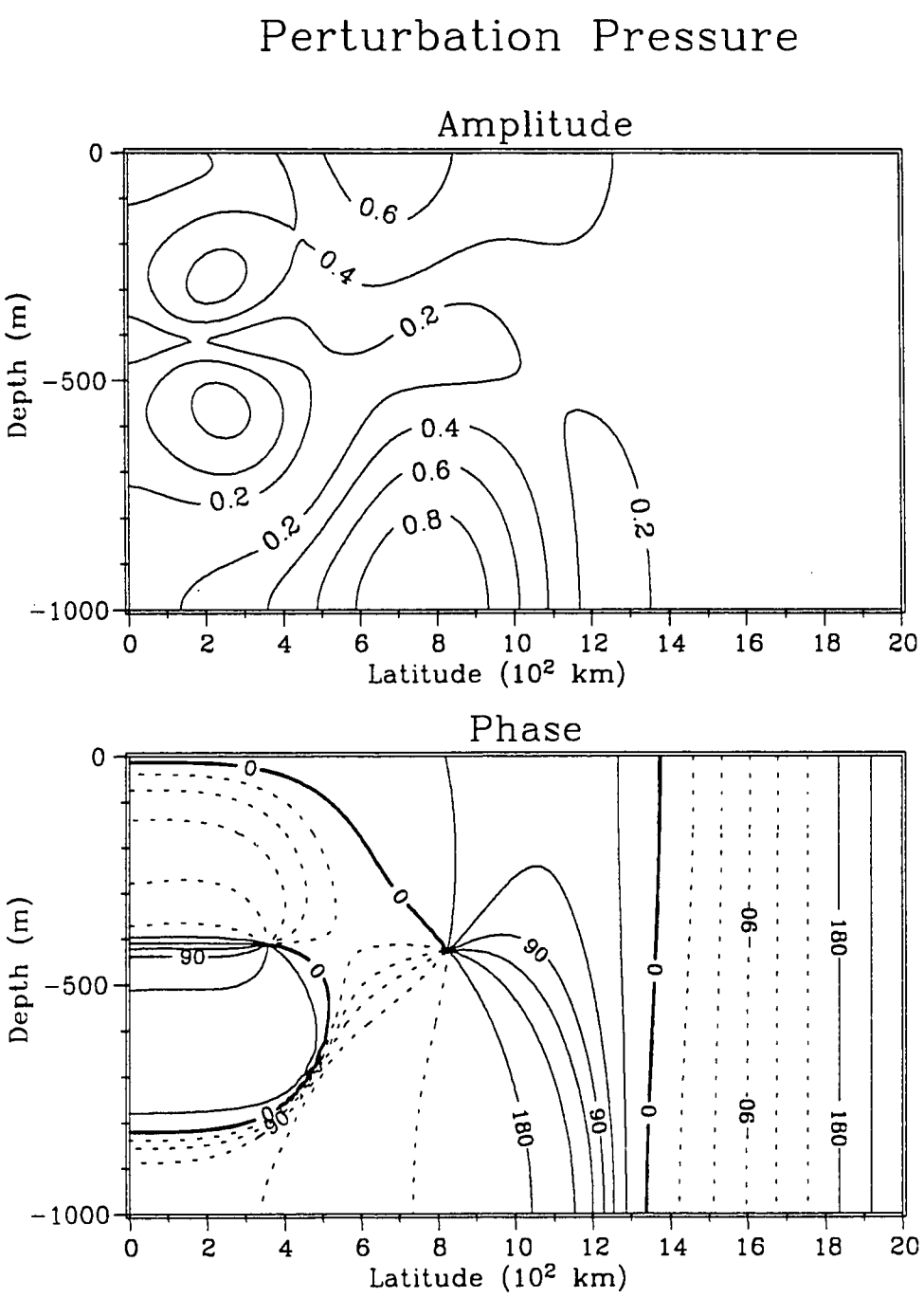


**Figure 5.21a: Pressure solution for the 3rd resonance for the sub-critical westward flow case, Case H.**

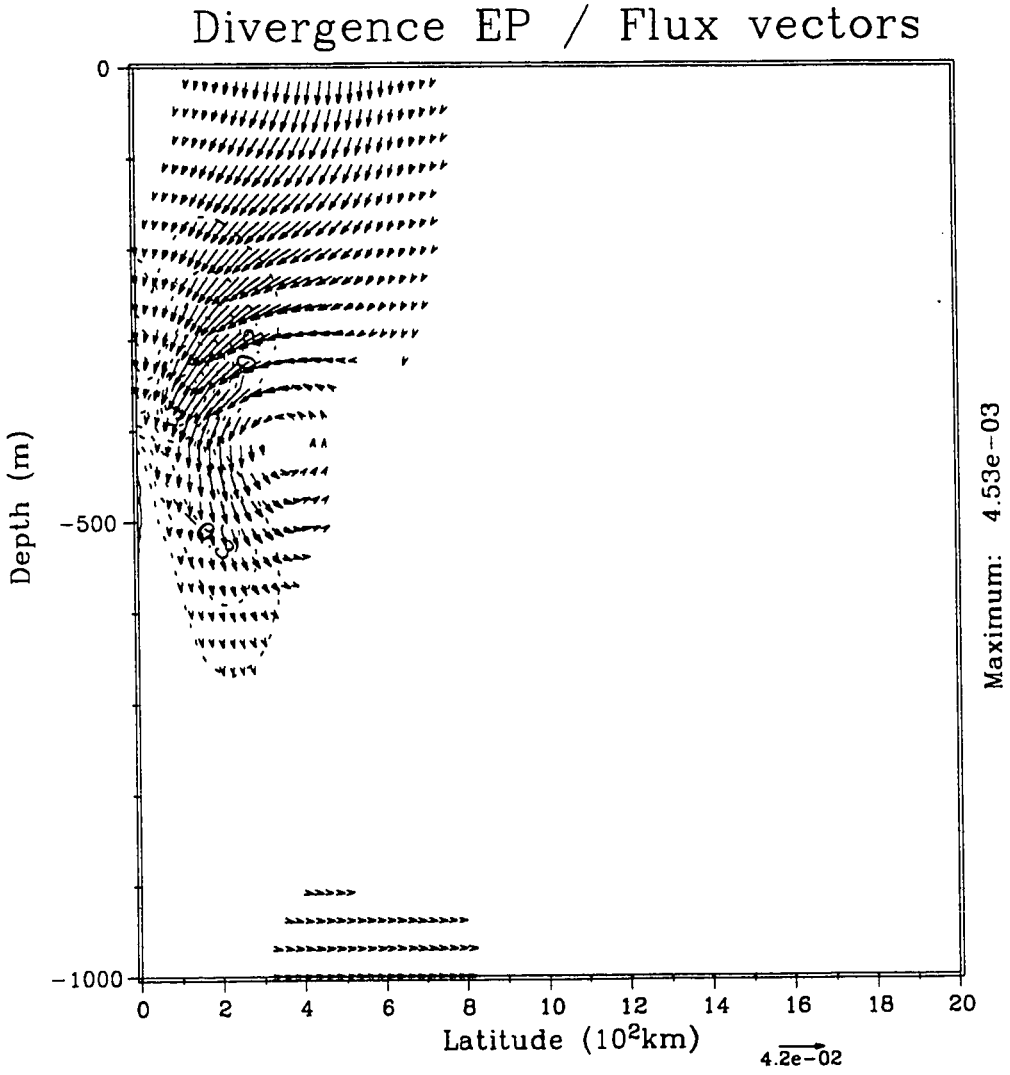


Figure 5.21b: E-P Flux results for the 3rd resonance for the sub-critical westward flow case, Case H.

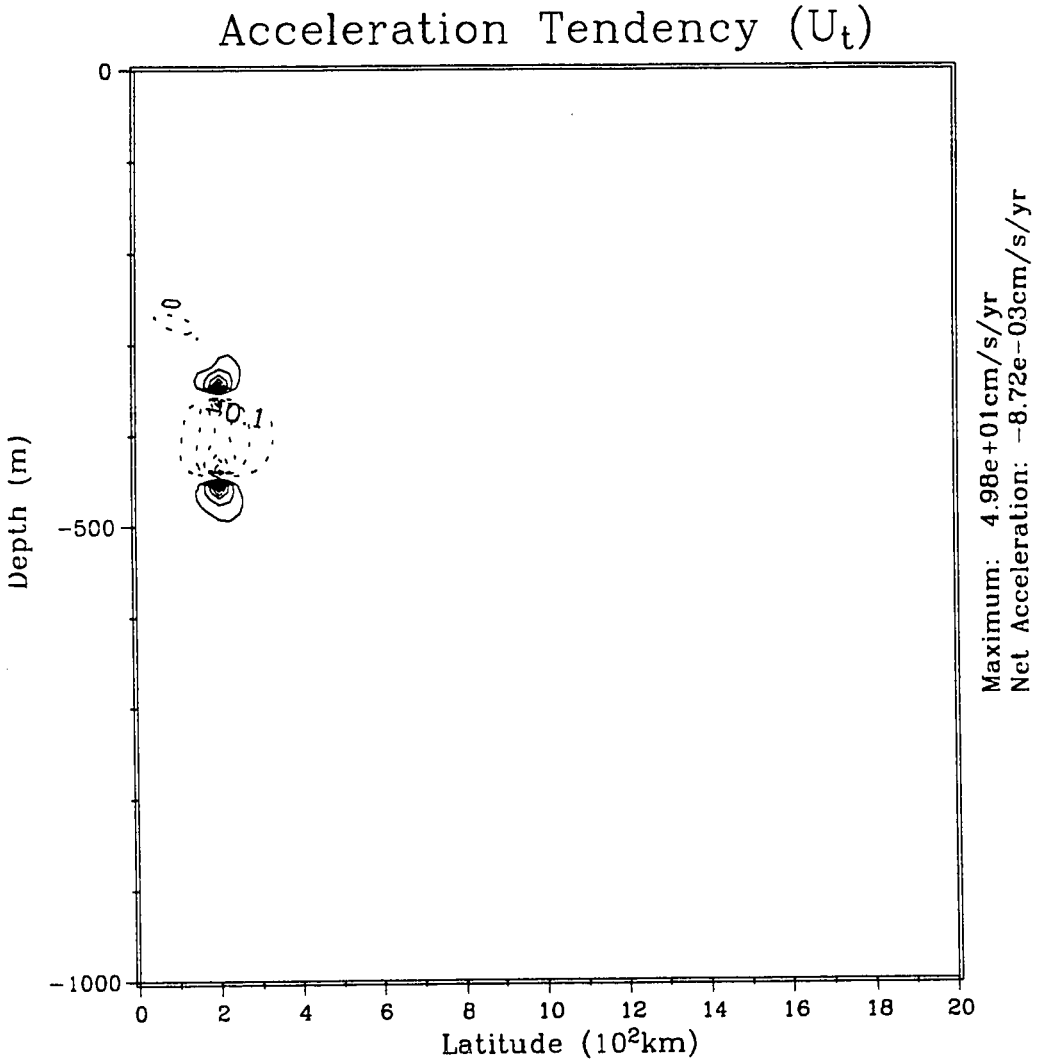


Figure 5.21c: $O(\epsilon^2)$ mean acceleration field for the 3rd resonance for the sub-critical westward flow case, Case H.

to shrink the vertical wave scales. Critical layer theory suggests that this shrinking is intensified as $Re(c-U_0) \rightarrow 0$. For the westward flow, the increase in the resonant westward phase speed extends the direct forcing region latitudinally by a factor of about 1.2. Consequently, the EP flux vectors, Fig. 5.21b, at the surface extend to about 8°N. The action of the current is to cause a strong convergence of EP flux towards the equator above the core. Since this flow is not critical with respect to this wave, a portion of the wave activity can traverse the flow. However, a significant number of the flux vectors recirculate into the core. In addition, some of the energy which apparently begins toward the poleward flanks of the forcing region completely eludes the flow and radiates downward and appears as a narrow beam between 7 and 8°N. This energy is likely responsible for the (3,1) modal content in the solution. Since the wave activity tends to be bent equatorward by the westward flow, the wave scattering that occurs does not reach nearly as high a latitude as evidenced by the lack of (5,1) signal in the resulting pressure field.

The induced acceleration in this case, Fig. 5.21c, is drastically different than in the standard eastward flow. The acceleration is concentrated at the flanks of the current, with westward acceleration at the core depth and two intense eastward regions of acceleration above and below. An important point is that the acceleration pattern is considerably different than the EP flux divergence pattern implying that the contribution of the residual streamfunction is significant. In this case we obtain a peak acceleration value of -49.8 cm/s/yr which is quite strong and would induce significant changes in the mean flow

over a relatively short period of time. The pattern suggests that the mean flow will broaden meridionally and tend to develop stronger vertical shear zones at positions above and below the core depth and slightly removed from the equator (~2°).

The most interesting question which arises in connection with a westward jet is the effect a critical surface has upon Rossby wave propagation. In the case of Kelvin waves in eastward flows, we saw that the presence of a critical surface near the equator was sufficient to prevent energy propagation into the deep ocean. This was true even if the meridional wave scale exceeded the flow scale. Is this also the case for the Rossby waves? If so, then due to the slower phase speeds for the Rossby waves the presence of relatively weak westward flow in the ocean could preclude vertical propagation of Rossby wave energy into the deep ocean.

The results from a spectral sweep show that at the critical phase speed (where $c=U_{max}$) and slower the response amplitudes drop off significantly. Therefore, as with the Kelvin waves, there is a lack of strongly resonant wave solutions for flows with critical layers. This suggests that critical layers may be strong barriers to vertical Rossby wave propagation and can thereby prevent the establishment of vertical modes. However, unlike the Kelvin wave case, the spectra does possess small amplitude modulations for $U_{max}/c>1$ which lead to weak local maxima in this region. Due to the presence of these local maxima, for consistency, for our study of Rossby waves critical layers we choose to investigate a phase speed at one of these local maxima.

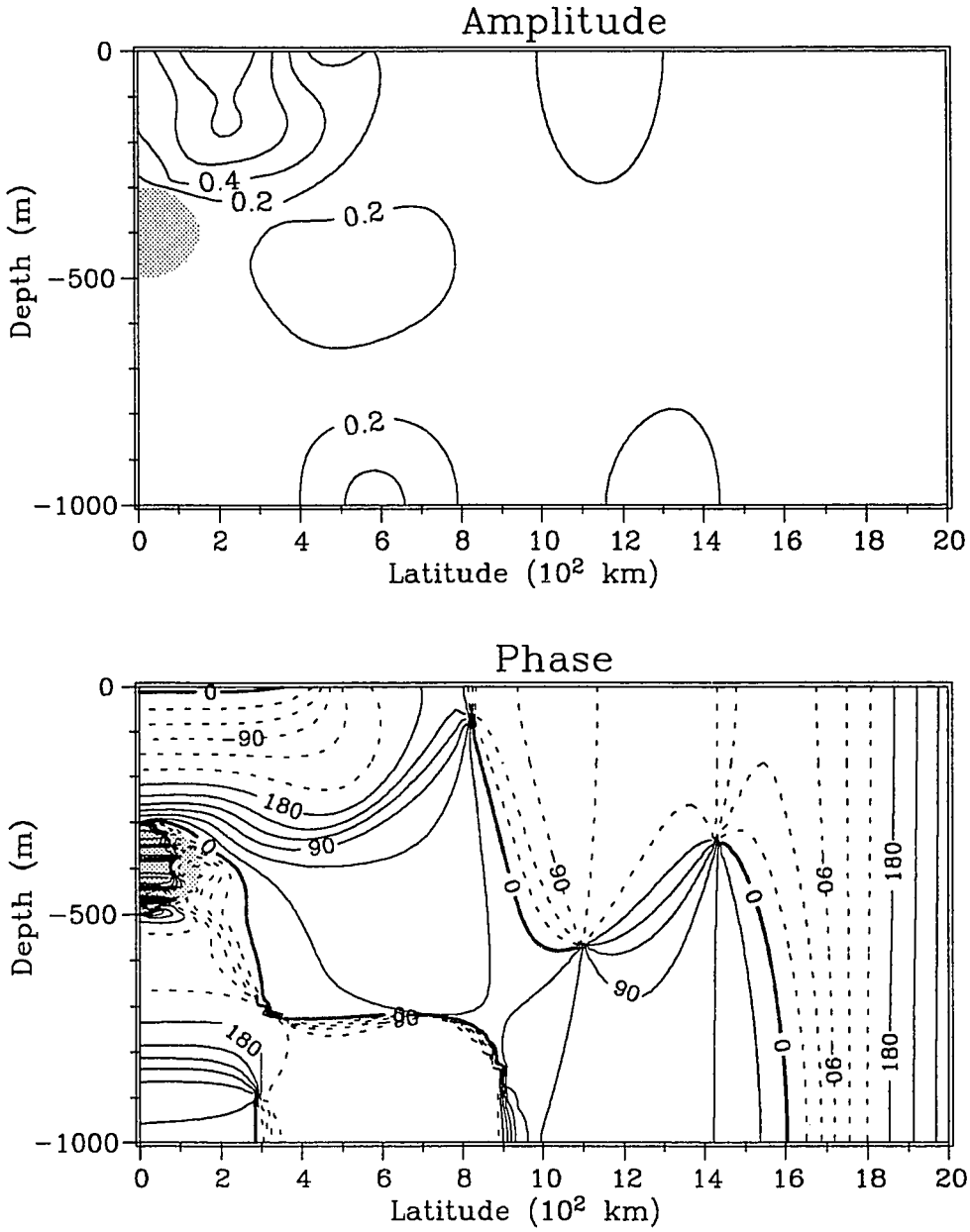


**Figure 5.22a: Pressure solution for the supercritical westward flow case, Case H. The region of supercritical flow, where U/c>1, is shaded.**

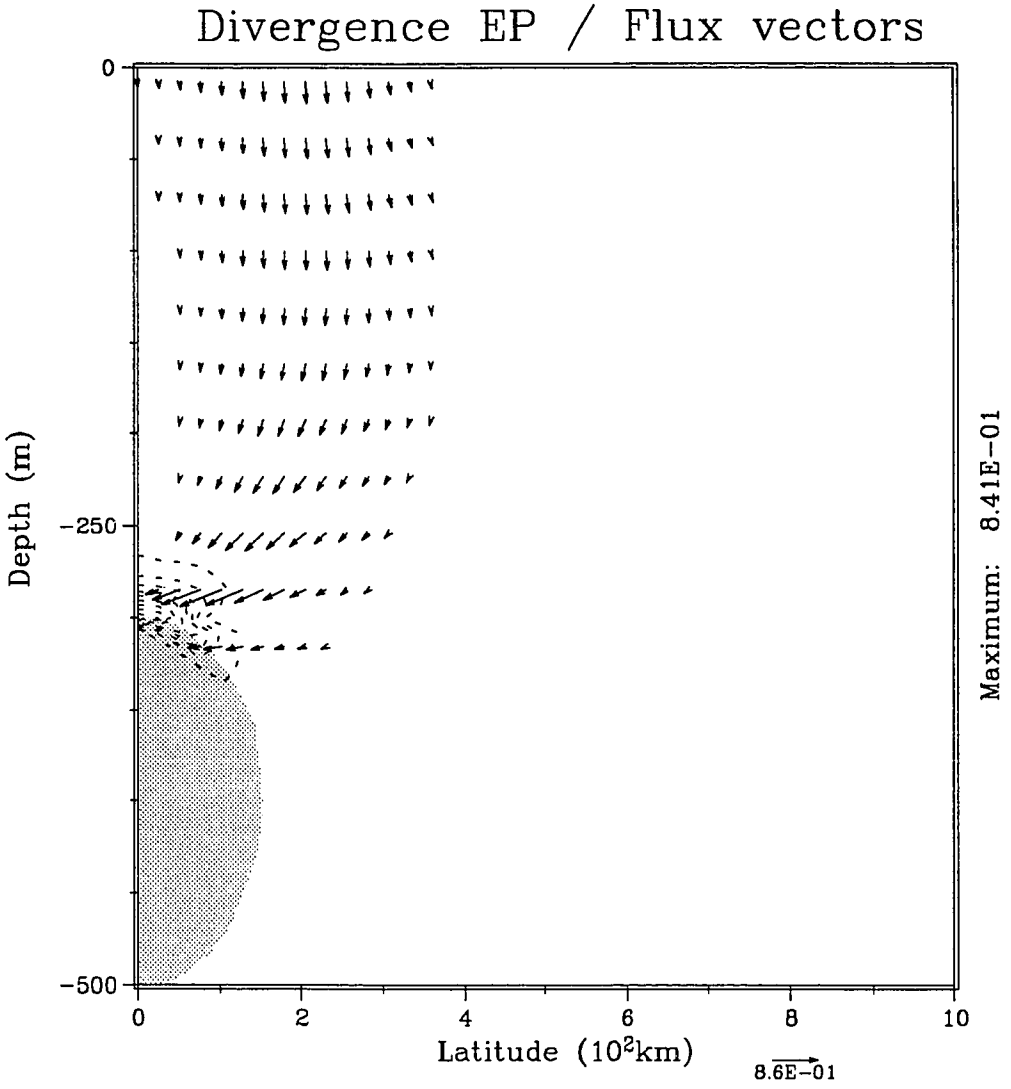


Figure 5.22b: E-P Flux results for the supercritical westward flow case, Case H. Note that since the remainder of the field is blank, only the upper 500m out to 10°N (*ie* ¼ of full domain) is presented for better visualization and the supercritical region is shaded.

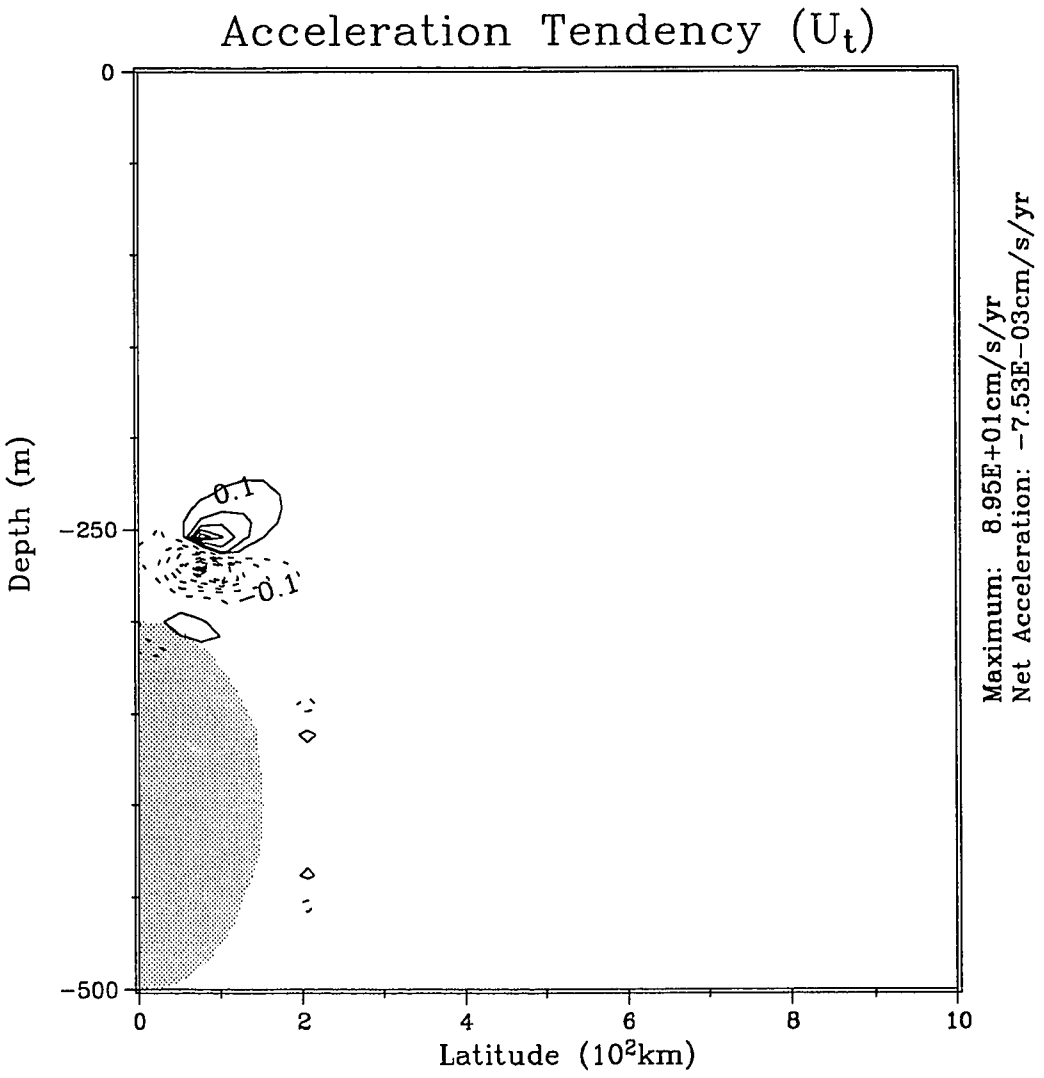


Figure 5.22c: $O(\epsilon^2)$ mean acceleration field for the supercritical westward flow case, Case H. As with 5.20b, only the upper 500m out to 10°N is presented and the supercritical region is shaded.

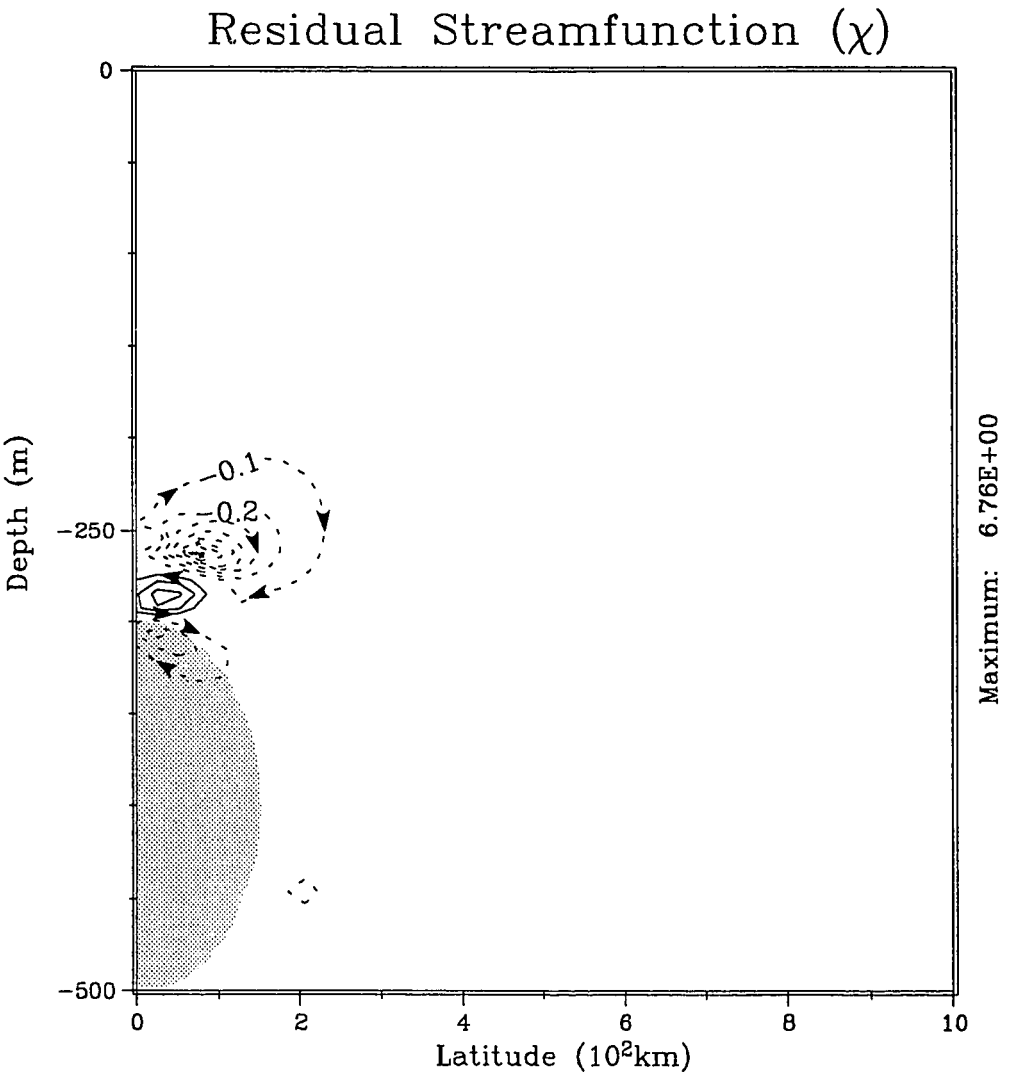


Figure 5.22d: $O(\epsilon^2)$ residual streamfunction for the supercritical westward flow case, Case H. As with 5.20b, only the upper 500m out to 10°N is presented and the supercritical region is shaded.

The pressure field obtained for the case where a critical surface exists is presented in Fig. 5.22a. For this case, the phase speed of the wave was chosen to be -24 cm/s. While the region of supercritical flow is shaded, the presence of the critical surface can also be detected quite clearly in the phase plot as a semi-circular region of rapid phase variation intersecting the equator at 300m and 500m and extending to ~1-2°N at the core depth of 400m. We see that, although the interaction with the flow is very intense, as evidenced by the sharp variations in amplitude and phase near the critical surface, the critical layer does not fully prevent wave activity from entering the deep ocean. However, the wave activity which does reach the deep ocean does so at higher latitudes as in the case of eastward flow. The behavior of the wave field near the equator (out to ~4°N) above the upper equatorial critical level is similar to that for the Kelvin wave in critical flow. In this region, the phase varies uniformly with depth and the amplitude contours are more or less vertically oriented. This character is indicative of a wave which is vertically propagating into the highly absorptive critical layer. At higher latitudes, the wave field is more mode-like with vertical variations in the amplitude and phase jumps at depth. This part of the solution is certainly due to wave scattering and/or reflection off the rapidly varying mean flow. The principle difference between the Kelvin and Rossby wave cases is that here the wave field can and does scatter meridionally into other wave structures that can reach the deep ocean.

The modal decomposition shows that the solution is not dominated strongly by any particular wave mode. The largest 5 wave modes in

decreasing order are the (1,4) with a projection of 18.0%, (1,6) with 14.7%, (1,5) with 14.2%, (1,7) with 10.4% and the (1,3) with 9.1%. We note that the largest 5 components are all first meridional mode waves of vertical mode structures higher than 3. This arises from the region described above where the wave is vertically propagating. The rapid decrease in vertical wave scale induced by the strong westward flow above the critical layer requires higher vertical mode content in the expansion to describe the solution. This result, also, is similar to the Kelvin wave in critical flow. The fact that no particular vertical structure dominates is due to the location of the mean flow. If the flow were near the bottom, over a large portion of the water column the wave would look like a third vertical mode. Only near the flow would the scales change and introduce higher vertical mode structures.

While the decomposition is dominated by first meridional mode content, the presence of the off-equatorial amplitude contours suggests the presence of higher meridional modes in the solution. Further down the list of no-flow wave modes contributing to the solution, we do find significant levels of variance in the higher meridional modes 3 and 5 (#8 (3,2)-5.9% and #10 (5,1)-2.1%). The presence of these particular two wave modes is apparent in the pressure field. The (3,2) mode is apparent in the second vertical mode-like structure occurring near 6°N and the (5,1) in the first vertical mode-like structure occurring near 13°N.

The results of the EP flux considerations, Fig 5.22b, show clearly the strong effect of the critical layer on the wave propagation. The majority of the net wave activity radiates into the critical region.

In fact, the effect of the critical region is strong enough to totally mask the wave radiation at higher latitudes which is inferred by the presence of the off-equatorial maximum in the pressure field. Near the critical layer the EP flux possesses strong convergence leading to large momentum transfers with the mean state. This result is nearly identical in principle to the result for the Kelvin wave and clearly implies strong critical layer absorption of the wave field.

The accelerations induced in this case are shown in Fig. 5.22c. The peak acceleration in this case is very strong and westward (-89.5 cm/s/yr). One obvious fact is that this peak acceleration does not occur at the critical surface, but rather in the region above. The resulting patterns, which are considerably different than the EP flux convergence, imply that the local contribution of the residual stream-function field, $\chi$, is very important. Therefore, due to its importance for this particular case, we present the resulting $O(\epsilon^2)$ residual circulation in Fig. 5.22d. The sense of the residual circulation is for the residual flow to be anticlockwise around hills in $\chi$ and clockwise around the valleys. In general, the Coriolis torque and advection of the mean momentum $[\chi_z(\beta y - U_y)]$ due to poleward (equatorward) residual flow will lead to eastward (westward) mean acceleration. Above the core depth, where $U_z$ is positive, vertical advection due to downward (upward) residual flow will yield eastward (westward) mean acceleration. Therefore, from comparison of Fig 5.22c and 5.22d, the residual circulation is in the direction to advect the mean state such that the resulting $O(\epsilon^2)$ accelerations are seen. Equatorward residual flow near the critical layer counteracts the westward acceleration tendency in-

duced by the convergent EP flux field to leave a weak eastward acceleration tendency. Above this region, where the EP flux convergence is small, the mean accelerations correspond directly to that expected from advection due to the residual circulation. In addition, comparing the 3 terms in the acceleration arising from the residual flow, we find that the Coriolis torque ($\beta y\chi_z$) which has a maximum over 3 times either of the relative vorticity terms ($U_y\chi_z$ or $U_z\chi_y$), dominates.

## 5.3 Realistic Flow Simulation: EUC and SEC in Variable N Ocean.

Now that we have a framework for understanding the effects that both eastward and westward flows have upon Rossby wave propagation near the equator, we present the results for a more realistic background state. This state is based upon the resting state variable $N^2$ profile presented in Eq. 5.4 and shown in Fig. 5.18. Upon this density field, we specify mean flows representative of the Equatorial Undercurrent and the South Equatorial Current. The mean flow is specified by linear superposition of two Gaussian jets as defined in Eq. 5.1. For the Undercurrent we assume $U_0$=75cm/s, $z_c$=150m, dz=75m and $\delta$y=150km and for the South Equatorial Current we assume $U_0$=-30cm/s, $z_c$=0m, $\delta$z=100m and $\delta$y=300km. The resulting flow field is presented in Fig. 5.23. The Undercurrent amplitude is slightly stronger than that in the variable $N^2$ case presented above. This was done to counteract the westward flow placed at the surface and yield an maximum eastward flow roughly the same as in that case. The South Equatorial Current is centered on the equator at the surface and is assumed to have a meridional decay scale

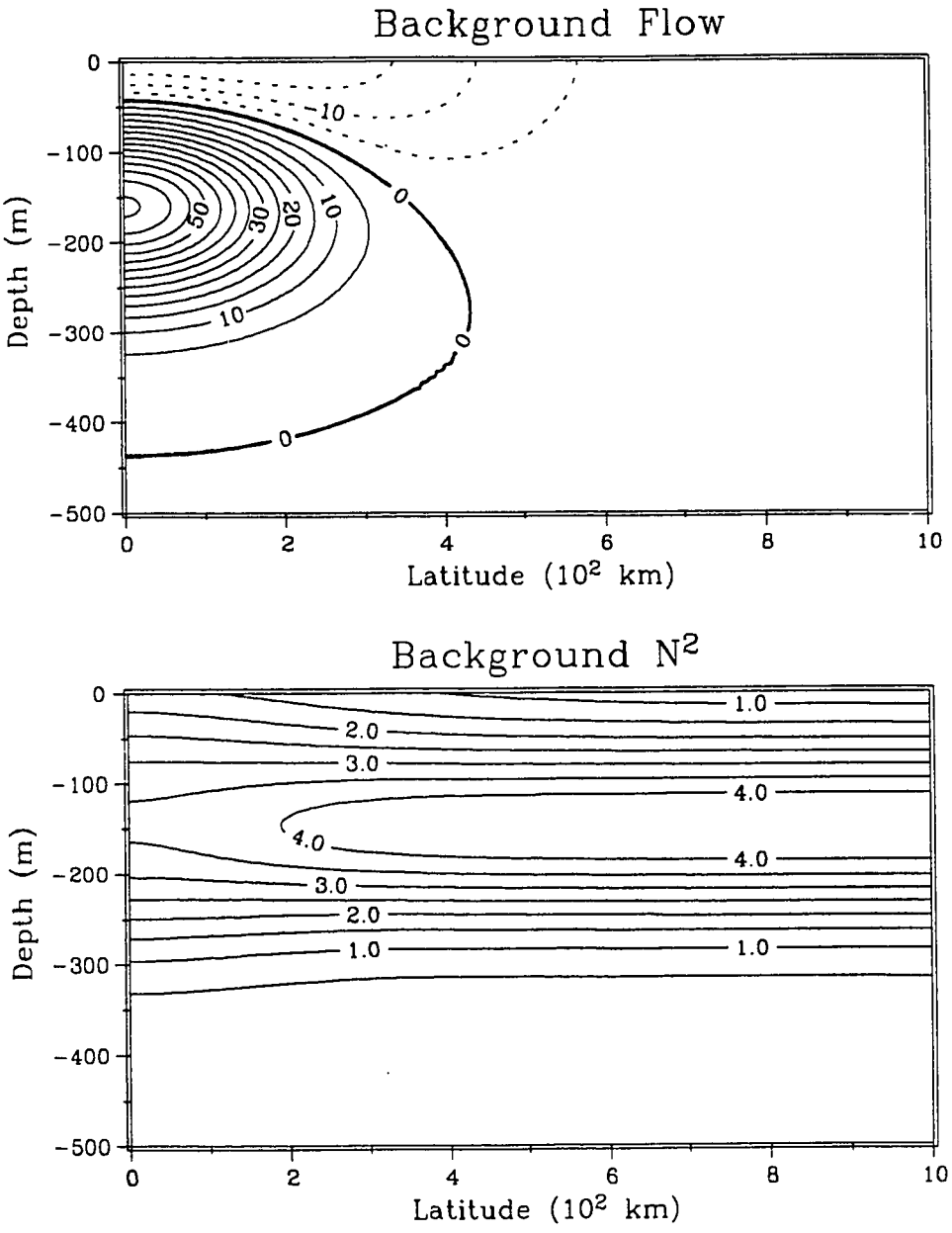


Figure 5.23: Background mean state for realistic simulation of Undercurrent and South Equatorial Current. (Top) Zonal velocity (cm/s), (Bottom) $N^2$ ($x10^{-4}s^{-2}$)

twice that of the Undercurrent and a somewhat larger vertical scale. In this way, the resulting flow field simulates the meridional bi-lobed shape for the surface westward flow seen in Fig. 2.1. The addition of the westward flow causes the vertical shear near the top of the Undercurrent to be stronger than any other case.

We will present the pressure field results for the first 3 resonances in the above mean state. Perturbation velocity fields (u, v and w) are presented in Appendix B. The emphasis here will be to note any similarities and differences in the modifications to the wave structure and dispersion to those seen in the idealized cases presented previously. For comparison, we present analogous figures for the first 3 vertical normal modes in the absence of mean currents in Figs. 5.24-5.26.

The solutions for the 1$^{st}$ resonance, which occurs at a phase speed of -89.5 cm/s in this flow, are presented in Fig. 5.27 to compare with Fig. 5.24. The pressure field, Fig. 5.27a, shows that, as with all other 1$^{st}$ resonances, the effect of the mean flow is weak. The most significant changes are the slight surface enhancement of the pressure field and a small poleward shift (~½°) in the near surface pressure maxima. This surface enhancement in the flow case, Fig. 5.27a, is apparent by the weakening of the 0.2 contour near the bottom compared to the no-flow case, Fig. 5.24a. The results of the modal decomposition show that, not surprisingly, 98.5% of the pressure variance projects upon the 1$^{st}$ vertical, 1$^{st}$ meridional no-flow Rossby wave mode. Comparison to the no-flow solution shows that the mean flow causes a poleward deflection and near-equatorial surface trapping of the net EP flux, Fig. 5.27b. This effect is similar to the meridional

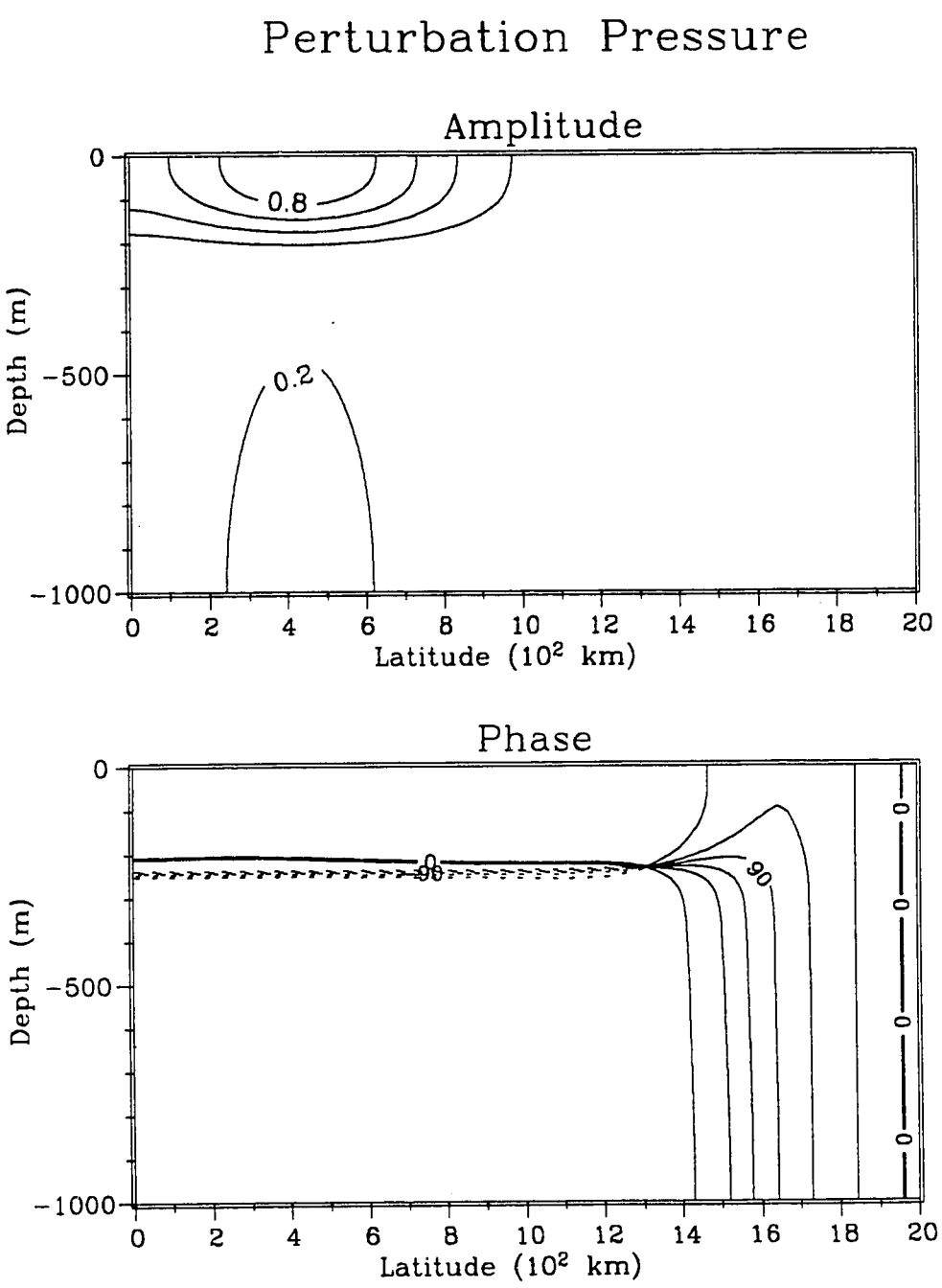


Figure 5.24a: Pressure solution for the 1st vertical mode in a variable N Ocean in the absence of mean flow.

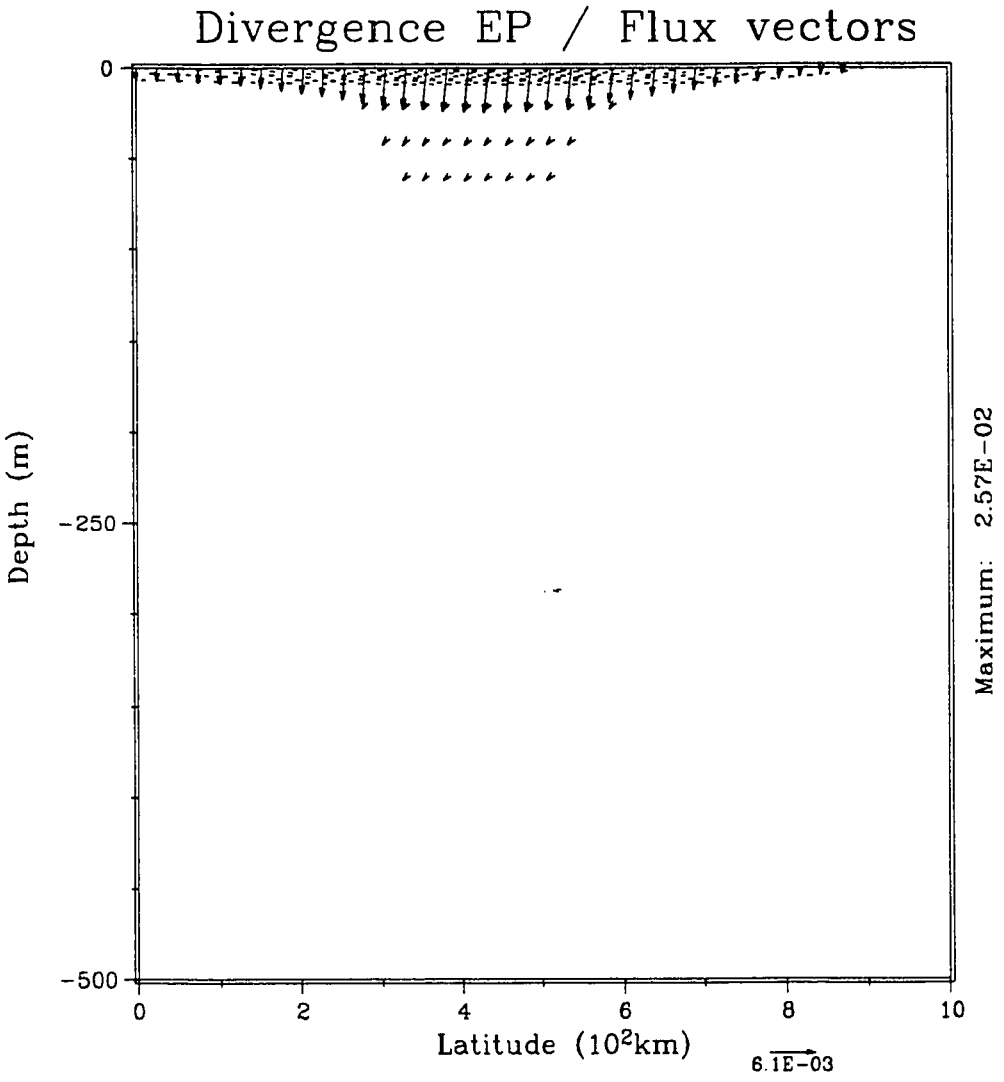


Figure 5.24b: E-P Flux results for the 1st vertical mode in a variable N Ocean in the absence of mean flow.

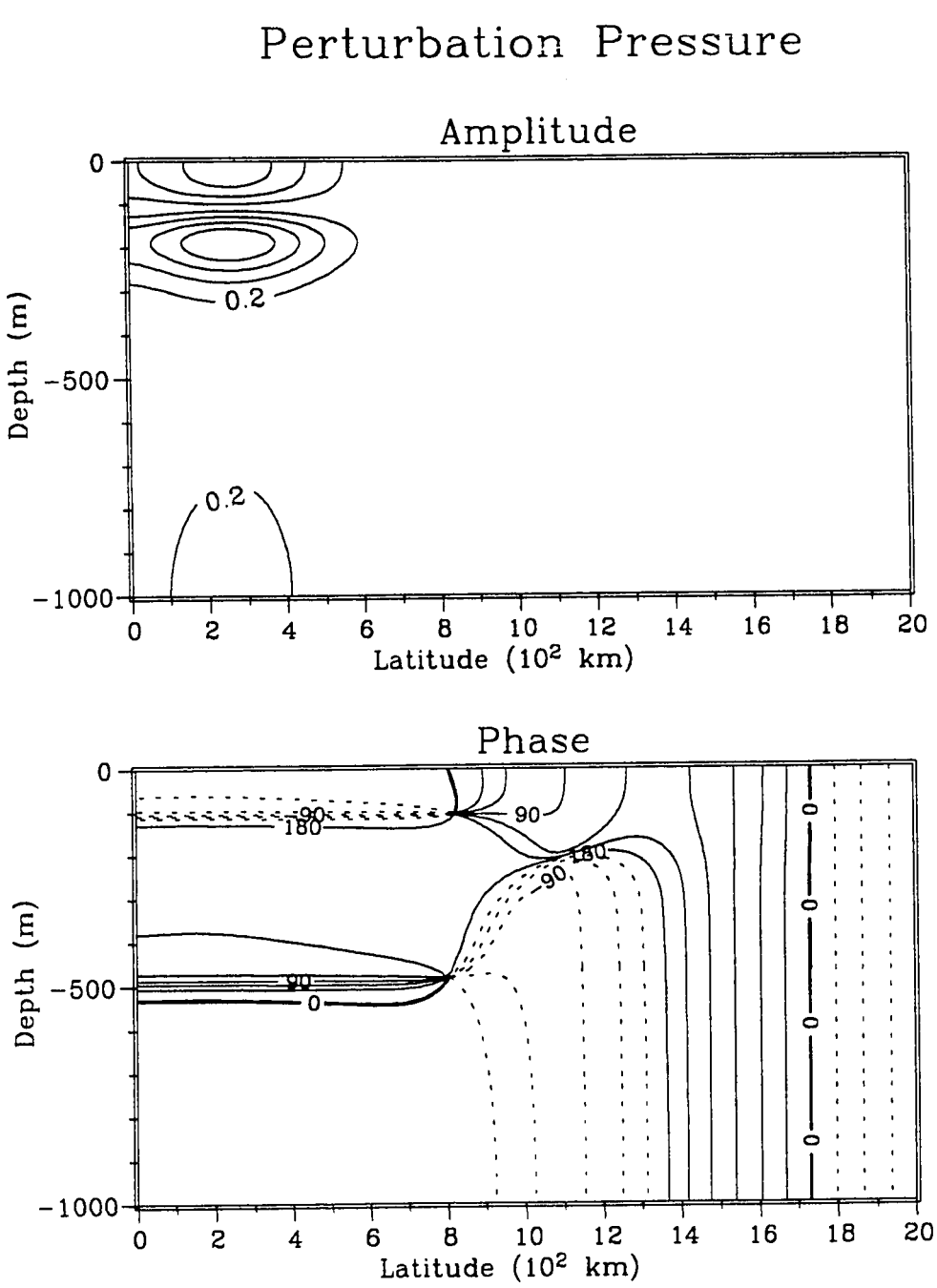


Figure 5.25a: Pressure solution for the 2nd vertical mode in a variable N Ocean in the absence of mean flow.

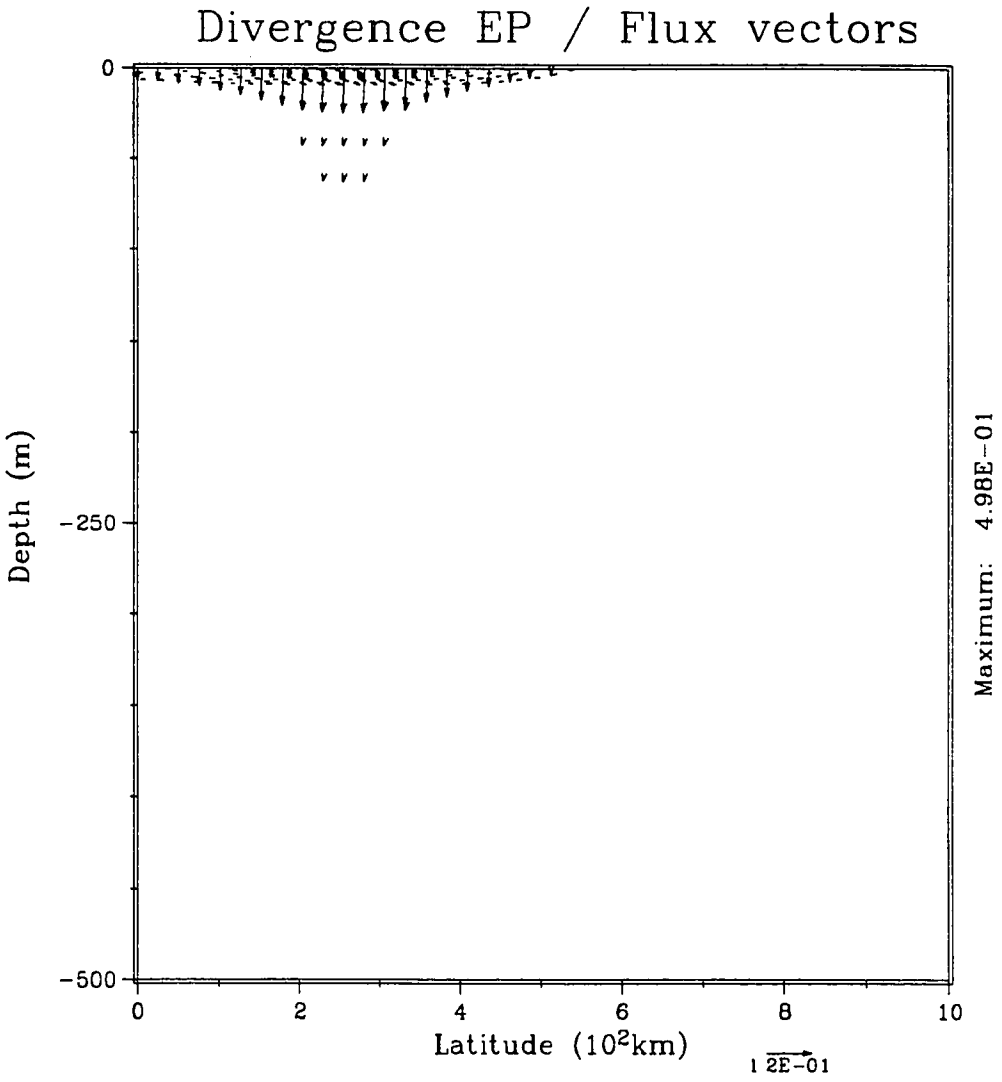


Figure 5.25b: E-P Flux results for the 2nd vertical mode in a variable N Ocean in the absence of mean flow.

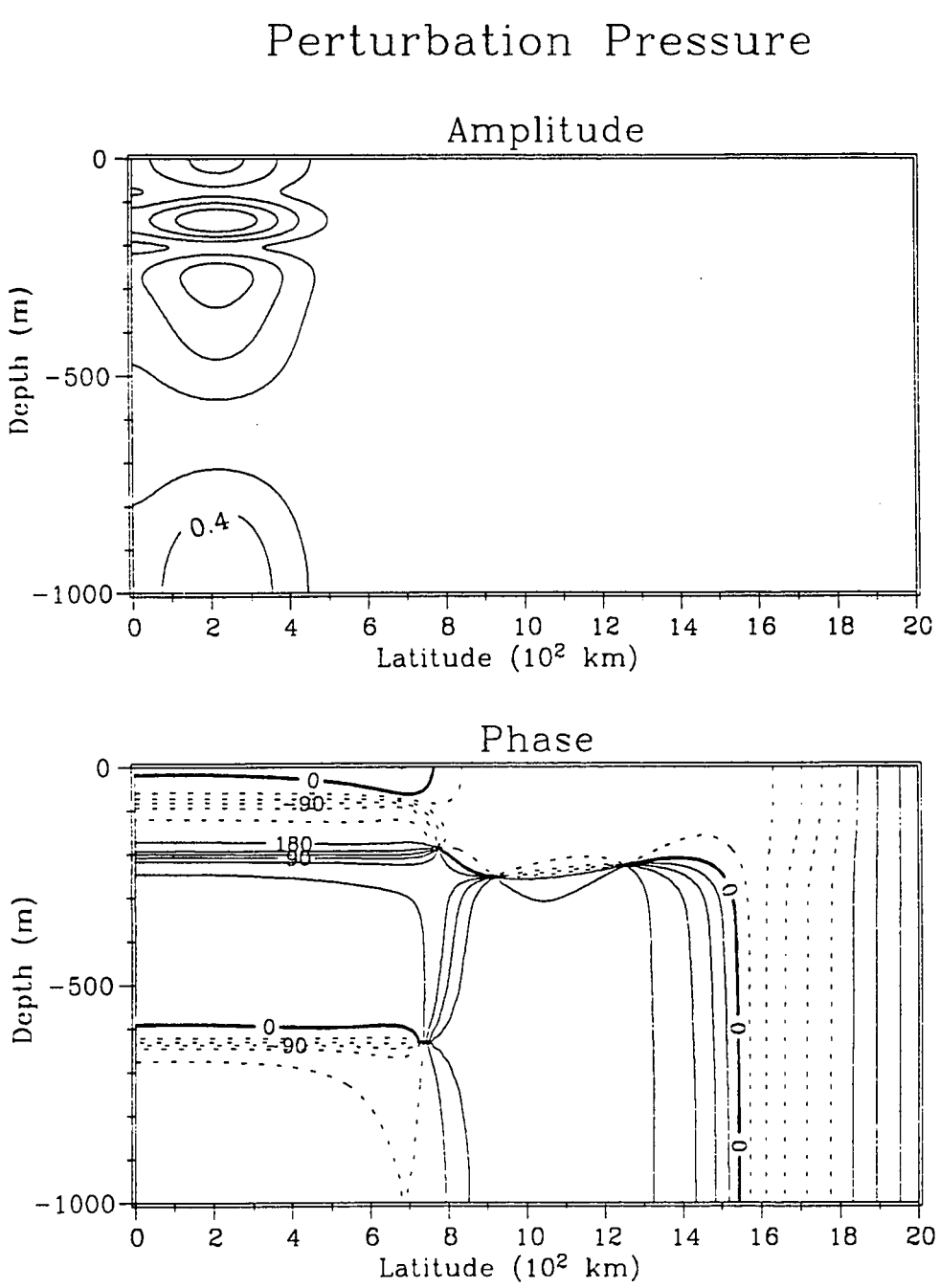


**Figure 5.26a: Pressure solution for the 3rd vertical mode in a variable N Ocean in the absence of mean flow.**

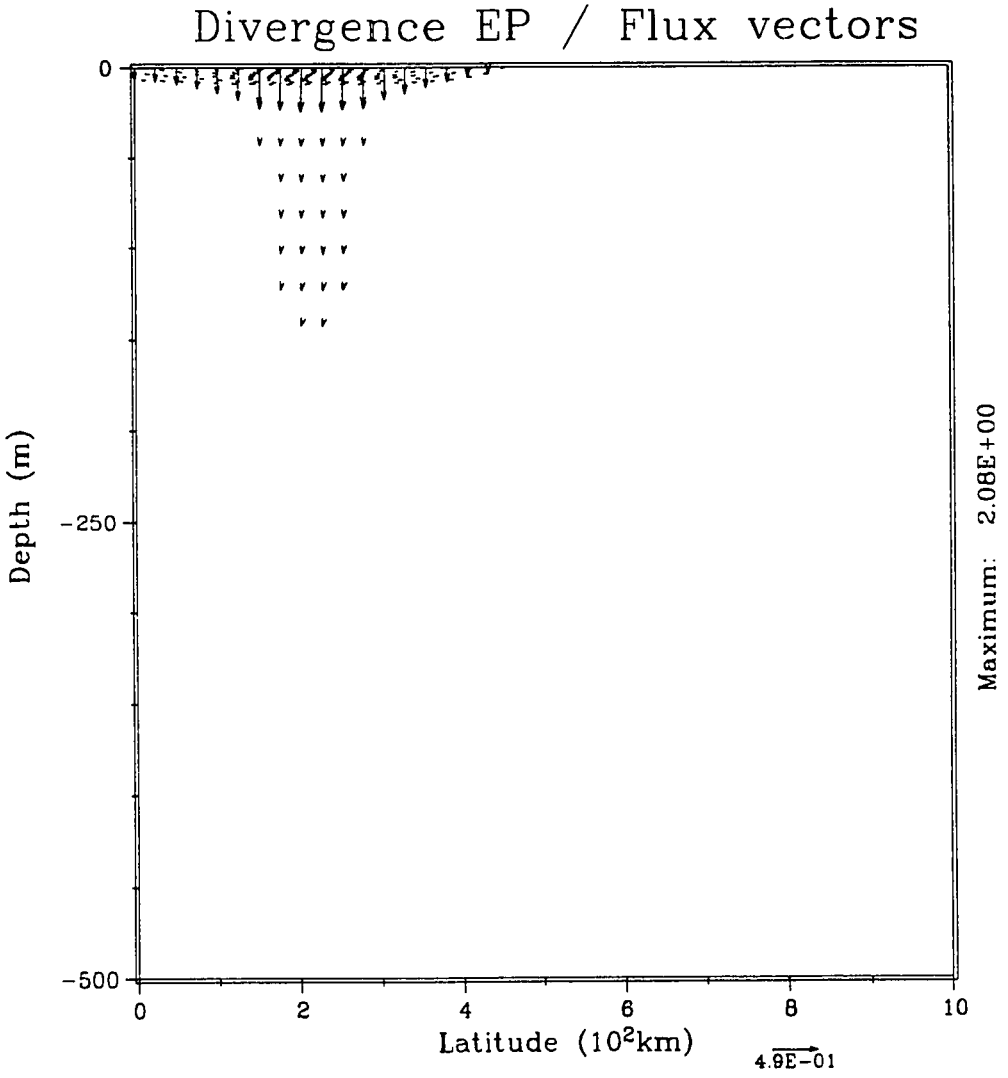


Figure 5.26b: E-P Flux results for the 3rd vertical mode in a variable N Ocean in the absence of mean flow.

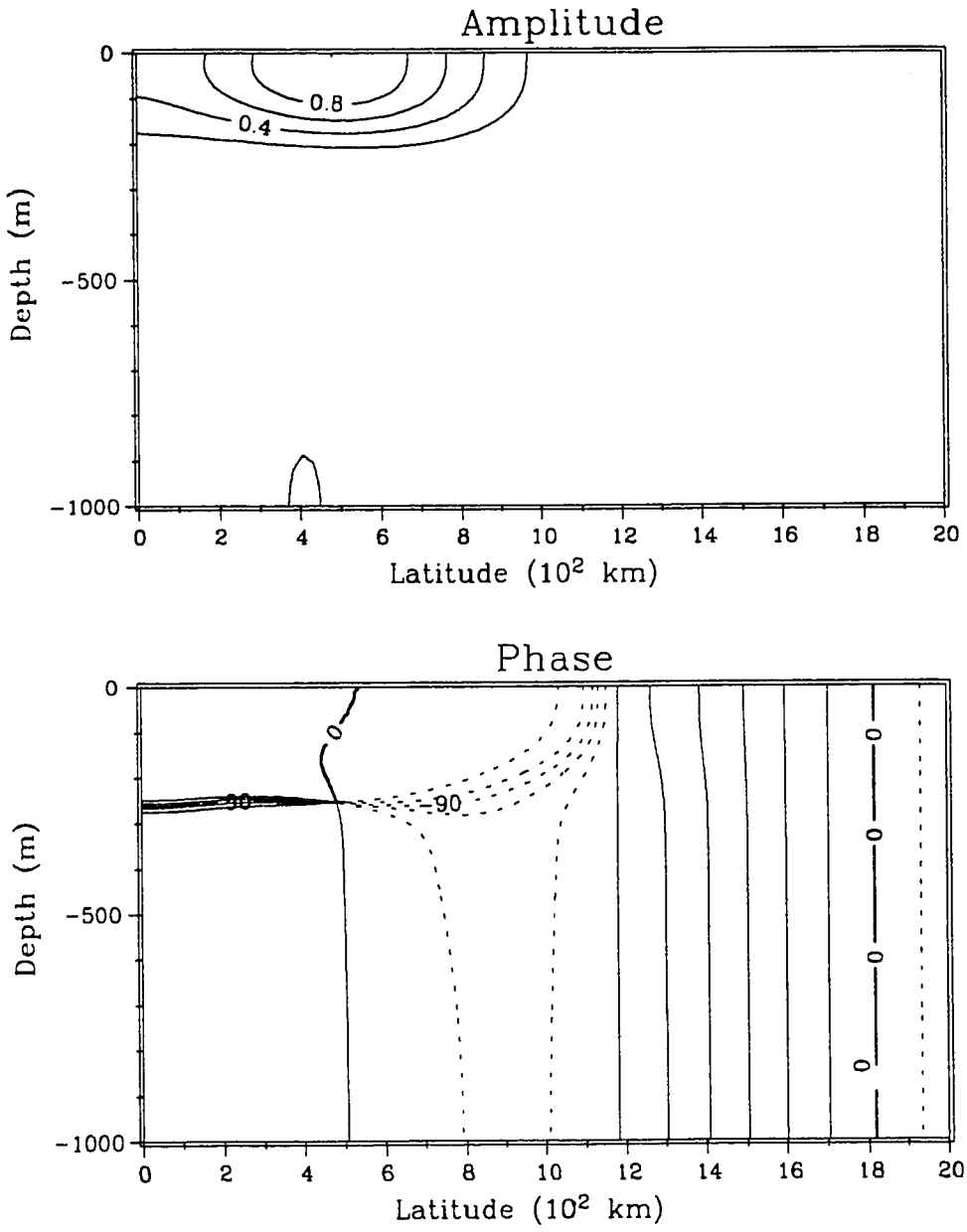


Figure 5.27a: Pressure solution for the 1st resonance in the simulated EUC/SEC system.

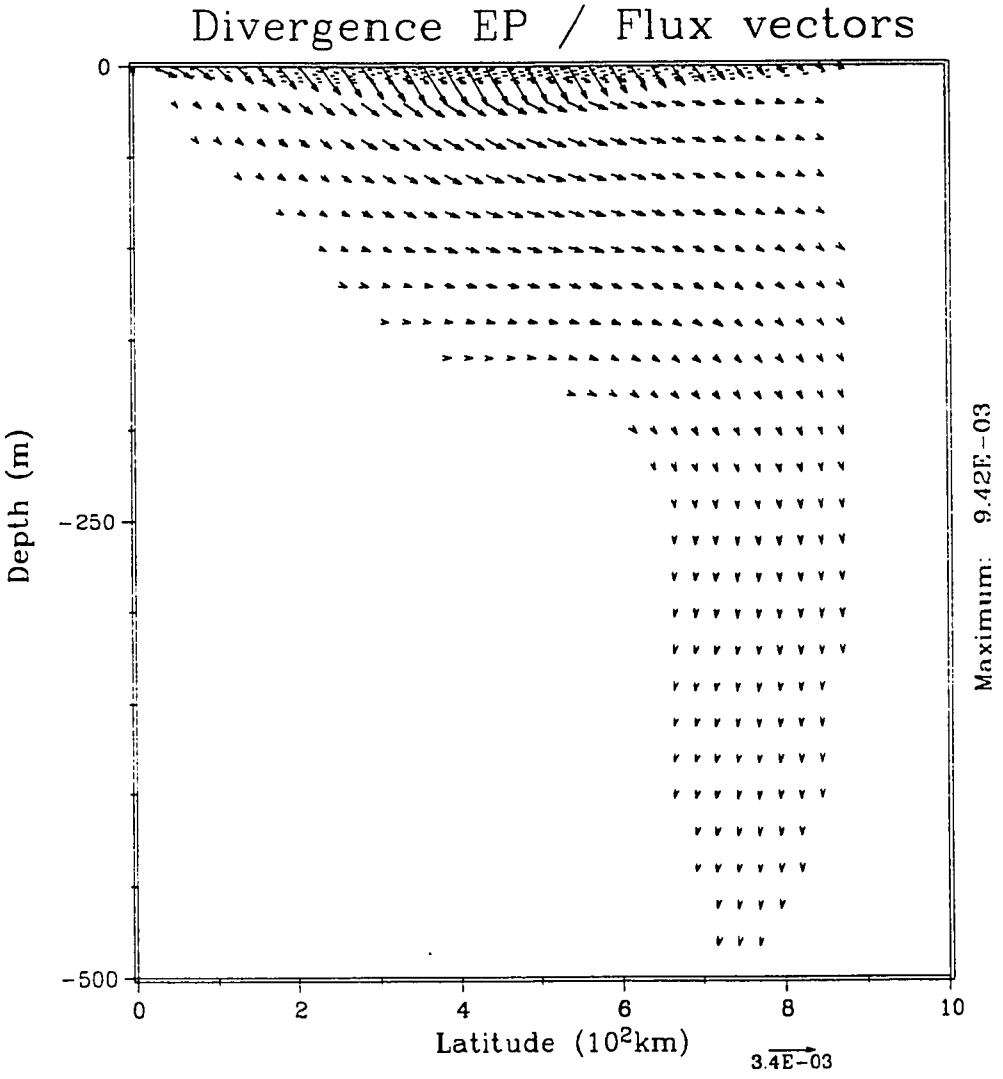


Figure 5.27b: E-P Flux results for the 1st resonance in the simulated EUC/SEC system.

scattering of wave activity found in previous results and is consistent with the changes in the pressure field.

The results for the 2nd resonance, which occurs at a phase speed of -42.0 cm/s in this flow field, are presented in Fig. 5.28. As in the idealized cases, the effects of mean flow begin to be more strongly manifested as the resonant phase speed decreases. The primary surface maxima in the pressure field, Fig. 5.28a, has shifted considerably poleward and a much weaker secondary maxima has formed equatorward. We see no evidence of either the second or third maxima at depth near the equator. The phase shows the off-equatorial peak to be much like a 1st vertical mode structure. In fact, the modal decomposition reveals that 95.3% of the variance projects upon a (m,n)=(3,1) mode Rossby wave structure, 1.7% projects upon the (1,1) and only 1.3% projects upon the (1,2) which was directly forced. The EP flux results, Fig. 5.28b, also show clearly that the wave activity input near the equator is being scattered poleward by the mean flow contributing to the excitement of the higher meridional mode structure.

The results for the third resonance, at -29.5 cm/s, also show an enhancement of the pressure field. The pressure field, Fig. 5.29a, is spread poleward leading to the formation of 3 maxima in the meridional direction indicative of a higher meridional mode wave structure. The modal decomposition yields projections of 70.7% upon the (5,1) structure, 13.8% upon the (1,2) structure and 6.7% upon the (3,1) structure. The EP flux field, Fig. 5.29b, shows a result nearly identical to that for the second resonance where the EP flux is directed poleward.

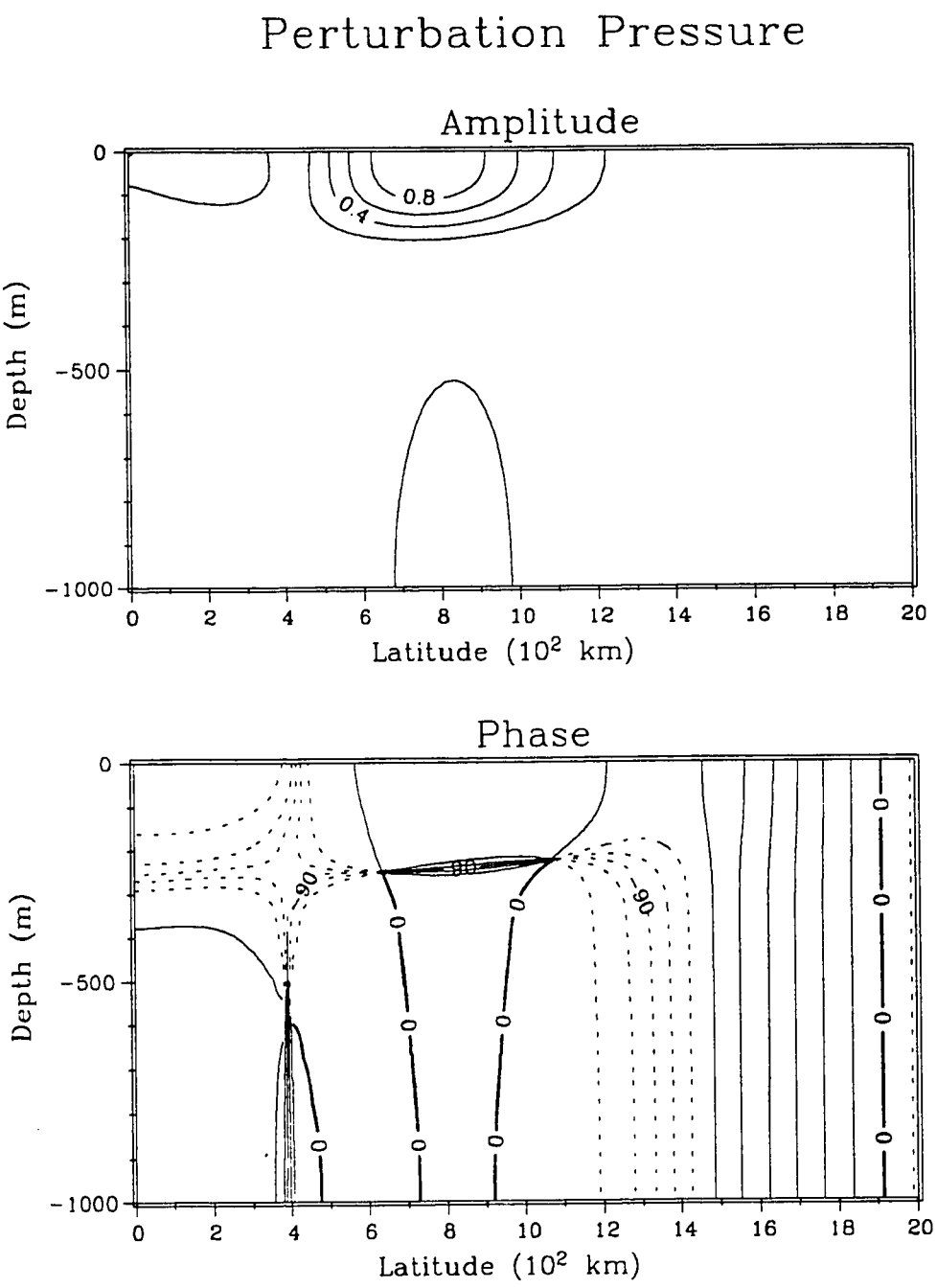


Figure 5.28a: Pressure solution for the 2nd resonance in the simulated EUC/SEC system.

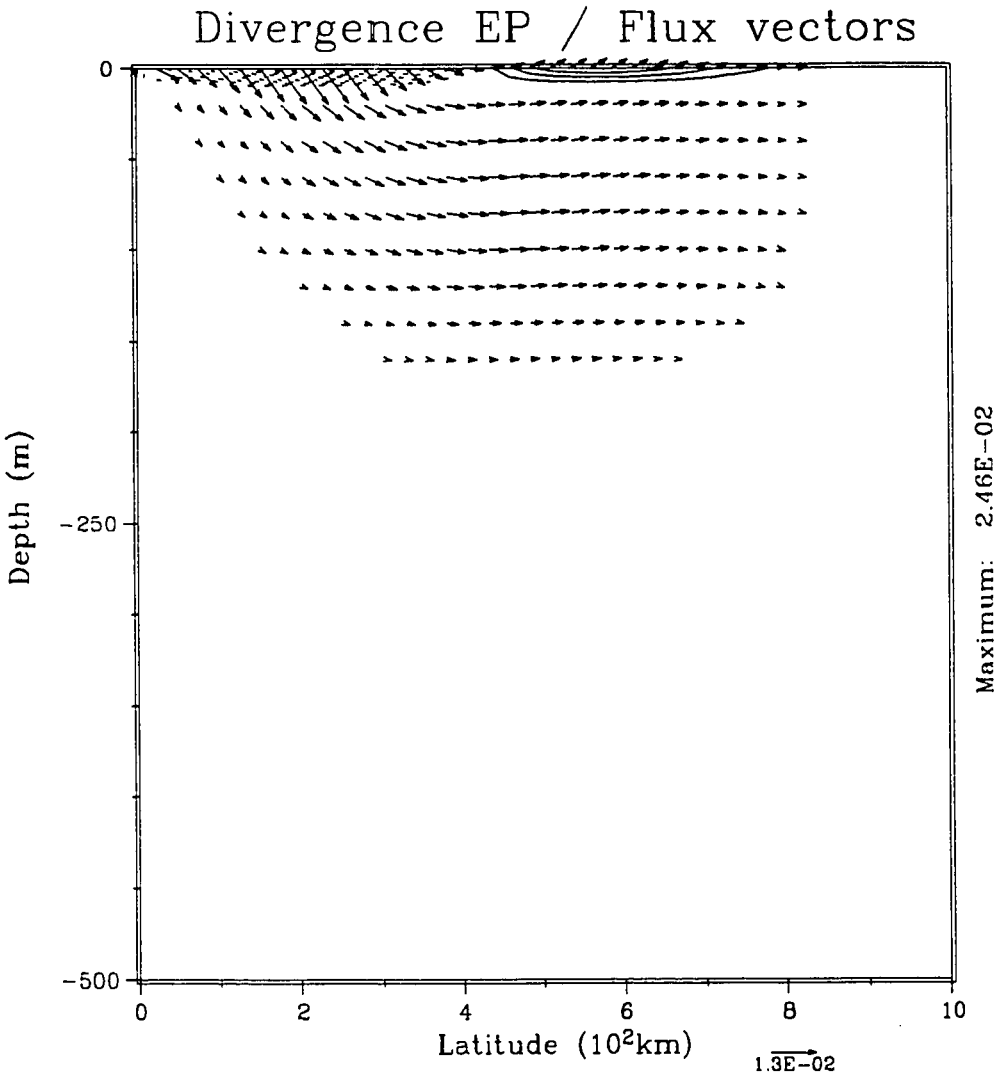


Figure 5.28b: E-P Flux results for the 2nd resonance in the simulated EUC/SEC system.

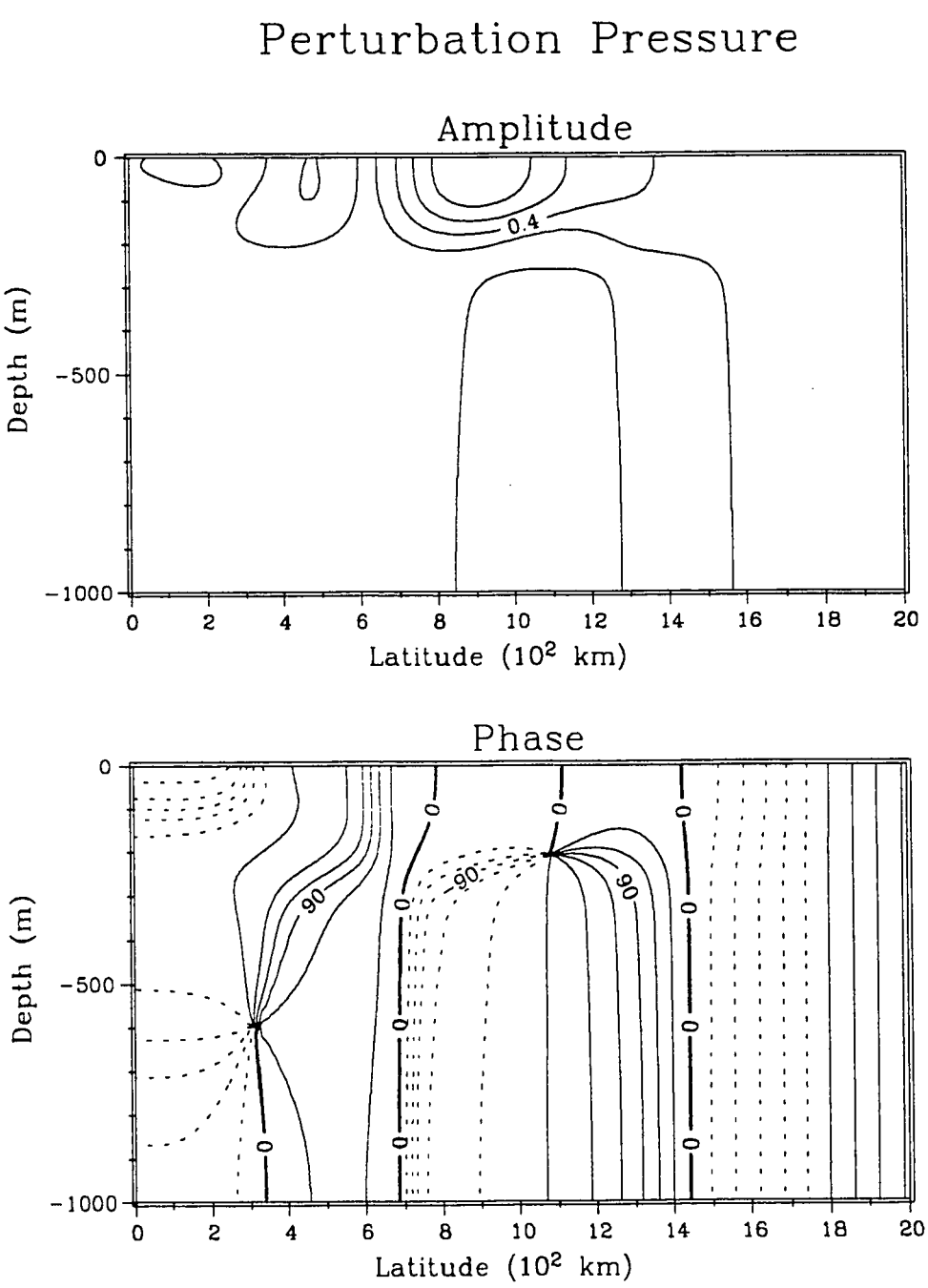


Figure 5.29a: Pressure solution for the 3rd resonance in the simulated EUC/SEC system.

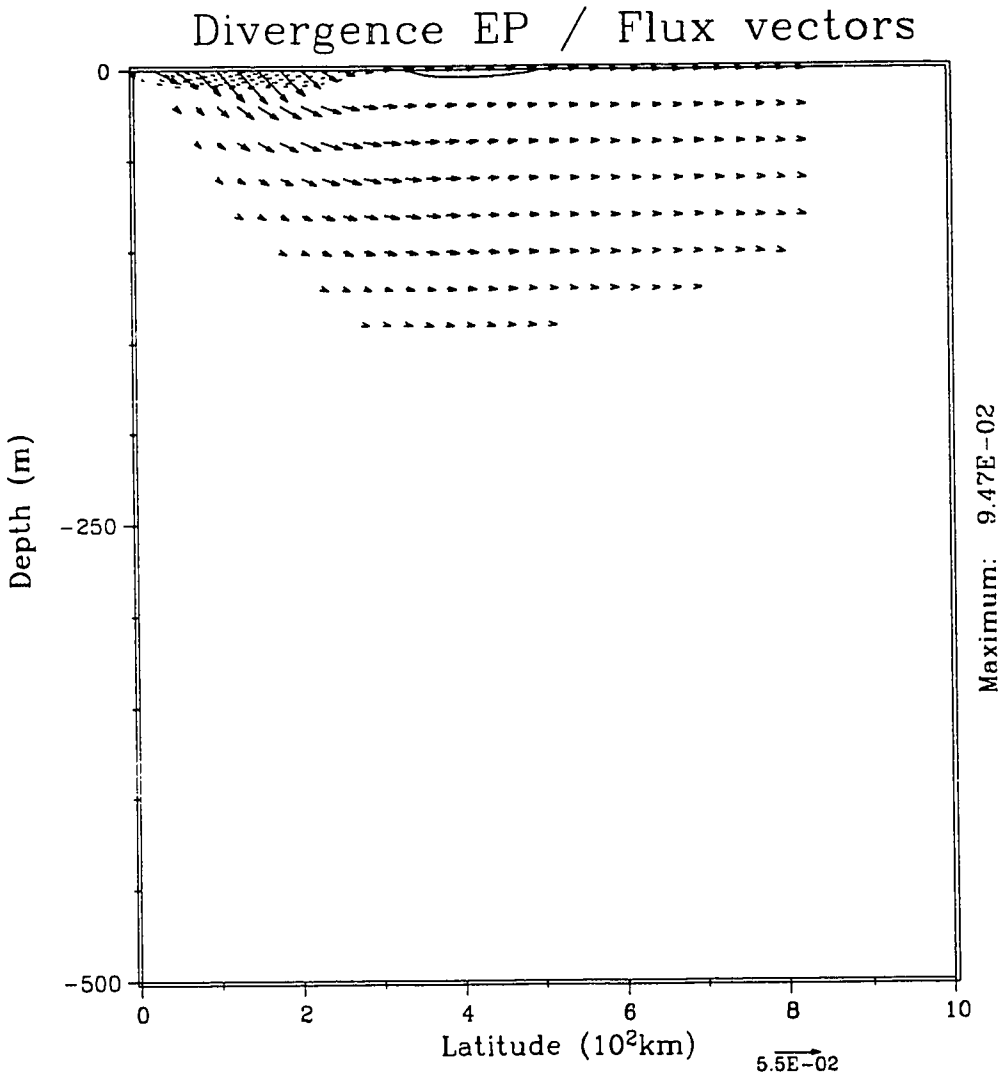


Figure 5.29b: E-P Flux results for the 3rd resonance in the simulated EUC/SEC system.

Therefore, we see that the effects seen for the realistic simulation are not conceptually different than those for the idealized cases, but rather, the intense current shear and smaller mean flow scales causes them to be stronger. An important effect of the stronger shear is that the flow is not very transmissive to high vertical mode Rossby wave energy. While this is effectively the same result seen for the Kelvin waves, in that case it was due to critical layer absorption whereas here it is due to the poleward scattering. These results, however, may explain the $1^{st}$ vertical mode dominance usually seen in observations taken from the real ocean.

# Chapter 6: Conclusions

The interaction of the equatorial Rossby waves in the longwave limit has been investigated in a continuously stratified numerical ocean model. The model is spectral temporally and zonally and therefore results in a two dimensional partial differential equation which is solved by finite differences. It allows for the realistic treatment of the effects of both vertical and meridional shear and variations in the background buoyancy field.

Analytic results for weak and slowly varying flow fields paint a picture of how the wave field is affected by the interaction with a mean flow. These results, which are limited to weak interactions, state that for an eastward flow the pressure field structure will expand meridionally and vertically due to the increase in the intrinsic frequency, $\sigma$-kU. In addition, the rate of vertical energy propagation for the waves is increased. These theories, while limited in their applicability for realistic equatorial oceanic mean flows, provide a valuable framework to aid the investigation of the more realistically sheared mean flow cases.

In addition to the stretching of wave scales expected from slowly varying wave theory, the numerical results show that one effect of strongly sheared equatorial mean flows is to cause poleward scattering of wave energy input near the equator. This scattering, which cannot be treated by the analytic theories, causes Rossby wave energy input at the surface with the structure of a $1^{st}$ meridional wave mode to be sent poleward. This scattering of wave activity, depicted by the reflection

of the net EP flux vectors off the mean shear above the core, causes large structural changes to the wave solutions. As a result, for realistic mean flows equatorial wave energy can appear at higher latitudes and a shadow zone can occur below the Undercurrent in the region near the equator.

However, an equatorially confined Undercurrent can also bend equatorward a portion of wave energy input at higher latitudes. This apparent disparity with the above result arises from the fact that the wave activity input at higher latitudes interacts primarily with the meridional shear at the flanks of the Undercurrent, while the wave activity input near the equator interacts most strongly with the vertical shear zone above the core. The presence of eastward countercurrents at the surface near these latitudes in the ocean, however, may make the former result moot. The poleward scattering (equatorial bending) manifests itself in modal decompositions as wave variance appearing in higher (lower) meridional wave modes. Consequently, the effect the Equatorial Undercurrent has upon Rossby wave propagation depends not only upon Undercurrent geometry but also on where the energy is input meridionally.

The case of westward flow shows that the shifts in resonant phase speed and the structural changes of the wave field can be very large. Due to the scattering nature of rapidly varying flow, the presence of an equatorially confined critical layer does not preclude the radiation of wave activity into the deep ocean as it did in the Kelvin wave case. However, the wave activity which reaches the deep ocean tends to do so at higher latitudes.

The wave induced accelerations for both the resting ocean and for an eastward Undercurrent are dominated by frictional dissipation of wave energy and, therefore, are weak. The induced accelerations for westward mean flows where Re(c-U)→0 show behavior similar to Kelvin waves in eastward flow, McPhaden *et al.* (1986), in that large divergences of the EP flux exist leading to large momentum transfers from wave to mean states. The primary difference from the Kelvin waves is that for the Rossby waves the wave-induced residual circulation is important locally and leads to significant accelerations. These accelerations are primarily induced by the Coriolis torque due to the residual meridional flow field.

Bibliography

Andrews, D.G. and M.E. McIntyre, 1976: Planetary waves in horizontal and vertical shear: The generalized Eliassen-Palm relation and the mean zonal acceleration., *J. Atmos. Sci.*, *33*, 2031-2048.

Andrews, D.G. and M.E. McIntyre, 1978: On wave action and its relatives., *J. Fluid Mech.*, *89*(4), 647-664.

Andrews, D.G., 1983: A conservation law for small-amplitude quasi-geostrophic disturbances on a zonally asymmetric basic flow, *J. Atmos. Sci.*, *40*, 85-90.

Andrews, D.G., Holton, J.R. and C.B. Leovy, 1987: *Middle Atmosphere Dynamics*, Appendix Ib, 147-149, Academic Press, New York.

Arfken, G., 1970: *Mathematical Methods for Physicists*, Academic Press, New York.

Birkhoff, G., 1972: The Numerical Solution of Elliptic Equations, Regional Conference Series in Applied Math., *11*, SIAM Publications, Philadelphia.

Boyd, J.P., 1976: The noninteraction of waves with the zonally averaged flow on a spherical earth and the interrelationships of eddy fluxes of energy, heat and momentum. *J. Atmos. Sci.*, *33*(12), 2285-2291.

Boyd, J.P., 1978: The effects of latitudinal shear on equatorial waves. Part I: theory and methods. Part II: applications to the atmosphere. *J. Atmos. Sci.*, *35*(12), 2236-2267.

Bretherton, F.P. and C.R. Garrett, 1969: Wavetrains in inhomogeneous moving media., *Proc. Roy. Soc. London, A302*, 529-554.

Chang, P. and S.G.H. Philander, 1988: Rossby wave packets in baroclinic mean currents., In press: *Deep Sea Res.*

Charney, J.G. and P.G. Drazin, 1961: Propagation of planetary-scale disturbances from the lower into the upper atmosphere., *J. Geophys. Res.*, *66*(1), 83-109.

Dorr, F.W., 1970: The direct solution of discrete Poisson equation on a rectangle, *SIAM Review*, *12*(2), 248-263.

Dunkerton, T., 1980: A Lagrangian mean theory of wave, mean-flow interaction with applications to nonacceleration and its breakdown, *Rev. of Geophys. and Space Phys.*, *18*(2), 387-400.

Edmon, H.J., B.J. Hoskins and M.E. McIntyre, 1980: Eliassen-Palm cross sections for the troposphere. *J. Atmos. Sci.*, *37*, 2600-2616.

Eliassen, A. and E. Palm, 1961: On the transfer of energy in stationary mountain waves., *Geofys. Publ.*, *22*(3), 1-23.

Forsythe, G.E. and W.R. Wasow, 1960: *Finite-Difference Methods for Partial Differential Equations*, John Wiley, New York.

Gradshteyn, I.S. and I.M. Ryzhik, 1980: *Table of Integrals, Series, and Products*, Corrected and Enlarged Edition., Academic Press, New York.

Haltiner, G.J. and R.K. Williams, 1980: *Numerical Prediction and Dynamic Meteorology*, John Wiley and Sons, New York.

Holton, J.R., 1970: The influence of mean wind shear on the propagation of Kelvin Waves. *Tellus*, *22*, 186-193.

Holton, J.R., 1975: *The Dynamic Meteorology of the Stratosphere and Mesosphere*. Meteor. Monogr., No. 37, Amer. Meteor. Soc..

Holton, J.R., 1979: Equatorial wave-mean flow interaction: A numerical study of the role of latitudinal shear., *J. Atmos. Sci.*, *36*: 1030-1040.

Holton, J.R., 1983: Eddy mean flow interaction diagnostics. In: *Proc of A'ha Huliko'a*, Hawaii winter workshop on the role of eddies in general circulation., pp 87-96.

Holton, J.R. and R.S. Lindzen, 1972: An updated theory for the quasi-biennial cycle of the tropical stratosphere., *J. Atmos. Sci.*, *29*(6):1076-1080.

Hoskins, B.J., 1983: Modelling of the transient eddies and their feedback on the mean flow., In: *Large Scale Dynamical Processes in the Atmosphere.*, B.J. Hoskins and R. Pearce, eds., Academic Press, 169-199.

Issacson, E. and H.B. Keller, 1966: *Analysis of Numerical Methods*, John Wiley and Sons, New York.

Johnson, E.S., 1987: The annual cycle observed during the Hawaii-to-Tahiti Shuttle interpreted as an Equatorial Rossby wave, PhD. Dissertation, Univ. of California, San Diego.

Killworth, P.D., 1979: On the propagation of stable baroclinic Rossby waves through a mean shear flow, *Deep Sea Res.*, *26a*, 997-1031.

LeBlond, P.H. and L. Mysak, 1978: *Waves in the Ocean*, Elsevier Sci. Pub. Co., Amsterdam.

Lindzen, R.S., 1970: Internal equatorial planetary-scale waves in shear flow. *J. Atmos. Sci.*, *27*, 394-407.

Lindzen, R.S., 1971: Equatorial planetary waves in shear: Part I. *J. Atmos. Sci.*, *28*, 609-622.

Lindzen, R.S., 1972: Equatorial planetary waves in shear: Part II. *J. Atmos. Sci.*, *29*, 1452-1463.

Lindzen, R.S. and J.R. Holton, 1968: A theory of the quasi-biennial oscillation., *J. Atmos. Sci.*, *25*(6):1095-1107.

Lindzen, R.S. and K.-Y. Kuo, 1969: A reliable method for the numerical integration of a large class of ordinary and partial differential equations., *Mon. Wea. Rev.*, *97*(10), 732-734.

Lukas, R.B. and E. Firing., 1985: The annual Rossby wave in the central, equatorial undercurrent. *J. Phys. Ocean.*, *15*, 55-67.

McCreary, J.P., 1981: A linear stratified model of the Equatorial Undercurrent. *Phil. Trans. R. Soc. Lond.*, *A302*, 385-413.

McCreary, J.P., 1985: Modeling equatorial ocean circulation. *Ann. Rev. Fluid Mech.*, *17*, 359-409.

McCreary, J.P. and S-Y. Chao, 1985: Three-dimensional shelf circulation along an eastern ocean boundary, *J. Mar. Res.*, *43*, 13-36.

McIntyre, M.E. and T.G. Shepard, 1987: An exact local conservation theorem for finite amplitude disturbances to non-parallel shear flows, with remarks on Hamiltonian structure and on Arnol'd's stability theorem., *J. Fluid Mech.*, *181*, 527-565.

McPhaden, M.J. and R.A. Knox, 1979: Equatorial Kelvin and inertio-gravity waves in zonal shear flow. *J. Phys. Ocean.*, *9*, 263-277.

McPhaden, M.J., J.A. Proehl and L.M. Rothstein, 1986: The interaction of equatorial Kelvin waves with realistically sheared zonal currents. *J. Phys. Ocean.*, *16*(9), 1499-1515.

McPhaden, M.J., J.A. Proehl and L.M. Rothstein, 1987: Note on the structure of equatorial waves. *J. Phys. Ocean.*, *17*(9), 1555-1559.

Meyers, G., 1979: Annual variation in the slope of the 14°C isotherm along the equator in the Pacific Ocean. *J. Phys. Ocean.*, *9*(5), 885-891.

Moore, D.W. and S.G.H. Philander, 1977: Modelling of the tropical ocean circulation. In: *The Sea*, v*6*, 319-361. New York: Wiley-Interscience.

Philander, S.G.H., 1979: Equatorial waves in the presence of the equatorial undercurrent. *J. Phys. Ocean.*, *9*, 254-262.

Proehl, J.A., M.J. McPhaden and L.M. Rothstein, 1986: A numerical approach to equatorial oceanic wave-mean flow interactions, In: *Advanced Physical Oceanographic Numerical Modelling*, J.J. O'Brien, Ed., NATO ASI Series, Series C: Math. and Phys. Sci. v186, D. Reidel Co., Dordrecht, Holland, 1986, 111-126.

Rhines, P.B. and Holland, W.R., 1979: A theoretical discussion of eddy-driven mean flows., *Dyn. Atmos. and Oceans.*, *3*, 289-325.

Ripa, P. and S.G. Marinone, 1983: The effect of zonal currents on equatorial waves., In: *Hydrodynamics of the Equatorial Ocean.*, C.J.C Nihoul, ed, Elsevier Science, pp 291-317.

Rothstein, L.M., M.J. McPhaden and J.A. Proehl, 1988: Wind forced wave-mean flow interactions in the equatorial waveguide: I. The Kelvin wave., In press, *J. Phys. Ocean.*

Schopf, P.S., D.L.T. Anderson and R. Smith., 1981: Beta dispersion of low frequency Rossby waves., *Dyn. Atmos. and Oceans.*, *5*, 187-214.

Varga, R.S., 1962: *Matrix Iterative Analysis*, Prentice-Hall, Englewood Cliffs, New Jersey.

## Appendix A: Numerical Considerations:

### A.1 - Methodology

A large variety of methods have been developed for the numerical solution of elliptic partial differential equations (see Birkhoff, 1972). Finite difference, finite element and spectral methods have all been employed with success. The three approaches differ in their basic philosophy. The finite difference methods replace the continuous differential equation with a discrete finite difference equation on a fixed grid. The finite element methods seek solution by reformulating the partial differential equation as a variational principle. While the spectral methods expand the unknown solutions in terms of a predetermined set of basis functions and employ the orthogonality relations of this set. All of these methods result in an algebraic system of equations. For certain choices of the basis set (spectral) and the minimization scheme (finite element) the three approaches can be made to be equivalent at discrete grid points. For rectangular domains which are used herein, the finite difference approach is the simplest to program and yet yields sufficiently accurate results. In addition, in the presence of strong shears, the possibility of wave scattering and strong deformation of the wave structures make spectral methods less useful in that a large number of terms may be required in the series to give accurate results. The finite element methods, while powerful in many problems, are too cumbersome for this study. The considerable effort required to generate the finite element grids would likely need to be repeated for each flow configuration. For the range

of flows used here this would be prohibitive. Consequently, we chose a finite difference approach.

The finite difference methods employed on elliptic partial differential equations are generally one of two types, iterative or direct. The iterative methods attempt to find solutions by successive correction of an initial "guess" until a sufficiently accurate solution is obtained. This is done by solving the finite difference equation for the dependent variable at a point in terms of its surrounding values. Then at each iteration a new value for the solution at this point is found from the old values at the surrounding ones. The iterative methods are simpler to program and in many problems are faster and more accurate than direct methods. However, this usually cannot be shown *a priori*. For coefficient matrices which are diagonally dominant, which is usually the case for elliptic problems, iterative methods, such as Successive Over-Relaxation (SOR), are guaranteed to converge to the correct solution. In contrast, the direct methods attempt to solve the linear system through a matrix reduction of the coefficient matrix or the calculation of its inverse. These methods usually take advantage of the sparseness and form of the coefficient matrix to reduce to upper triangular form, whereupon the solution is obtained by backsubstitution. For a direct method to be useful for problems of any size, the method must take full advantage of the sparseness of the matrix. For example, classical Gaussian elimination cannot be used for most problems due to excessive storage requirements for the coefficients and the accumulation of large roundoff error due to the large operations count. For a detailed

discussion of both iterative and direct methods see Forsythe and Wasow (1960), Varga (1962), Issacson and Keller (1966) or Dorr (1970). For application to atmospheric problems see Haltiner and Williams (1980). For the present problem, the coefficient matrix is not diagonally dominant due to the presence of the cross-derivative term in (2.9). Therefore, convergence of iterative methods, though still possible, is not assured. Some effort was expended investigating the use of the Gauss-Seidel, Alternating Direction Implicit (ADI) and SOR iterative methods with little success. More sophisticated iterative techniques were not considered. As a result of these failures, we concentrated on the use of direct methods to solve the difference equation problems.

In order to understand the procedure it is essential to consider the form of the coefficient matrix. Therefore we begin by discretizing the domain in y and z such that

$$y_i = (i-\tfrac{1}{2})\delta y \qquad i = 1,2,3,\ldots,NY \qquad \text{(A.1)},$$

$$z_j = j\delta z \qquad j = 1,2,3,\ldots,NZ \qquad \text{(A.2)}$$

and expand (2.9) using centered differences into finite difference form. The centered difference expansion employs "nearest neighbor" points and neglects terms in the Taylor series proportional to $\delta y^2$ and $\delta z^2$. Therefore the resulting expressions are accurate to second order in the stepsize. The $\frac{1}{2}\delta y$ shift in the y discretization allows for the simple expression of the meridional gradient of pressure at the equator which arises from the symmetry condition there. For antisymmetric wave modes this shift is eliminated and p is set to zero at the equator. Due to the presence of the cross-derivative term, $p_{yz}$ , the centered differences require the following nine point stencil to evaluate:

$$
\begin{array}{lccc}
\uparrow & p_{i-1,j+1} & p_{i,j+1} & p_{i+1,j+1} \\
z & p_{i-1,j} & p_{i,j} & p_{i+1,j} \\
 & p_{i-1,j-1} & p_{i,j-1} & p_{i+1,j-1} \\
 & & y \rightarrow &
\end{array}
$$

Evaluating for every grid point leads to NY·NZ equations for the pressure at the NY·NZ grid points. To construct the coefficient matrix in the most compact form which conserves symmetry, a linear mapping is performed with a new index, L, defined through

$$L = NY\cdot(j-1) + i \quad \text{for} \begin{cases} i=1,2,3,\ldots,NY \\ j=1,2,3,\ldots,NZ \end{cases} \qquad (A.3).$$

This mapping was chosen since, in general, NY is much less than NZ and therefore the bandwidth of the resulting coefficient matrix is minimized. This is important because the operations count and memory requirements are strongly related to the bandwidth of this matrix. Consequently, for grid point i,j (⇒L) away from boundary points, the finite difference equation can be written in the form

$$\begin{aligned} &Q_L p_{L-NY-1} + R_L p_{L-NY} - Q_L p_{L-NY+1} + S_L p_{L-1} + T_L p_L + U_L p_{L+1} \\ &\qquad - Q_L p_{L+NY-1} + V_L p_{L+NY} + Q_L p_{L+NY+1} = [\text{Forcing}]_L \end{aligned} \qquad (A.4)$$

From this it can be seen that the finite difference problem is a traditional linear matrix equation, $\tilde{\tilde{A}}\vec{X} = \vec{B}$, where $\tilde{\tilde{A}}$ is the coefficient matrix, $\vec{X}$ the solution vector containing the pressure at the grid points, and $\vec{B}$ the vector containing boundary conditions and any internal forcing terms. Furthermore, the coefficient matrix is seen to be of block (or banded)-tridiagonal form with bandwidth 2(NY+1). The bandwidth is here defined as the number elements between the first and

last nonzero element, inclusively, on any row of the coefficient matrix. Perhaps the simplest way of visualizing the coefficient matrix is as a square tridiagonal matrix of order NZ whose elements are square tridiagonal matrices of order NY. The matrix in symbolic form is:

$$\approx{A} = \begin{bmatrix} \approx{C}_1 & \approx{D}_1 & 0 & . & 0 \\ \approx{B}_2 & \approx{C}_2 & \approx{D}_2 & 0 & . \\ 0 & . & . & . & 0 \\ . & 0 & \approx{B}_{NZ-1} & \approx{C}_{NZ-1} & \approx{D}_{NZ-1} \\ 0 & . & 0 & \approx{B}_{NZ} & \approx{C}_{NZ} \end{bmatrix} = \left[\approx{B}_j, \approx{C}_j, \approx{D}_j\right] \qquad (A.5)$$

Employing the compact notation on the extreme right-hand side (and ignoring the boundary conditions and forcing for illustration), the tridiagonal matrices $\approx{B}_j$, $\approx{C}_j$ and $\approx{D}_j$ are then, in terms of the coefficients of (A.4), given by

$$\begin{aligned} \approx{B}_j &= [Q_i, R_i, -Q_i]\big|_j \\ \approx{C}_j &= [S_i, T_i, U_i]\big|_j \\ \approx{D}_j &= [-Q_i, V_i, Q_i]\big|_j \end{aligned} \qquad (A.6)$$

where i and j refer to the y and z dependent grid positions, respectively.

It is just the above form which lends itself to efficient solution by direct methods. The approach that we have chosen was used successfully by McCreary and Chao (1985) in their study of trapped waves on the continental shelf and they supplied us with the code for their solver. The procedure is essentially a Gaussian elimination with operations only performed for the nonzero band of elements of the

coefficient matrix. This reduces the operations count from $NY^3NZ^3/3$ of the classical elimination to $NY^3NZ$ and the memory requirements from $NY^2NZ^2$ to $2NY^2NZ$. Operationally, passes are made through the matrix eliminating sub-diagonal elements. This can be done efficiently by using knowledge of the form of the coefficient matrix. Since this is a banded matrix, elimination can only generate non-zero elements within the original bandwidth centered on the main diagonal. This is what allows for the memory savings and demonstrates why the minimization of the bandwidth of the coefficient matrix is essential. Following this elimination sweep, the solution is found through backsubstitution.

Another direct method which has been used on problems of this type is the block reduction (Isaacson and Keller, 1966; Lindzen and Kuo, 1969). This method uses a generalization of the tridiagonal matrix solver (or two pass method) on the matrix form of the coefficient matrix (A.5). While this method requires a similar number of operations, the drawback is that it requires NZ matrix inversions of linear combinations of the $\tilde{\tilde{B}}_j$ and $\tilde{\tilde{C}}_j$ matrices (which are of order NY) for a variable coefficient problem. These inverses could in principle be stored but the overhead can become enormous. The real power of this method arises when one is interested in solving a partial differential equation many times subject to different forcing functions. In this case, the first pass where the inverses are computed, need be done only once and the inverses saved. The second pass is then performed for each forcing function to obtain a solution. For this study, the interest is in varying the background fields which results in a new differential equation and thus this savings would not be realized.

## A.2 Accuracy

The first step in the solution of a partial differential equation by finite differences is to demonstrate that the finite difference equation represents a consistent approximation to the desired partial differential equation. To prove numerical consistency, one must show that the truncation error of the finite difference equation approaches zero as the stepsizes tend to zero. The truncation error is found by subtracting the finite difference equation (A.4) from the partial differential equation (2.9) and is given in the present problem by

$$\tau = \frac{\delta y^2}{6}\left[\tfrac{1}{2}\frac{\partial}{\partial y}+A\frac{\partial}{\partial z}+C\right]\frac{\partial^3 p}{\partial y^3} + \frac{\delta z^2}{6}\left[\tfrac{1}{2}A\frac{\partial}{\partial y}+B\frac{\partial}{\partial z}+D\right]\frac{\partial^3 p}{\partial z^3} + O(\delta y^3,\delta z^3) \quad (A.7).$$

Taking the limit of small stepsizes, one can show that the truncation error tends to zero for all choices of $\delta y$ and $\delta z$. Therefore the method is unconditionally consistent for this governing equation. The truncation error is also useful in that it can be shown that the error bound of the finite difference approximation is proportional to $\tau$ (Issacson and Keller, 1966). Therefore this illustrates that the method used here is second order accurate in the stepsizes.

In order to address the actual accuracy of the numerical method we first perform test cases. These cases are quite limited in applicability to the final model due to the dearth of analytical solutions in the presence of flow sheared in both y and z. Clearly the first step is to study the scheme in the absence of mean flow for which the analytic solutions are known. To this end, we first solve the finite difference equation, (A.4), for U=0 in an ocean of 1000m depth which extends to

20°N. The case we chose was for the 1st meridional, 3rd vertical mode Rossby wave whose analytic phase speed is -35.3 cm/s. This mode was chosen because it represents the highest order meridional and vertical mode that we anticipate investigating directly and therefore has the most stringent resolution requirements. The accuracy was tested for this case by varying both the vertical and meridional resolution and comparing the numerical solution to the analytic.

The results of this comparison is presented in Table A.1. As we can see, the results are essentially independent of the chosen vertical resolutions. For this parameter set this is not surprising. For a third vertical mode wave in the absence of flow, the analytic vertical wavelength is 666.6m. Therefore, the minimum resolution used represents 66.6 grid points per wavelength. This is much more than sufficient to resolve the wave in the vertical. However, unlike the vertical, the accuracy for the meridional direction was dependent upon the resolution. We see from Table A.1, that the accuracy in the rms sense doubles by changing the resolution to 40 points from 30, with a less substantial increase occurring from 40 to 50 points. For this case the equatorial decay scale, $\sqrt{c/\beta}$, is 124.4km and the turning latitude, which is (2m+1) times the decay scale, is 373.3km. This translates to 5.6 grid points within the equatorial turning latitude for the lowest resolution, 7.5 for the medium case and 9.3 for the highest. While these numbers seem small, recall that we are using symmetry to solve for only half the domain. Also recall that the first meridional mode Rossby wave goes through one oscillation between the two turning latitudes. Therefore, a reasonable estimate for the latitudinal

TABLE A.1: Accuracy of the finite difference solution for the m=1 Rossby wave for U=0 as a function of grid spacing. Results are quoted as the percent of the wave amplitude.

| | Maximum Difference NY | | | RMS Difference NY | | |
|---|---|---|---|---|---|---|
| NZ | 30 | 40 | 50 | 30 | 40 | 50 |
| 101 | 8.05 | 4.86 | 3.14 | 0.70 | 0.35 | 0.28 |
| 131 | 7.95 | 4.85 | 3.13 | 0.69 | 0.35 | 0.28 |
| 161 | 7.94 | 4.85 | 3.13 | 0.69 | 0.35 | 0.28 |
| 201 | 7.96 | 4.82 | 3.13 | 0.69 | 0.35 | 0.28 |

wavelength of the first meridional mode is twice the turning latitude. This translates to roughly 11.6 grid points per latitudinal wavelength for the lowest resolution, 15.0 for the medium and 18.6 for the highest. One can see from these numbers that the three latitudinal resolutions do represent a significant change in the number of grid points per wavelength.

However, there is some reason to believe that the vertical resolution requirements may be more extreme in the presence of flow and variations in $N^2$. The WKBJ analysis suggests that wave scales will decrease in the presence of westward flow. In addition, non-WKBJ effects such as scattering and critical layer processes point to a need for higher vertical resolution. As discussed in Proehl *et al.* (1986), the critical layers which are parameterized through Rayleigh friction possess a finite thickness which can be estimated by simple arguments. In the present model, due to the assumption of Rayleigh friction, the critical layer is the region around the critical surface (where $c=U_0$) in which friction is important. Therefore, the total thickness of this layer is determined by the distance away from the critical surface at which friction fails to be of crucial importance in the momentum balance. From inspection of the partial differential equation (2.9) the friction only enters in through the coefficient E in the form $(c-U_0+\iota\kappa/k)^{-1}$. Therefore frictional damping is strongly enhanced where $c=U_0$, ie. around the critical surface. An estimate of the thickness of the frictional layer can then be defined as twice the distance from the critical surface to the point at which $|\iota\kappa/k|=|c-U_0|$. Performing a power series expansion of the background flow about $U_0=c$ gives

estimates of

$$\delta y_{crit} = \frac{2\kappa U_0}{\sigma \partial_y U_0} \quad \text{and} \quad \delta z_{crit} = \frac{2\kappa U_0}{\sigma \partial_z U_0} \tag{A.8}$$

for the thickness of the critical layer in the horizontal and vertical directions. For the current scales $L_0$=100km and $H_0$=100m at the annual frequency and zonal wavenumber of the resting state third vertical mode these thicknesses are of order 20km and 20m, respectively. Because the waves are forced at the surface and propagate downward, the results of Holton (1970) suggest that the vertical scale of the critical layer is the more important scale to resolve in the numerical model. Therefore, we expect that the $\delta z$ needed for accurate solution is less than 10m.

Unfortunately, for the types of flow that are geophysically relevant, no analytic solutions exist to test the accuracy of the method. As a result, we developed two consistency checks to assure numerical accuracy of the derived pressure fields. Once the numerical pressure field is known, one computes the dynamic variables u,v,w and $\rho$ from the expressions (2.4-2.6 and 2.8). It is important to note that to derive these relations no use is made of the continuity equation (2.7). Consequently, one important requirement of the numerical solution is that it satisfy continuity. If so, then the solution is an accurate solution of the desired partial differential equation (2.9). Therefore, in all cases we perform this continuity test to assure numerical accuracy. This check is tantamount to backsubstitution into the original partial differential equation. For comparison to the actual accuracy given above, the case of no flow was subjected to the consistency check just described and the results are presented in Table

A.2 under the heading 'Residual Volume'.

The second, closely related, test arises from the use of the energy conservation equation, 2.15. As with continuity, we obtain u, v, w and $\rho$ and calculate the residual. While this is not a totally independent check on accuracy, it is a required characteristic of the numerical solution. In addition, it does give a measure of how well we can approximate the total energy balance of the wave field. This is mentioned because the energy budgets for the waves are of interest and we wish to confirm both that the numerical scheme conserves mass and energy and that the solution is sufficiently accurate to give a meaningful result. The results for this check are presented in Table A.2 under the heading 'Residual Energy'.

As with the accuracy analysis, the two consistency checks show that accuracy is essentially unaffected by vertical resolution and significantly increased by increasing meridional resolution from 30 to 40 points with a less substantial increase occurring for the increase to 50 points. These results give confidence in the use of these consistency checks as proxies for direct accuracy calculations.

While these consistency checks give us confidence in the solution accuracy, in practice the resolution they predict is not entirely sufficient for our purposes. The reason for this is that not all the terms that we are interested in the energy budget are of equal magnitude. In fact, what we find is that for most cases the input of energy due to pressure work at the surface is in near balance with the frictional dissipation. Consequently, the energy exchanges with the mean flow, which are of interest, are often an order of magnitude

TABLE A.2: Consistency check of accuracy of the finite difference solution for the m=1 Rossby wave for U=0 as a function of grid spacing. Results are quoted as the percent of the amplitude of the dominant terms in the budget.

| | Residual Volume | | | Residual Energy | | |
|---|---|---|---|---|---|---|
| | NY | | | NY | | |
| NZ | 30 | 40 | 50 | 30 | 40 | 50 |
| 101 | 4.31 | 2.91 | 2.22 | 1.27 | 0.82 | 0.62 |
| 131 | 4.58 | 2.49 | 1.80 | 1.53 | 0.88 | 0.68 |
| 161 | 4.29 | 2.26 | 1.59 | 1.62 | 0.91 | 0.70 |
| 201 | 4.13 | 2.12 | 1.44 | 1.32 | 0.96 | 0.72 |

smaller than these dominant terms. So a residual of 1-2% of the dominant terms becomes 10-20% for the mean flow exchange terms. This is enough to introduce questions about the significance of the energy exchanges. We found that increasing the meridional resolution to 80 points over 20° latitude was enough to reduce the residual energy term to at worst O(5%) of the exchange terms. It is noteworthy that in doing this, the values of the mean flow exchange terms changed very little. Rather the increased resolution primarily caused the dominant terms to change to reduce the residual so that it represented a smaller fraction of the weaker terms. In other words, the lower resolution was in fact doing very well at estimating the exchanges of energy between the waves and the mean flow. For best results, however, the resolution of 80 points meridionally was used throughout.

Appendix B: Realistic Flow Results - Velocity Fields:

Discussion in the main body of this dissertation was entirely based upon changes to the perturbation pressure fields. Pressure was chosen because it was solved for directly and, therefore, was most accurately obtained numerically. However, in order to allow for comparison with observations, the perturbation flow fields (u, v and w; which are calculated from the pressure solutions) for the realistic flow configuration of section 5.3 are presented here. These results (which are consistent with the pressure results) are not discussed and are presented for the interested reader only. The figures are ordered as follows:

| Figure | Description |
|---|---|
| B.1a-c | u,v,w for 1st vertical mode for resting ocean |
| B.2a-c | u,v,w for 1st resonance in realistic EUC/SEC flow |
| B.3a-c | u,v,w for 2nd vertical mode for resting ocean |
| B.4a-c | u,v,w for 2nd resonance in realistic EUC/SEC flow |
| B.5a-c | u,v,w for 3rd vertical mode for resting ocean |
| B.6a-c | u,v,w for 3rd resonance in realistic EUC/SEC flow |

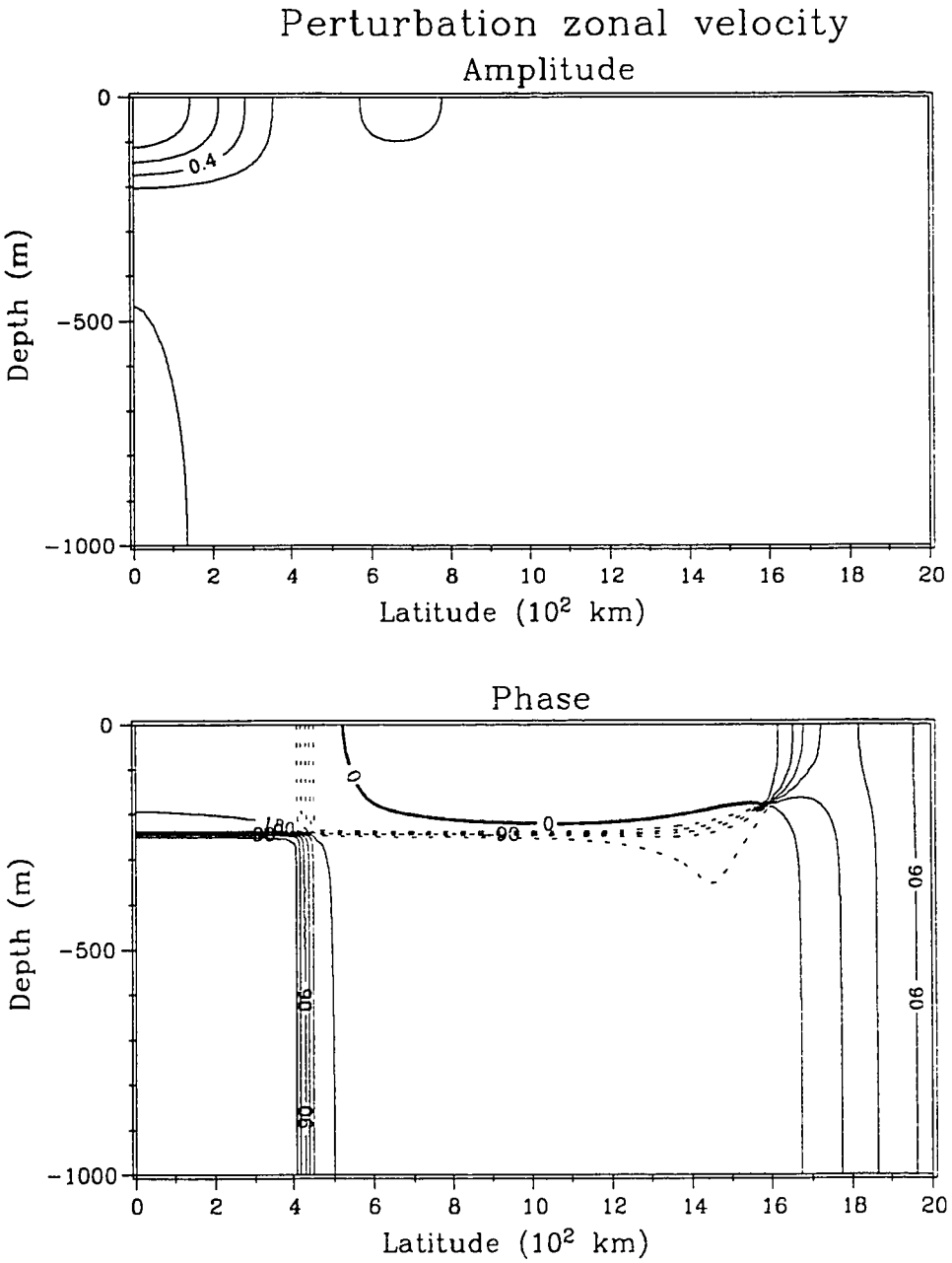


**Figure B.1a: Perturbation zonal velocity for the 1st vertical mode in resting ocean.**

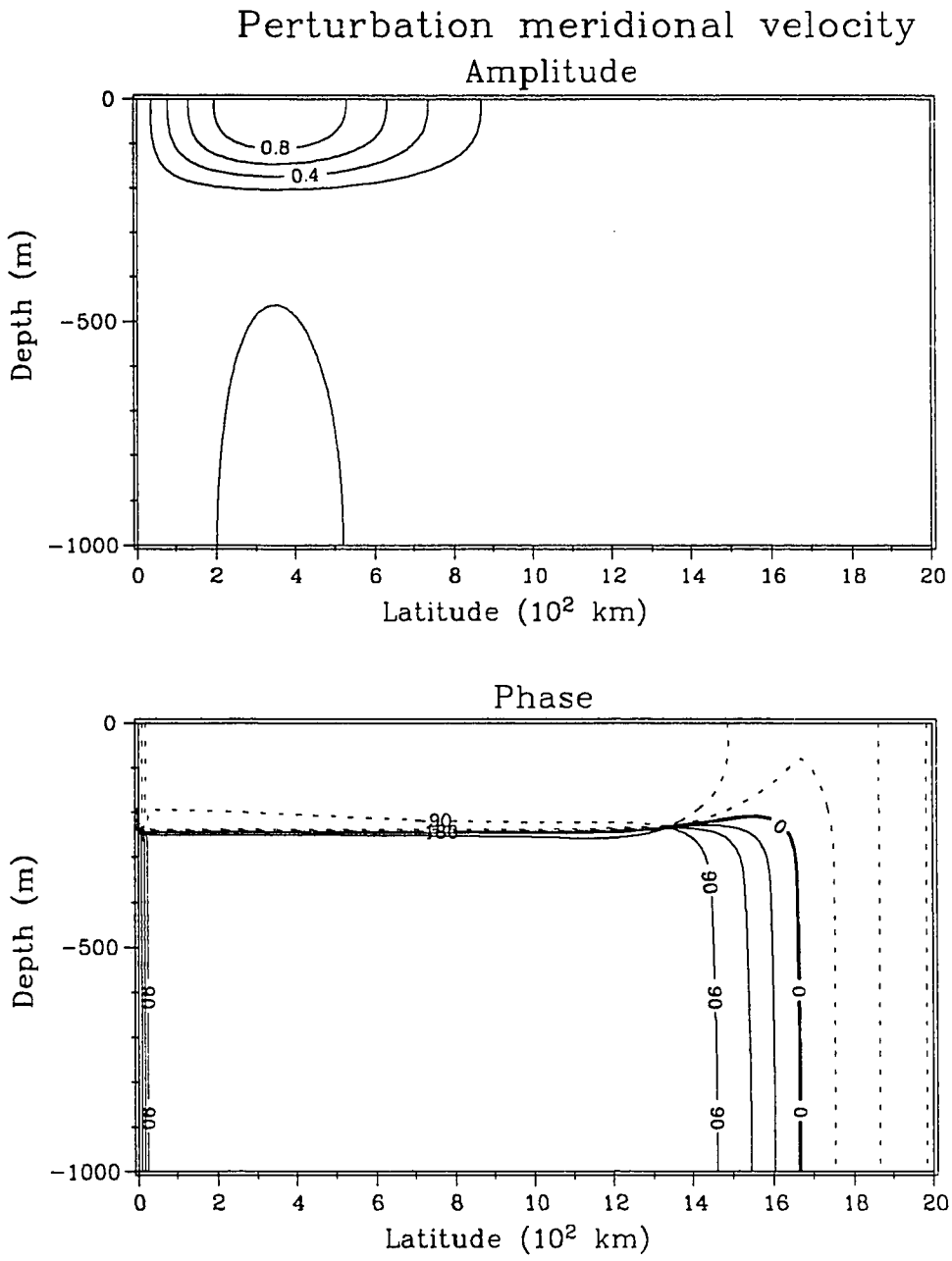


**Figure B.1b: Same as B.1a except for meridional velocity**

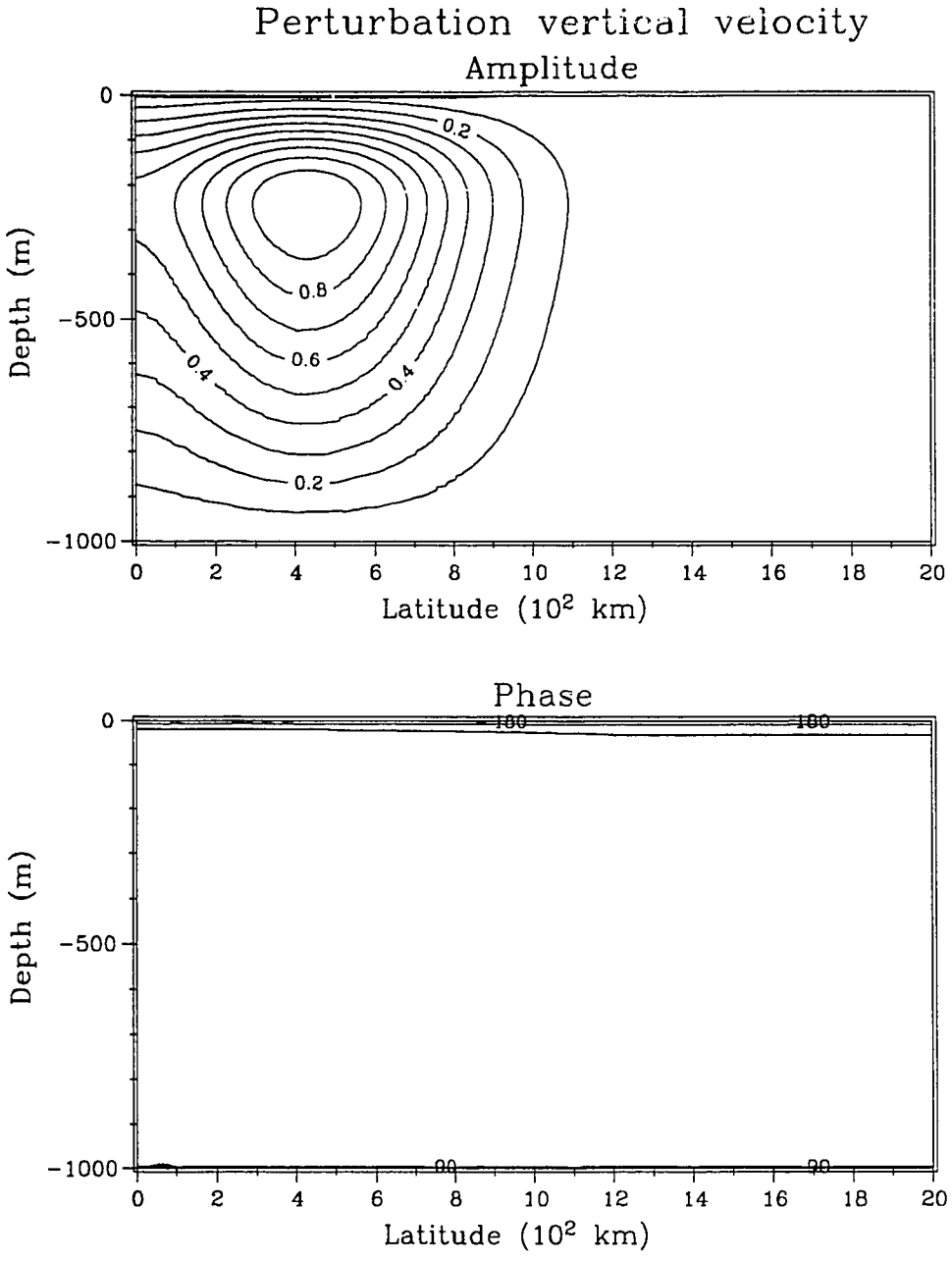


**Figure B.1c: Same as B.1a except for vertical velocity**

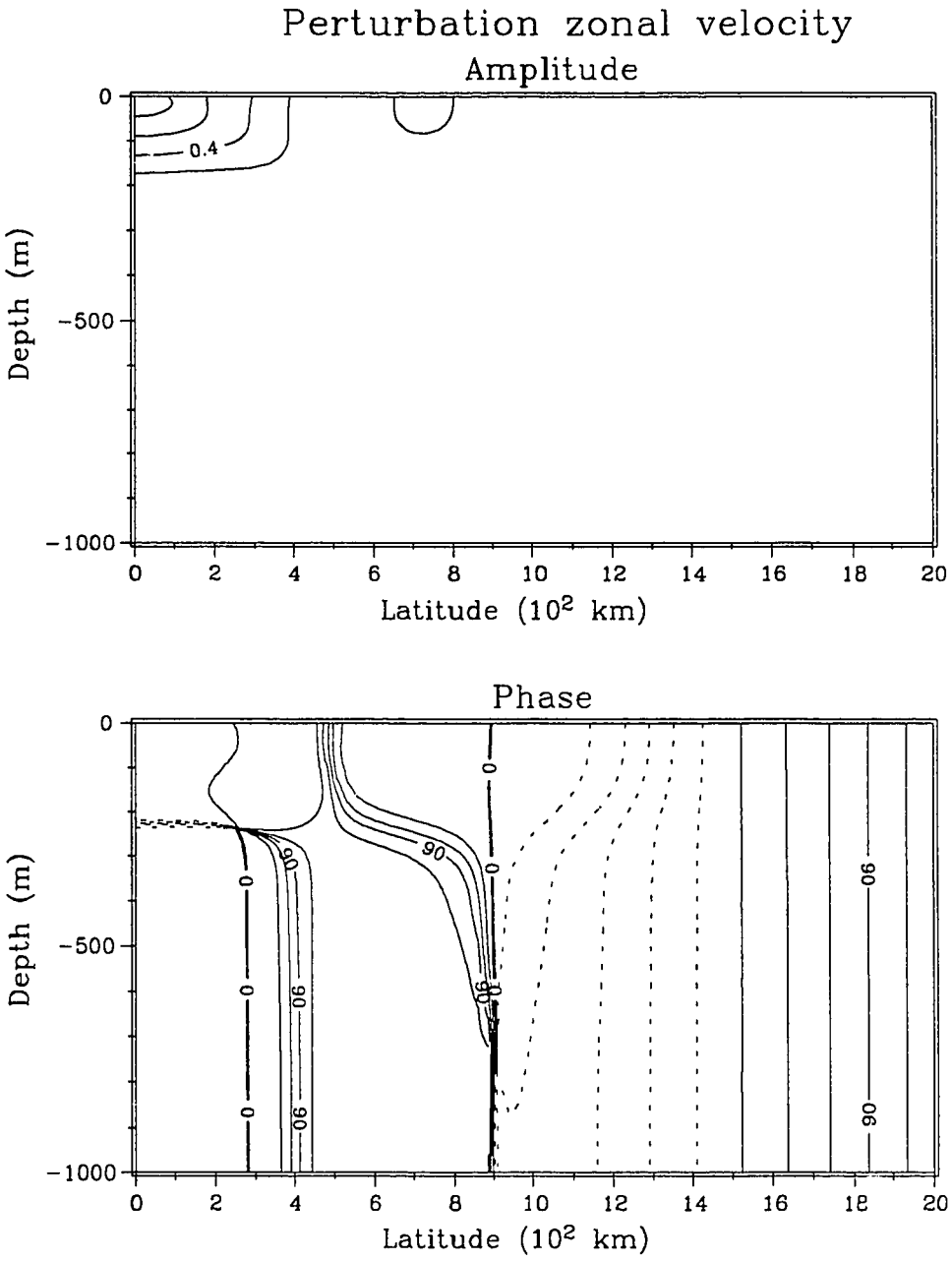


Figure B.2a: Perturbation zonal velocity for the 1st resonance in the realistic simulation of Undercurrent and South Equatorial Current.

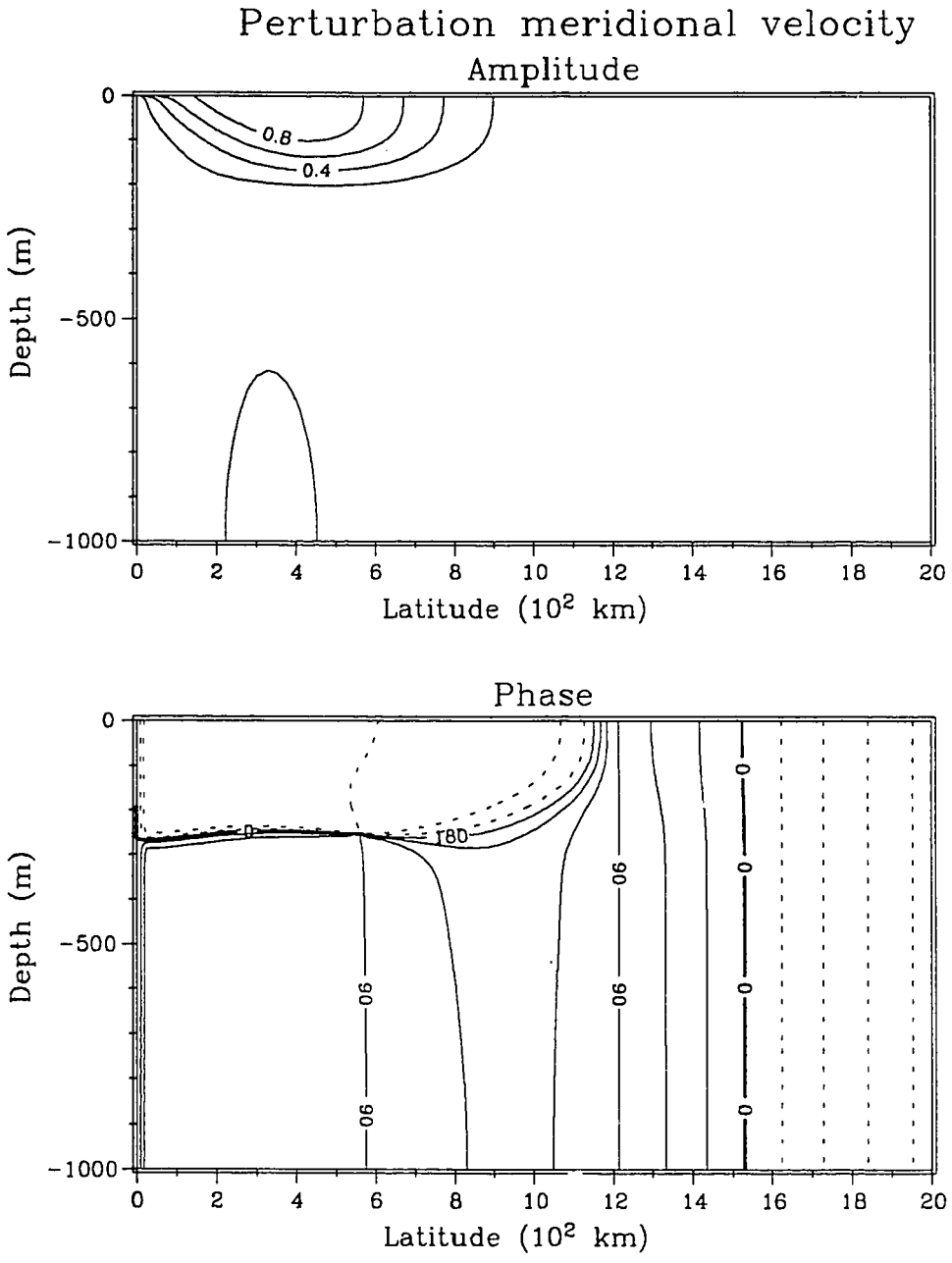


**Figure B.2b: Same as B.2a except for meridional velocity**

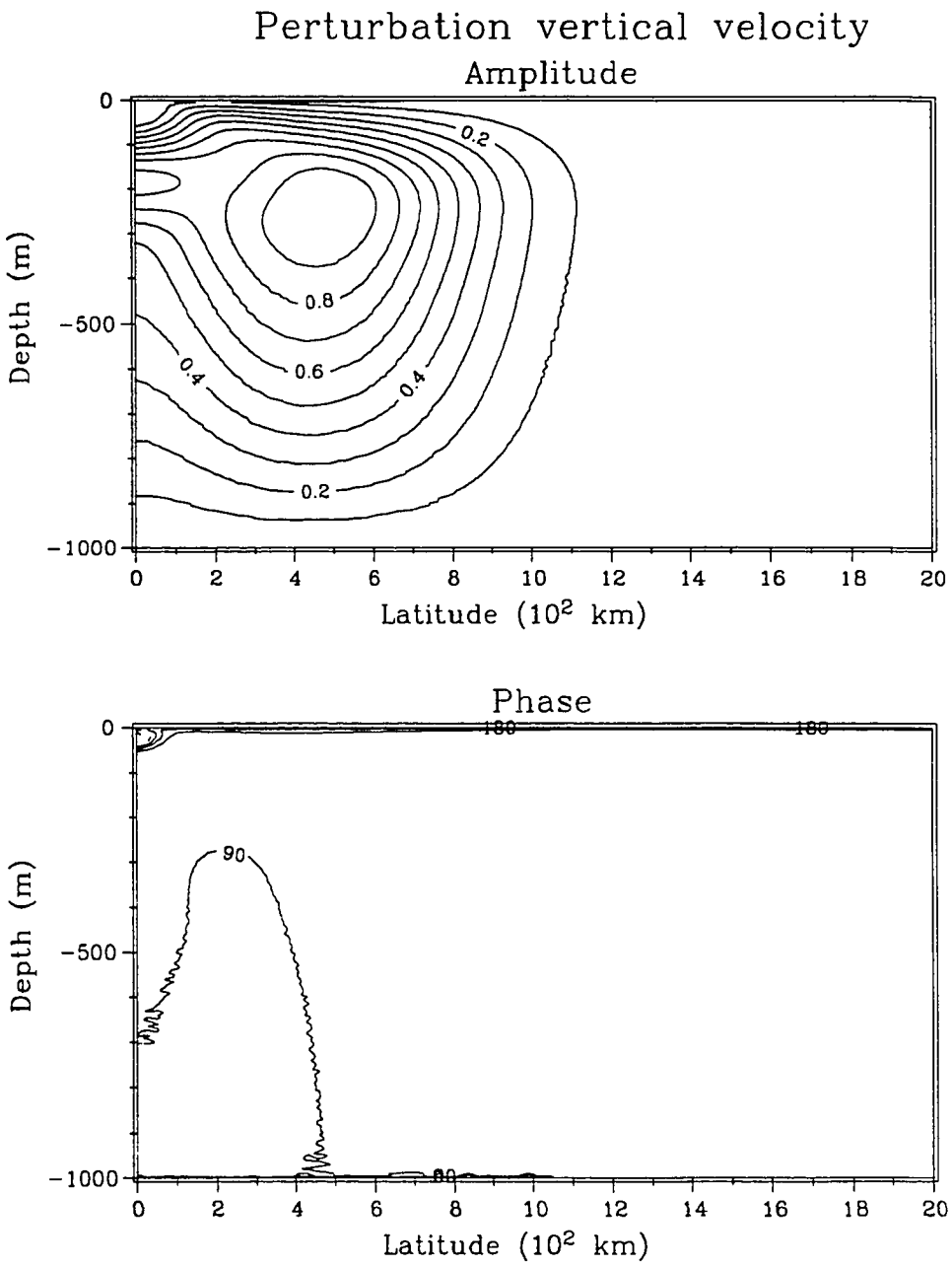


**Figure B.2c: Same as B.2a except for vertical velocity**

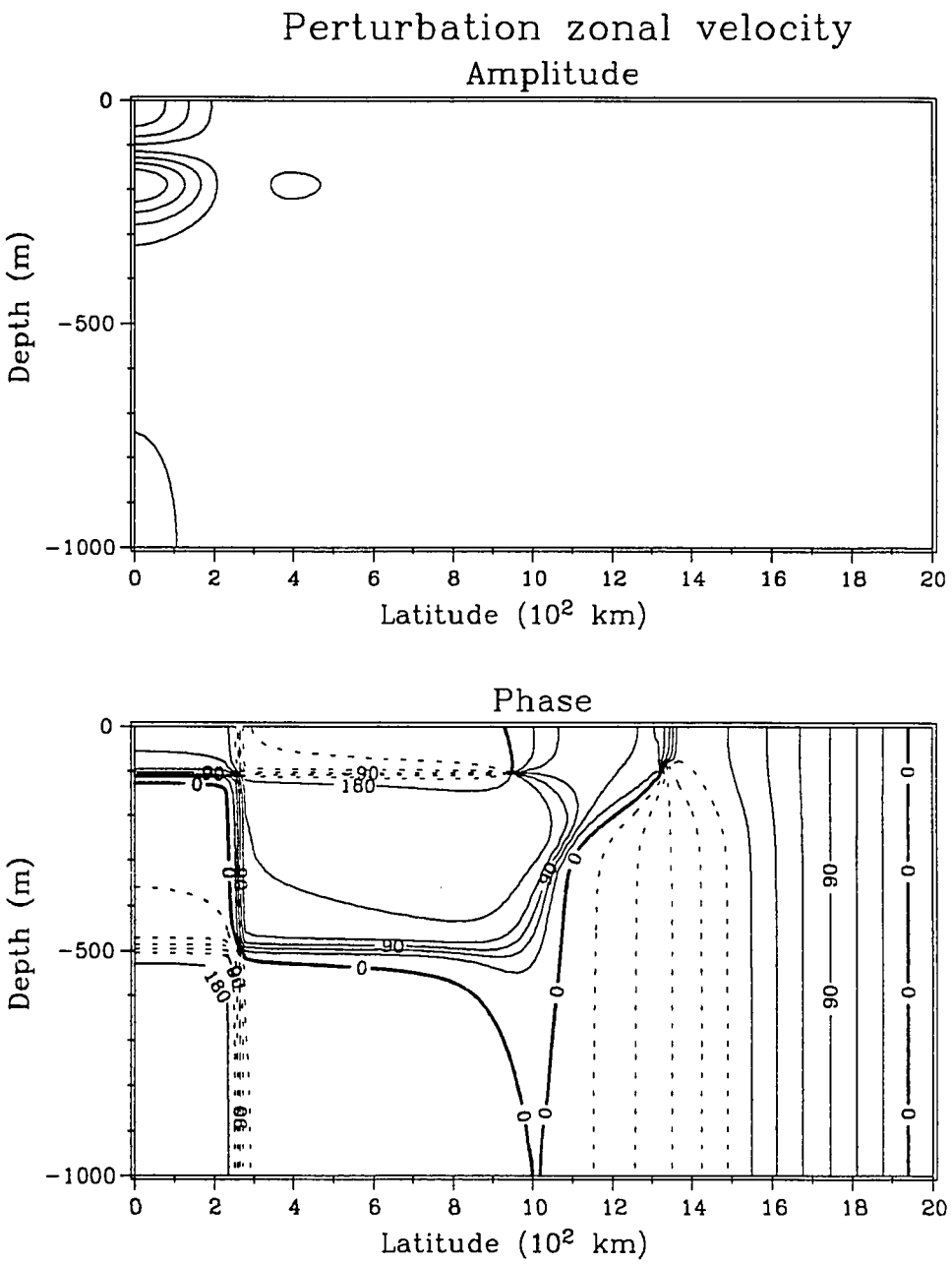


Figure B.3a: Perturbation zonal velocity for the 2nd vertical mode in resting ocean.

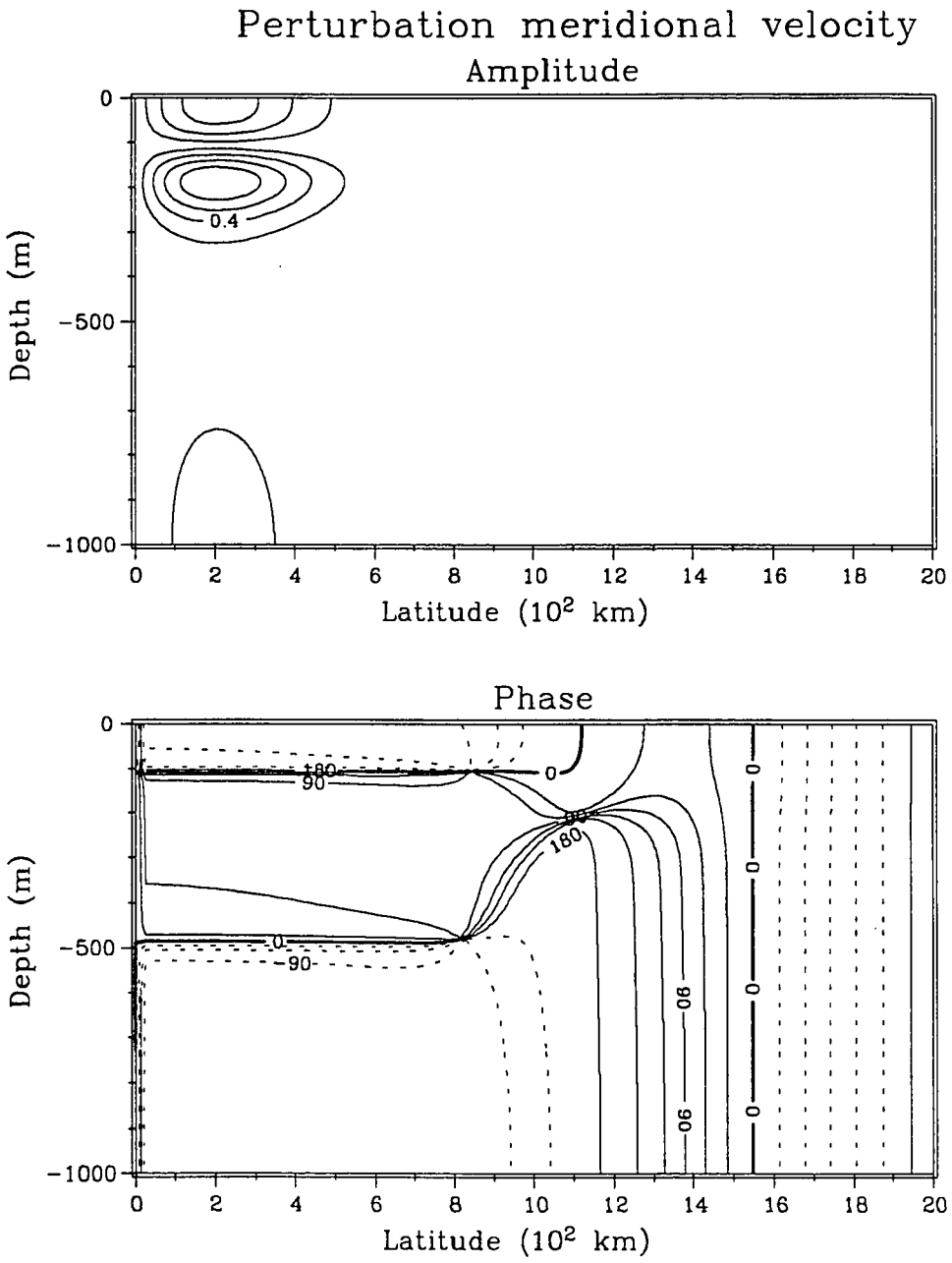


**Figure B.3b: Same as B.3a except for meridional velocity**

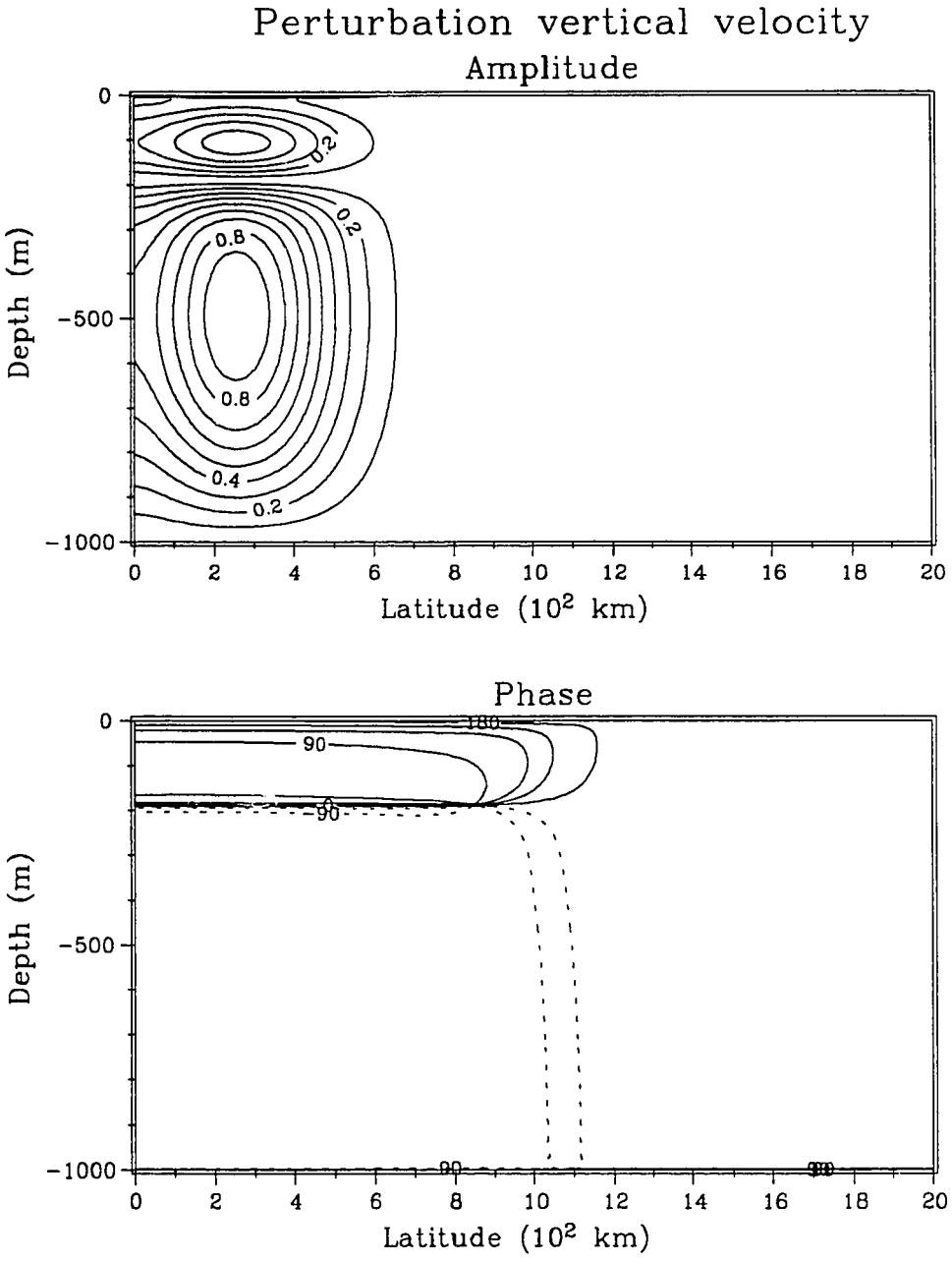


Figure B.3c: Same as B.3a except for vertical velocity

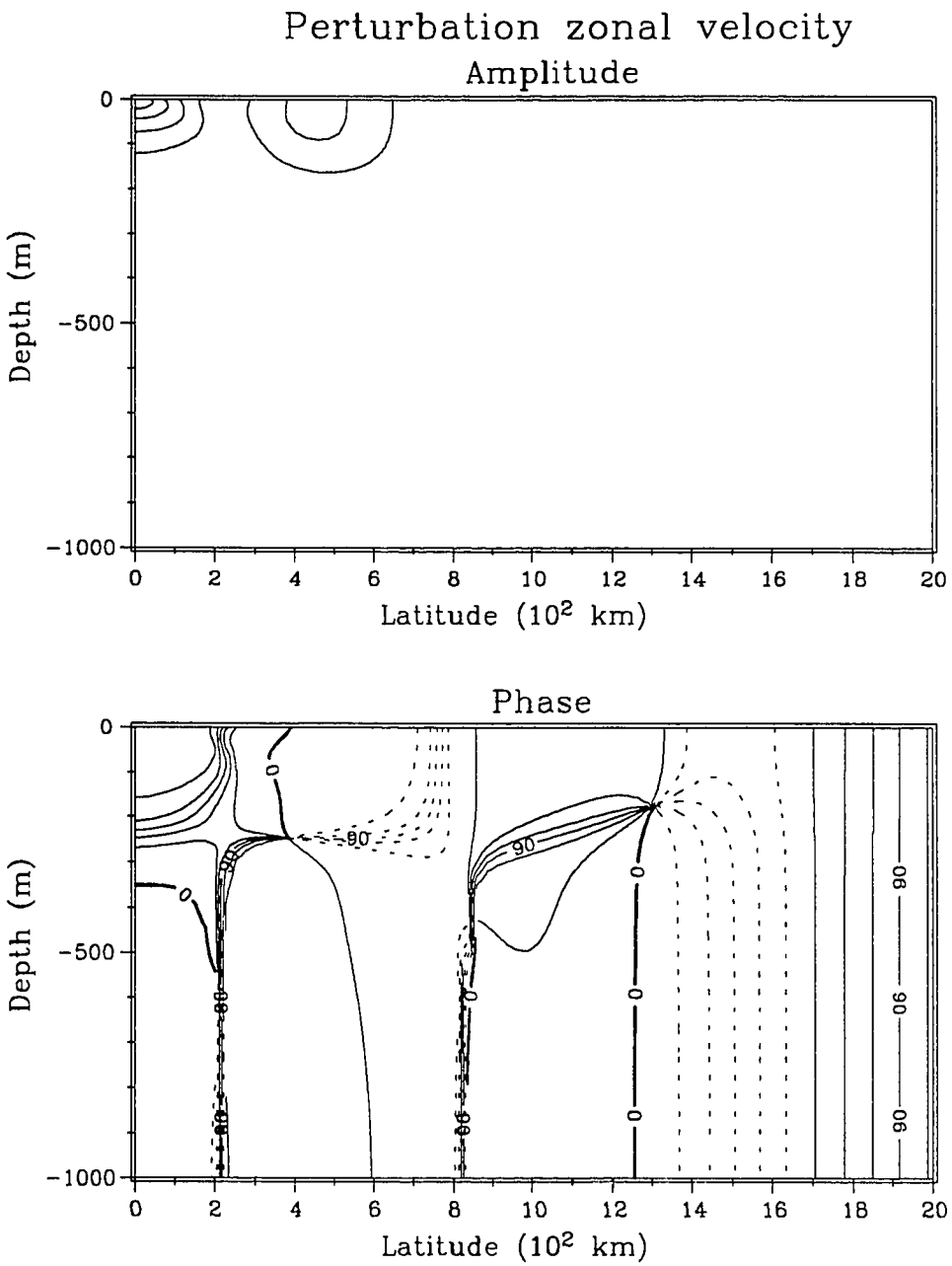


Figure B.4a: Perturbation zonal velocity for the 2nd resonance in the realistic simulation of Undercurrent and South Equatorial Current.

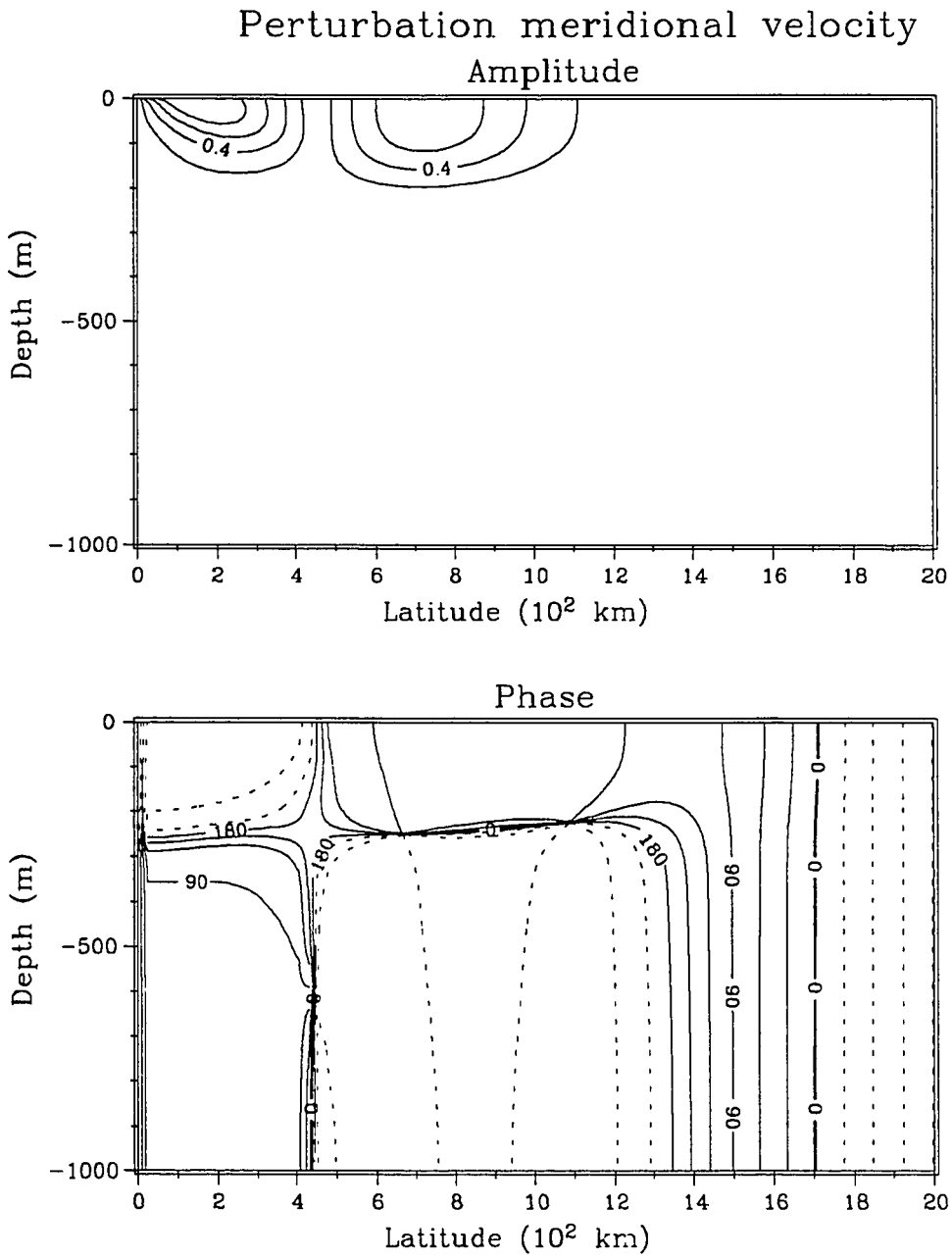


**Figure B.4b: Same as B.4a except for meridional velocity**

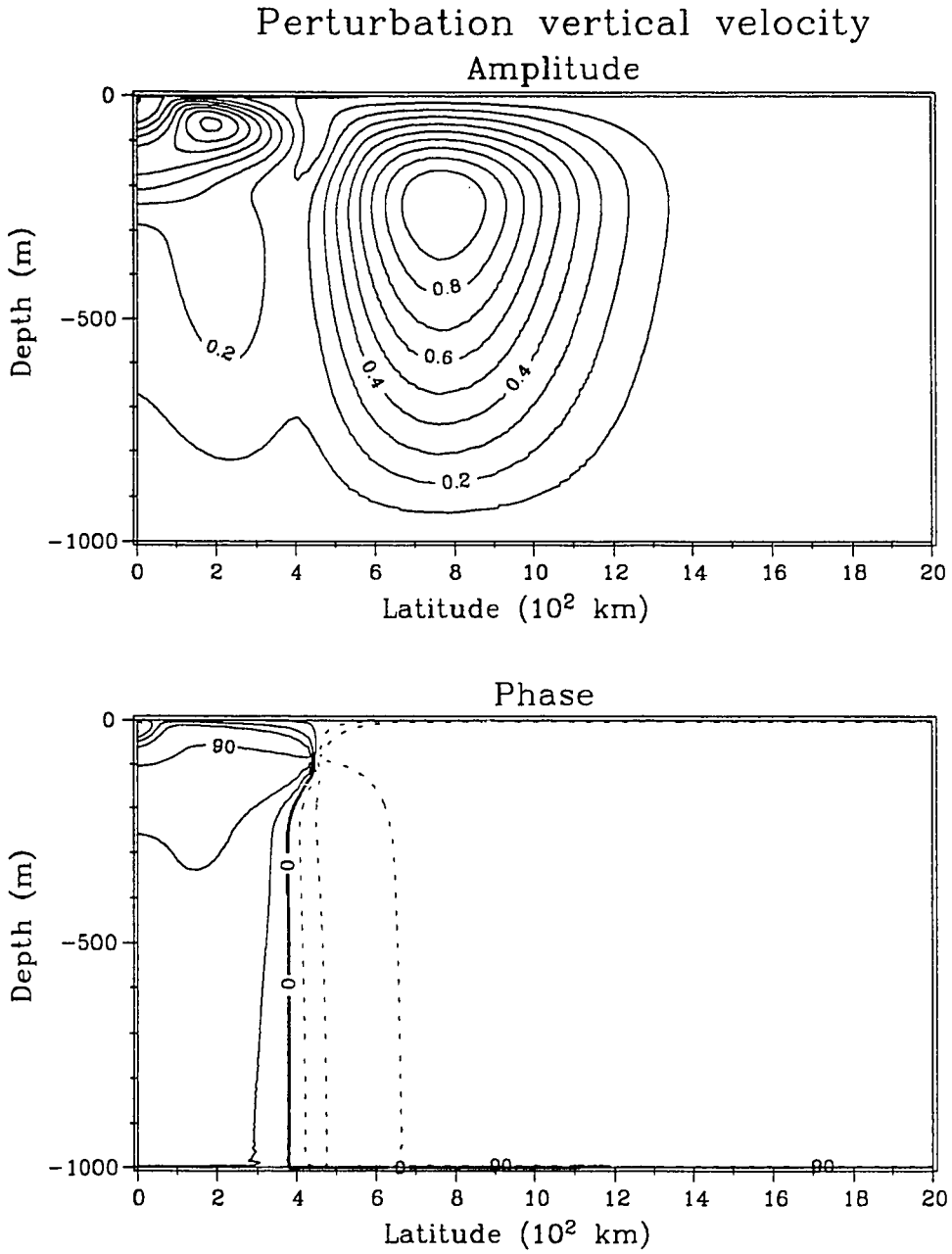


Figure B.4c: Same as B.4a except for vertical velocity

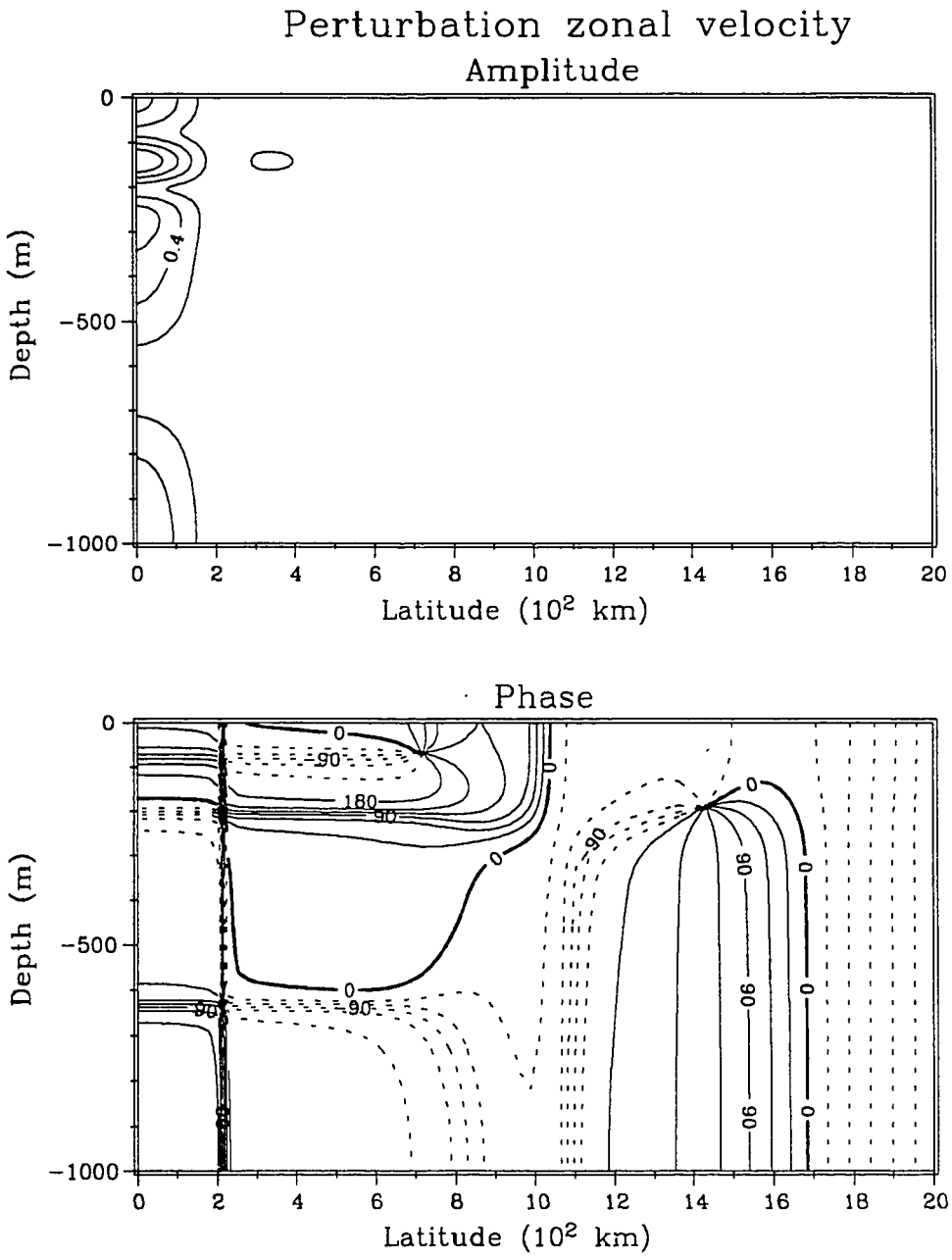


Figure B.5a: Perturbation zonal velocity for the 3rd vertical mode in resting ocean.

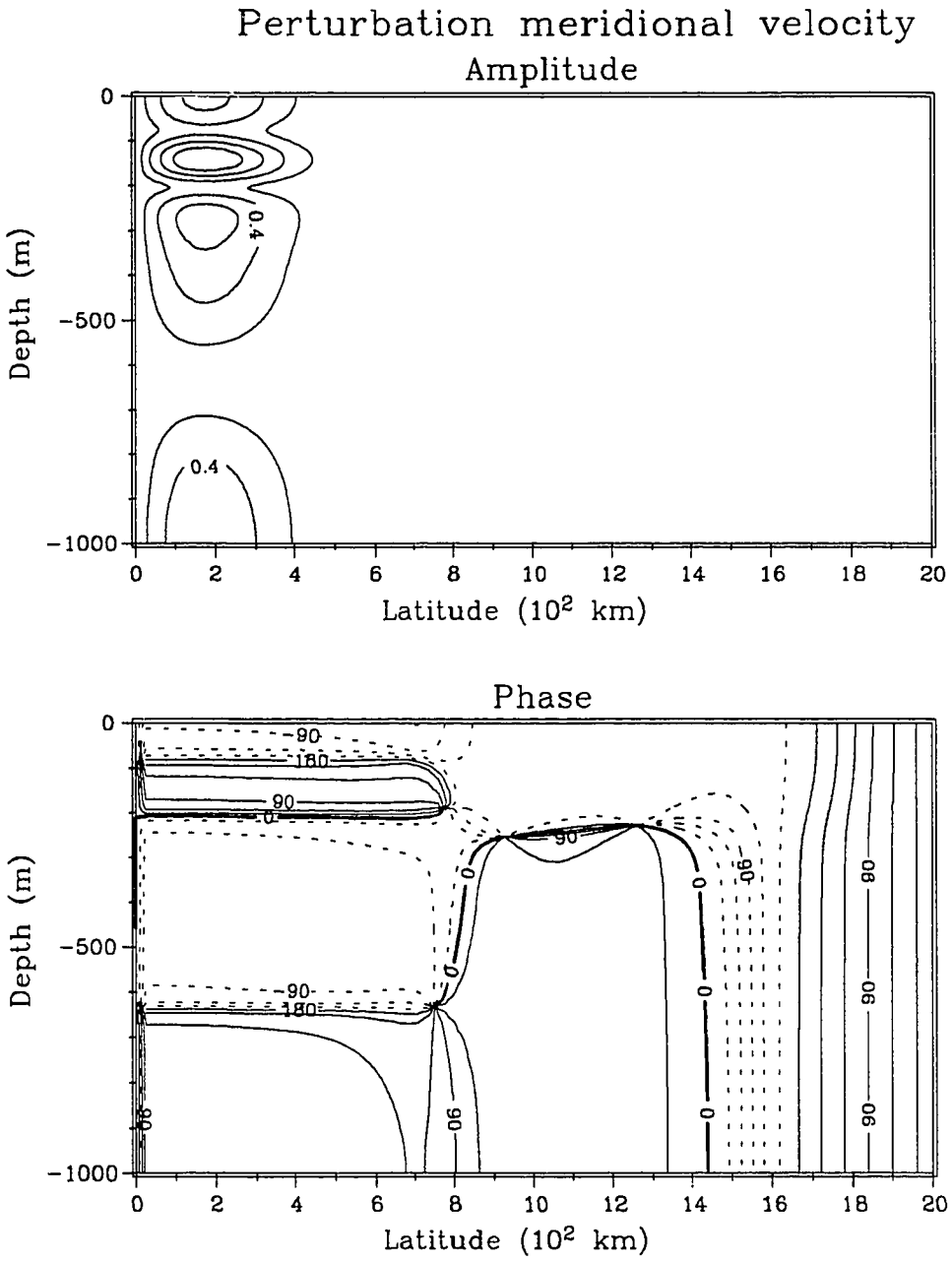


**Figure B.5b: Same as B.5a except for meridional velocity**

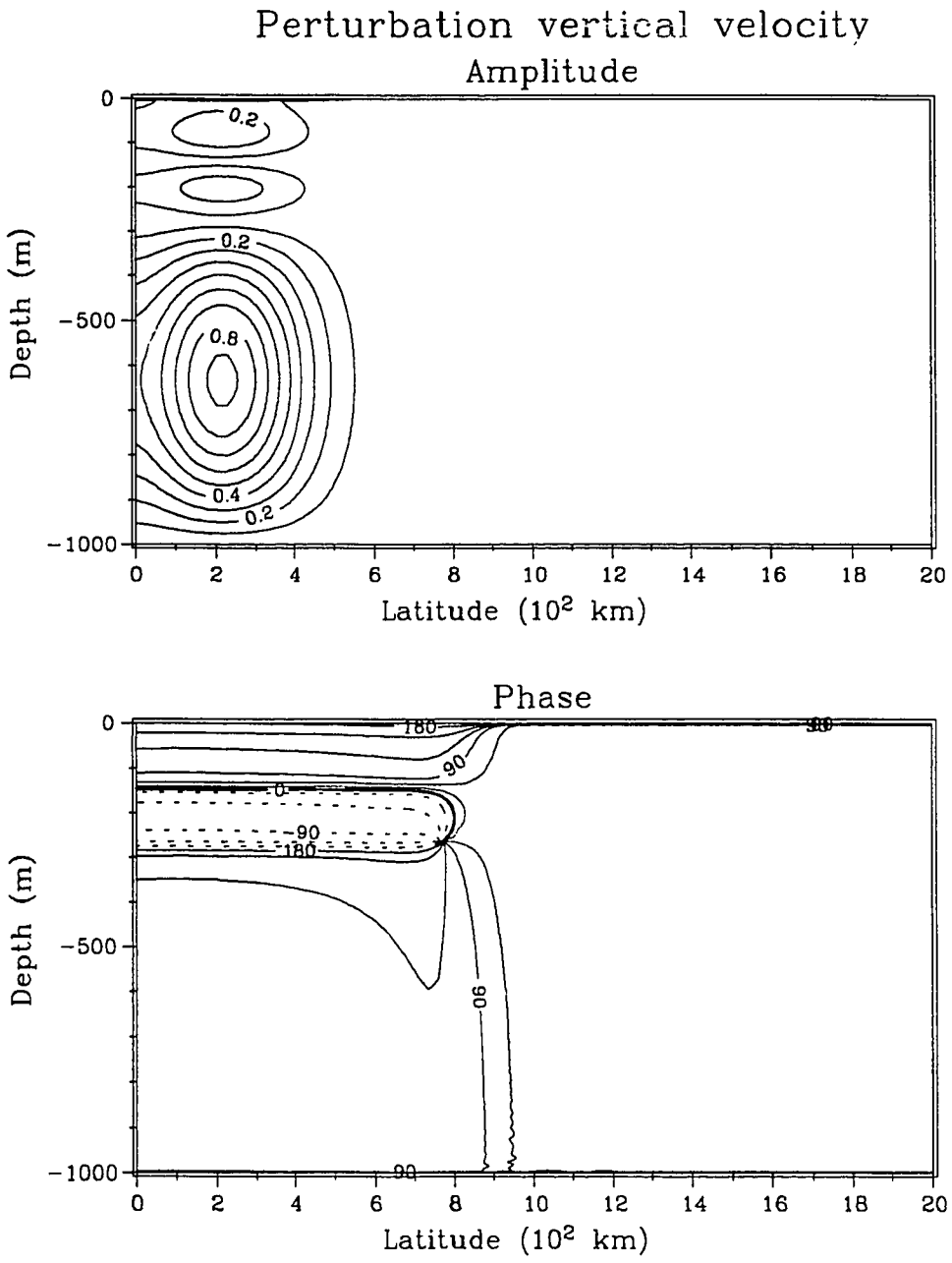


**Figure B.5c: Same as B.5a except for vertical velocity**

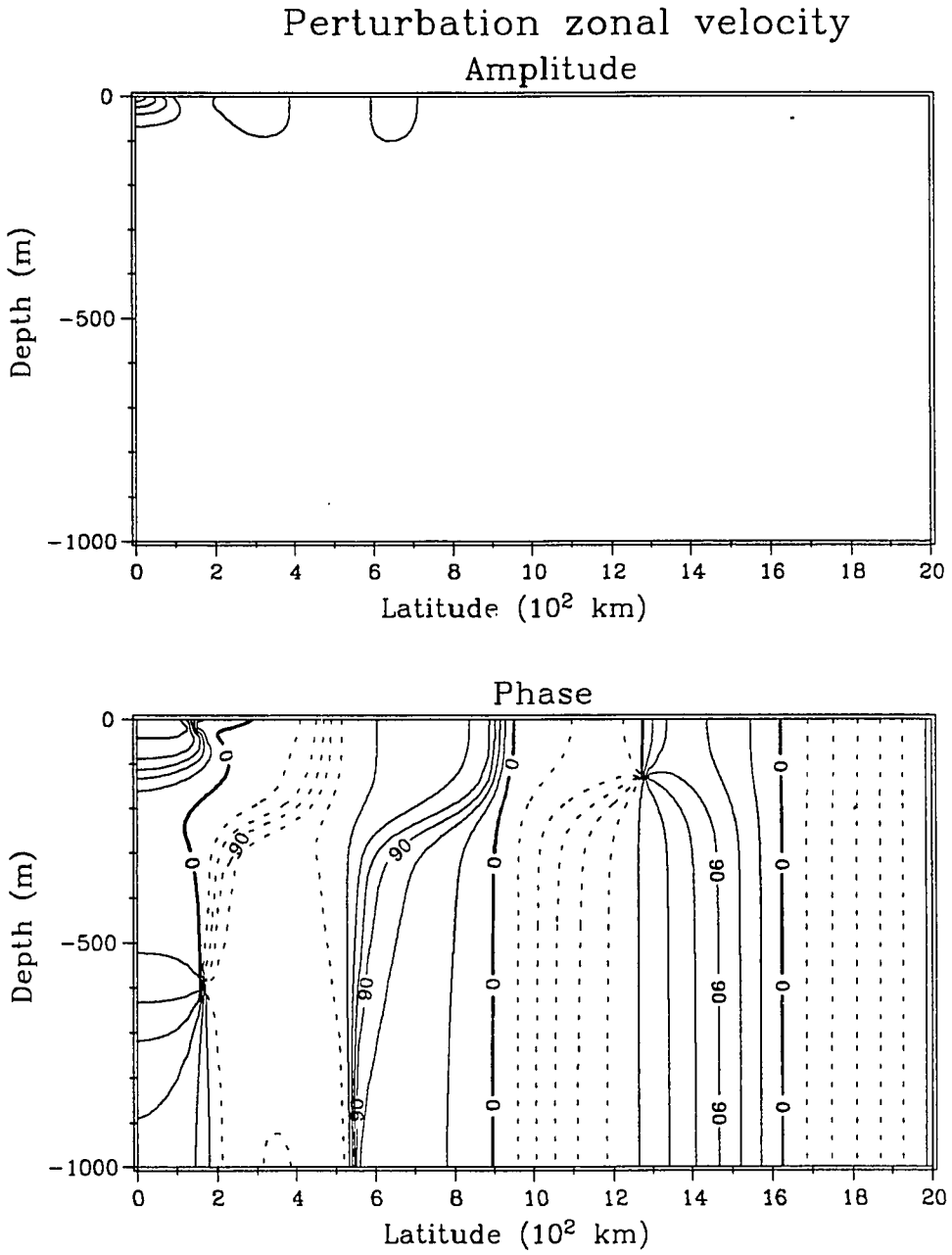


Figure B.6a: Perturbation zonal velocity for the 3rd resonance in the realistic simulation of Undercurrent and South Equatorial Current.

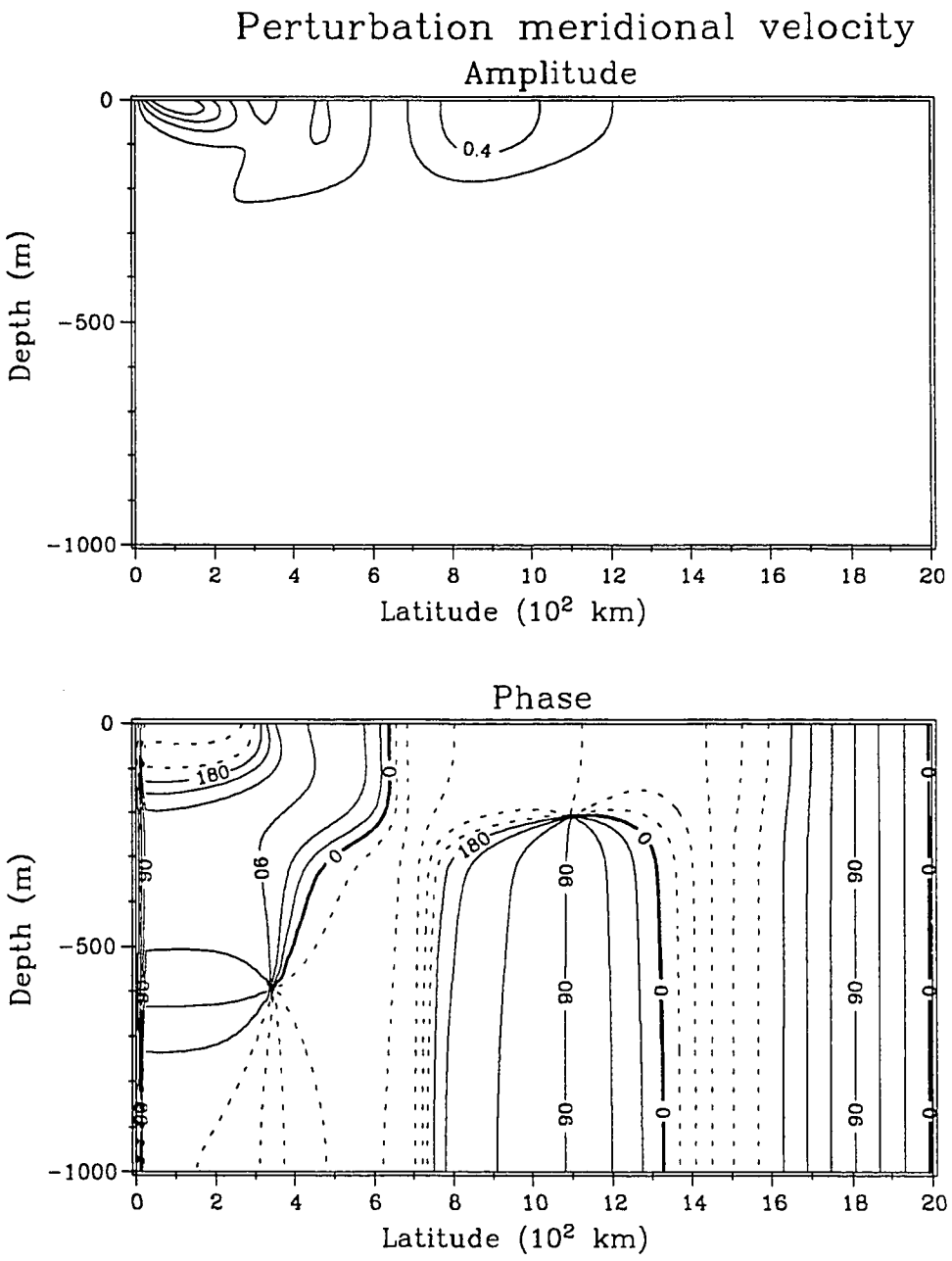


**Figure B.6b: Same as B.6a except for meridional velocity**

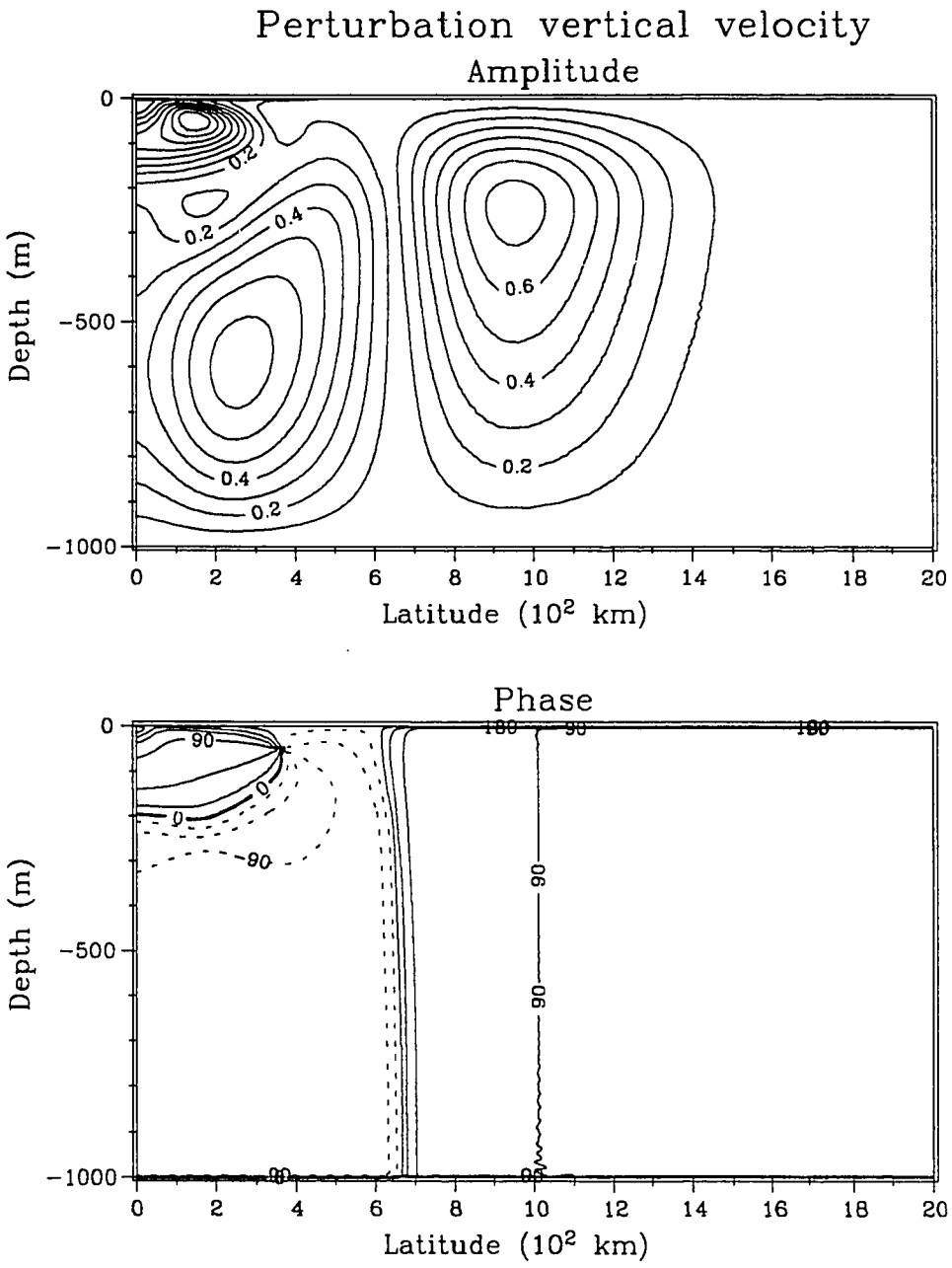


Figure B.6c: Same as B.6a except for vertical velocity

# Vitae

Jeffrey A. Proehl

## PERSONAL

Born 28 Sept 1958; Decatur, Illinois; Married to Jean Ann (Brewer); 1 child (Christopher).

## EDUCATION

| | |
|---|---|
| M.S., 1982 | in Physical Oceanography, University of Washington, Seattle, WA. Research topic: Low Frequency Response of Wide Deep Estuaries to Non-Local Atmospheric Forcing |
| B.S., 1980 | Cum Laude, in Marine Sciences, University of South Carolina, Columbia, SC. Transfer from University of Wisconsin - LaCrosse, LaCrosse, WI. |
| High School, 1976 | LaCrosse Central High School, LaCrosse, WI. |

## PUBLICATIONS


1. Kjerfve, B. and J.A. Proehl, 1979: Velocity variability in a cross-section of well-mixed estuary. *J. Mar. Res. 37*(3):409-418.

2. Kjerfve, B., L.H. Stevenson, J.A. Proehl, T.H. Chrzanowski and W.M. Kitchens, 1981: Estimation of material fluxes in an estuarine cross-section: a critical analysis of spatial measurement density and errors. *Limnology and Oceanography, 26*(2):325-335.

3. Kjerfve, B., J.A. Proehl, F.B. Schwing, H.E. Seim and M.M. Marozas, 1982: Temporal and spatial considerations in measuring estuarine water fluxes. In: *Estuarine Comparisons*, V. Kennedy, ed, pp 37-51.

4. Proehl, J.A. and M. Rattray Jr., 1984: Low frequency response of wide, deep estuaries to non-local atmospheric forcing., *J. Phys. Ocean., 14*(5):904-925.

5. McPhaden, M.J., J.A. Proehl and L.M. Rothstein, 1986: The interaction of equatorial Kelvin waves with realistically sheared zonal currents., *J. Phys. Ocean., 16*(9):1499-1515.

6. Proehl, J.A., M.J. McPhaden and L.M. Rothstein, 1986: A numerical approach to equatorial oceanic wave-mean flow interactions. In: *Advanced Physical Oceanographic Numerical Modeling*, J.J. O'Brien, Ed., pp 111-126.

7. McPhaden, M.J., J.A. Proehl and L.M. Rothstein, 1987: On the structure of low frequency equatorial waves., *J. Phys. Ocean., 17*(9):1555-1559.

8. Rothstein, L.M., M.J. McPhaden and J.A. Proehl, 1988: Wind forced wave-mean flow interactions in the equatorial waveguide: I. The Kelvin Wave. In press, *J. Phys. Ocean.*